Hyperpolarized Silicon Particles as In-vivo Imaging Agents

Dissertation Advisor: Charles M. Marcus Maja Clare Cassidy

Hyperpolarized Silicon Particles as In-vivo Imaging Agents

Abstract

This thesis describes the development of hyperpolarized silicon particles as a new type of magnetic resonance imaging (MRI) agent. Silicon particles are inexpensive, non-toxic, biodegradable, targetable, and have unique physical properties that lead to extremely long nuclear polarization times. The ^{29}Si nuclei are hyperpolarized by low temperature dynamic nuclear polarization using naturally occurring defects at the particle surface and directly imaged using ^{29}Si MRI. The imaging window achievable is several orders of magnitude longer than other hyperpolarized imaging agents. The technique requires no additional imaging agent to be incorporated into the silicon, and so toxicity complications are reduced.

The construction of a system for low temperature dynamic nuclear polarization and a NMR spectrometer for studying the nuclear polarization dynamics in silicon particles is described. Room temperature nuclear spin relaxation (T_1) times are investigated for a variety of silicon particles spanning five orders of magnitude in mean diameter, from 10nm nanoparticles to mm-scale granules. The nuclear T_1 times of all Si particles are found to be long, ranging from many minutes to several hours at room temperature. T_1 is found to be a function of particle size, dopant concentration, synthesis method and crystallinity.

A core-shell model to describe the electron and nuclear spin dynamics in the particles is developed. The decay in nuclear hyperpolarization is studied as a function of ambient magnetic field and temperature, demonstrating that the long spin relaxation times persist despite changing environmental conditions. A new technique is reported for enhancing the dynamic nuclear polarization in silicon particles using modulated microwave irradiation. A theoretical model for understanding this enhanced polarization process is developed. As well as providing an efficient mechanism for polarizing the ^{29}Si nuclei within the particle, the surface defects are also found to be efficient at polarizing ^{1}H nuclei in frozen solutions surrounding the particles.

Several in-vivo applications of hyperpolarized ^{29}Si MRI are demonstrated, including gastrointestinal imaging, intravenous imaging and mapping blood flow in a tumor. The spin relaxation rates are found to be unaffected by surface functionalization, the particles tumbling in solution, or the in-vivo environment.

Contents

Listing of figures

To Chris, for being so patient.

Acknowledgments

"Nothing of me is original. I am the combined effort of everyone I've ever known."

Chuck Palahniuk, *Invisible Monsters*

As the days of my PhD and the Marcus Lab at Harvard draw to a close, there are many people I must thank for helping me achieve the results that ares described in this thesis.

Firstly I have to thank Charlie for inviting me to join his research group and for managing such a well-organized environment where we had everything we needed to get our work done. I am particularly grateful for him giving me the intellectual freedom[1] to push these new ideas forward, and for giving me the confidence to trust my own instincts in a research area that was new to both of us. It was an adventure that spanned two coasts as well as a range of fields across physics, materials science and biomedicine that stretched me further than I ever could have imagined.

Menyoung Lee was an absolute delight to work with and together we formed a great team, despite (or perhaps because of) him being almost opposite to me in every way imaginable.

I learnt a great deal working with Sekhar Ramanathan and David Cory at MIT, and thank them for so generously letting me work on experiments in their lab during the first year of my PhD while we were awaiting delivery of the cryostat to Harvard.

There were several people that were involved in preliminary experiments for the project that greatly influenced the directions that my later work took. The efforts of Jacob Aptekar, Alex Johnson, Rob Barton, Linh Pham, Matt Rosen, Ross Mair, Alison Hill, Melis Anahtar, Yin Ren, Chris Farrar and guidance of Ron Walsworth, Sangeeta Bhatia and Bruce Rosen were crucial to this project getting off the ground. I also thank the many other undergraduates and high school stu-

[1] and most importantly money

dents I had the pleasure of working with: Winston Yan, Alex Ogier, Sam Rodriques, Carmen Lara, Dan Reeves, Jeff Hudson and Chinh Vo for their contributions to the project.

I am particularly grateful to Sekhar Ramanathan, Matt Rosen, Ross Mair and Winston Yan for their friendship and continued intellectual support of the project over last few years.

I thank Tonya Atkins and Susan Kauzlarich from UC Davis for their efforts synthesizing the excellent silicon nanoparticles samples described in Chapter 6, as well as Joel Agar from LBL for providing us with the sample of isotopically enriched ^{29}Si which was used for measurements in Chapters 7 and 9.

The in-vivo experiments described in Chapter 8 would never have become a reality without the generosity, optimism and hard work of Pratip Bhattacharya at HMRI in Pasadena. Thank you for patiently teaching me so much about biology and biomedicine, and for believing me when I continued to assure you that things would eventually work, despite things taking much longer than expected[2]. These experiments also would not have been possible without the fine surgery skills of Henry Chan. However it was his creative thinking and all around great attitude that propelled me forward and made the long days and nights of the in-vivo experiments tolerable. Thanks to Brandon Armstrong, Larry Robertson, Niki Millward and Pom Sailasuta for joining me on the relentless battle against the scanner.

Despite following a slightly different (and bicoastal) trajectory than its other members, the Marcus Lab has really felt like home for me the past few years. The culture of humor, hard work and positive attitude within the lab as well as the desire to do the right thing is truly inspirational and it was a privilege to have been part of it.

In my early days in the lab I was welcomed each morning by lovely german singing from Christian Barthel[3] and Ferdinand Kuemmeth[4]. Assimilation tactics and good advice was always received from Jimmy Williams[5] and David Reilly. I have enjoyed many stimulating discussions as well as outdoor adventures[6] with Patrick Herring, who seems to know most things about almost everything. Thanks to Jim Medford for maintaining my magnet so reliably for the almost year I was in Pasadena, and for being my stand-in experimental partner any time an experiment, theory or code needed some sanity checking[7].

Thanks to the many other post-docs, graduate students and undergraduates who I overlapped with: Hugh, Patrick Gallagher, Johannes, Willy, Andrew, Angela, Doug, Vlad, Javad, Teesa, San-

[2]and sometimes evidence pointing to the contrary

[3]possibly the funniest person I have ever met

[4]possibly the smartest person I have ever met

[5]particularly on converting Australian english colloquialisms to American

[6]usually involving both rapid ascents and descents of mountains

[7]as well as for keeping me up to date on all popular culture I have somehow missed out on for my entire life

dro, Max, Edward, Merritt, Ruby, Anna, Yiming, Jeff, Ilse, David Marcos, Yongjie, Shu, Susan, Morten, Gento, Valla, and many more I probably have forgotten. I have very much enjoyed your company.

I am extremely grateful to our lab administrators: Danielle Reuter, Jess Martin and Rita Filipowitz for keeping the lab running smoothly, and somehow keeping the experiment (and me) funded in Pasadena for so long. I also thank the administrators in the SEAS school office for handling my administrative matters professionally and always with a friendly smile.

I benefited greatly from the technical expertise of Nick Dent from Oxford Instruments, Leon Kozul from Aerowave, Naresh Deo from Quinstar, as well as Louis De Feo and his talented staff in the SEAS machine shop. I really appreciated the skill and dedication of the technical staff of the Center for Nanoscale Systems at Harvard, in particular this thesis benefited from the help of David Bell, Dave Lange, Fettah Kosar and John Tsakirgis. I also thank Bill Collins and Shaw Hwang from the chemistry department's magnetic resonance facility for assistance with low temperature ESR measurements, and Bill Croft for assistance with XRD measurements. Thanks to Brian Ross, Keiko Kanamori, Thao Tran, Colleen Oinuma, Shawn Wagner, Larry Jones, Edna Smith, Janet Baer, Jo and Fran at HMRI, especially for the excellent animal care.

I thank the members of my quals and dissertation committee: Donhee Ham, Navin Khaneja, Bob Griffin and Bob Westervelt for their guidance and careful reading of this thesis. I am grateful to the NIH and the NSF as well as the Harvard NSEC for the funding that kept these experiments afloat, and to the Menzies Foundation and the Harvard Club of Australia for keeping me afloat.

Outside lab, I very much enjoyed being a teaching fellow for Harry Lewis, where I not only learnt a great deal about digital security and privacy, but also about undergraduate education both at Harvard and the US, and developed an appreciation for the importance of a broad based education for all students.

I would like to express my sincere thanks to the staff at HUHS for making sure I received excellent care while at Harvard and also on the west coast. Finally, I thank my family and Chris for their love and support, and for reminding me that most things can be achieved through hard work and by remembering to get up each morning.

1

Introduction to Nanomedicine and Medical Imaging

The ability to diagnose and treat disease at the cellular level offers a revolutionary approach to clinical medicine. This revolution is not new however, the idea of "the mechanical surgeon inside the blood vessel" to observe, report and perform surgery was originally proposed in Richard Feynman's famous 1959 lecture "There's plenty of room at the bottom"[1]. The developments in nanotechnology that have followed in the subsequent half century have allowed us to

grow materials, such as particles [2–6], rods [7], wires [8, 9] and tubes [10, 11], on the micro and nanoscale with tailored materials properties [12–14]. These micro and nano vectors act as scaffolds for drugs and targeting compounds, with the hope of targeting specific sites of disease and delivering a payload at the correct time. The vectors range in size, covering several orders of magnitude from nanometers up to many microns, which cover a wide range of biological sizes from proteins to viruses up to the scale of individual cells (Fig. 1).

Besides the obvious benefits received from being a comparable size to biological elements, the nano-micro size scale brings about two key advantages. Firstly, the materials have an extremely high surface to volume ratio that enables a high concentration of targeting compounds to be attached. Secondly, confinement at the nanoscale also brings about unique properties that differ to that of the bulk, such as photoluminescence [2] or Raman activation [12].

The first applications of nano medicine utilized these high surface to volume ratios for controlled release of drugs and polymers in-vivo [15–17]. The breakdown rate of a material in-vivo is strongly dependent on the surface coating and surface area exposed to the in-vivo environment, not only on the underlying material, and so by tuning the particle size and coating to a known breakdown rate, drug delivery can be optimized for specific applications. Lipid-based nanoparticles, such as liposomes or micelles, are simple self-assembled spheres ($\sim$ 30-100 nm in size) made up of phospholipid molecules, the same materials as cell membranes. The cores of these particles can be loaded with a payload of drugs [17], RNA [18], or peptides [19] that is released slowly over time. Due to their biocompatibility, they were amongst the first nanomedicines approved by the FDA for clinical use[1]. When administered intravenously, small chemicals such as drugs, RNA, and peptides ($<$ 5 nm in size) are quickly cleared from the body via renal pathways within tens of minutes, often without completely reaching their intended target. When continued within a larger micelle or liposome, this immediate clearance is prevented, improving circulation times and ultimately allowing a lower drug dose to be administered to achieve the same clinical

[1]Out of the current $\sim$ 12 nanomedicines FDA approved, 10 are micelles and liposome based.

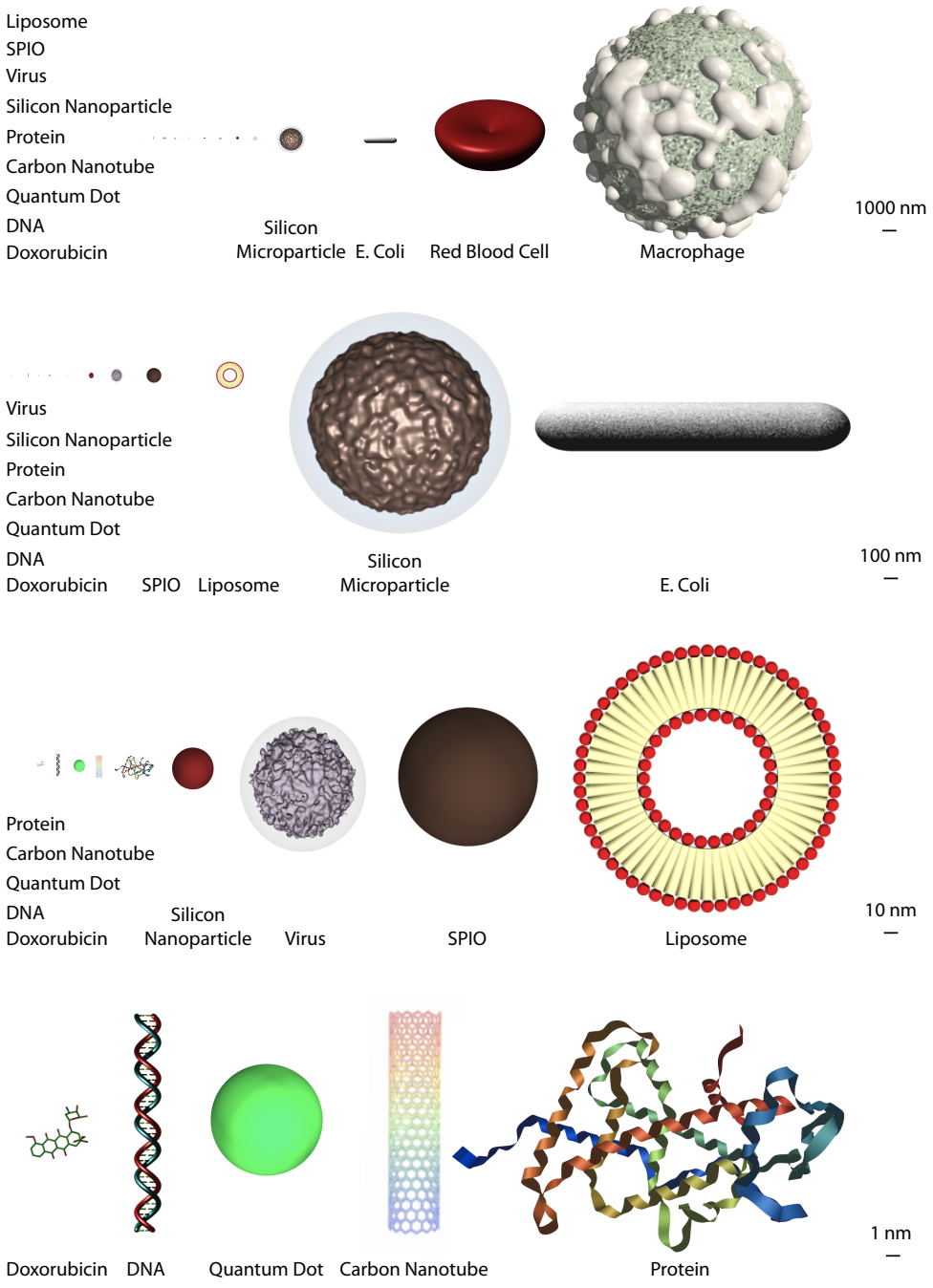

Figure 1: Size scales of biological and nano materials. The silicon nanoparticles and microparticles shown are approximately the size of those used in this thesis.

treatment. For example, the commonly used cancer drug doxorubicin (Dox) is hydrophobic and therefore has short circulation times. It has been shown that liposomes loaded with Dox are more effective than Dox alone in treating a variety of solid tumors [20–22] and are now FDA approved (Doxil, Johnson and Johnson)[2]. Many other micro and nano vectors under development utilize similar breakdown techniques, with the aim of improving delivery of poorly water-soluble drugs [20, 23], delivering drugs across poorly penetrable membranes such as the blood brain barrier [24, 25], or deliver multiple drugs simultaneously for combination therapy [26].

As well as particle size, the shape, surface charge and surface chemistry are all important factors in determining how nano and micro vectors behave in-vivo [27–29]. Unless these conditions are optimized, circulation times are limited as nanomaterials are quickly consumed by macrophages and accumulate in the organs of the mononuclear phagocyte system (MPS) such as the liver and spleen. Many initial demonstrations of targeting took advantage of this effect, allowing improved drug delivery to the liver and immune system [30]. Similarly, demonstrations of in-vivo targeting of nanomaterials to tumors has been largely due to passive accumulation resulting from the enhanced permeability and retention (EPR) effect, which occurs simply due to a higher concentration of blood vessels in the tumors [31, 32].

Although very biocompatible, the simple phospholipid chemistry of micelles and liposomes limits both their size and breakdown rate, and does not provide a structural mechanism for attaching targeting compounds. The desire for active targeting and better control of sizes and breakdown properties has resulted in a significant amount of research into finding new biocompatible vectors that can take the role of multifunctional agents that combine targeting, drug delivery and imaging. Examples of these new materials include polymer nanoparticles [33, 34], carbon based structures such as nanotubes [35, 36], and solid structures such as silica [37] and porous silicon [38, 39]. As the design of these new nanomaterials has become more complex, testing the effects of small changes in these parameters on targeting, circulation time, and biocompatibility has become ex-

[2]It should be noted that Doxil and many other liposomes for chemotherapy have suffered from extreme supply issues leading to their rationing

tremely necessary. Non-invasive imaging is key in providing this information in a fast and cost effective manner. Additionally, recent works have investigated the concept of incorporating diagnostics as well as therapy into the nano medicine [40]. Successful diagnostics requires transfer of information of the in-vivo environment, not only the vector's location, but also its concentration, local chemical environment, or binding success to the treating physician. Non invasive imaging is therefore a key requirement for these new types diagnostic nanomaterials in a clinical setting.

1.1 Medical imaging modalities

Recent years has seen a growth in the use of non-invasive imaging technologies in the clinical setting, either providing structural, or biochemical information for diagnosis. Generally they can be classified into those utilizing ionizing radiation, such as X-ray and computerized tomography (CT) and positron emission technology (PET)/single photon emission computerized technology (SPECT) and those using non-ionizing radiation such as optical imaging (OI), magnetic resonance imaging (MRI), or ultrasound (US). Each technique has specific advantages and disadvantages in terms of resolution, sensitivity, and cost (Fig. 1.1.2). New techniques combine these modalities to produce detailed co-registered images that provide visualization of molecular information within an anatomic framework. We will briefly review these techniques, and then discuss their use in imaging of nano materials.

1.1.1 X-ray imaging and CT

The first non-invasive medical imaging was performed in 1895, when Wilhelm Rontgen used X-rays generated from a cathode ray tube to image the bone structure of his wife's hand. X-ray imaging operates on the simple principle that soft tissue is more transparent than hard tissue such as bone. Since then, the technique has seen remarkable improvement with the development of focussed x-ray sources and solid state detectors allowing resolution down to 1 mm. The low cost and

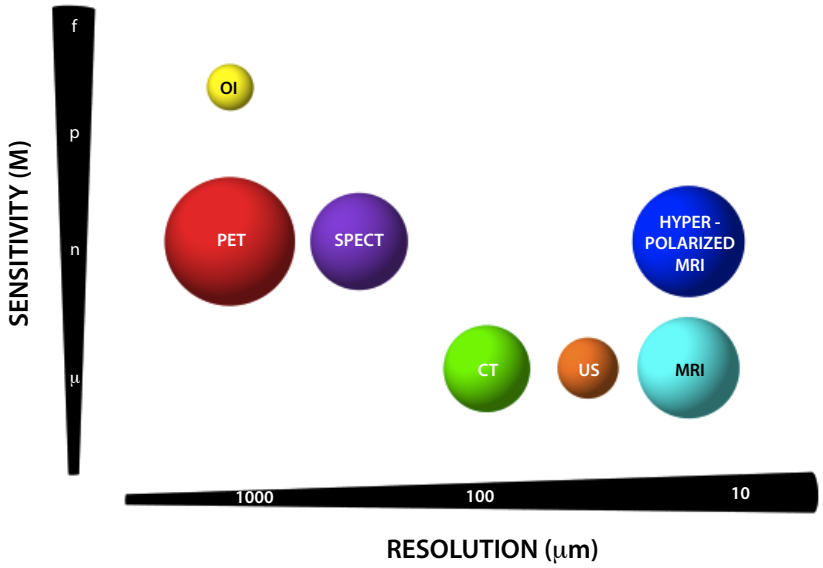

Figure 1.1.1: Sensitivity, resolution and cost trade-offs of clinical imaging modalities. The relative costs are denoted by the size of the bubble. It should be noted that MRI and PET can provide biochemical information as well as structural information in the image.

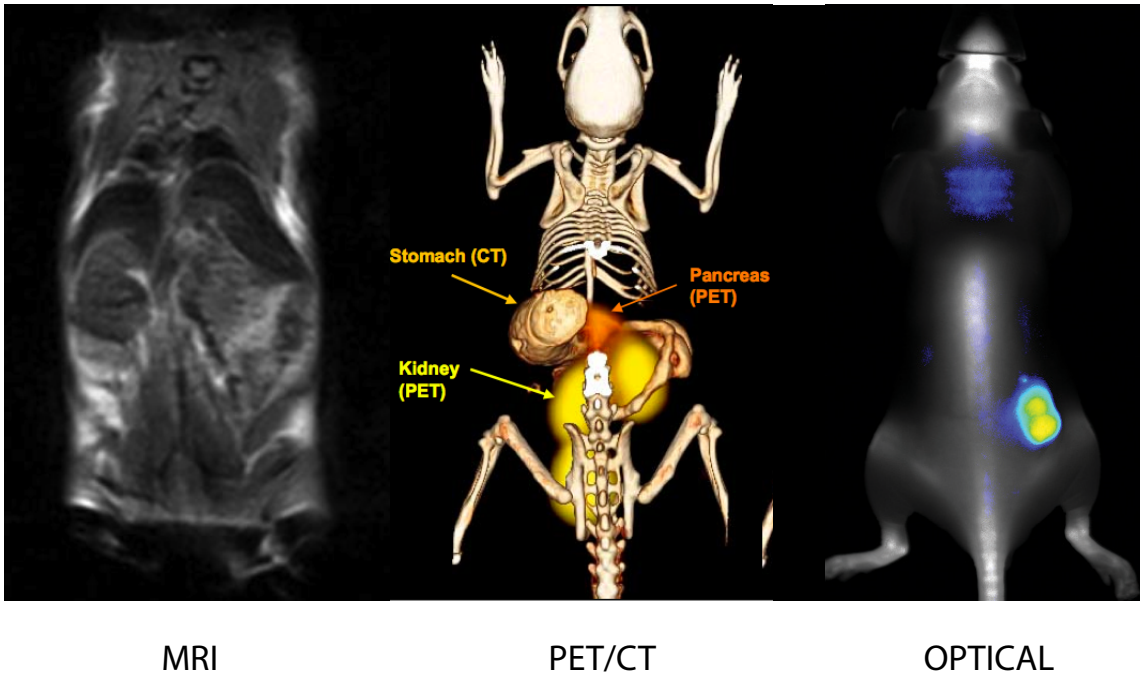

Figure 1.1.2: Examples of images obtainable with commercial small-animal ^{1}H MRI, PET/CT [41] and optical [42] imaging systems.

fast image acquisition rate combined with the excellent structural resolution has led to the technology becoming an essential tool in clinical medicine. The development of computer tomography (CT) X-ray in the 1970s, where the X-ray source and detector are quickly rotated around the area, has allowed for the creation of detailed 3D structural images with isotropic resolution in the sub mm regime. Additional contrast in x-ray and CT images (for example angiography, where a picture of the blood vessels is generated) can be achieved by injection of a 'heavy' element (bromine, iodine, gold etc.) that strongly absorb x-rays. Comparison of images with and without contrast results in a picture of the where the contrast agent was located. The strong absorption of X-rays by tissue leads to safety concerns, however, and clinical studies have shown that there is s statistically significant increase in cancer risk for people exposed to multiple CT scans [43].

1.1.2 PET and SPECT

Instead of an external radiation source like in x-ray and CT, positron emission tomography (PET) and single-photon emission computerized tomography (SPECT) use an injectable contrast agent as the source of radiation for imaging. These techniques are know collectively as nuclear medicine, as they monitor the decay of a radionuclide through the collection of gamma rays. In PET, a radionuclide undergoes β^+ decay, emitting a positron. The positron travels a small distance (of order 1 mm) before interacting with an electron. The particles annihilate each other and a gamma ray pair is emitted. These photons are detected as temporally resolved pairs 180 degrees apart from each other on a external detector. Statistical analysis of many thousands of events allows a picture to be built up of the location of the decaying nuclei. SPECT operates on a similar principle, however instead the nucleus emitting a positron, it directly emits a gamma ray which is collected on an external detector. For 3D SPECT images, the detector is rotated around the body similar to 3D CT, while for PET, a series of cylindrical detectors is often used. Much higher resolution is achievable with PET than SPECT, as the time difference between arrivals of photon pair provides more radiation event localization information. Together these techniques offer numerous appli-

	Isotope	Half life	Compound	Clinical Application
PET	^{11}C	20 min.	^{11}C-methionine, ^{11}C-thymidine	Cancer
		20 min.	^{11}C-palmitic acid	Myocardial disease
		20 min.	^{11}C-altropane, ^{11}C-CFT,	Dopamine receptors: Parkinson's disease, schizophrenia, drug addiction
	^{13}N	10 min.	^{13}N Ammonia	Myocardial disease
	^{15}O	2 min.	^{15}O2	Metabolism: Cancer, Stroke, Altzeimers
	^{18}F	110 min.	^{18}F- Fluorodeoxyglucose	Glucose metabolism: cancer, stroke, altzeimers
			^{18}F-5-fluorouracil	Cancer
	^{82}Rb	2 min.	Rubidium chloride	Myocardial perfusion imaging
SPECT	^{99}Tc	6 hr.	^{99}Tc-tetrofosmin	Myocardial disease
			^{99}Tc-HMPAO	Glucose metabolism
	^{123}I	13 hr.	Iobenguane	Neuroendocrine or neurological tumor
	^{111}In	3 days	In-vitro labelled leukocytes	Immune system

Table 1.1.1: Radionuclides used in clinical medicine and their half-lives.

cations for both structural and functional imaging over a range of timescales. A list of clinically approved PET and SPECT isotopes, together with their half-lives and applications is shown in Table 1.1.1. The radioisotope can be a simple soluble dissolved ion that has chemical properties that allow it to be concentrated in ways of medical interest for disease detection, such as a radioisotope of ^{82}Rb (PET) or ^{99}Tc (SPECT), or it can be functionalized as part of a metabolic agent, the most common of which is ^{18}F-Fluorodeoxyglucose.

Due to the relative short half-lives of PET nuclides, the cyclotron used to produce the radioactive compound must be located close to the imaging facility. A cyclotron that can produce a range of radioisotopes is extremely expensive to buy and operate, and so use is not widespread. Additionally, organic radiotracer molecules that will contain a positron-emitting radioisotope cannot

be synthesized first and then the radioisotope prepared within them, because bombardment with a cyclotron to prepare the radioisotope destroys the organic carrier. Instead, the isotope must be prepared first, then afterward, the chemistry to prepare the organic radiotracer accomplished very quickly. SPECT nuclei have much longer half lives, and so can be shipped from a central production facility to the location of delivery.

The energy of the emitted gamma rays has a significant interaction with all aspects of the body, causing DNA replication errors, chromosomal abnormalities and cell death [46]. Given in high enough doses, this energy is sufficient to kill cells and so some long lived radionuclides are used in targeted chemotherapy [47]. Short-lived radionuclides minimize the radiation dose to the subject, however repeated exposures to these imaging procedures show an increased rate of cancer similar to X-ray/CT [48].

1.1.3 MRI

Magnetic resonance imaging (MRI), and its underlying phenomenon, nuclear magnetic resonance (NMR) are based on the interaction of the magnetic moment of atomic nuclei with an external magnetic field. NMR was first demonstrated independently by Bloch [44] and Bloembergen, Pound and Purcell [45], and rapidly evolved into an important tool for chemistry, biochemistry and physics in subsequent decades. MRI imaging was first demonstrated by Lauterbur in 1973 [49], and has evolved into an essential tool in diagnostic medicine. Many atomic nuclei possess a magnetic moment and can hence be investigated by NMR, but the clinical use of MRI has to date largely been restricted to ^{1}H as it is found at very high concentration (about 80 M) in biological tissues. The strength of the signal for imaging is proportional to the number of spins, the polarization and the number of signal averages acquired, and so a large number of spins ($\sim 10^9$) are required for imaging. The ^{1}H nucleus is more strongly coupled to the external field than other nuclei (as described by its gyromagnetic ratio γ) and so has a higher thermal polarization at a given magnetic field and temperature. The resonant frequency, or Larmor frequency, of each nu-

cleus in a magnetic field is determined by this coupling $\omega_n = \gamma B_o$, giving each nuclear species a spectroscopic fingerprint. Additionally, small changes in the local magnetic environment of each nucleus, such as the presence of other spins can cause small shift in this resonant frequency allowing individual chemicals to be determined.

Three dimensional images are generated by applying small perturbing magnetic fields $\frac{\delta B_z}{dx}$, $\frac{\delta B_z}{dy}$ and $\frac{\delta B_z}{dz}$ in the direction of the main magnetic field with respect to the three spatial dimensions x, y, and z. This causes the Larmor frequency to be shifted for spatially separated nuclei by $\delta\omega = \gamma\delta B$, and a two dimensional Fourier transform of the received data generates a map of signal intensity versus position.

MRI is most frequently used for obtaining structural information about opaque objects by comparing areas of differing ^{1}H concentrations within the body. However, spectroscopic identification allows the location and concentrations of individual chemicals to be determined with a technique called chemical shift imaging (CSI) [50].

Contrast in ^{1}H MRI is most commonly generated by manipulation of the parameters in the imaging sequence, as different tissues (bone, soft tissue) have different spin relaxation (T_1) and spin coherence (T_2) times. This contrast can be artificially enhanced by introducing a paramagnetic material, the most common of which are gadolinium chelates. These chelates have seven unpaired electrons that produce a significant magnetic moment which shortens the T_1 of the local ^{1}H nuclei and thus alters signal intensity in the region near the contrast material. [3]

In comparison to CT, PET and SPECT, ionization effects from MRI studies are negligible, as the electromagnetic energy involved in the imaging process is much lower, resulting in frequencies in the MHz (10^6 Hz) range rather than $10^{15} - 10^{18}$ Hz.

[3] Recently the US FDA has issued a warning of increased risk of kidney failure for patients with kidney disease who are subjected to contrast enhanced MRI exams [51]. This has prompted the search for alternatives to Gd.

1.1.3.1 Hyperpolarized MRI

A consequence of the small energy ($E = \hbar\omega_n$) of the nuclear magnetic moment is that at standard clinical magnetic fields and temperatures the nuclear polarization is low ($\sim$ 1 part in $10^{-5} - 10^{-7}$). One way of increasing the signal of a nuclear species is to increase its nuclear polarization using a process known as hyperpolarization. Hyperpolarization was initially developed for making spin polarized targets for neutron scattering experiments in the 1960's, however is now used across a number of fields including physics, materials science, biology and medicine. A variety of techniques can be used for hyperpolarization, including optically pumping, low temperature dynamic nuclear polarization, Overhauser dynamic nuclear polarization and parahydrogen induced hyperpolarization. Many nuclei can be hyperpolarized using these techniques, however usually for clinical applications hyperpolarization is performed on spin-1/2 nuclei, as their lack of quadrupolar moment means that their relaxation is insensitive to electric fields. A schematic of the periodic table showing commonly hyperpolarized nuclei and their associated techniques is shown in Fig. 1.1.3.

A number of clinical applications of hyperpolarization have been developed in the past two decades. Hyperpolarized noble gases have shown great promise in structural imaging of the lungs [52, 53], whilst hyperpolarized ^{13}C and ^{15}N metabolites have been used for studies of metabolism and pH in oncology [54–57].

The key requirement for hyperpolarization is the transfer of spin angular momentum from a highly spin polarized source to the target nuclear spins, allowing the nuclear polarization to be increased by three to six orders of magnitude. This polarized spin bath takes the form of an optically pumped Rb vapor for noble gas experiments [58], or for liquid state metabolites, a free radical that is mixed in with the substrate of interest [59–61], or parahydrogen in combination with an organo-metallic catalyst [57, 61].

A key metric for a hyperpolarized material to be used *in-vivo* is the length of time it remains

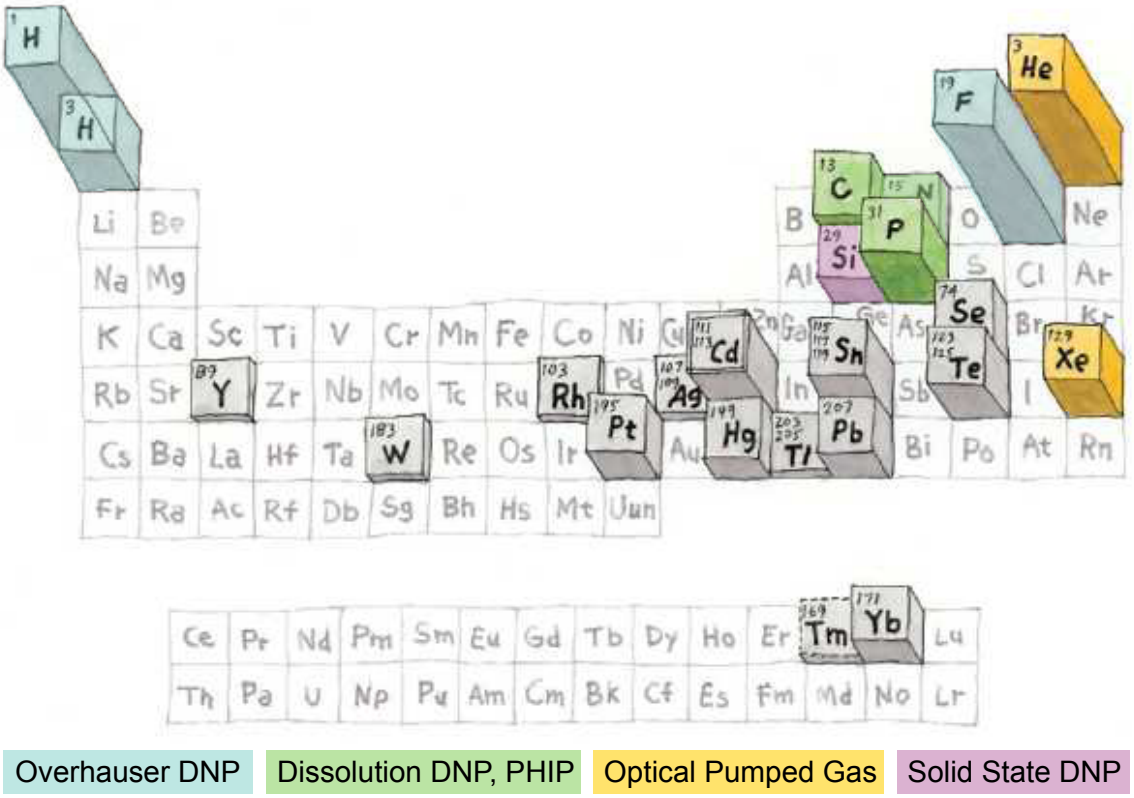

Figure 1.1.3: Period table of nuclei suitable for in-vivo hyperpolarization. Spin 1/2 nuclei are depicted as columns out of the page. The height of the column is proportional to the strength of the gyromagnetic ratio. This image is a modified version of an image provided to the author by Prof. Jan Henrik Ardenkjaer-Larsen.

hyperpolarized after this spin transfer has taken place (T_1). Unlike materials that polarize to thermal equilibrium, once the polarization has been consumed, or T_1 relaxation has taken place, the material must undergo hyperpolarization again to restore the signal. A list of clinically relevant hyperpolarized materials, their in-vivo T_1 times and clinical applications are shown in Table 1.1.2.

1.2 In-vivo imaging of nanomaterials

In-vivo imaging of nanomaterials allows understanding and characterization of the in-vivo kinetics of the nanomaterial, can provide diagnostic information, and also provide a means to predict

Nucleus	Compound	Hyperpolarization Method	*In-vivo* T_1(s)	Clinical Application
^{1}H	Water	Overhauser	< 1 [62]	Perfusion imaging
^{13}C	Pyruvate	DNP	48 [63]	Metabolic imaging - TCA cycle
^{13}C	Acetate	DNP	< 5 [64]	Metabolic imaging - peptides
^{13}C	Fumarate	DNP	29 [63]	Metabolic imaging - TCA cycle
^{13}C	Bicarbonate	DNP	43 [63]	Metabolic imaging - TCA cycle
^{13}C	Succinate	DNP	27 [65]	Metabolic imaging - TCA cycle
^{129}Xe	Xenon - cage	Optical pumped	66 [66]	Binding
^{129}Xe	Xenon (gas)	Optical pumped	5 [67]	Lung imaging
^{3}He	Helium (gas)	Optical pumped	20 [68]	Lung imaging
^{86}Kr	Krypton (gas)	Optical pumped	2 [69]	Lung imaging
^{15}N	Choline	DNP/PHIP	280 [70]	Cancer metabolism

Table 1.1.2: Hyperpolarized materials used in in-vivo studies.

possible toxicity and therapeutic behavior. The nanomaterial can be designed to have intrinsic properties that allow for direct imaging, or an artificial imaging material can also be integrated into the scaffold of the nanomaterial. Each of the in-vivo imaging techniques has a number of advantages and disadvantages that restrict them to specific applications.

1.2.1 Optical imaging of nanoparticles

Optical imaging of fluorescent markers has revolutionized in-vitro laboratory studies in biochemistry, allowing fast, sensitive, reliable and reproducible detection of the interactions of biomolecules with each other and molecular species. However, in-vivo applications of chemical fluorophores have been limited, as the molecules have poor stability and easily photobleach. Semiconductor quantum dots, such as CdSe and PbSe have emerged as a better alternative for in-vivo optical imaging, as they have a much higher quantum efficiency, can be engineered to have a broad absorption spectrum and the output emission can be extremely narrow and strongly dependent on

dot size. Cell autofluorescence and strong scattering in the visible regime that reduces resolution has led meant that most attention has been focussed on materials that emit in the near infrared (NIR) (> 700nm). At longer NIR wavelengths (> 950nm), the signal is strongly attenuated due to strong absorption by water and lipids, before a second imaging window opens up at $\sim$1350 nm. The practical imaging resolution is less than 1 cm penetration depth, and so clinical applications have focussed on endothelium imaging, or utilizing a confocal endoscopic camera. Carbon nanotubes have been shown to have strong fluorescence in the second NIR window [7], allowing deeper in-vivo imaging through layers of skin with higher sensitivity. It is common for small (< 10 nm) optically active nanomaterials to be loaded into a larger nanomaterial scaffold together with drugs, siRNA, proteins and peptides in order to provide tracking of the delivery of these in-vivo. Despite successful in-vivo imaging trials in small animals, clinical applications of most optically active quantum dots have not progressed due to concerns regarding the biodegradability of metallic nanoparticles and toxicity of degradation by-products, or in the case of nanotubes, the toxic structural characteristics of the nanomaterials themselves. Nevertheless, optical imaging is often the first and easiest technique for preclinical imaging in laboratory studies, due to its low cost and simplicity.

1.2.2 CT imaging of nanomaterials

Gold has a much higher atomic number and x-ray absorption coefficient than iodine, and so can provide enhanced contrast in CT imaging. Colloidal gold nanoparticles are a simple and relatively non-toxic way of delivering gold intravenously, have been used for CT imaging of the vascular structure [71–74]. Additionally the radiation dose in radiotherapy is enhanced at interfaces between elements of high and low atomic number, and so nanoscale gold has been used for killing tumor cells.

1.2.3 PET of nanomaterials

PET imaging of nano particles is performed by attaching a radionuclide of interest to the nanoparticle surface as a final stage in the process before injection. The ^{18}F isotope is the most commonly used for isotope due to its long half life. Using this technique for imaging is independent of properties of the nanovector, rather depending on the availability of chemical modification strategies that can be used to quickly attach the ^{18}F before delivery.

1.2.4 MRI of nanomaterials

The enhanced contrast generated by the paramagnetic properties of Gd chleates are further improved by utilizing a material with a stronger paramagnetic effect and by concentrating the amount of paramagnetic material in the local region of imaging. Superparamagnetic iron oxide (SPIO) nanoparticles were one of the first materials that had these properties, and a number of variations have been FDA approved for many clinical uses (see Table 1.2.1). When placed in a magnetic field, iron oxide develops a large magnetic moment which creates a large magnetic field gradient that shortens the local spin-spin relaxation (T_2) of nearby ^{1}H nuclei, creating regions with signal voids in the resulting image, an effect known as negative contrast. Due to this FDA approval, and the ubiquity of ^{1}H MRI, the incorporation of iron oxide into nanovectors is now a common technique for imaging new types of nanomaterials under development.

Paramagnetic nano particles can also be used for combined imaging and therapeutic applications. Radiofrequency irradiation of a high concentration of iron oxide nanoparticles results in local heating that causes cell death [75]. Use of nano materials with even high magnetic moments has also been investigated. Cobalt particles have a seven times higher sensitivity than SPIO [76], however readily oxidize and breakdown in-vivo, leading to significant toxicity effects [77].

An alternative method for generating high contrast is to image another nucleus apart from ^{1}H that is not found naturally in high concentrations in the body. For instance, the ^{19}F nuclei

Compound	Product name	Particle Size (nm)	Concentration (mg Fe/ kg body weight)	Approved Application
Ferumoxide	Ferridex	120-180	0.56	Liver and spleen lesions
Ferumoxtran	Combidex	15-50	2.5	Lymph nodes, metastatic activity, macrophage imaging
Ferumoxsil	GastroMARK	> 3500	160 mg Fe / dose	GI contrast
Feristene	Abdoscan (EU only)	300	90 mg Fe / dose	GI contrast
Ferucarbotran	Resovist	60	4.5	Liver and spleen lesions, cell labelling
Feruglose	Clariscan	20	3	Liver lesions

Table 1.2.1: FDA approved iron-oxide imaging agents. The concentration doses listed are in mg of Fe/ kg of patient body weight obtained from the manufacturer. Typically there is $10^{-3} - 10^{-6}$ pg Fe/particle. It should be noted that although receiving FDA approval, all agents are discontinued from production at the time of writing.

in fluorinated micelles and lipid based nanoparticles has been successfully imaged by MRI [78].

1.3 Motivation for this thesis

Despite several thousand unique studies of in-vivo applications of nanovectors, very few technologies have progressed to the stage of gaining approval for human use and being used in the clinic. The ideal imaging nanovector is:

- Non-toxic
- High-contrast - only low concentrations required
- Positive contrast
- Without background signal
- Visible deep into opaque structures
- Does not use ionizing radiation
- Affordable - to manufacture, as well as image
- Able to provide diagnostic as well as structural information

In approving nano vectors for clinical use, the FDA (and related agencies) weigh up the benefit of additional diagnostic information or therapeutic action to the patient. Toxicity has been the most significant issue facing the clinical approval of nano vectors, as the long term effects of many vectors are unknown. In particular, particles made up of heavy metals that may not be renally cleared, or systems that act as oxidizing agents under some in-vivo conditions have shown contradictory results in animal toxicity studies. Silicon has emerged as a material of choice for coating other nano materials as a first step in reducing their toxicity, and more recently as a stand-alone material for nano vectors. In the in-vivo environment, silicon breaks down into silicic acid which is renally cleared in a relatively short period of time [39].

1.3.1 Structure of this thesis

This thesis details the development of a new type of MRI imaging technique for monitoring silicon particles in-vivo. We have attempted to replicate many of the key features of other successful techniques in both nanomedicine and medical imaging, and create a technology that offers the long imaging windows associated with ^{18}F PET (Table 1.1.1), without the use of ionizing radiation. The ^{29}Si nuclei are hyperpolarized by low temperature dynamic nuclear polarization and directly imaged using ^{29}Si MRI. The imaging window achievable is several orders of magnitude greater than other hyperpolarized agents (Table 1.1.2), is positive contrast and without a background signal. The technique requires no additional imaging agent to be incorporated into the silicon, and so toxicity complications are reduced. It is applicable to a wide range of particle sizes that can be selected based on the in-vivo application and imaging window required. The technique is not unique to the silicon particles investigated within this thesis, and may be applicable to a variety of silicon particles already under development in biomedical research, opening up the possibility of imaging targeting, drug loading and release in a low toxicity nanoparticle medium.

- **Chapter 2** outlines the main theories of nuclear and electron spin effects in semiconductors with specific focus on spin-1/2 nuclei. Understanding the microscopic spin dynamics was crucial for a deep understanding of the materials science, in particular mechanisms for spin relaxation for making long T_1 particles, and electron-nuclear spin interactions for optimizing the hyperpolarization process in silicon particles.

- **Chapter 3** describes initial measurements of the room temperature ^{29}Si spin lattice relaxation time in a variety of silicon particles.

- **Chapter 4** describes measurements and theory on the decay of nuclear hyperpolarization in undoped and doped silicon micro particles.

- **Chapter 5** details a new technique for enhancing the dynamic nuclear polarization in silicon particles using modulated microwave irradiation.

- **Chapter 6** describes the rational design and synthesis of high-quality silicon nanoparticles ($\sim$ 10 nm) as well as their dynamic nuclear polarization properties.

- **Chapter 7** describes using the surface of silicon particles for polarizing ^{1}H rich frozen solutions surrounding the particles.

- **Chapter 8** details the use of the hyperpolarized silicon particles as in-vivo magnetic resonance imaging agents, with applications for gastrointestinal imaging, intravenous imaging, intraperitoneal imaging, and perfusion imaging.

- **Chapter 9** describes a number of additional results: effects of optical irradiation on the room temperature spin relaxation and low temperature dynamic nuclear polarization of silicon micro and nanoparticles, the temperature dependence of the decay of nuclear spin hyperpolarization in a variety of silicon particles, and the effect of a ^{1}H rich solution of the DNP process.

- **Chapter 10** provides some concluding remarks, and an assessment of the future viability of this technology.

The thesis is also accompanied by a number of appendices that provide technical details for the construction of the DNP polarizer, its operation, describes details of surface functionalization strategy and the animal surgery procedures.

2

Silicon : Materials Properties and Spin Interactions

Silicon has been the workhorse material of the semiconductor microelectronics industry for over half a century, and its materials properties investigated through a myriad of techniques. Due to the availability of high quality samples, as well as tunable properties (from insulating to metallic) accessible via doping, it was one of the first materials investigated for nuclear magnetic resonance and dynamic nuclear polarization experiments [79–86].

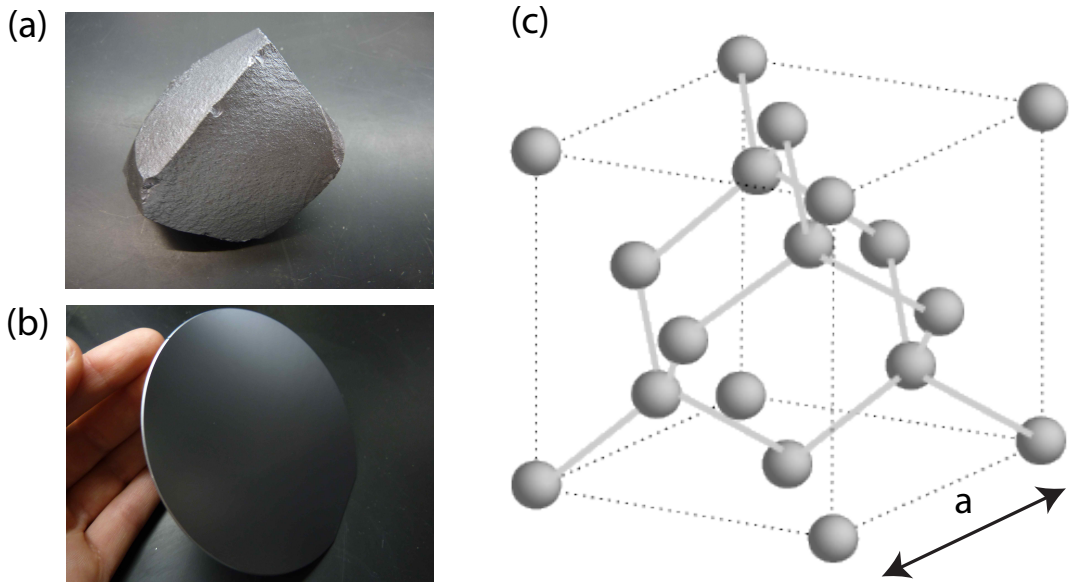

Figure 2.1.1: Photographs of (a) bulk silicon and (b) a high-resistivity silicon wafer. (c) Schematic of the silicon lattice showing the diamond cubic crystal structure.

Silicon is the second most abundant element on earth (26.3%), preceded only by oxygen (48.9%). Silicon is highly reactive, and so usually these two elements are found together in a class of materials known as silicates. Pure silicon can be extracted from silicates by a variety of chemical purification techniques including high temperature reduction and electrolysis. Once purified, it can exist in either amorphous or crystalline form, or as a polycrystalline structure consisting of multiple morphologies. The crystalline form consists of a pair of interleaved body centered cubic lattices with lattice spacing $a = 0.54309$ nm, (Fig. 2.1.1), often referred to as a 'diamond' cubic lattice. This lattice is isotropic, meaning that no axis of orientation is preferential over another.

2.1 Materials properties of silicon

Within the lattice, a number of isotopes of silicon that exist. Their mass numbers, natural abundance and nuclear spins are listed in Table 2.1.1 . The ^{29}Si nuclei are the only non-zero spin iso-

Isotope	Natural Abundance	Spin
^{28}Si	92.23%	0
^{29}Si	4.67%	1/2
^{30}Si	3.1%	0
^{32}Si	trace[1]	0

Table 2.1.1: Isotopes of silicon

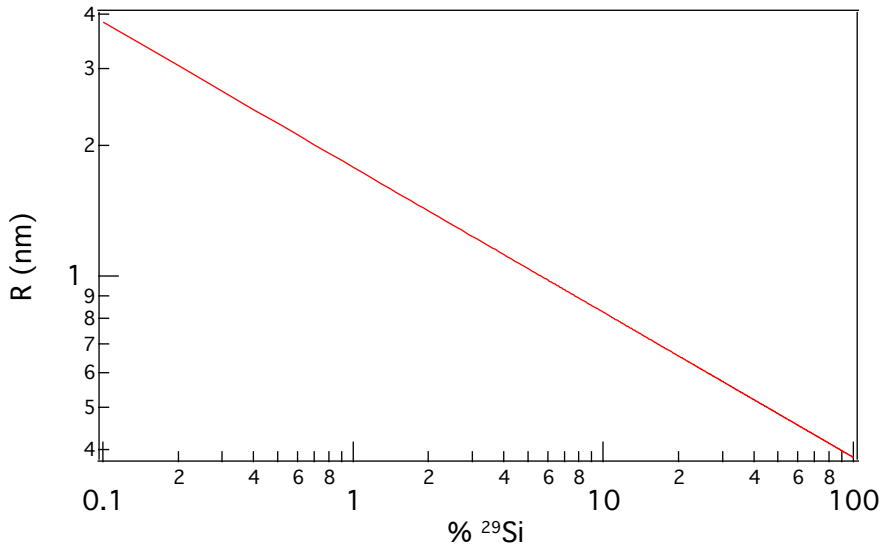

Figure 2.1.2: Average nearest neighbor spacing of ^{29}Si nuclei for different levels of isotopic enrichment.

topes, and they are what is detected in nuclear magnetic resonance experiments.

The ^{29}Si nuclei have a natural abundance of 4.67%, however this can be varied by a process known as isotopic enrichment. Changing the isotopic fraction changes the spacing R between the ^{29}Si nuclei and can have a drastic effect on the nuclear spin properties. In this thesis we investigate particles of natural abundance and enriched particles (92% ^{29}Si) provided as bulk material by Joel Ager at Lawrence Berkeley Labs.

For a dilute spin system of concentration N_S, such as the ^{29}Si nuclei in silicon, the average distance between neighboring ^{29}Si nuclei may be obtained by taking a Poisson distribution and set-

[1]Half-life of 170 years

ting the probability $exp(-4\pi N_S r^3/3)$ of finding no other particle within a distance r of a particle at the origin, equal to $1/2$. This gives

$$R = 0.55 a N_S^{-1/3}. \tag{2.1}$$

For natural abundance ^{29}Si, this results in an average nearest neighbor distance of $\sim$ 1nm (Fig. 2.1.2).

2.1.1 Doping and bandstructure

Silicon is a group IV element on the periodic table, having four electrons in its outer shell. It is a semiconductor with an indirect band gap of 1.12 eV and a band gap of 3.4 eV at the Γ point. In pure silicon at 300 K, the thermal activation of carriers within in the crystal is small, of order 10^{10} cm^{-3} [87], and the material is largely insulating. However, silicon atoms may be replaced in the lattice by elements from group III, or group V of the periodic table, most commonly boron and phosphorus, which either provide an excess hole or electron, transforming the material from a near insulator (resistivity > 100 k Ω cm^{-1}) to a metal (resistivity <0.1 Ω-cm) (Fig. 2.1.3) [88]. In addition to these atoms that dope silicon close to the valance or conduction band, a number of elements can be used as mid-gap dopants, including gold, copper, or samarium [80].

2.2 Magnetic resonance

Before discussing the specifics of electron and nuclear magnetic resonance in silicon, we will review the basis of magnetic resonance in spin-1/2 systems. It should be noted that the spin interactions in silicon are extremely similar to those in diamond and much of the theory describing the two systems is interchangeable [89–92].

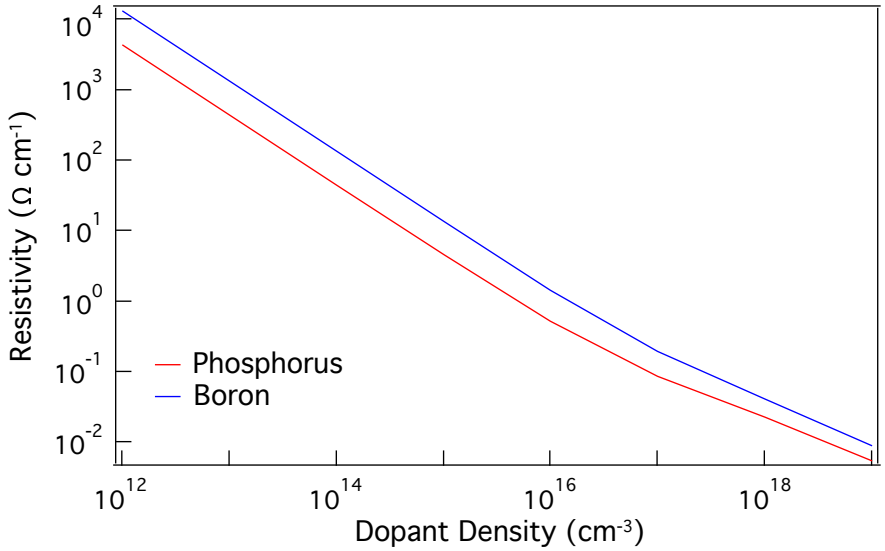

Figure 2.1.3: Resistivity as a function of dopant density for phosphorus (n-type) and boron (p-type) doping [88].

2.2.1 Angular momentum

A fundamental property of both the atomic nucleus and electron is the spin, which is described by the spin quantum number S. The electron spin universally holds a value of $S = 1/2$, while nuclei may possess either half-integer and integer values of spin. A nucleus may have no spin angular momentum ($S = 0$) if the number of protons and neutrons in the ground state are both even, or possess a spin ($S > 0$) if either the number of protons or neutrons in the nucleus is odd. The total angular momentum of particles with spin S is quantized and take values of the form,

$$\vec{S} = [S(S+1)]^{1/2}\hbar. \tag{2.2}$$

The associated quantum number is known as the magnetic quantum number, m, and can take values from +S to -S, in integer steps (m =-S,-S+1...+S) resulting in $2S + 1$ allowed orientations.

The presence of spin angular momentum $\vec{S}$ gives rise to a magnetic moment $\vec{\mu}$ which is directly proportional to the spin according to

$$\vec{\mu} = \gamma\vec{S}. \tag{2.3}$$

The proportionality constant γ, is known as the gyromagnetic ratio, and determines the strength of this relationship.[2] As a consequence of this formula, any nucleus with a nonzero spin angular momentum will have a corresponding magnetic moment and can interact with a magnetic field.

For an electron of charge $(-e)$ and mass m_e, where e is the elementary charge, instead of a gyromagnetic ratio γ, we refer to the spin magnetic moment as

$$\vec{\mu} = \frac{g_e \mu_B}{\hbar} \vec{S} \tag{2.4}$$

where g_e is the electron g-factor, and

$$\mu_B = \frac{-e\hbar}{2m_e} \tag{2.5}$$

is the Bohr magneton.

A free electron has a g-factor $g_e = 2.002$, however within a material, the g-factor will be strongly dependent on the electron's local environment. There are a number of different electronic defects within silicon that are identified by different g-factors that depend on whether it is a conduction electron or bound to a lattice site, and the local environment of the electron such as the orientation of the crystal lattice and strain (Table 2.2.1).

2.2.2 Zeeman effect

The simplest interaction between a magnetic moment and a static external magnetic field $\vec{B}_0$ has an energy

$$E_m = -\vec{\mu}.\vec{B}_0. \tag{2.6}$$

[2] The gyromagnetic ratio for each nucleus is unique, and can act as a form of spectroscopic fingerprint when determining chemical composition.

Defect	g_{e1}	g_{e2}	g_{e3}	Description
P_b	2.0012	2.0081	2.0081	Si-Si_3 at silicon -silicon oxide interface
P_b	2.006			Orientation averaged P_b defect
G_8	2.005	2.0112	2.0096	Si-Si_3 at Si vacancy
G_7	2.0012	2.0135	2.0150	Si-Si_3 at divacancy
P_1	2.0023	2.0118	2.0106	Si-Si_3 at pentavacancy
G_2	2.0151	2.0028	2.0038	Si-S bent bond
B_1	2.0092	2.0026	2.0033	Si-Si bent bond
G_1	2.0087	1.9989	1.9989	Si-Si bent bond over vacancy
E_X	2.0025			
E'	2.0018	2.0005	2.0003	O_3-Si Si-O_3 vacancy
$Si:P$	1.99872			Phosphorus dopant in silicon

Table 2.2.1: Electronic defects identified in silicon and silicon oxides [93].

If we assume the static field to be oriented along $\hat{z}$ ($\vec{B}_0 = B_0\hat{z}$), then

$$E_m = -\gamma B_0 S_z. \tag{2.7}$$

For a spin-1/2 system where $m = \pm 1/2$, the energy difference between the -1 state and the +1 state is:

$$\Delta E = E_- - E_+ = (\frac{1}{2}\gamma B_0 + \frac{1}{2}\gamma B_0) = \gamma B_0. \tag{2.8}$$

This splitting is known as the Zeeman effect, and the corresponding energy the Zeeman energy, and is shown for a spin 1/2 system in Fig. 2.2.1. It should be noted that this diagram corresponds to a particle with negative γ, as is the case with ^{29}Si and the electron. For nuclei with $\gamma > 0$, such as ^{1}H, the spin angular momentum is aligned with the magnetic moment and the picture is reversed. The magnitude of the splitting is directly proportional to the strength of the external magnetic field, resulting in an increased energy bias towards the +1 spin state at higher magnetic field (a spin anti-aligned with the magnetic field). This energy difference can be written in terms

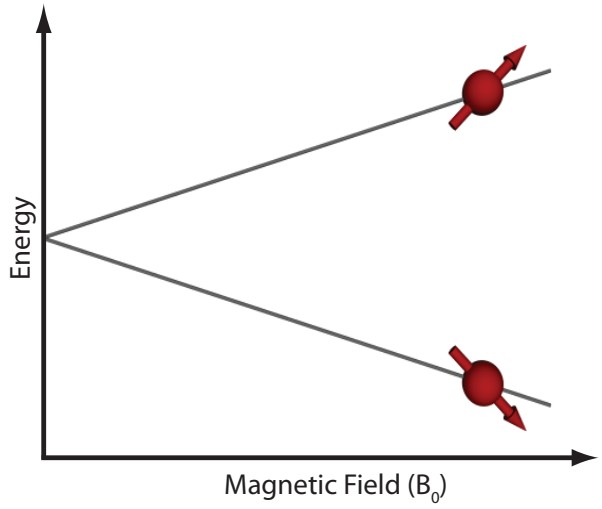

Figure 2.2.1: The energy between the spin up states and spin down states scales linearly with magnetic field. This diagram corresponds to a particle with negative γ, as is the case with ^{29}Si and the electron.

of a frequency ($\Delta E = \hbar\omega$), results in the relationship,

$$\omega_o = \gamma B_o. \tag{2.9}$$

The frequency ω_o is referred to as the Larmor frequency, and represents the transition energy between two spin states in an applied magnetic field.

2.2.3 Thermal polarization

Each spin with nonzero magnetic moment will interact with an external magnetic field. However to be observable, the magnetic moments must add up to form a net nonzero spin polarization, resulting in a macroscopic magnetization vector parallel to $\vec{B}_o$,

$$\vec{M} = \sum \vec{\mu}_{up} + \sum \vec{\mu}_{down}. \tag{2.10}$$

It is this net magnetization that can be probed with a small rotating, transverse field and is what

provides the net oscillating magnetic flux that induces a detectable signal in magnetic resonance experiments.

For a system of N = $n_+ + n_-$ distinguishable particles[3], the net nuclear polarization P can be defined as

$$P = \frac{(n_+ - n_-)}{(n_+ + n_-)}. \tag{2.11}$$

The populations at thermal equilibrium obey Boltzmann statistics, and so the number of particles in the i^{th} state is

$$n_i = N\frac{g_i exp[-(E_i/k_B T)]}{\sum_i g_i exp[-(E_i/k_B T)]} \tag{2.12}$$

where g_i is the degeneracy of the i^{th} state and k_B is the Boltzmann constant.

For a spin 1/2 system, the degeneracy is 2, which gives a thermal polarization value of

$$P = tanh\left(\frac{\gamma\hbar B_\circ}{2k_B T}\right). \tag{2.13}$$

The magnetization and thus the NMR signal is proportional to the polarization and the total number of nuclei within the sample.

There are a number of key observations that can be made from this result, shown in Fig. 2.2.2. First, increasing the static magnetic field will correspondingly increase the spin polarization (Fig. 2.2.2 (a)). Similarly, a decrease in the temperature will have the same effect, as there is less thermal energy available to excite the spin to the higher energy state (Fig. 2.2.2(b)). Finally, the spin polarizations for electron and different nuclei differ significantly across a range of temperatures and magnetic fields. Exploiting this large difference in polarization between the electron and nuclei is an underlying component of the technique of dynamic nuclear polarization.

[3]distinguishable because their de Broglie wavelength is shorter than the inter particle spacing

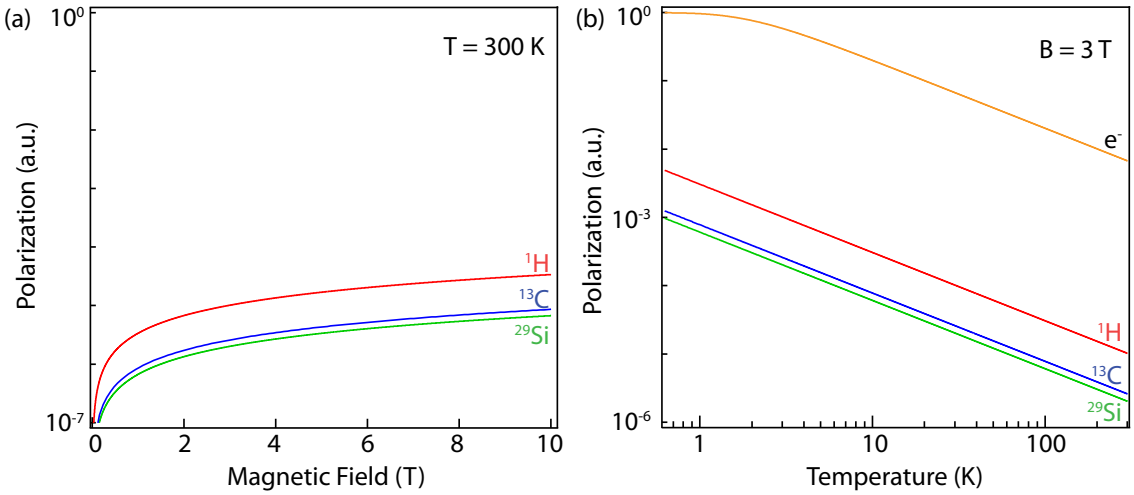

Figure 2.2.2: (a) Magnetic field dependence of nuclear polarizations at T= 300 K. (b) Temperature dependence of electron and nuclear polarizations at B = 3 T.

2.2.4 Measuring nuclear polarization

2.2.4.1 The rotating frame

A useful simplification for describing the interactions between a spin and a magnetic field is a concept known as the rotating frame approximation, where the observer is considered to be within a reference frame rotating around the $\vec{B}_0$ axis at the Larmor frequency. A spin precessing in the static magnetic field is thus considered motionless to the observer.

Within this frame, the application of a transverse rf magnetic field B_1 at the Larmor frequency appears as a static magnetic field in either the x or y directions. In the rotating frame the spins will appear to precess around this static field, with the rate of rotation, and thus angle traversed, depending on the strength of B_1. By applying a pulse of a certain amplitude and length, the spins will rotate from the z-axis into the xy-plane resulting in a $\pi/2$ pulse (Fig. 2.2.3(a)). Applying a pulse at double the length or amplitude inverts the magnetization along the x axis, resulting in a π pulse (Fig. 2.2.3(b)).

The axis of rotation depends on the relative phases of successive pulses. Typically, the first pulse in the sequence is designated as a pulse rotating around the x axis, with y pulses those with a $\pi/2$

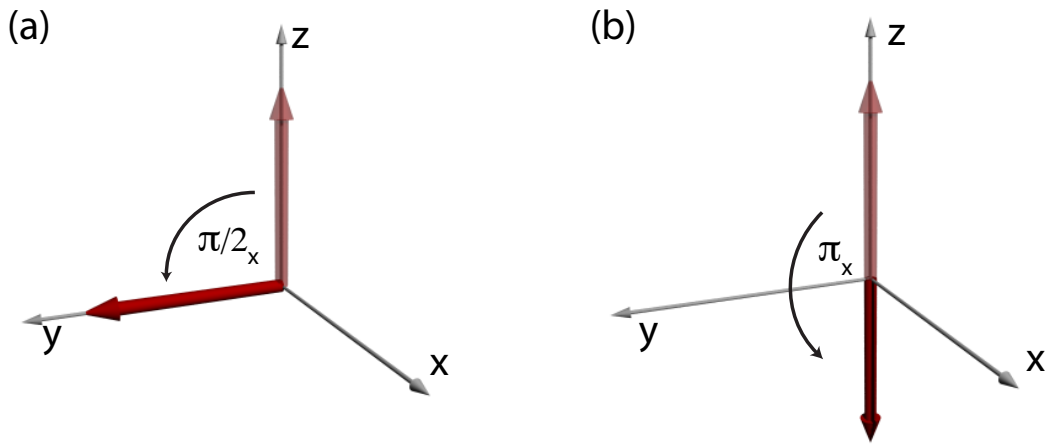

Figure 2.2.3: Application of a $\pi/2$ pulse around the x axis rotates the magnetization into the x-y plan. A π pulse inverts the direction of the magnetization

phase shift relative to the original x-pulse. Accurate control of the phase allows an arbitrary axis of rotation to be defined.

2.2.4.2 The NMR signal

The application of any transverse B_1 pulse applied to an ensemble of nuclear spins causes a fraction of the magnetization to be rotated into the transverse plane. In the laboratory reference frame, this magnetization precesses at the Larmor frequency around the z-axis, and via electromagnetic induction, the precessing magnetization will induce a current in an rf coil which surrounds the sample. This current creates an oscillating voltage at the input to the resonant circuit that is the signal observed in an experiment (Fig. 2.2.4(a)), known as a free induction decay (FID). The Fourier transform of this time dependent signal shows a peak at the resonant frequency of the nucleus (Fig. 2.2.4(b))[4].

[4]We typically acquire the signal several kHz off the resonant frequency to prevent mixing with the DC component of the spectrum

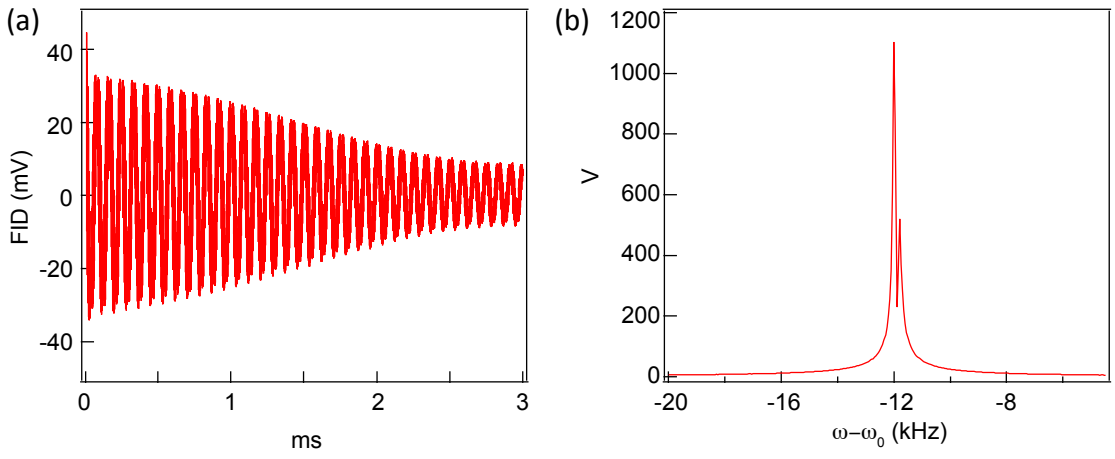

Figure 2.2.4: (a) Free induction decay (b) Fourier transformed NMR peak.

2.2.4.3 Ernst angle condition

When the signal to noise is particularly weak and multiple averages are required, the signal acquired in a fixed measurement period can be maximized by applying a series of pulses at an angle a_E where

$$cos(a_E) = e^{-T_R/T_1}, \tag{2.14}$$

T_R is the repetition time between subsequent pulses and T_1 is the spin-lattice relaxation time of the material (discussed in the following section). This is known as the Ernst equation, with a_E the Ernst angle. It is particularly useful for measurements of small samples or weak nuclear species under high temperature Boltzmann conditions and when the spin-lattice relaxation time is very long.

2.2.5 Spin relaxation

2.2.5.1 Spin-lattice (T_1) relaxation

The spin-lattice relaxation time, or T_1 time, is the time-constant with which the nuclear spin returns to thermal equilibrium with the lattice following a perturbation (Fig. 2.2.5). For liquids and gases, T_1 is typically on the order of ms to s, but in some materials, such as silicon, it may be up

to many hours or even days [79]. For a homogeneous system, where all nuclei have the same local environment with the static field orientated along $\hat{z}$, there will be a single value for the time constant and the magnetization along the z-axis M_z will follow the rate equation

$$\frac{dM_z}{dt} = \frac{-(M_z - M_0)}{T_1}. \tag{2.15}$$

In composite materials, where each spin has a differing local environment, then the T_1 of the bulk is the ensemble averaged T_1 over all nuclei within the material. This may be described by a single time-constant for a distribution of spins, or by a weighted sum of exponentials when there are multiple distinct baths of nuclei with different spin properties. For instance, in silicon micro and nano particles, we observe a biexponential process, one bath corresponding to nuclei in the 'core' of the particle, and another corresponding to nuclei on the surface.

For a single spin, the value of T_1 is determined by the strength of the magnetic interaction of the nuclear spin with the environment, and how effectively the environment can provide or absorb the required energy to induce nuclear spin flips. Nuclear spin flip events are induced by a magnetic field at the Larmor frequency of the spin, and so for this to occur, the environment must possess a spectral component at this frequency [94]. The environmental noise results from the motion of the magnetic moment of other spins in the system, either by spin flip-flops, or their physical motion. This is stochastic process which can be described by a correlation time τ_c, with a resulting frequency spectrum

$$J(\omega_n) = \frac{\tau_c}{1 + \omega_n^2 \tau_c^2}. \tag{2.16}$$

For a given Larmor frequency ω_n, the spectral function in Eq. 2.16 has a maximum when $\tau_c = \omega_n$. Thus, any magnetic field within the environment fluctuating at the nuclear Larmor frequency will induce spin lattice relaxation.

In liquids, the rapid tumbling of molecules and bond rotation results in a local field for each spin that fluctuates from the differing positions of spins within the same molecule, or for other

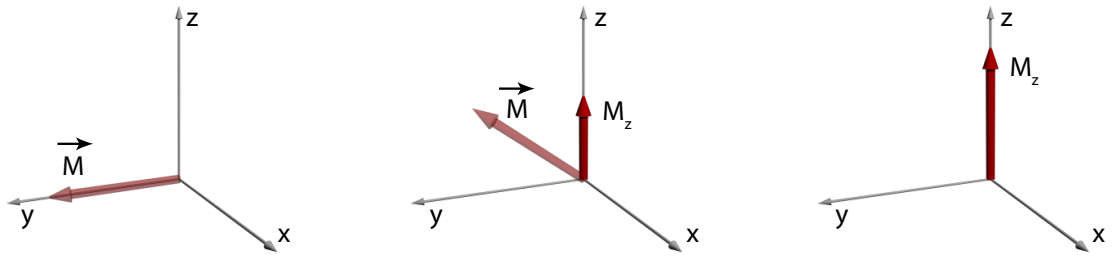

Figure 2.2.5: The spin lattice relaxation is the time for the nuclear spin to return to thermal equilibrium after a perturbation into the x-y plane.

molecules. In semiconductors such as silicon, the movement of free electrons and holes in the conduction band and their associated magnetic moments provides a source of this local fluctuating magnetic field [94]. Additionally, the spins of fixed paramagnetic impurities or neutral dopants located at lattice defect sites fluctuate rapidly and are a major source of relaxation for nearby nuclei.

2.2.5.2 Spin-spin (T_2) relaxation

The spin-spin relaxation time, or decoherence time, is the time scale to which the transverse component of the magnetization decays to its equilibrium value (Fig. 2.2.6). This decay is cause by an inhomogeneous magnetic field over the sample volume, and is described by

$$\frac{dM_x}{dt} = -\frac{M_x}{T_2}, \frac{dM_y}{dt} = -\frac{M_y}{T_2}. \tag{2.17}$$

It may be divided into a component resulting from inhomogeneities in the static local magnetic field environment, that is reversible and may be removed through echoing [95–97], and a component that is time dependent, such as the magnetic interaction between nuclear spins, or paramagnetic defects, and therefore non-reversible. T_2^* is the relaxation that includes the reversible components while T_2 is the intrinsic relaxation once all reversible components have been removed.

The local field determines the shape of the resonance line. For a Lorentzian line with full width

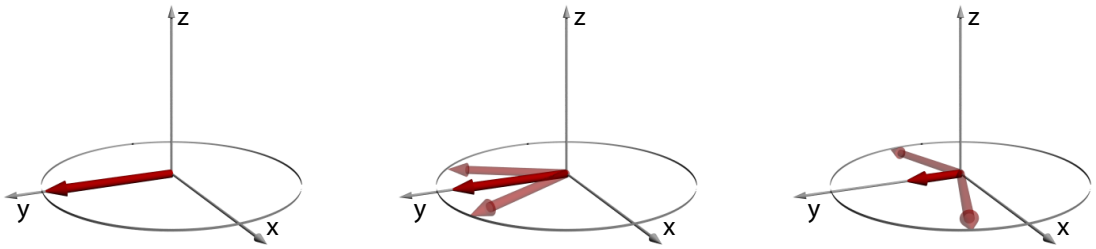

Figure 2.2.6: The spin-spin relaxation time is the time taken for the coherence to go to 0.

at half maximum of the resonance peak (FWHM), T_2^* may be determined by

$$T_2^* = \frac{1}{\pi \, \mathrm{FWHM}}. \tag{2.18}$$

2.2.5.3 Spin-spin relaxation in silicon

For a crystalline silicon sample, the dipolar field due to the nuclei results in a $T_2^* \sim 2$ ms. An unusual phenomenon has been observed by Barrett et al. [98] for dilute ^{29}Si nuclear spins in a crystalline lattice. Whereas usually the magnetization decoheres to zero, they observe a decay in the decoherence to a steady state (non-zero) value under the application of a Carr-Purcell-Meiboom-Gill (CPMG) pulse sequence $(\pi/2)_X - [\tau - (\pi)_Y - \tau - \text{echo}]^n$ [96, 97]. We have also observed this phenomenon in both Boltzmann polarized and hyperpolarized silicon samples (Fig. 2.2.7) in the bulk and on the nanoscale.

2.2.6 Spin interactions

The understanding of the interaction of electron and nuclear spins between each other and the environment is fundamental to understanding the processes of polarization and relaxation at the microscopic level. The processes are somewhat inverse to each other, with the mechanisms driving depolarization also able to drive polarization.

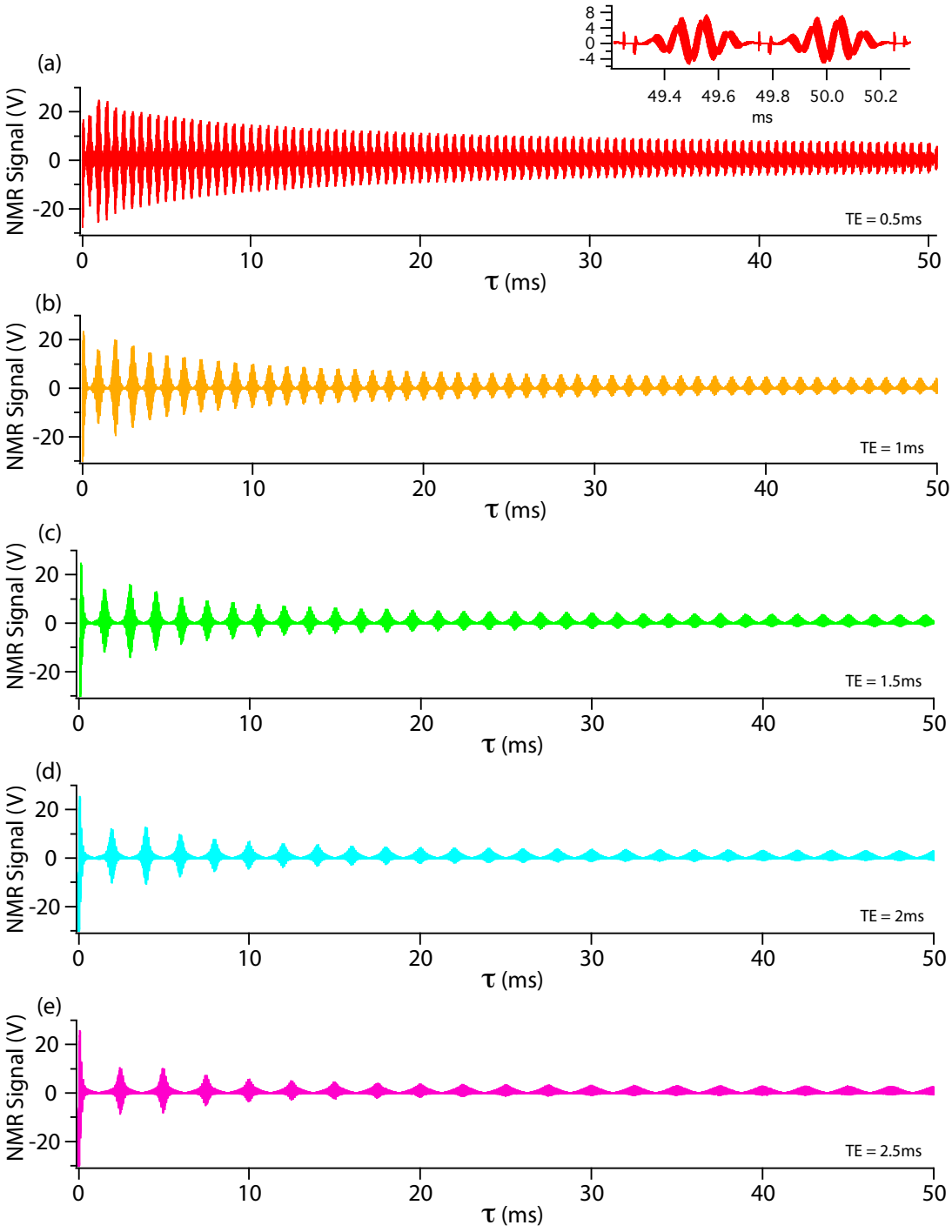

Figure 2.2.7: Long-tail echoes in silicon microparticles observed under DNP conditions using a CPMG pulse sequence for increasing echo times.

2.2.6.1 Spin-phonon coupling

Acoustic phonons, which occur due to vibrations in the crystal lattice, result in a modulation of the interatomic distances between nuclei in the lattice and thus produce an oscillating magnetic field. The phonons that have a spectral component at the nuclear or electron Larmor frequency will drive spin flips and cause relaxation.

The rate of direct spin-lattice relaxation for this process is given by [89],

$$T_1^{-1} = \frac{54\pi\nu^2}{\hbar^2\rho v_o^5}\left(\frac{\mu_B^2}{a^3}\right)^2 k_B T \tag{2.19}$$

where ρ is the mass density, ν the phonon oscillator frequency, v_o the velocity of sound in the crystal, a the lattice spacing and μ_B the Bohr magneton.

From this it follows that

$$T_1^{-1} \propto B_o^2 T \tag{2.20}$$

where B_o is the magnitude of the external field and T is the temperature. The direct process is a weak nuclear relaxation mechanism, since the acoustic spectrum of a solid at the nuclear Larmor frequency (in the MHz regime) is weak. This is because acoustic waves of this frequency have long wavelengths, in contrast with the relatively small displacements of atoms within the lattice. In addition, in silicon the speed of sound is relatively high (8×10^3 m/s) and the $1/v^5$ dependence of the relaxation rate results in a low relaxation rate [99].

An inelastic scattering, or Raman process is another mechanism for providing the energy required for a spin relaxation event. At temperatures less than the Debye temperature ($\Theta_D = 645K$ for silicon), the relaxation rate due to inelastic scattering processes is given by [94],

$$T_1^{-1} \propto \frac{1}{\rho v_o^{10}}\left(\frac{\beta^2}{r_o^3}\right)^2\left(\frac{k_B T}{h}\right)^7 \tag{2.21}$$

giving a relaxation rate that is proportional to the magnetic field and the seventh power of the temperature.

As the scattering process only requires a change in phonon frequency equal to the electron or nuclear Larmor frequency ($\omega'_q - \omega_q = \omega_n$), the Raman process is significantly stronger relaxation mechanism for electrons in silicon rather than the direct phonon process at standard magnetic fields and temperatures.

2.2.6.2 Hyperfine interaction

The contact hyperfine coupling is a scalar coupling between a single electron $\vec{S}$ and nucleus $\vec{I}$ with its strength A determined by the overlap of the two wavefunctions. The Hamiltonian describing the spin component of this coupling has the form [5]

$$H_{hf} = A(\vec{I}.\vec{S}) = -\frac{8\pi}{3}\gamma_e\gamma_n\hbar\delta(r_{IS})(\vec{I}.\vec{S}) \tag{2.22}$$

with γ_n and γ_e the nuclear and electron gyromagnetic ratios, respectively, r_I the vector connecting the position of the electron with the position of the nucleus and and $\delta(r_{IS})$ the electron wavefunction at the position of the nucleus. The operator $(\vec{I}.\vec{S})$ can be expanded into:

$$(\vec{I}.\vec{S}) = \mathrm{I_xS_x} + \mathrm{I_yS_y} + \mathrm{I_zS_z} = \frac{1}{2}(\mathrm{I_+S_-} + \mathrm{I_-S_+}) + \mathrm{I_zS_z} \tag{2.23}$$

where $S_+ = S_x + iS_y$ and $S_- = S_x - iS_y$ are the respective raising and lowering operators. The term between $(I_+S_- + I_-S_+)$ indicates that the contact hyperfine interaction can induce simultaneous flips of the interacting spins in opposite direction,

$$|\uparrow\downarrow\rangle \leftrightarrow |\downarrow\uparrow\rangle \tag{2.24}$$

with the arrow notation representing $|$electron spin, nuclear spin$\rangle$.

[5] we ignore the orbital components here

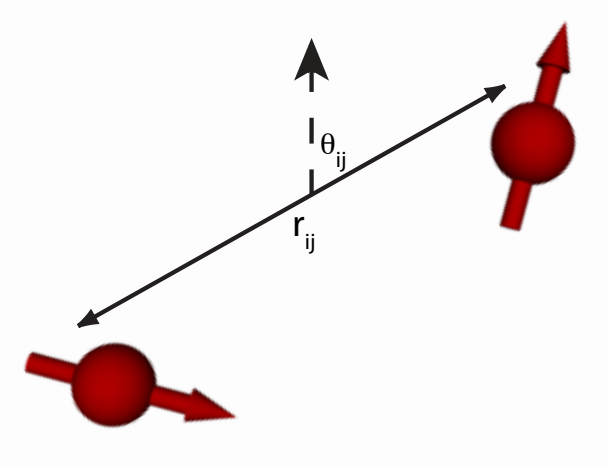

Figure 2.2.8: The strength of the dipole dipole coupling between two spins i and j is inversely dependent on the cube of the distance between them.

For an *s* type electron located concentric to the nucleus, the interaction is isotropic and simplifies to

$$\delta(r_I)(\vec{I}.\vec{S}) = |\psi(0)|^2 \tag{2.25}$$

where $\psi(0)$ is the electronic wave function normalized to unity in an atomic volume.

2.2.6.3 Dipole-dipole coupling

The dipolar coupling between two spins is an interaction that arises due to the intrinsic magnetic dipole of each spin (Fig. 2.2.8). The magnetic moment of each spin generates a local magnetic field which the other spin then interacts with, similar to its interaction with the main magnetic field B_0.

The Hamiltonian describing the interaction between two spins I_i and I_j takes the form

$$H_{dd} = \frac{\mu_0}{4\pi} \sum_{i<j} \frac{\gamma_i \gamma_j \hbar}{r_{ij}^3} \left(I_i.I_j - 3\frac{(I_i.r_{ij})(I_j.r_{ij})}{r_{ij}^2} \right) \tag{2.26}$$

where r_{ij} is the vector joining the position of the spin at location i with the spin at location j.

The operator in the dipolar Hamiltonian is traditionally expanded into:

$$I_i.I_j - 3\frac{(I_i.r_{ij})(I_j.r_{ij})}{r_{ij}^2} = A + B + C + D + E + F. \tag{2.27}$$

where

$$A \propto (1 - 3cos^2\theta)I_z^i I_z^j \tag{2.28}$$

$$B \propto (1 - 3cos^2\theta)(I_+^j I_-^i + I_-^j I_+^i) \tag{2.29}$$

$$C \propto sin\theta cos\theta e^{i\varphi}(I_+^j I_z^i + I_z^j I_-^i) \tag{2.30}$$

$$D \propto sin\theta cos\theta e^{i\varphi}(I_-^j I_z^i + I_z^j I_+^i) \tag{2.31}$$

$$E \propto sin^2\theta e^{-2i\varphi} I_+^i I_+^j \tag{2.32}$$

$$F \propto sin^2\theta e^{2i\varphi} I_-^i I_-^j \tag{2.33}$$

where the polar angles θ and φ specify the orientation of the vector between spins I^i and I^j with respect to the static magnetic field B_o.

From this we can see that the dipolar interaction can induce spin flips in the opposite direction, or in the same direction,

$$A : |\uparrow\uparrow\rangle \leftrightarrow |\downarrow\downarrow\rangle \tag{2.34}$$

$$B : |\uparrow\downarrow\rangle \leftrightarrow |\downarrow\uparrow\rangle \tag{2.35}$$

$$C : |\uparrow\uparrow\rangle \leftrightarrow |\uparrow\downarrow\rangle \tag{2.36}$$

$$D : |\downarrow\uparrow\rangle \leftrightarrow |\downarrow\downarrow\rangle \tag{2.37}$$

$$E : |\uparrow\uparrow\rangle \leftrightarrow |\downarrow\uparrow\rangle \tag{2.38}$$

$$F : |\uparrow\downarrow\rangle \leftrightarrow |\downarrow\downarrow\rangle \tag{2.39}$$

For a given energy level $\hbar E_i^\circ = \gamma\hbar B_\circ M$ in the spin Hamiltonian, there are many ways in which the individual values of $I_z^i = m^i$ can be added to give a total magnetization $M = \Sigma m^i$. According to first-order perturbation theory, only those parts of the perturbing Hamiltonian that have matrix elements that do not disturb the total magnetization will induce transitions without the addition of energy into the system. From the equations above, we can see that only the terms A and B of the dipolar Hamiltonian satisfy this condition. The term A describes the effect of a static magnetic field on the dipoles, while the term B allows a simultaneous reversal of the two spins in opposite directions, commonly referred to the flip-flop interaction. The first higher order terms C and D introduce transitions between the state |M> and states $|M-1\rangle$ and $|M+1\rangle$ respectively ($\Delta M = \pm 1$), which are brought about through the coupling of the spin system to a rf-field. The E and F terms of the dipolar Hamiltonian correspond to transitions with $\Delta M = \pm 2$, which occur at a much smaller probability than the C and D transitions.

The dipolar coupling is the dominant coupling mechanism between nuclei in solids. In liquids and gases, however, rapid rotation of the molecules causes the local field seen by a given spin to

fluctuate rapidly in time, averaging out the dipolar interaction between spins. The size scale for which the rotational correlation time becomes relevant is on the order of several nanometers, but is dependent on the viscosity of the medium. In Appendix D we model the effect of rotational narrowing for nanoparticles of different sizes in different mediums. The line broadening that occurs when a nanoparticle stops freely rotating may be used to directly detect the binding of nanoparticles to large targets such as cancer cells and proteins.

2.2.6.4 Spin diffusion

Spin diffusion is a process that allows the transportation of nuclear or electron spin polarization over macroscopic distances, and provides a mechanism for relaxation and polarization for nuclei that are large distances away from a relaxing site. The concept was first proposed by Bloembergen as a mechanism for explaining the faster than expected spin-lattice relaxation in nonconducting solids [99].

Spin diffusion is an energy conserving process that is mediated by dipolar flip-flop interactions between nuclear spins. For a pair of like spins in a strong magnetic field, non-secular terms can be excluded and the dipolar Hamiltonian in Eq.2.27 reduces to

$$H_{dd} = \frac{\mu_o}{4\pi}\hbar^2\gamma^2 \sum_{i<j} \frac{1 - 3cos^2\theta_{ij}}{2r_{ij}^3}(2I_z^iI_z^j - \frac{1}{2}I_+^iI_-^j + I_-^iI_+^j). \tag{2.40}$$

This provides a mechanism for a spin flip-flop between nuclei of the same species without loss of energy. Spin diffusion can be modeled as a differential equation, similar to the conduction of heat. The rate of change in nuclear polarization $P(r,t)$ at position r for a spatially inhomogeneous distribution of nuclear polarization due to nuclear spin diffusion is given by,

$$\left(\frac{dP(r,t)}{dt}\right)_{diff.} = \sum_{\alpha,\beta=1}^{3} D^{\alpha\beta}(\frac{\partial^2}{\partial x^\alpha \partial x^\beta})P(r,t), \tag{2.41}$$

where $D^{\alpha\beta}$ is the $\alpha\beta$ component of the spin-diffusion tensor. If the lattice is isotropic, such as for silicon, diffusion will progress equally in all directions and we can assume $D^{\alpha\beta} = 0$ for $\alpha \neq \beta$ and $D^{1,1} = D^{2,2} = D^{3,3} = D$. This equation then simplifies to,

$$(\frac{dP(r,t)}{dt})_{diff.} = D\nabla^2 P \tag{2.42}$$

For a diamond lattice such as silicon, the diffusion constant is well described by [100],

$$D = Wa^2 = \frac{a^2}{50T_{2n}} \tag{2.43}$$

where W is the probability of a flip-flop transition between nuclei due to dipole-dipole interaction, a is the distance between nearest neighbor nuclei and T_{2n} the nuclear decoherence time [100].

If the external magnetic field B_0 is greater than nuclear dipolar field,

$$B_{\mathrm{n,dd}} \sim \mu_0 \mu_n / (4\pi a^3), \tag{2.44}$$

this rate is independent of magnetic field and temperature [94]. The nuclear dipolar field for natural abundance silicon is $B_{\mathrm{n,dd}} = 0.08\ mT$, which is approximately equal to the earth's magnetic field. At such extremely low fields ($B_0 < B_{\mathrm{n,dd}}$), spin transitions corresponding to the non-secular components of the dipolar Hamiltonian will occur (that are forbidden at higher fields by the conservation of nuclear Zeeman energy), and nuclear spin relaxation will occur as fast as decoherence.

2.2.6.5 Spin diffusion barrier

At high magnetic fields, nuclear spin diffusion described in Eq. 2.40 is an energy conserving process, and hence the Zeeman energies of the two spins I^i and I^j must match for spin diffusion to occur. For a system of nuclear spin with fixed paramagnetic impurities dispersed amongst them, the paramagnetic impurity creates a large magnetic field gradient close to it and therefore nuclei

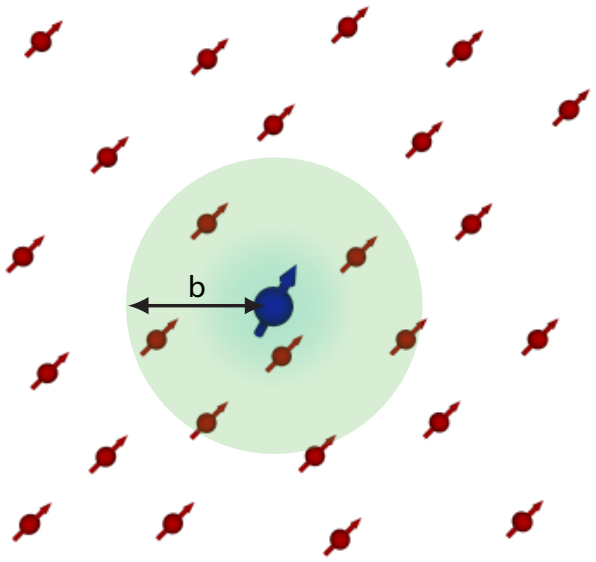

Figure 2.2.9: Spin diffusion barrier. The large magnetic field gradient surrounding a paramagnetic impurity results in nearby nuclei having different Zeeman energies. Inside this region, spin diffusion is suppressed.

nearby will have significantly different Zeeman energies. Inside this region, known as the spin diffusion barrier, spin diffusion is suppressed (Fig. 2.2.9).

The spin diffusion barrier was defined by Khutsishvili as the distance, b, from the paramagnetic impurity at which the difference of the hyperfine-shifted Zeeman frequencies of two neighboring nuclei is equal to the dipolar broadened NMR line width [100].

$$b = (\frac{\gamma_e}{\gamma_n})^a, \tag{2.45}$$

for $\hbar\gamma_e B_o > 2k_B T$ or

$$b = (\frac{\hbar\gamma_e^2 B_o}{\gamma_n 2k_B T})^a, \tag{2.46}$$

for $\hbar\gamma_e B_o < 2k_B T$ where $a \sim 1/4$

For paramagnetic defects in silicon at 300 K, the spin diffusion barrier is of order 1.5 nm.

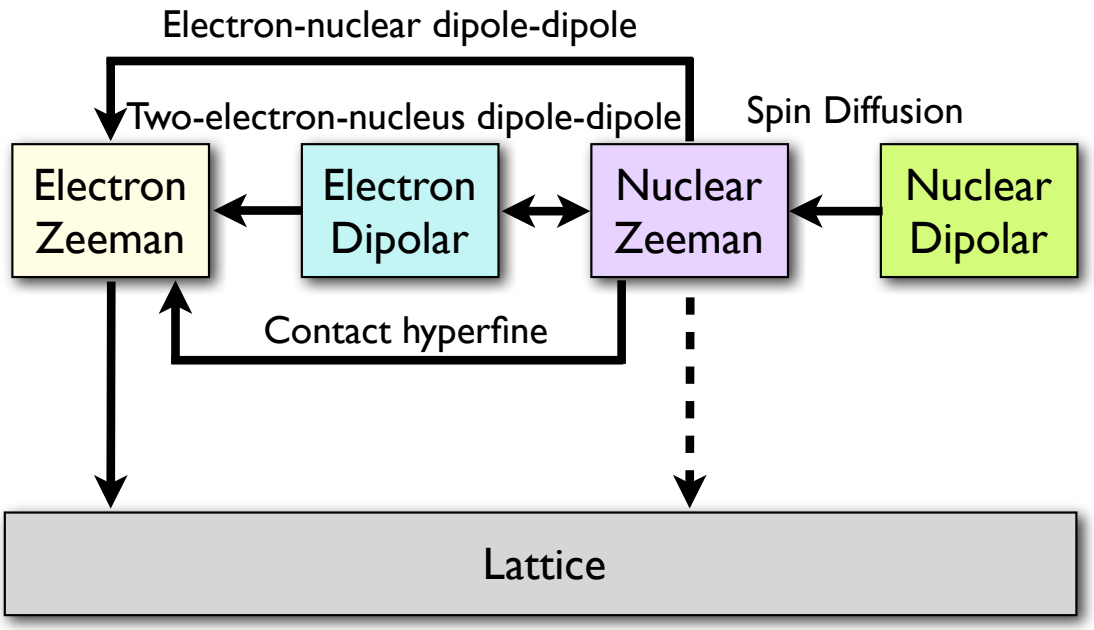

Figure 2.3.1: Spin relaxation processes in silicon.

2.3 Microscopic view of spin relaxation in silicon

The ^{29}Si spin relaxation process in silicon can be driven by a number of mechanisms depending on the microscopic structure of the material (Fig. 2.3.1). As the phonon coupling between the ^{29}Si nuclei and the lattice is weak, nuclear spin relaxation is mediated by electron relaxation processes. For a system that is highly doped, or where there is a high concentration of thermally or excited carriers, the contact hyperfine interaction provides the primary mechanism for relaxation. For more pure samples, however, relaxation will be driven by contributions from diffusion limited relaxation, and direct relaxation to fixed paramagnetic defects, such as impurities or vacancies in the crystal lattice.

2.3.1 Nuclear relaxation by conduction electrons

The contact hyperfine interaction can induce an electron-nucleus spin flip, with the energy required for this flip resulting from a change in the Zeeman energies $\hbar(\omega_e - \omega_n)$ provided by a change in the kinetic energy of the electron. As electrons obey Fermi statistics, most conduction electrons cannot take or give up this energy due to the Pauli exclusion principle. Only the fraction $k_B T/E_F$ on top of the Fermi distribution contributes to the nuclear relaxation process, where E_F is the electron Fermi energy.

The field provided by the conduction electron at the nucleus can be considered as a fluctuating local field on the timescale τ_c as described in Eq. 2.16. Assuming one conduction electron per atom, the timescale for τ_c will be approximately the time the electron spends localized on a given atom $\sim \frac{\hbar}{E_F}$.

The order of magnitude probability of this interaction taking place can be estimated by [94],

$$T_1^{-1} = |H_{hf}^2| \frac{\hbar}{E_F} \frac{k_B T}{E_F} = (\frac{8\pi}{3})^2 \gamma_e^2 \gamma_n^2 \hbar^3 |\psi(0)|^4 \frac{k_B T}{E_F} \tag{2.47}$$

For a non-spherical Fermi surface, for example for holes which have a p-type wave function, we must replace $|\psi(0)|^4$ by $|\psi_k(0)|^2 . |\psi_{k'}(0)|^2$.

For a concentration of mobile carriers N_0, Bloembergen calculated this to be [101]

$$T_{1,carriers}^{-1} = 8\pi^2 h^{-4} m^{3/2} d^6 N_0 (3 k_B T)^{1/2} A^2, \tag{2.48}$$

where d is average separation between dopant atoms, and A is the strength of the hyperfine coupling which is proportional to the intensity of the carrier's wavefunction at the nuclear site. This rate assumes that the nuclei are spin-1/2 and the experiment is being carried out at high fields, and that the electron relaxation time T_{1e} is sufficiently short such that the electron spins are well thermalized with the lattice and the temperature is sufficiently high such that the electronic

Zeeman energy is smaller than $k_B T$.

2.3.2 Nuclear relaxation by fixed impurities

For a system without mobile carriers, the rate of change of the nuclear polarization can be described by contributions from direct relaxation by localized paramagnetic impurities and depolarization by nuclear spin diffusion by,

$$\frac{dP(r,t)}{dt} = \left(\frac{dP(r,t)}{dt}\right)_{diff.} + \left(\frac{dP(r,t)}{dt}\right)_{direct}. \tag{2.49}$$

The contribution from direct relaxation of the nuclear spins to by paramagnetic defects is given by

$$\left(\frac{dP(r,t)}{dt}\right)_{direct} = \frac{P_o - P(r,t)}{T_{1n,direct}(r)}, \tag{2.50}$$

where

$$T_{1n,direct}(r)^{-1} = \frac{C+K}{|R-r|^6} \tag{2.51}$$

Here $|R-r|$ is the distance of the nuclear spin packet from the paramagnetic defect, and C and K the constants describing the strengths of the interaction between a nuclear spin and one or two electron spins respectively.

We can define a diffusion radius β, that describes the crossover region between direct relaxation dominating ($r < \beta$) and spin diffusion dominating ($r > \beta$) the relaxation process [100]. β can be interpreted as the distance from the paramagnetic impurity up to where direct nuclear relaxation

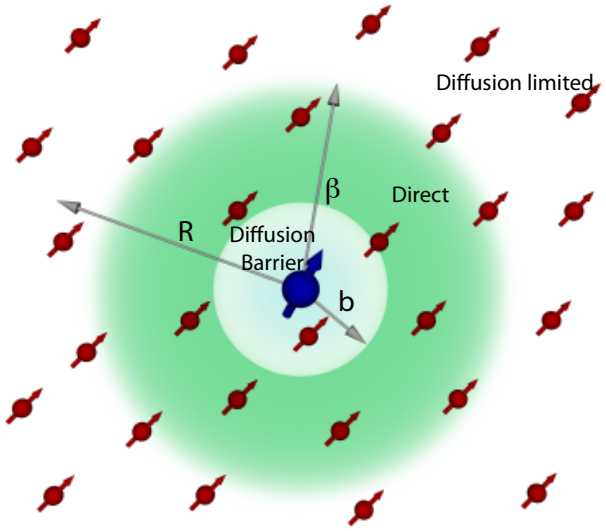

Figure 2.3.2: Spin diffusion radius. A diffusion radius β describes the crossover between direct relaxation dominating over spin diffusion mediated relaxation.

is effective and is given by

$$\beta = (\frac{C+K}{D})^{\frac{3}{4}}. \tag{2.52}$$

Typically in silicon the diffusion radius β is two to three orders of magnitude larger than the diffusion barrier b.

2.3.2.1 Relaxation via electron-nuclear dipolar interactions

An electron relaxing to the lattice by a T_{1e} process will also have a dipolar interaction with a nearby nuclear spin. The dipolar terms given by Eq. 2.30 and Eq. 2.31 in the dipolar expansion for this single electron and nucleus system have components $S_z I_+$ that leads to mixing of the wave functions that may induce a nuclear spin flip unaccompanied by an electron spin flip. This process requires an energy $\hbar\omega_n$ that is much smaller than the energy $\hbar(\omega_e \pm \omega_n)$ involved in the other process in the dipolar expansion.

The rate that this transition occurs will be proportional to the square of the coefficients in Eq.

2.30 and Eq. 2.31,

$$T_{1,1e}^{-1} = \frac{3}{2}\frac{\gamma_e^2\gamma_n^2\hbar^2}{r^6} sin^2\theta cos^2\theta S(S+1)\frac{2T_{1e}}{1+\omega_n^2 T_{1e}^2} \tag{2.53}$$

Averaging over the angular dependence, we can simplify this (for a spin-1/2 system such as silicon) to be

$$T_{1,1e}^{-1} = \frac{C}{r^6} \tag{2.54}$$

where

$$C = \frac{3}{10}\gamma_e^2\gamma_n^2\hbar^2\frac{2T_{1e}}{1+\omega_n^2 T_{1e}^2}. \tag{2.55}$$

2.3.2.2 Relaxation via electron-electron dipolar interactions

For samples with a high concentration of electronic defects, a g-factor anisotropy will exist in the ESR line, $g(\omega)$, that results in inhomogeneous broadening. A consequence of this is that there are many electrons with a range of different g-factors in the sample, and the ESR line can be considered to be made up of a number of spin-packets, each of intrinsic width T_{2e}^{-1} (Fig 2.3.3). These electrons are strongly dipolar spin coupled, which means that they equilibrate to the same polarization, or effective spin temperature across the sample.

Provided the broadening of the ESR line is sufficiently greater than the nuclear Larmor frequency, within the sample there will be separated electrons that differ in frequency by the nuclear Larmor frequency [102]. These electrons can perform a flip-flop, yielding an energy quantum $\hbar(\omega_{e1} - \omega_{e2}) = \hbar\omega_n$. This flip flop between the pair creates a fluctuating magnetic field, which can in turn induce a nuclear transition.

If the time scale for this flip-flop interaction within the electron system (T_{2e}) is sufficiently fast,

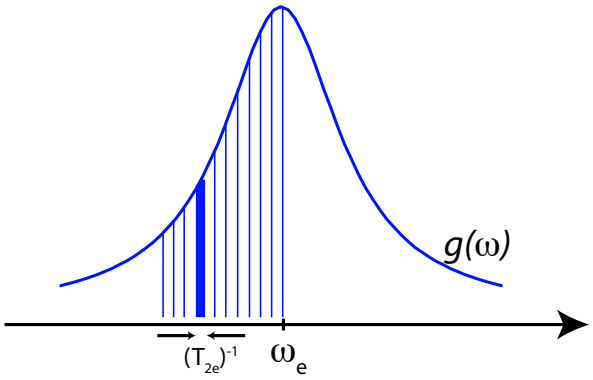

Figure 2.3.3: Spin packet description of inhomogeneous ESR lines.

a thermal equilibrium will be established within this system and the electron spin-spin relaxation time T_{2e} rather than T_{1e} will approximate the correlation time of the local fields experienced by the nuclei [103]. This establishes a coupling between the between the nuclear Zeeman reservoir and the lattice via the electron dipolar reservoir (Fig. 2.3.1). Nuclear relaxation can therefore occur as the electron dipolar reservoir relaxes to the lattice at a rate T_{1e}. The rate of nuclear relaxation induced by thermal contact between the nuclear Zeeman and the electron dipole-dipole interaction reservoirs is characterized by the rate $T_{1,2e}^{-1}$, which is given by [103]

$$T_{1,2e}^{-1} = \frac{K}{r^6} \tag{2.56}$$

where

$$K = \frac{3}{10}\frac{\gamma_e^2\hbar^2}{B_o^2}\frac{\omega_n^2 T_{2e}^{ss}}{1+\omega_n^2 T_{2e}^{ss2}}\int_{-\infty}^{\infty}\frac{g(\omega)g(\omega-\omega_n)}{g(0)}d\omega \tag{2.57}$$

and $g(\omega)$ the normalized electron absorption line shape function. The integral in takes into account the fact that the Larmor frequencies of the two electrons performing the flip-flop have to differ by ω_n to cause a nuclear spin flip. Further, it is evident that the coupling between the nuclear Zeeman and the electron dipole-dipole interaction reservoirs is strongly field-dependent if $\omega_n T_{2e}^{ss2} \gg 1$ and strongly field independent if $\omega_n T_{2e}^{ss2} \ll 1$.

2.4 Dynamic nuclear polarization in silicon

Dynamic nuclear polarization can be considered as an inverse process to the relaxation processes described in Section 2.3, with contributions from direct and diffusion mediated nuclear polarization but with the added effect of a term that describes the relaxation of the nuclear polarization caused by inactive defects.

$$\frac{dP(r,t)}{dt} = \left(\frac{dP(r,t)}{dt}\right)_{direct} + \left(\frac{dP(r,t)}{dt}\right)_{diff.} - \left(\frac{dP(r,t)}{dt}\right)_{relax.} . \tag{2.58}$$

The relative contributions of these terms depends on the nature of the sample, with the direct polarization mechanism determined by one of three mechanisms described below (Fig. 2.4.5)

2.4.1 DNP via the contact hyperfine interaction in highly doped materials - The Overhauser Effect

The Overhauser effect was theoretically predicted in 1953 by Albert Overhauser [104], and demonstrated first in metals by Carver and Slichter in 1956 [105]. The effect arises from the contact hyperfine interaction between electrons and nuclei if (opposed to the situation for relaxation described above) the electron spins are not in equilibrium with the lattice, for instance if they are being driven by a resonant rf field.

For a system of spin-polarized conduction electrons in a magnetic field, their distribution will follow a Fermi function

$$f_{\pm} = \left[1 + exp\left(\frac{E \pm \frac{1}{2}\hbar\omega_e - E_F^{\pm}}{k_B T}\right)\right]^{-1} \tag{2.59}$$

where $E_F^{\pm}$ are the Fermi energies of the two orientations of the electron spin, and E is the kinetic energy of the electrons. Saturating the electron spin transition at a frequency ω_e corresponds to $f_+ = f_-$, or $E_F^+ - E_F^- = \hbar\omega_e$.

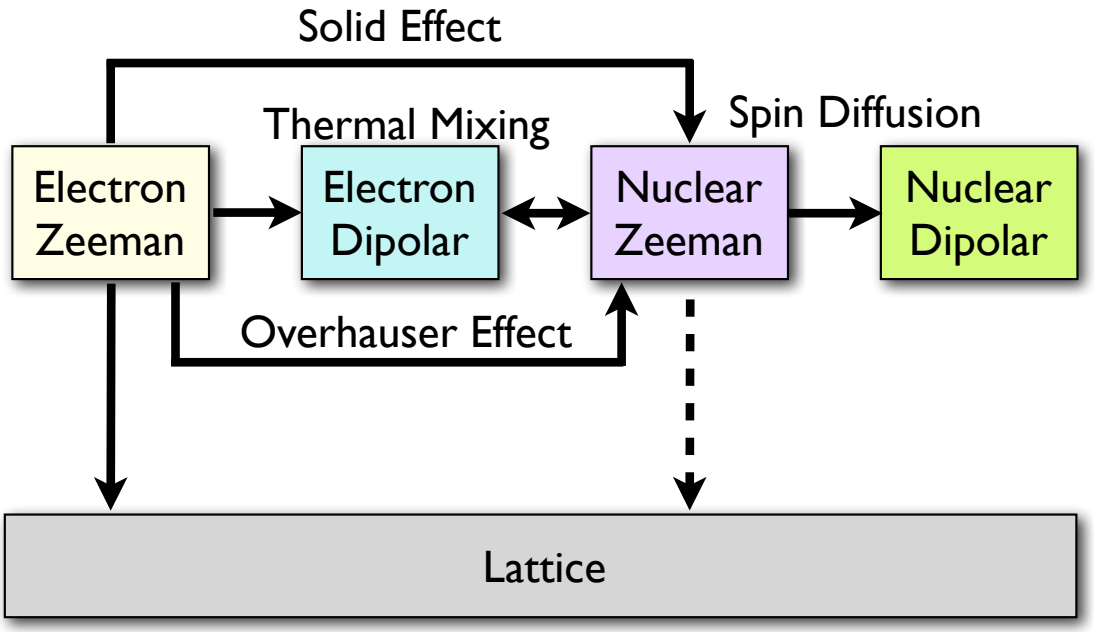

Figure 2.4.1: Nuclear polarization in silicon can occur any of three mechanisms; the Overhauser effect, the Solid effect and Thermal Mixing. Polarization of distant nuclear spins occurs via nuclear spin diffusion.

Assuming that there is strong coupling between the electronic and nuclear Zeeman spin baths, the steady state ratio of the population of nuclei in the spin up state n_+, compared to the spin down state n_- is [94],

$$\left(\frac{n_+}{n-}\right)_{st} = exp\left(\frac{E_F^+ - E_F^- - \hbar\omega_n}{k_B T}\right). \tag{2.60}$$

For electrons in thermal equilibrium $E_F^+ = E_F^-$ and this ratio is equal to the Boltzmann ratio $exp(\frac{-\hbar\omega_n}{k_B T})$. Under continuous driving of the electron spin system at frequency ω_e, the electron polarization goes to zero ($E_F^+ - E_F^- = \hbar\omega_e$) and the nuclear polarization will be enhanced by,

$$\left(\frac{n_+}{n_-}\right)_{st} = exp\left(\frac{\hbar(\omega_e - \omega_n)}{k_B T}\right). \tag{2.61}$$

For incomplete saturation of the electron spin system (for instance at low microwave powers), a saturation parameter s is included (0<s <1)

$$\left(\frac{n_+}{n-}\right)_{st} = exp\left(\frac{\hbar(s\omega_e - \omega_n)}{k_B T}\right). \tag{2.62}$$

The saturation factor was defined as [105]

$$s = \gamma_e^2 B_1^2 T_{1e} T_{2e} / (1 + \gamma_e^2 H_1^2 T_{1e} T_{2e}) \tag{2.63}$$

where B_1 is the amplitude of the driving microwave field.

In silicon, DNP of ^{29}Si nuclei by the Overhauser effect has been demonstrated in P-doped silicon doped well above the metal insulator transition, where the electron system collapses into an exchange narrowed line [106] and in silicon doped with P and Sb just below the metal-insulator transition at low temperatures and high microwave powers [107]. Instead of doping, the carriers can be generated by applying above band gap optical irradiation. This has been used for hyperpolarization of ^{29}Si nuclei [83] and ^{31}P nuclei in phosphorus doped silicon [108].

2.4.2 DNP via isolated paramagnetic impurities - The Solid Effect

DNP may be also generated by a dipolar interaction between an electron and a nucleus, in a similar nature to the relaxation mechanisms described in Section 2.3.2.1. When the system consists of a dilute bath of isolated electronic defects, the mechanism is a dipolar interaction between a single electron and single nuclear spin. A schematic diagram of the energy levels of the isolated electron-nucleus system is shown in Fig 2.4.2. In a high magnetic field and at low temperatures, the electron spin bath becomes highly polarized, while the nuclear spin bath remains relatively unpolarized. The system remains populated in the bottom two states ((I)-(II) in Fig 2.4.2). The dipolar interactions in Eq. 2.28 and Eq. 2.29 permits simultaneous reversals of the electron and nuclear spins in opposite directions (flip-flops) ((I)-(IV) in Fig 2.4.2) as well as reversals in the same direction (flip-flips) ((II)-(III) in Fig 2.4.2). These simultaneous flip-flip reversals require the total energy of the spin system to change by $\hbar(\omega_e \pm \omega_n)$, and the process will not occur without the missing energy being supplied by the microwave field. Provided that the electron linewidth $(T_{2e}^*)^{-1}$ is much smaller than the nuclear Larmor frequency $(T_{2e}^*)^{-1} \ll \omega_n$, the application of an alternating field with frequencies $\omega_e - \omega_n$ will cause an electron-nuclear flip-flop (Fig 2.4.2 (a)) that results in polarization of the nuclear spin bath without causing an equivalent flip-flip (which will be off resonance). Likewise, the application of an alternating field with frequencies $\omega_e + \omega_n$ will cause an electron-nuclear flip-flip with flip-flops off resonance that results in depolarization of the nuclear spin bath (Fig 2.4.2 (b)). As long as the electron spin lattice relaxation time is much faster than the nuclear spin lattice relaxation time ($T_{1e}^{-1} \gg T_{1n}^{-1}$), a single electron can drive multiple nuclear polarization events and a sizable nuclear polarization can get built up. For a microwave field with amplitude $2B_1$ and frequency ω^*, the probability of an electron spin transition simultaneously accompanied by a nuclear spin transition is

$$\Gamma_{\pm} = \frac{\pi}{2}\gamma_e B_1^2 g(\omega - \omega^*)\tau C \tag{2.64}$$

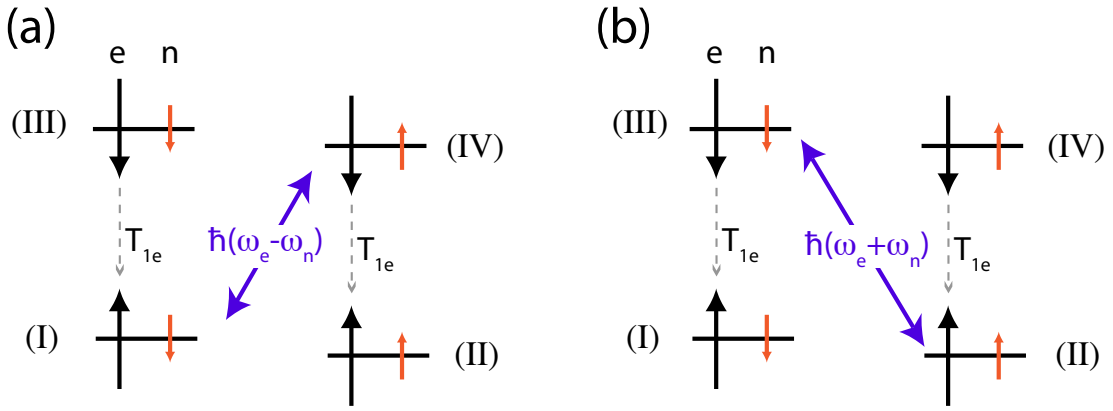

Figure 2.4.2: DNP by the Solid Effect

where $g(\omega - \omega^*)$ is the normalized shape of the electron spin resonance line.

Provided that this driving process happens much faster than the time scale for non-resonant relaxation, $\Gamma_\pm \gg C$ (or $\pi\gamma_e B_1^2 g(\omega - \omega^*)\tau \gg 1$), then the nuclei can be polarized up to the electron spin polarization. The strict condition for this is [94]

$$\frac{N_I}{T_{1n}}\frac{T_{1e}}{N_S} \ll 1 \tag{2.65}$$

where N_I is the density of nuclear spins, and N_S the density of electron spins.

This effect is commonly referred to as the Solid Effect. The for a system consisting of isolated defects the overall rate of nuclear polarization can be described by

$$\frac{dP(r,t)}{dt} = \frac{P_0 - P}{T_x} + D\nabla^2 P - C\sum \frac{M - M_0}{|r - r_m|^6} - \Gamma_\pm \sum \frac{P - \eta P_0}{|r - r_m|^6} \tag{2.66}$$

where $\eta = \gamma_e/\gamma_n$ is the maximum DNP enhancement factor. As these electrons are isolated from each other and from many of the nuclear spins in the sample, spin diffusion still plays a role.

The Solid Effect has been observed in a variety of systems including Nd^{3+} doped LMN [109] and $Ca(OH)_2$ doped with isolated (O_2^-) centers [110]. In silicon, it was first observed by Henstra *et al.* in a boron doped silicon sample [86], and later by Hayashi *et al.* in phosphorus doped iso-

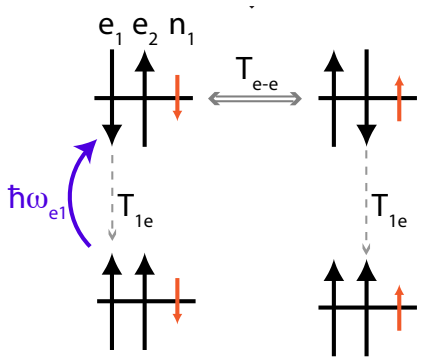

Figure 2.4.3: The two-electron-nucleus spin system.

topically purified silicon sample [106]. In this thesis, we observe DNP via the solid effect in small amorphous silicon nanoparticles.

2.4.3 DNP via a bath of paramagnetic impurities - Thermal Mixing

For a system with a high concentration of unbonded electrons, as described in Section 2.3.2.2, the ESR line is inhomogeneous broadened it can be considered to consist of a series of dipolar-coupled spin packets each of homogeneous width T_{2e}^{-1}. Provided that $T_{2e}^{-1} \ll \omega_n$, the system can be evaluated as a network of dipolar coupled electron pairs where for each pair the two electrons differ in Zeeman energy by the nuclear Zeeman energy.

To understand the polarization mechanism under microwave irradiation, we first consider a simple model consisting of a two dipolar coupled electrons of energy $\hbar\omega_{e1}$ and $\hbar\omega_{e2}$ and a nucleus of energy $\hbar\omega_n$ subject to the condition $\hbar(\omega_{e1} - \omega_{e2}) = \hbar\omega_n$. A schematic diagram of the energy levels of the electron and ^{29}Si nuclear spin systems is shown in Fig 2.4.3.

At low temperature and high magnetic fields the electron spin bath (black arrows) becomes highly polarized while the net polarization of the ^{29}Si nuclear bath remains low (red arrows). Microwave irradiation at a frequency ω_{e1} drives continuous rotations of electrons in packet e_1 on a time scale t_{sat}. Dipolar flip-flops between electrons within the same packet, as well as other packets, occur at a rate $T_{2e,SS}^{-1}$ that is much faster than their coupling to the lattice, set by T_{1e}^{-1}. Therefore

an electron in packet e_1 can undergo a spin flip-flop with a spin in packet e_2 without loss of dipolar energy ($\downarrow\uparrow \Leftrightarrow \uparrow\downarrow$). As the two electrons differ in Zeeman energy by the nuclear Zeeman energy, the dipolar interaction generates a fluctuating I_Z magnetic field that can flip a nearby nuclear spin and still conserve total energy [94]. The electron will thermalize with the lattice at a rate T_{1e}^{-1}, before being able to pair up with another nucleus and repeat the cycle. Provided T_{1e} is much faster than the nuclear spin lattice relaxation time T_{1n}, a significant nuclear polarization will be built up.

A net positive enhancement in nuclear polarization will be seen when the electron being flipped has a resonant frequency below ω_e corresponding to cooling the electron dipolar spin bath, and a net negative enhancement in nuclear polarization when the electron being flipped has a resonant frequency above ω_e, corresponding to heating the electron dipolar spin bath. The dynamic nuclear polarization enhancement is therefore proportional to the derivative of the ESR line $\frac{dg}{d\omega}$ as a function of frequency [100, 103].

Realistically the packets e_1 and e_2 in Fig. **??** are not isolated from other packets within the electron spin system. The dipolar order can transfer to another pair of spins e_3 and e_4, which can undergo a spin flip-flop and polarize a nearby nuclear spin n_2 (Fig. 2.4.4), further enhancing the nuclear polarization.

Spectral diffusion describes the rate of transfer of dipolar order through this strongly coupled electron spin system. For an inhomogeneously broadened electron line consisting of several frequency separated dipolar broadened spin packets (Fig. 2.16), the time required for an absorbed quantum to diffuse through the inhomogeneous line by multiple transitions among the homogeneous spin packets follows a Lorentzian diffusion kernel [111], where the magnetization $M(t, \delta, \delta_0)$ at time t at a frequency δ away from the irradiation frequency δ_0 is,

$$M(t, \delta, \delta_0) = \frac{mt/\pi}{(mt)^2 + (\delta - \delta_0)^2} \tag{2.67}$$

where $m = (\Delta\omega)_{1/2}/(2t_L)$ is the spectral diffusion parameter for the spin system. Here $(\Delta\omega)_{1/2}$

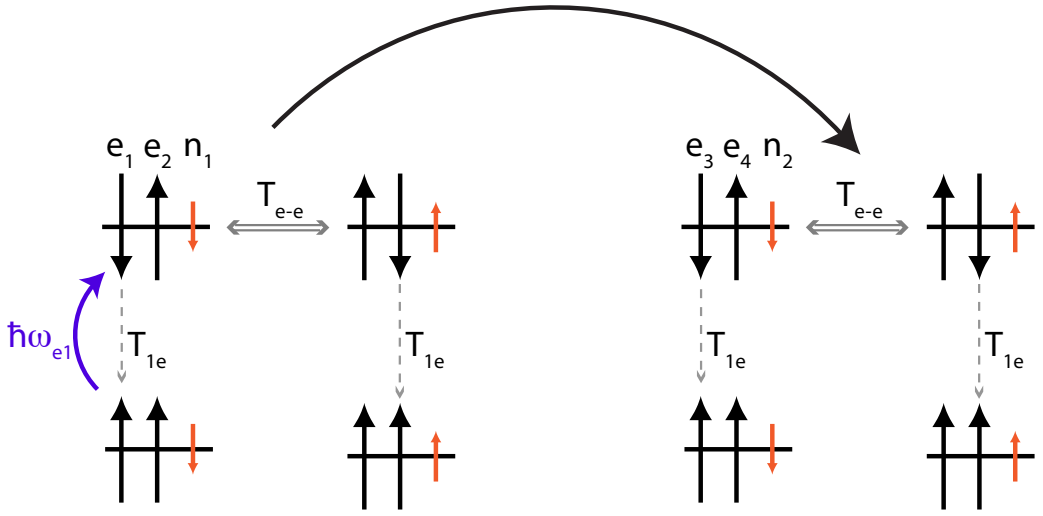

Figure 2.4.4: DNP by thermal mixing

is the electron line width and $t_L^{-1} = {T_{1e}}^{-1} + {T_{1e}}^{-2}$ is the spectral diffusion time.

Spectral diffusion is very efficient provided that the dipolar linewidth is not too small with respect to the inhomogeneous linewidth, but is smaller than the nuclear Larmor frequency ($(T_{2e})^{-1} \ll \omega_n \ll (T_{2e}^*)^{-1}$). For defects at the silicon-silicon oxide interface, the paramagnetic defect concentration we measure is on order 10^{17} spins-cm^{-3}, which gives a homogeneous line-width of about $\sim$ 1.8 MHz, compared to the electron linewidth of $\sim$ 60 MHz and a ^{29}Si NMR frequency of 24 MHz.

As the packets are not independent, it is not possible to write down a closed solution for the internal spin dynamics of the system under DNP conditions if only a small section of the ESR line is subject to microwave irradiation. Therefore, a simple rate constant for polarization can not be isolated was was for the case for the Overhauser Effect or Solid Effect [102]. Solomon [112] and Provotorov [113] suggested an approach which instead considers the spin temperature of each of the electron dipolar and Zeeman spin baths, rather than the microscopic dynamics of the individual spins. Under this approach, the electron dipolar spin system is assumed to rapidly acquire a single spin temperature that is distinctly different to the spin temperature of the electron

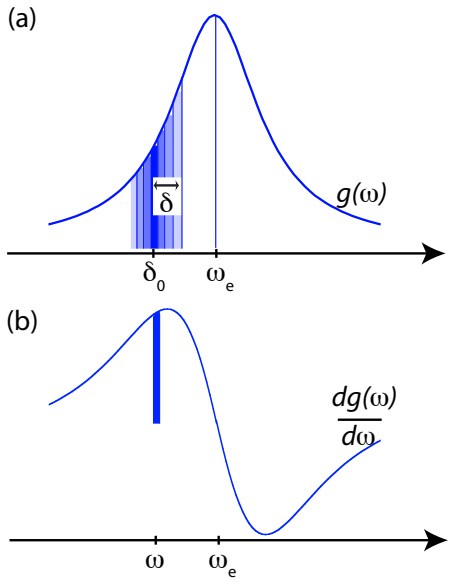

Figure 2.4.5: The electron line $g(\omega)$ consists of a number of independent, but coupled, spin packets. Irradiation at a frequency δ_o causes spectral diffusion of of dipolar order to packets within a range frequency δ. The resulting dynamic nuclear polarization shows a frequency dependence that scales with the derivative of the ESR line.

spin Zeeman system [114]. This approach was then extended by Borghini [115] to include the spin temperature of the nuclear Zeeman bath, and the effect acquired the name Thermal Mixing. Thermal Mixing is not strictly speaking a DNP mechanism by itself, as the electron dipolar baths and nuclear Zeeman baths will reach the same spin temperature without any applied microwave irradiation. However it becomes a mechanism for DNP when the electron spin dipolar system is 'cooled' by the application of a microwave field.

In this thesis, we observe dynamic nuclear polarization by thermal mixing for ^{29}Si nuclei close to the surface of highly oxidized silicon micro and nanoparticles.

3

Nuclear Spin Properties of Silicon Particles

Magnetic resonance imaging of hyperpolarized nuclei provides high image contrast with little or no background signal. To date, in-vivo *applications of pre hyperpolarized materials have been limited by relatively short nuclear spin relaxation times. Here, we investigate silicon nanoparticles as a new type of hyperpolarized magnetic resonance imaging agent. Nuclear spin relaxation times for a variety of Si nanoparticles are found to be remarkably long, ranging from many minutes to hours at room temperature, allowing hyperpolarized nanoparticles to be transported, administered, and imaged on practical time scales. These results suggest that Si nanoparticles can be used as a targetable, hyperpolarized mag-*

netic resonance imaging agent with a large range of potential applications.[1]

3.1 Introduction

The use of nanoparticles for biomedical applications has benefited from rapid progress in nanoscale synthesis of materials with specific optical [116–118] and magnetic properties [119], as well as biofunctionalization of surfaces, allowing targeting [120–122], *in-vivo* tracking [116, 122, 123], and therapeutic action [118, 124]. Porous silicon nanostructured material are of interest for molecular and cell-based biosensing, drug delivery, and tissue engineering applications [38, 39]. For magnetic resonance imaging (MRI), superparamagnetic nanoparticles have extended susceptibility-based contrast agents toward targeted imaging [119], though achieving high spatial resolution with high contrast remains challenging, especially in regions with natural magnetic susceptibility gradients. An alternative approach is direct MRI of hyperpolarized materials with little or no background signal. Hyperpolarized noble gases [66, 125, 126] and ^{13}C-enhanced biomolecules [61] have demonstrated impressive image contrast, but are limited by short *in-vivo* enhancement times ($\sim$ 10 s for noble gases [125], $\sim$ 30 s for ^{13}C biomolecules [61, 64]).

Nuclear magnetic resonance (NMR) in silicon has been widely investigated for half a century [79], and with renewed interest recently in the context of quantum computation [127]. It is known that bulk silicon can exhibit multi-hour nuclear spin relaxation (T_1) times at room temperature [79] and can be hyperpolarized via dynamic nuclear polarization (DNP) [128]. The low natural abundance of spin-1/2 ^{29}Si nuclei (4.7%) embedded in a lattice of zero-spin ^{28}Si nuclei isolates the active nuclear spins from one another and from the environment, leading not only to long T_1 times, but also decoherence (T_2) times of up to tens of seconds [127]. Moreover, the

[1] This chapter is reproduced in part from the manuscript *Hyperpolarized Long-T1 Silicon Nanoparticles for Magnetic Resonance Imaging* with authors J. W. Aptekar*, M. C. Cassidy*, A. C. Johnson, R. A. Barton, M. Y. Lee, A. C. Ogier, C. Vo, M. N. Anahtar, Y. Ren, S. N. Bhatia, C. Ramanathan, D. G. Cory, A. L. Hill, R. W. Mair, M. S. Rosen, R. L. Walsworth, C. M. Marcus, published in ACS Nano 3, 4003 (2009). Copyright (2009) American Chemical Society.

weak dipole-dipole coupling of the sparse ^{29}Si atoms, together with the isotropic crystal structure and the absence of nuclear electric quadrupole moment conspire to keep any induced nuclear polarization aligned with even very weak external fields as the nanoparticle tumbles in space, which occurs, for instance, in fluid suspensions.

This Chapter investigates in detail two critical properties of Si nanoparticles for their use as targetable hyperpolarized MRI imaging agents. First, we demonstrate for the first time that Si nanoparticles retain long T_1 times at room temperature into the sub-micron regime, and investigate how T_1 depends on size for a variety of commercial and ball-milled Si nanoparticles. This dependence is compared to a model of nuclear spin diffusion [128], yielding reasonable consistency between theory and experiment. Second, we demonstrate that long-T_1 Si nanoparticles hyperpolarized by brute force polarization can be imaged using a gradient echo method.

3.2 Samples and experimental methods

3.2.1 Nanoparticle preparation and size separation

Nominally undoped float-zone grown Si wafers (Silicon Quest International) were ⟨111⟩ oriented, with residual p-dopants and nominal resistivity 30-100 kΩ-cm, depending on batch. Highly doped wafers (Virginia Semiconductor) were Czochralski grown, ⟨100⟩ oriented, boron-doped (p-type), with nominal resistivity 0.01-0.02 Ω-cm.

Ball-milled particle were processed as follows. Whole wafers were shattered using a mortar and pestle. Batches of 8.5 g wafer shards were dry ground for 10 minutes at 400 rpm in a planetary ball mill (Retsch PM100) using ten 1 cm diameter zirconia balls. The resulting powder was mixed with 20 ml of ethanol and milled under similar conditions for another 3.8 h. For a final milling, also at 400 rpm, fifty 3 mm diameter zirconia balls were used. The slurry was milled for times ranging from 1 h to 26 h, to give an approximately uniform size distribution between 100 nm and 1 μm. The ball-milled silicon nanoparticles in ethanol were separated by size using a centrifuga-

tional sedimentation process. Parameters were calculated using the Stokes equation [129]. From repeated sonication and centrifugal separation a number of discrete particle size groups could be obtained.

3.2.2 Scanning electron microscopy and size characterization

Scanning electron microscopy and particle-measuring software (Gatan Digital Micrograph) were used to determine the size distributions of the nanoparticles. Dilute suspensions of silicon nanoparticles in ethanol were sonicated for ten minutes before being pipetted onto a vitreous carbon planchett which was mounted on a standard specimen holder with conducting carbon tape. An acceleration voltage of 2 kV was used. For each sample, $>$ 1000 particles were analyzed, sourced from $\sim$ 50 images. Particle agglomeration seen in dry Meliorum and MTI samples has been reported in similarly sized silica nanoparticles [130], but is not expected to occur after pegylation. In these cases (Meliorum, MTI), individual measurement of the particle diameter from SEM images was used instead of software analysis.

Particle size determines regimes of application to biomedicine [131] as well as NMR properties [128]. We investigated room-temperature NMR properties of Si particles spanning four orders of magnitude in mean diameter, from 40 nm to 1 mm. Particles were made by various methods, including ball-milling of nominally undoped (high-resistivity 30−100 kΩ-cm) and highly doped (low-resisitivity 0.01 − 0.02 Ω-cm) commercial silicon wafers, followed by segregation by size (see Methods). We also investigated chemically synthesized Si nanoparticles with mean diameters 40 nm (wet synthesis, > 99.99% elemental purity, Meliorum Corp.), 60 nm (wet synthesis, > 99.99% elemental purity, Meliorum Corp.), 140 nm (plasma synthesis, > 99% elemental purity, MTI Corp.) and 600 nm (electrical explosion synthesis, > 98% elemental purity, Nanostructured & Amorphous Materials, Inc.), obtained commercially. Figure 3.2.1 shows representative scanning electron microscope (SEM) images of all measured particles, along with volume-weighted size distributions obtained by SEM image analysis.

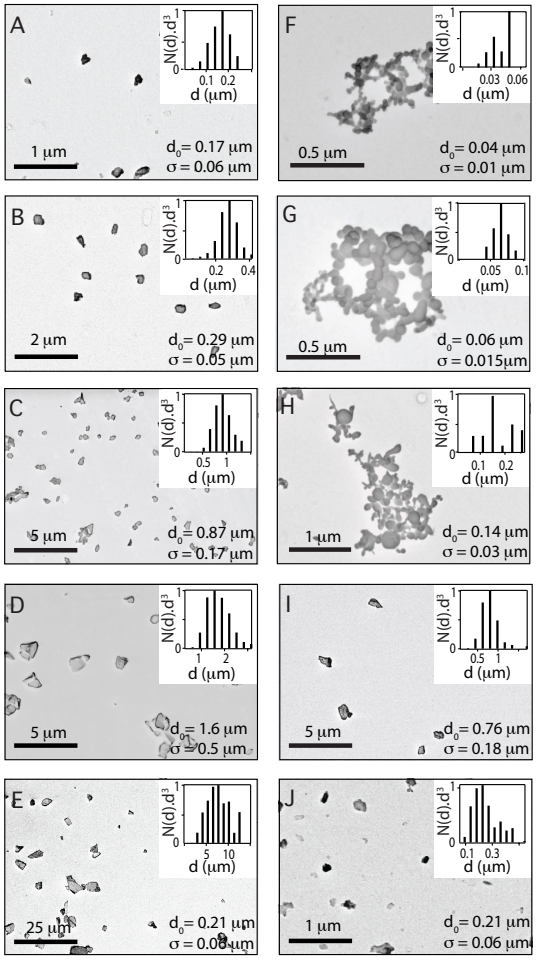

Figure 3.2.1: Electron micrographs of Si nanoparticles (**A**)-(**E**) ball milling high-resistivity silicon wafer, (**F**)-(**G**) wet synthesis (Meliorum) (**H**) plasma synthesis (MTI), (**I**) electrical explosion (NanoAmor) and (**J**) ball milling low-resistivity wafer. Insets: Volume-weighted histograms of diameters following size segregation along with averages d_o and standard deviations σ based on gaussian fits to distributions.

3.2.3 Electron spin resonance

Continuous wave electron spin resonance (cw-ESR) measurements were taken on bulk samples of particles using a JEOL **FE-3XG** X-Band spectrometer at a frequency of 9.106 GHz. The a.c. field (amplitude 0.01mT, f_{mod} = 100 kHz) was swept from 315 mT to 335 mT over a period of 30 s. For each sample, a single peak at B = 324 mT, corresponding to a g-factor of 2.006 was recorded. This is consistent with the reported g-factor of P_b defects at the silicon-silicon dioxide interface [132]. ESR spectra of ball milled silicon particles with sizes 0.17 μm and 1.6 μm. are shown in Fig. 3.2.2. Curves are scaled vertically by sample weight, giving a measure of density of electron spins. Smaller particles have greater defect density, scaling roughly as the inverse diameter (inset, Fig. 3.2.2), suggesting that the defects are on the surface of the nanoparticle [128].

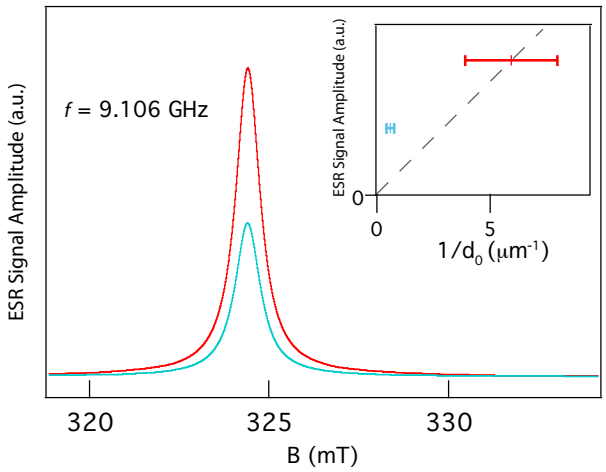

Figure 3.2.2: Electron spin resonance measurements of silicon particles. Weight adjusted ESR spectra of ball milled silicon particles with sizes 0.17 μm and 1.6 μm. Inset: ESR peak area vs inverse particle diameter.

3.2.4 NMR measurements

Nuclear T_1 times of the Si nanoparticles, segregated by size and packed dry in teflon NMR tubes, were measured at room temperature at a magnetic field of 2.9 T using a spin-echo Fourier transform method with a saturation recovery sequence. Following a train of sixteen hard $\pi/2$ pulses

to null any initial polarization, the sample was left at field to polarize for a time τ_{pol}, followed by a Carr-Purcell-Meiboom-Gill (CPMG) sequence $(\pi/2)_X - [\tau - (\pi)_Y - \tau - \text{echo}]^n$ with $\tau = 0.5\,\text{ms}$ and $n = 200$. In Si and other nuclear-dipole-coupled materials echo sequences can yield anomalously long decay tails [98]. However, the Fourier amplitude of the echo train still provides a signal proportional to initial polarization [98]. Values for T_1 are extracted from exponential fits, $A \propto 1 - e^{-\tau_{pol}/T_1}$, to the amplitude, A, of Fourier transform of the echo train for 200 echoes as a function of polarization time (see Fig. 3.3.1 inset for an example).

3.3 ^{29}Si NMR measurements: T_1 and T_2 at room temperature

Figure 3.3.1 shows T_1 as a function of volume-weighted average particle diameter for the various samples, as well as a shell-core nuclear spin diffusion model [128], which has no free parameters. The model assumes T_1 is determined by nuclear spin diffusion to the particle surface, where nuclear spin is quickly relaxed. Undoped ball-milled samples follow a roughly linear dependence on size, $T_1 \propto d_0$, for $d_0 <\sim 10\,\mu$m, saturating at $T_1 \sim 5\,$h for larger particles. The trend of increasing T_1 in larger particles is qualitatively consistent with the shell-core model, and suggests that T_1 is governed by surface relaxation. Electron spin resonance (ESR) measurements (Fig. 3.2.2) show a single peak corresponding to a g-factor of g=2.006, characteristic of P_b-type defect centers at the Si-SiO_2 interface [132]. The shift toward lower T_1 compared to the core-shell model presumably reflects relaxation within the core, which can be attributed to defects and strain induced either by ball milling [133] or noncrystallinity, depending on the method of synthesis. The highly doped ball-milled particles have $T_1 \sim 200\,$s, independent of size. Here T_1 is shortened due to relaxation by free carriers. Smaller commercial particles formed by wet synthesis (> 99.99% elemental purity, Meliorum) and plasma synthesis (> 99% elemental purity, MTI) have T_1 times as long as 700 s, exceeding the predictions of the core-shell model. Larger commercial particles formed by electrical explosion (> 98% elemental purity, NanoAmor) have shorter T_1 than the comparably

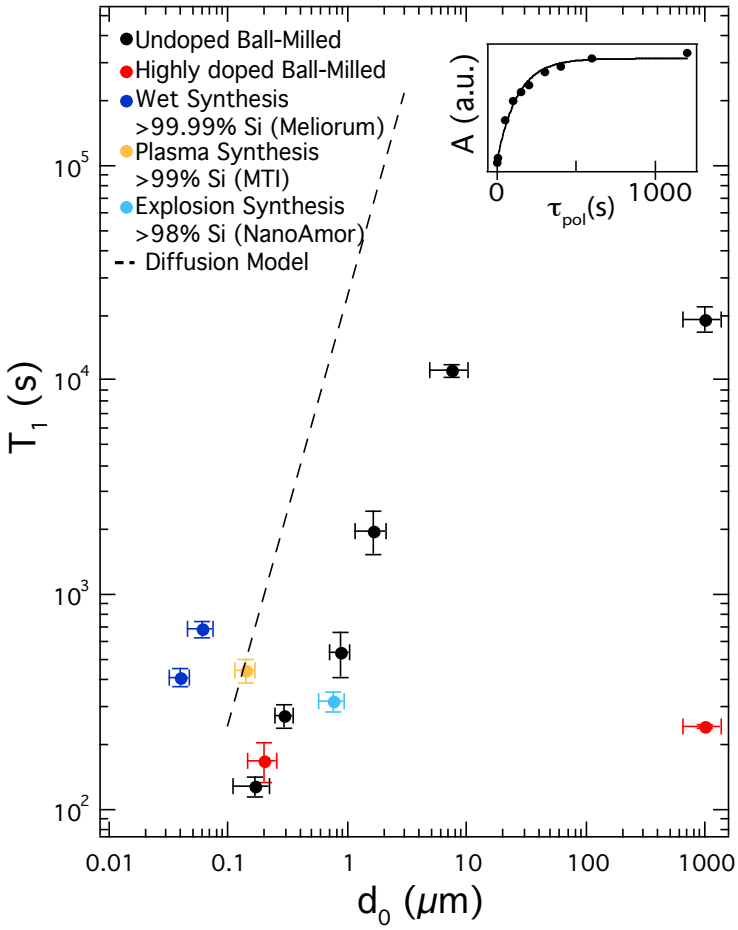

Figure 3.3.1: NMR properties of silicon particles. Nuclear spin relaxation (T_1) times at 2.9 T as a function of particle diameter d_o for various Si particles. Vertical error bars are from exponential fits to relaxation data; horizontal error bars are σ of size distributions (see Fig. 1). Inset: Fourier-transform NMR peak amplitude, A, as a function of polarization time τ_{pol} (see text) for the ball-milled high-resistivity particles with $d_o = 0.17$ μm. T_1 values were measured using a saturation recovery spin echo pulse sequence described in the text.

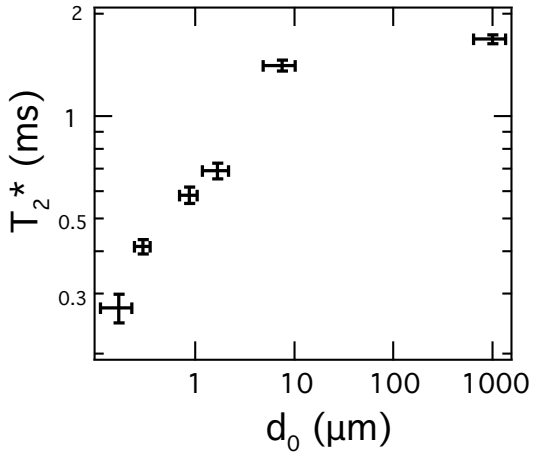

Figure 3.3.2: T_2^* as a function of nanoparticle size measured at room temperature at 4.7 T for ball milled particles.

sized high-resistivity ball-milled particles.

We have also measured the inhomogeneous dephasing times, T_2^*, as a function of mean particle diameter for undoped ball milled samples at 4.7 T (Fig. 3.3.2). T_2^* ranges from 0.3 ms for $d_o \sim$ 0.2μm to 1.8 ms for for $d_o \sim$ 1000μm. We note that while T_1 changes by two orders of magnitude over the range of measured particle sizes, T_2^* changes only by factor of ~ 6.

3.3.1 MRI of hyperpolarized Si nanoparticles

A first demonstration of imaging hyperpolarized Si nanoparticles is shown in Fig. 3.3.3. A phantom in the shape of the letter H was filled with undoped ball-milled particles ($d_o = 1.6\mu$m) and allowed to equilibrate at low temperature (4.2 K) and high field (5 T) for 60 h [61], which enhanced the nuclear spin polarization a factor of ~ 16 compared to room-temperature polarization at that field. The sample was then removed and imaged at room temperature at 4.7 T (using a Bruker DMX-200 spectrometer with a micro-imaging gradient set). The transfer from the low temperature environment to the imager required $\sim$ 60 s, much shorter than the T_1 of the nanoparticles. The phantom was imaged using a small-tip-angle gradient-echo sequence [134] with the following parameters: tip angle $\theta = 9^\circ$, echo time $\tau = 1.2$ ms, field of view = 15 mm, sample thickness = 2.5 cm, single

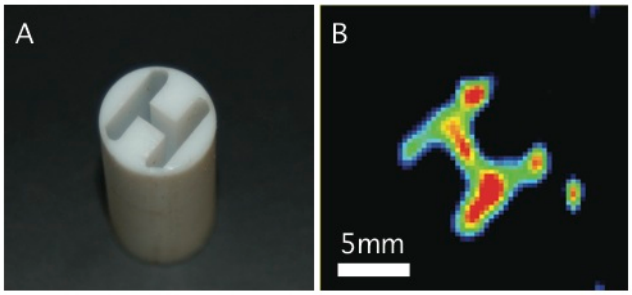

Figure 3.3.3: ^{29}Si magnetic resonance imaging of hyperpolarized Si nanoparticles. (**A**) An H-shaped phantom filled with high-resistivity Si particles ($d_o = 1.6\ \mu m$) pre-polarized at low temperature (T = 4.2 K) and high magnetic field (B = 5 T) for 60 h and warmed and transferred to a 4.7 T imager. (**B**) Single ^{29}Si image of phantom in A. See text for imaging details. No ^{29}Si Si image could be obtained without hyperpolarization using the same sequence.

pass (no averaging), acquisition time = 11 s. The resulting image is shown in Fig. 3.3.3(b). MRI of the same sample equilibrated in the field of the imager at room temperature yielded no detectable image.

3.4 Conclusion

We have demonstrated several key features of Si nanoparticles that establish their potential as a hyperpolarized imaging agent for MRI, including long nuclear relaxation times and receptivity to surface modification with biologically compatible ligands. Room temperature nuclear relaxation (T_1) times for all measured particles were found to be considerably longer than those of previously reported hyperpolarized MRI imaging agents [61, 125, 126], in the range of tens of minutes to hours. Moreover, T_1 in the Si system can be tuned by size and doping, allowing optimization for specific applications in biomedical imaging. We examined T_1 as a function diameter for particles made by ball-milling undoped silicon wafters as well as chemically synthesized nanoparticles. Preliminary measurements on other surface functionalized silicon nanoparticles indicate that the functionalization process does not reduce the nuclear T_1 of the particles. MRI of Si nanoparticles was demonstrated at modestly enhanced polarization using low-temperature

equilibration. While these polarizations are presumably too small for practical use, the results demonstrate that nanoparticles can be successfully transported through large magnetic and temperature gradients without a significant loss of an enhanced polarization. Significantly higher nuclear polarizations (exceeding 10^4) are expected using DNP, with corresponding improvements in image resolution and contrast [61, 126]. Optimizing DNP to achieve high polarization will the subject of future work. In conclusion, the data presented here are necessary for establishing the utility of Si nanoparticles as a flexible platform for imaging agents in MRI.

Acknowledgments

We thank D. C. Bell, F. Kuemmeth, T. F. Kosar, C. Lara, D. Reeves, S. Rodriques, and J. R. Williams for technical contributions and D. J. Reilly, C. Farrar and B. Rosen for valuable discussions. This work was supported by the NIH under grant R21 EB007486-01A1, U54 CA119335, R01 CA124427 and by the NSF through the Harvard NSEC. Part of this work was performed at the Harvard Center for Nanoscale Systems (CNS), a member of the National Nanotechnology Infrastructure Network (NNIN), which is supported by the National Science Foundation under NSF award no. ECS-0335765.

4

Magnetic Field Dependence of the Decay of Nuclear Hyperpolarization in Silicon Microparticles

We investigate the low-field relaxation of nuclear hyperpolarization in undoped and highly doped silicon microparticles at room temperature following removal from high field. For nominally undoped particles, two relaxation time scales are identified for ambient fields above 0.2 mT. The slower, $T_{1,s}$, is roughly independent of ambient field; the faster, $T_{1,f}$, decreases with increasing ambient field. A model in which

nuclear spin relaxation occurs at the particle surface via a two-electron mechanism is shown to be in good agreement with the experimental data, particularly the field-independence of $T_{1,s}$. For boron-doped particles, a single relaxation time scale is observed. This suggests that for doped particles, mobile carriers and bulk ionized acceptor sites, rather than paramagnetic surface states, are the dominant relaxation mechanisms. Relaxation times for the undoped particles are not affected by tumbling in a liquid solution.[1]

4.1 Introduction

Silicon has long been a staple of the microelectronics industry and so has been the subject of intense materials research. In recent years, nanoscale silicon has attracted attention due to its unique electronic and optical properties [135–137], and as a potential agent for medical imaging and drug delivery [38, 39, 138]. Spin phenomena in silicon has been investigated using nuclear magnetic resonance (NMR) for over a half-century [79, 81, 99, 101, 108, 139–141], while material properties and fabrication has continually developed. For instance, the nuclear spin-lattice relaxation time, T_1, provides information about dopants and impurities [79, 99, 101]. Notably, the low natural abundance (4.7%) of spin-1/2 ^{29}Si nuclei in a lattice of zero spin nuclei leads to T_1 of many hours [79, 138] and coherence times up to tens of seconds [141] in undoped bulk crystalline silicon.

These remarkable NMR properties have stimulated interest in silicon as a platform for solid-state quantum computing [142–144], and as a long-lived imaging agent for hyperpolarized magnetic resonance imaging (MRI) [138]. In particular, there have been renewed efforts to understand dynamic nuclear polarization (DNP), a process where saturation or pumping of paramagnetic impurity states by microwave fields or optical illumination can lead to nuclear spin polarizations orders of magnitude larger than thermal equilibrium polarizations [83, 84, 106, 128, 145].

[1] This chapter is reproduced with permission from the manuscript *Decay of nuclear hyperpolarization in silicon microparticles* with authors M. Lee, M. C. Cassidy, C. Ramanathan and C. M. Marcus, published in Phys. Rev. B 84, 035304 (2011). Copyright (2011) by the American Physical Society.

Enhancing polarization by these methods is commonly referred to as hyperpolarization.

Application of silicon as a hyperpolarized imaging agent for MRI requires an understanding nuclear spin relaxation over a broad range of applied fields, from high fields where polarization is induced and imaged, to low fields where the agent is transferred from the polarizer and administered. Previous detailed studies have focussed on low-temperatures, investigating the dependence of T_1 on applied magnetic field, doping [146–148] and strain [149]. It was found that T_1 increased with applied magnetic field, which was explained in terms of the field dependence of electron-nuclear dipole-dipole interaction. The nuclear T_1 was also shown to scale inversely with the concentration of mobile carriers [79, 101]. In silicon nanoparticles, the observed increase in nuclear T_1 with increasing particle size was attributed to diffusion-mediated relaxation via defects at the particle surface [138]. Recent measurements have shown that the relaxation and coherence times of ^{31}P donor-bound electron spin are dramatically reduced near the silicon surface due to P_b defects, in comparison to known values in the bulk [150]. Studies of electrically [108] and optically [140] detected hyperpolarization of ^{31}P donor nuclear spins near the silicon surface, however, do not consider effects of the surface on nuclear spin relaxation.

In this Chapter, we investigate the decay of hyperpolarization of ^{29}Si nuclei in silicon microparticles at room temperature and low ambient magnetic fields. The hyperpolarization for this experiment was induced by waiting for nuclear spins to fully relax to thermal equilibrium in a high-field, room temperature polarizing environment, prior to the placement of sample in the low-field depolarizing environment. Thus the sample was kept at room temperature at all times, ensuring that the applied magnetic field, not sample temperature, was responsible for all measured effects on low-field nuclear spin relaxation that are reported here. We find the decay is bi-exponential, with a slow time scale that is independent of ambient field, and a fast time scale that shows only a modest decrease with increasing ambient field. We develop a model of nuclear spin relaxation in silicon particles that takes into account the heterogeneous makeup of the sample, with direct nuclear relaxation occurring only near the surface, while nuclei in the particle core are relaxed indi-

rectly by spin diffusion. This model extends a previous spin diffusion model [128], which predicts T_1 increasing with the square of the particle diameter. We find that the weak magnetic field dependence observed experimentally is inconsistent with a simple extended spin-diffusion model based on relaxation on individual bound electrons. However, by generalizing the model further to include nuclear spin relaxation mediated by pairs of dipolar-coupled electrons, the essentially field-independent relaxation is recovered by the model [92, 100, 151, 152]. The experimental methods presented here, as well as the use of magnetic field dependence of nuclear T_1 as a probe for testing the relative importance of these different model processes, have precedent in a similar investigation performed on diamond and its ^{13}C nuclear spin relaxation [92, 153, 154].

4.2 Samples and experimental methods

Microparticles made from nominally undoped and boron-doped ball-milled Si wafers were investigated. As shown previously [138], undoped Si microparticles have very long high-field relaxation times ($T_1 \sim 10^4$ s), relevant for hyperpolarized MRI. Undoped samples were produced by ball-milling high-resistivity (> 10 kΩ·cm) float-zone Si wafers (Silicon Quest International) followed by size separation by centrifugal sedimentation, yielding a mean particle diameter of 5 μm [138]. Boron-doped Si microparticles with doping density $\sim 5 \times 10^{18}$ cm^{-3} have much faster nuclear spin relaxation, $T_1 \sim 10^2$ s at high magnetic field. The boron-doped microparticles were produced by ball-milling Czochralski-grown Si wafers (Virginia Semiconductor, resistivity 0.01-0.02 Ω·cm) followed by size separation, yielding a mean particle diameter on the order of 10 μm. Except where noted, samples consisted of a 0.1 mL teflon tube filled with particles. All NMR measurements were carried out at $B_0 = 2.9$ T using a custom-built probe and spectrometer.

Polarization at 2.9 T following a saturation sequence of sixteen $\pi/2$ pulses was measured as a function of time, t_{pol}, using a Carr-Purcell-Meiboom-Gill (CPMG) sequence [96–98], $(\pi/2)_X - [t/2 - (\pi)_Y - t/2 - \text{echo}]^n$ with $t = 1$ ms and $n = 400$. After each data point, the sample was re-saturated and the measurement repeated. As seen in Fig. 4.3.1(a) and Fig. 4.3.4(a), the build-

up of polarization is well described by a single exponential function of t_{pol} for both undoped and doped samples.

Depolarization at low ambient fields was measured after first polarizing at 2.9 T for 8 h ($\sim 3\ T_1$ at 2.9 T), then raising the probe out of the magnet bore to a position where ambient (or holding) fields of 0.2 mT, 6 mT, 130 mT, and 300 mT had been previously calibrated using a Lakeshore 460 gaussmeter. In addition, a nominal zero-field measurement used a commercial zero-gauss chamber (Lakeshore 4060) with ambient field below 1 μT. Following depolarization in ambient field, the sample was returned to field center (2.9 T) and the remaining nuclear polarization was measured using the CPMG sequence described above. The transit time between positions was $\sim$ 5 s, fast compared to T_1 but slow compared to nuclear Larmor times. The sample was fully repolarized following each data point.

In addition to NMR measurements, room temperature electron spin resonance (ESR) measurements were carried out to characterize electronic defects and carriers of the two sample types. The ESR spectrum of the undoped sample showed a single peak at $B = 324$ mT measured at ESR frequency $f = 9.099$ GHz, corresponding to a g-factor centered at 2.006, with a linewidth of 0.47 mT. The ESR spectrum of the boron-doped sample showed a single peak at $B = 336$ mT measured at ESR frequency $f = 9.444$ GHz, again corresponding to a g-factor of 2.006. A g-factor of 2.006 is consistent with reported values for P_b defects at the Si-SiO_2 interface, and is not consistent with g-factors of other common dopants or oxide states [93, 132].

For each sample, an estimate of the electron spin concentration on the particle surface was made by taking ESR spectra with a piece of phosphorus-doped silicon wafer ($0.01 - 0.1\ \Omega$·cm) also inserted in the spectrometer cavity. The addition of the wafer piece resulted in the appearance of additional ESR signal due to the n-type doping. Comparing the peak areas and using the known doping level of the wafer piece yielded an order-of-magnitude estimate of the mean volume density of defect spins, which was $\sim 10^{18}$ cm^{-3} in both samples. Assuming a surface-to-volume ratio of 300 nm-radius spheres, this mean volume density corresponds to a surface defect concentration

of 10^{13} cm^{-2}.

4.3 Results

4.3.1 Undoped microparticles: measurements

Polarization and depolarization data for the undoped microparticles are shown in Fig. 4.3.1. Polarization is well described by a simple exponential,

$$P = P_{0,B_0}\left(1 - e^{-t_{\mathrm{pol}}/T_1}\right), \tag{4.1}$$

with best-fit value $T_1 = 8200 \pm 600$ s, consistent with previous measurements [138]. Equilibrium polarization is small, $P_{0,B_0} = \tanh[(\hbar\gamma_n B_0)/(2k_B T)] = 2\times10^{-6}$. Here, k_B is Boltzmann constant, $T = 300$ K is room temperature, and $\gamma_n = 5.31 \times 10^7\ s^{-1}\,\mathrm{T}^{-1}$ is the nuclear gyromagnetic ratio for ^{29}Si.

In contrast to the build-up of polarization at 2.9 T, depolarization at low ambient fields, B_{dep}, decays with two distinct time scales, which we characterize using a bi-exponential form,

$$\begin{aligned} P = P_{0,B_{\mathrm{dep}}} + \left(P_{0,B_0} - P_{0,B_{\mathrm{dep}}}\right) \\ \times \left((1-a)e^{-t_{\mathrm{dep}}/T_{1,\mathrm{f}}} + ae^{-t_{\mathrm{dep}}/T_{1,\mathrm{s}}}\right), \end{aligned} \tag{4.2}$$

where $T_{1,\mathrm{f}}$ and $T_{1,\mathrm{s}}$ are fast and slow relaxation times, and a is the fraction of spins whose polarization decays slowly. Best-fit values of a, $T_{1,\mathrm{f}}$ and $T_{1,\mathrm{s}}$ are shown in Table 4.3.1. Note that the slow relaxation time depends very weakly on B_{dep}, with $T_{1,\mathrm{s}} \sim 1.4$ - 1.5×10^3 s in all cases. In contrast, fast relaxation becomes somewhat faster (shorter $T_{1,\mathrm{f}}$) with increasing B_{dep}, while the fraction of slow relaxers increases.

Inside the zero-gauss chamber the residual ambient magnetic field is specified to be below

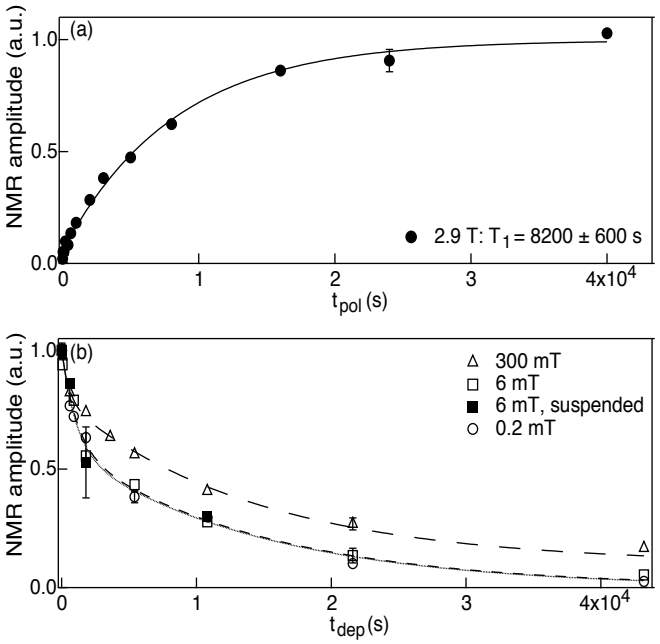

Figure 4.3.1: Relaxation of nuclear spin polarization of undoped silicon particles. (a) Recovery of spin polarization following saturation at $B_o = 2.9$ T. (b) Decay of nuclear magnetization at $B_{dep} = 0.2$ mT (circles), 6 mT (open squares), and 300 mT (triangles), after polarization at 2.9 T, and same data for particles suspended in methanol at 6 mT (filled squares). Curves show best fits to Eq. 1. No signal was observed after 1 second for data taken in the zero-field chamber ($< 1\mu$T).

B_{dep}	a	$T_{1,f}$ (s)	$T_{1,s}$ (s)
300 mT	0.765 ± 0.027	531 ± 179	13850 ± 1030
6 mT	0.593 ± 0.050	903 ± 232	15310 ± 2070
0.2 mT	0.591 ± 0.120	1124 ± 544	14910 ± 5360
< 1 μT		< 1	

Table 4.3.1: Exponential weights and relaxation times fitting to experimental data. $T_{1,f}$ and $T_{1,s}$ are fast and slow relaxation times with which two additive components of the spin polarization decay. a is the relative amplitude of the component which decays at $T_{1,s}$.

the few-μT scale, much weaker than the typical nuclear dipolar field, $B_{n,dd} \sim \mu_o \mu_n / (4\pi a^3) = 0.08$ mT, where $a \sim 4$ Å is the mean separation between randomly distributed ^{29}Si nuclei. At such extremely low fields, spin transitions will occur that are forbidden when $B > B_n$ by the conservation of nuclear Zeeman energy, and nuclear spin relaxation is as fast as decoherence [94]. As expected, we find that in the zero-gauss chamber nuclear polarization decays very quickly, with no visible signal for $t_{dep} > 1$ s.

To investigate the effect of microparticle tumbling on depolarization, a fluid mixture of one part Si microparticles and four parts methanol by weight was compared to a sample of packed dry powder. Depolarization times at 6 mT ambient field showed no significant difference in relaxation times.

4.3.2 Undoped microparticles: model

We interpret NMR and ESR data for the undoped microparticles within a model shown schematically in Fig. 4.3.2, comprising nuclear dipolar diffusion in a core region and relaxation via paramagnetic sites in a shell region near the Si/SiO_2 interface. In undoped silicon, direct coupling of ^{29}Si nuclear spins to phonons is weak [99, 100], and dipolar coupling to paramagnetic impurities and defects typically dominates nuclear spin relaxation. Within our model, the bi-exponential form of Eq. 1 reflects the existence of two populations of nuclear spins within each microparticle: a fraction a, located in the core of the particle, has a long spin relaxation time $T_{1,s}$ mediated by

nuclear spin diffusion; the remaining fraction $(1 - a)$, located within a shell near the Si/SiO_2 interface, has a short relaxation time $T_{1,f}$ mediated by electron-nuclear spin interaction associated with paramagnetic centers at the $Si\text{-}SiO_2$ interface.

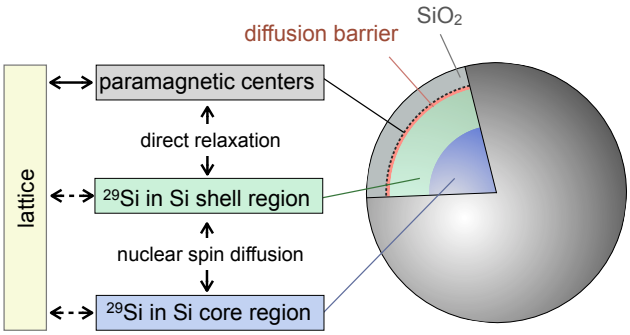

Figure 4.3.2: Model showing the spin reservoirs and relaxation pathways in undoped silicon particles. Nuclei in the core region of the particle relax by transferring their magnetization to the nuclei in the shell region, nearer to the surface, by spin diffusion. The nuclei near the surface can relax quickly due to strong dipolar coupling to paramagnetic defects at the Si/SiO_2 interface.

For $B_{dep} > B_{n,dd}$, the nuclear dipolar spin diffusion rate is independent of magnetic field [84], and is well described by a diffusion constant $D = Wa^2 \sim a^2/(50\, T_2)$, where W is the probability of a flip-flop transition between nuclei due to dipole-dipole interaction, and T_2 is the nuclear decoherence time [100]. This is consistent with our observation that $T_{1,s}$ is roughly independent of B_{dep} across a broad range of values.

The thickness of the shell region is set by the nuclear spin diffusion radius, $\beta = (C/D)^{1/4}$, where C is a constant describing the nature of the dipolar interaction occurring between the nuclei and electrons. Nuclei situated at a distance r from the electrons at the particle surface may relax through a dipolar interaction with the electrons at a rate $\propto C/r^6$ [100].

We consider two physical mechanisms of relaxation in shell region, one in which each nuclear spin interacts with a single electron spin, and the other in which each nuclear spin interacts with a pair of electron spins. The two-electron model captures a crucial physical mechanism by allowing energy matching between electron-spin-pair flip-flops and nuclear spins flips in a magnetic field,

leading to efficient nuclear relaxation with weak dependence on magnetic field.

Modeling nuclear spin relaxation as arising from interaction with individual paramagnetic centers is appropriate for sparsely distributed impurities. This regime has been studied experimentally, for instance, in diamagnetic crystals such as LiF [155, 156] and CaF_2 [157]. In this case, the orientation-averaged dipole interaction strength is given by

$$C_{(1e)} = \frac{3}{10}\frac{\hbar^2\gamma_e^2}{T_{1e}B_{\mathrm{dep}}^2}, \tag{4.3}$$

where γ_e is the gyromagnetic ratio of the electron and T_{1e} the electron spin-lattice relaxation time [100]. This model yields a magnetic field dependence of diffusion-limited relaxation ($R \gg \beta$) at least as strong as $T_{1,\mathrm{s}} \propto B_{\mathrm{dep}}^{1/2}$ because the diffusion radius β and relaxation rate $\propto C$ depend explicitly on field, even when D is field independent [100, 157, 158]. This prediction is incompatible with our experimental results, which show a much weaker field dependence.

In light of this inconsistency, we consider a model of nuclear relaxation at the particle surface that includes three-spin processes involving pairs of interacting electrons, which gives

$$C_{(2e)} = \frac{3}{10}\frac{\hbar^2\gamma_e^2}{B_{\mathrm{dep}}^2}\frac{B_{\mathrm{dep}}^2\gamma_n^2 T_{2e}}{1 + B_{\mathrm{dep}}^2\gamma_n^2 T_{2e}^2}\int_{-\infty}^{\infty}\frac{g(\omega)g(\omega-\omega_n)}{g(0)}\,\mathrm{d}\omega, \tag{4.4}$$

where T_{2e} is the electron spin-spin coupling and $g(\omega)$ is the normalized electron absorption lineshape function [92, 151]. This model has been previously applied to systems with more concentrated paramagnetic impurities, including $La_2Mg_3(NO_3)_{12}\cdot 24H_2O$ [159, 160] and more recently ^{13}C nuclear spin relaxation in diamond [92, 153]. This model accounts for flip-flop transitions between nearby electron pairs, occurring on a time scale $T_{2e} \ll T_{1e}$, which provide the fluctuating magnetic field that can flip nuclear spins. That is, when the dipolar coupling of electron pairs matches the nuclear Zeeman energy, a three-spin interaction can occur that exchanges the spins of the two electrons while flipping a nuclear spin [103]. This process depends on the density of transitions between electronic dipolar energy states that match the nuclear Zeeman energy. For a

Lorentzian electron lineshape, the integral in (3), which describes the probability of finding two electrons within the ESR line differing in frequency by ω_n, can be replaced by $2/(4+\omega_n^2 T_{2e}^2)$. For low B_{dep}, such that $\gamma_n B_{dep} < \gamma_e B_{e,dd} \sim T_{2,e}^{-1}$, where $B_{e,dd}$ is the electronic dipole field felt by a typical nucleus, the density of nuclear-spin-flip transitions will be independent of B_{dep}, hence the rate of direct nuclear spin relaxation by this process will also be independent of B_{dep} [92, 151].

We infer an upper bound for $B_{e,dd}$ from the measured ESR linewidth of 0.47 mT, which gives $\gamma_n^{-1}\gamma_e B_{e,dd} \sim 1.7$ T for the scale of B_{dep} below which nuclear T_1 should be roughly field independent within this three-spin model. The low end of the field-independent range is set by the nuclear dipolar field $B_{n,dd} \sim 0.08$ mT. This range is consistent with the experimental observation that $T_{1,s}$ is roughly field independent from 0.2 mT to 300 mT. Weak field dependences of $T_{1,f}$ and a are likely due to the weak field dependence of T_{1e}.

Very close to each paramagnetic impurity, nuclear spin diffusion is suppressed, creating a barrier to diffusion of radius $b = a(\hbar\gamma_e^2 B_{dep}/\gamma_n 2k_B T)^{1/4}$, due to gradients in the nuclear Larmor frequency [100]. This effect is included in the simulations (described below), but because $\beta \gg b$ it only weakly affects overall relaxation times.

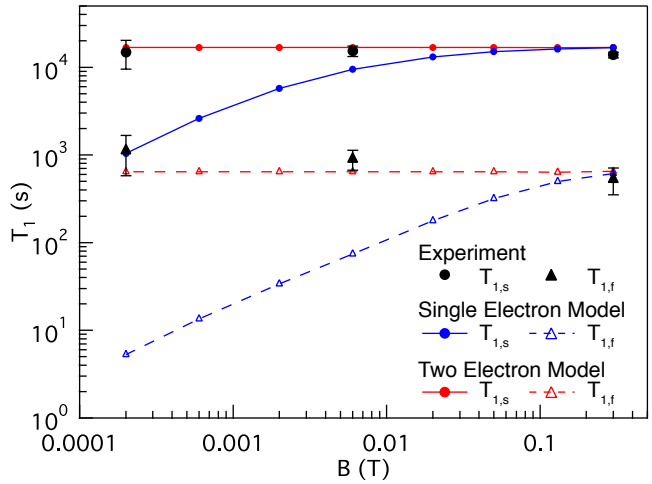

Figure 4.3.3: Experimental slow (black circle) and fast (black triangle) relaxation times, $T_{1,s}$ and $T_{1,f}$, from Table 4.3.1, for bi-exponential nuclear spin relaxation, along with simulation results for a model that includes either one-electron or two-electron processes.

We have simulated nuclear spin relaxation as a function of ambient field for a spherical silicon microparticle with native ^{29}Si concentration and paramagnetic sites at the surface. For both one and two electron processes, the average polarization $P(t_{\mathrm{dep}})$ is approximately bi-exponential, similar to the experimental data. Fits to the relaxation curves gave $T_{1,\mathrm{s}}$ and $T_{1,\mathrm{f}}$ values shown in Fig. 4.3.3. The particle diameter was taken to be 700 nm, smaller than the actual mean particle size. This compensated the spherical assumption, which gave too small of a surface where defects reside. Other parameters in the model were nuclear T_2 of 10 ms (and corresponding nuclear spin diffusion constant 0.3 nm^2/s), electron T_{1e} of 200 ns, and electron T_{2e} of 25 ns. Figure 4.3.3 shows the striking contrast in field dependence between the two models, and that the three-spin process compares relatively well with experiment.

4.3.3 Results for boron-doped microparticles

Nuclear polarization and depolarization of boron-doped Si microparticles are shown in Fig. 4.3.4. Both $P(t_{\mathrm{pol}})$ and $P(t_{\mathrm{dep}})$ are well fit by single-exponential relaxation curves with time constants T_1 that increases with increasing ambient field. The reduction of T_1 by 1-2 orders of magnitude in the doped case reflects the dominant contribution of nuclear relaxation from mobile carriers [101], as well as from ionized acceptors distributed uniformly through the particle instead of just at the surface (Fig. 4.3.5), bypassing the relatively slow nuclear spin diffusion process.

For the specified dopant density, the average distance between dopants is $\sim$ 2.5 nm and the Bohr radius $\sim$ 1.3 nm [161], both an order of magnitude less than the diffusion radius for both single electron and two-electron processes across the range of ambient fields under study. The contribution of mobile carriers can be expressed as an additional relaxation rate which is independent of magnetic field, $T_{1,\mathrm{carriers}}^{-1} \propto N_o A^2$ where N_o is concentration of mobile carriers, and A is the strength of the hyperfine coupling [101].

The measured T_1 is consistent with previous reports of nuclear relaxation rate due to mobile

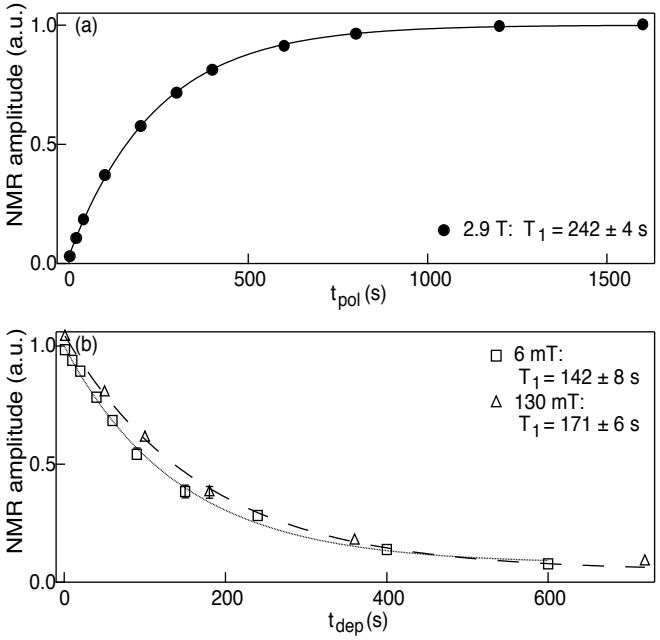

Figure 4.3.4: Nuclear spin lattice relaxation in boron-doped silicon microparticles. (a) Recovery of spin polarization after saturation at $B_o = 2.9$ T. (b) Decay of nuclear magnetization at $B_{dep} = 6$ mT (open square), and 130 mT (triangle), after polarization at 2.9 T. Error bars in (a) are displayed but smaller than the data points shown.

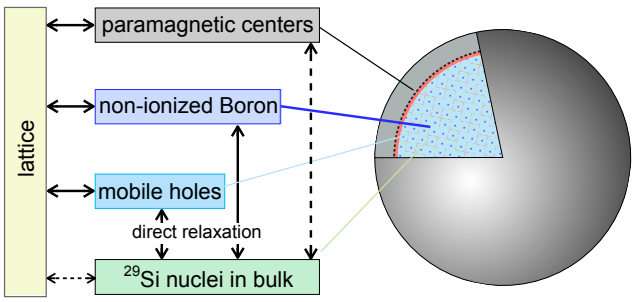

Figure 4.3.5: Rate model showing dominant nuclear relaxation pathways of direct relaxation on mobile holes and short diffusion to ionized boron acceptors throughout the bulk of the particle. Long distance spin diffusion to surface impurities is relatively slow and direct coupling of the nuclei to the lattice is weak.

holes in p-type silicon doped to similar concentrations [79]. The contribution to nuclear relaxation by ionized acceptors as well as surface paramagnetic defects at the surface are responsible for the mild magnetic field dependence of T_1 seen in Fig. 4.3.4(b). We were unable to observe an ESR signal from the mobile carriers, presumably due to their short relaxation times leading to broad ESR lines.

4.4 Conclusion

We have investigated the relaxation of polarization of natural-abundance ^{29}Si nuclei in undoped and doped silicon microparticle samples as a function of ambient magnetic fields at room temperature. In undoped micron-scale particles, the decay of nuclear polarization from a hyperpolarized value was measured from microtesla to 0.3 T. For fields stronger than the nuclear dipolar field, a bi-exponential decay of nuclear magnetization was observed, with a fast component of $\sim 10^2$ s that depends weakly on field and a slow component of $\sim 10^4$ s that is roughly field independent. The relative amplitude of the slowly decaying component increases with the magnetic field, but only slightly. Bi-exponential relaxation suggests the presence of two nuclear spin baths distinguished by their proximity to paramagnetic impurities at the particle surface. The timescales of nuclear spin relaxation are largely independent of ambient field B_{dep} from 0.2 to 300 mT. This independence from B_{dep} is quantitatively consistent with a model of nuclear spin relaxation dominated by a three-spin mechanism in which flip-flop transitions of two electrons at the nuclear Larmor frequency flip a nuclear spin. In highly doped silicon, simple exponential relaxation with a faster T_1 of order a few hundred seconds is observed.

These results can be compared with similar experiments performed in diamond, another material with dilute (1.1 %) spin-1/2 nuclei among a majority of zero-spin nuclei in an fcc lattice [90–92]. Measurement of the nuclear T_1 in natural diamond as a function of magnetic field indicate a contribution of three-spin processes to ^{13}C spin relaxation [92]. Other investigations of nuclear spin relaxation in ^{13}C-enriched diamond [153] and in nanocrystalline diamond [154]

have shown that the relaxation of nuclear magnetization was not well described by a simple exponential approach to equilibrium. The NMR studies in nanocrystalline diamond revealed that the particles consist of a crystalline core and a surrounding shell. All these observations in diamond are similar to our results in silicon microparticles.

Finally, we comment that multi-hour and field-independent nuclear relaxation times for a substantial fraction of the nuclear spin population, including for particles in a fluid suspension, is important for for the use of silicon microparticles as a hyperpolarized MRI imaging agent.

Acknowledgments

We thank David Cory for generous access to the ESR spectrometer. We acknowledge support from the National Science Foundation under NSF-0702295, the BISH Program (CBET-0933015),and the Harvard NSF Nanoscale Science and Engineering Center. Fabrication used the Harvard Center for Nanoscale Systems (CNS), an NSF National Nanotechnology Infrastructure Network (NNIN) site (ECS 0335765). ML acknowledges support from Samsung.

5

Modulation Enhanced Dynamic Nuclear Polarization in Silicon Microparticles

Enhanced dynamic nuclear polarization (DNP) of silicon particles is demonstrated by applying a modulation to the microwave frequency used for irradiation of the electron spin system. The highest polarization enhancements are recorded when the microwave frequency is modulated at a rate much greater than the electron spin lattice relaxation rate, where multi-electron dipolar spin processes can contribute to the polarization process. Using this technique we can generate a bulk ^{29}Si nuclear polarization of up to $\sim 10\%$ that is suitable for in-vivo ^{29}Si magnetic resonance imaging at biologically relevant concentra-

tions.[1]

5.1 Introduction

Generating high nuclear spin polarizations, or hyperpolarization, is important across a wide range of fields in physics, chemistry and biology. Initially investigations focused on generating spin-polarized targets for neutron scattering experiments [94], however more recent studies have been directed at understanding many body spin dynamics [152] and in semiconductors such as silicon for the initialization of nuclear spin states for donor based quantum computing [108, 128]. Very recently, large nuclear spin polarizations have proved especially useful for revealing the structure of complex biomolecules [59] and for in-vivo studies of metabolic processes in cancer using hyperpolarized metabolites [55, 61], and hyperpolarized ^{29}Si nanoparticle tracers [138]. Dynamic nuclear polarization (DNP) is one technique whereby the nuclear polarization may be lifted high above its equilibrium through the interaction with a system of unbonded electrons. Applying off-resonant microwave irradiation drives dipolar flip-flop interactions between strongly coupled electron spins, creating an oscillating magnetic field that may in turn polarize nearby nuclear spins. Continuous wave microwave (μW) irradiation is generally applied at a single frequency with a bandwidth constrained to that of the μW cavity of the source (typically < 1 MHz). For any electron spin system that has a broadened resonance line the resulting nuclear polarization is limited, as only a small fraction of the total electron spin system actively contributes to the DNP process. Microwave frequency modulation was previously been used in DNP of polarized butanol targets, where an enhancement of up to 65% of the deuterium polarization and 10% of the proton polarization was generated [162], but a detailed understanding of the effect was not revealed.

[1] This chapter is in preparation for publication as *Modulation Enhanced Dynamic Nuclear Polarization in Silicon Microparticles* with authors M. C. Cassidy, M. Lee, and C. M. Marcus.

This Chapter reports enhanced ^{29}Si DNP in silicon microparticles generated by modulation of the microwave frequency used for irradiation of the electron spin system. Using this we generate up to a 500% increase in the ^{29}Si nuclear polarization under DNP conditions. The highest polarization enhancements are recorded when the microwave frequency is modulated over a frequency bandwidth that covers the electron spin resonance line at a rate much greater than the electron spin lattice relaxation rate T_{1e}. The relative enhancement and ultimate nuclear polarization achieved are strongly dependent on applied microwave power and temperature, and so this technique may be used to compensate for more readily available low power microwave sources, or in cases where the experimental temperature is limited.

5.2 Samples and experimental methods

The sample consisted of $\sim$ 20 mg of natural abundance (^{29}Si = 4.7%) high purity polycrystalline silicon powder (Alfa Aesar, d = $\sim$ 3 μm). DNP experiments were performed in a continuous flow cryostat at 4 K (unless specified), in a 2.89 T superconducting NMR magnet (ω_n = 24.404 MHz). The sample was packed in a thin walled teflon tube which was held in direct contact with the flowing helium vapor. A custom insert for the cryostat and a home built spectrometer with a saddle coil were used for NMR detection. A +20 dBm (100 mW) Gunn diode tunable from 80 – 82 GHz was used as the microwave source. The output of the Gunn was amplified to +33 dBm (2 W) using a solid state amplifier for high power measurements. The DC bias of the Gunn diode was modulated with a symmetric ramp function at a rate f_{mod} and amplitude corresponding to a bandwidth of BW_{mod} which provided a uniform modulation across the entire bandwidth. The nuclear polarization was measured with a saturation recovery sequence, whereby the residual nuclear polarization is nulled with a series of $\pi/2$ pulses, and the sample is allowed to polarize for a period of time t_{pol} before the nuclear polarization is measured with a single $\pi/2$ pulse. Further details of the experimental setup are described in Appendix A.

5.3 Results

5.3.1 Microwave frequency dependence

Figure 5.3.1(a) shows the derivative of the X-band continuous wave electron spin resonance (CW-ESR) spectrum of the sample measured at 4 K [163]. Natural oxidation of the silicon surface creates a rich network of unbonded electron spins ($\sim 10^{14}\text{cm}^{-2}$) [164] at the silicon:silicon dioxide interface that can be used for DNP [128]. These unbonded electron spins, or P_b defects, have a g-factor that is dependent on the orientation of the underlying silicon crystal lattice (g=2.002-2.010) [132]. This range in g-factors averaged over the different orientations of the underlying lattice in a spherical particle, together with internal crystal strain results in the broad ESR line observed. The microwave frequency dependence of the ^{29}Si NMR peak area, P_{DNP}, which is directly proportional to the ^{29}Si nuclear polarization, is shown in Fig. 5.3.1(b) and plotted over the same range of g-factors as the data in Fig. 5.3.1(a). The ^{29}Si nuclear polarization scales proportional to the derivative of the ESR line ($\frac{dG}{dB}$) [100] with the cross over frequency between negative and positive nuclear polarization occurring at the average value of the electron g-factor of the system (g=2.0065). Centering the microwave source at each frequency point and then modulating (f_{mod}= 60 kHz, BW_{mod} = 70 MHz) significantly increases the ^{29}Si nuclear polarization generated for the same polarization time t_{pol} = 300 s, as well as causing the microwave frequency response to shift outward with increasing modulation bandwidth.

A simplified schematic diagram of the energy levels of the electron and ^{29}Si nuclear spin systems is shown in Fig. 5.3.1(c). The electron spin system consists of spins with a wide range of g-factors and we can consider it made up of a network of pairs of dipolar-coupled electron spin packets separated in frequency by the ^{29}Si nuclear Larmor frequency. At low temperature and high magnetic fields the electron spin bath (black arrows) becomes highly polarized while the net polarization of the ^{29}Si nuclear bath remains low (red arrows). Microwave irradiation at a frequency ω_{e_1} drives continuous rotations of electrons in packet e_1 on a time scale t_{sat}. For a system of strongly dipolar

coupled electron spins such as this, the rate of electron dipole-dipole interactions is much greater than the rate of electron spin lattice relaxation ($T_{2e,SS}^{-1} \gg T_{1e}^{-1}$). The electrons in packet e_1 can undergo a spin flip-flop with a spin in packet e_2 without loss of dipolar energy ($\downarrow\uparrow \Leftrightarrow \uparrow\downarrow$). If the two electrons differ in Zeeman energy by the nuclear Zeeman energy ($\hbar(\omega_{e1} - \omega_{e2}) = \hbar\omega_n$) where ω_{e1} and ω_{e2} are the respective electron Larmor frequencies and ω_n the nuclear Larmor frequency, the dipolar interaction generates a fluctuating I_Z magnetic field that can flip a nearby nuclear spin and still conserve total energy [94]. The electron in packet e_2 will thermalize with the lattice at a rate T_{1e}^{-1}, before being able to pair up with another nucleus and repeat the cycle. Provided T_{1e} is much faster than the nuclear spin lattice relaxation time T_{1n}, a significant nuclear polarization will be built up.

Representative ^{29}Si NMR spectra with and without modulation after 300 s (dashed lines) and 10800 s (solid lines) of polarization at 4 K are shown in Fig. 5.3.1(d). The spectra are similar to that of other studies of polycrystalline silicon [128] and consist of a broad peak (3 kHz linewidth), corresponding to amorphous silicon, observed for all values of t_{pol}, and a narrow feature (500 Hz linewidth), corresponding to crystalline silicon, appearing for $t_{pol} > 600$ s. The particles have a core-shell structure, consisting of a number of crystalline cores surrounded by a polycrystalline and amorphous silicon shell. DNP occurs at in the silicon:silicon dioxide interface, and thus polarizes the amorphous and polycrystalline regions of the particle first. The crystalline cores which are specially separated from the polarization sites are polarized by nuclear spin diffusion at a rate $\frac{\delta P}{\delta t} = D\nabla^2 P$. The diffusion constant $D = Wa^2 \sim a^2/(50\, T_2)$, where W is the probability of a flip-flop transition between nuclei due to dipole-dipole interaction, and T_2 is the nuclear decoherence time [100]. The thermal signal acquired under Ernst angle conditions at 300 K($\theta = 5^\circ$, $t_{rep} = 2$ s, 80000 averages) is shown in the inset. No ^{29}Si signal is observable at 4 K without microwave irradiation, but by comparing the thermal signal at 300 K with the DNP enhanced signal we estimate a total nuclear polarization of $\sim$ 10% after $\sim$ 18 hours of polarization at +33 dBm applied microwave power (f_{mod} = 10 kHz, BW_{mod} = 30 MHz).

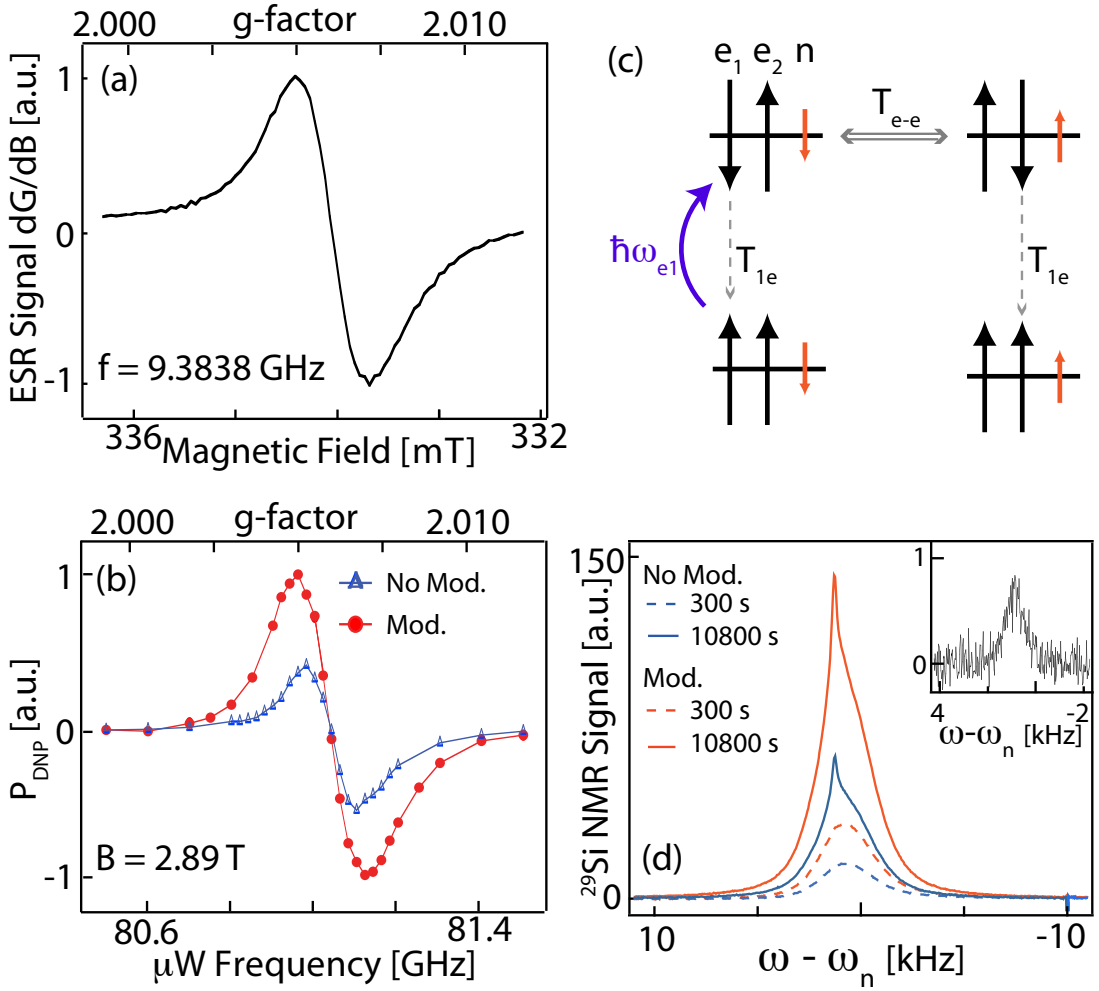

Figure 5.3.1: (a) X-band CW-ESR spectrum acquired at 4 K. (b)^{29}Si NMR peak area as a function of μW frequency with (f_{mod}= 60 kHz, BW_{mod} = 70 MHz) and without frequency modulation for t_{pol} = 300 s at + 20 dBm applied microwave power. Lines are provided to guide the eye. The data in (a) and (b) are plotted over the same range of g-factors to aid in comparison. (c) Schematic representation of the energy levels of the ^{29}Si nuclei (red arrows) and the electron spin bath (black arrows) at high magnetic fields and low temperatures. The arrows show the mechanism for generating a positive nuclear polarization. Details of the mechanism are described in the text. (d) ^{29}Si NMR spectra for t_{pol} = 300 s (dashed lines) and t_{pol} = 10800 s (solid lines) with and without μW frequency modulation (+ 20 dBm applied microwave power). The thermal signal at 300 K acquired under Ernst angle conditions is shown in the inset.

5.3.2 Time dependence

Figure 5.3.2(a) shows the time evolution of the the nuclear polarization at +20 dBm applied power with and without modulation of the microwave source. Two distinct rate constants are observed, and the data is well fit by a bi-exponential function of the form $P_{\mathrm{DNP}} = \left(Ae^{-t_{\mathrm{pol}}/\tau_{\mathrm{f}}} + Be^{-t_{\mathrm{pol}}/\tau_{\mathrm{s}}}\right)$. We define $P_{\mathrm{mod,DNP}}$ as the polarization under DNP conditions with frequency modulation and $P_{\mathrm{o,DNP}}$ as the polarization under DNP conditions without frequency modulation. The polarization time constants τ_{f} and τ_{s} are extracted from time dependence measurements for the case of no modulation and BW_{mod} = 10 MHz, 40 MHz, 70 MHz and 100 MHz and plotted in Fig. 5.3.2(b). At low modulation bandwidths, modulating the μW frequency causes these polarization times to increase with modulation bandwidth, while these times are reduced at higher bandwidths resulting in a polarization enhancement $\varepsilon = \frac{P_{\mathrm{mod,DNP}}}{P_{\mathrm{o,DNP}}}$ that increases over time. Examination of the modulated and unmodulated spectra for each time point in Fig. 5.3.2(a), reveals that the 500 Hz crystalline feature emerges at the same time points despite the addition of modulation. Modulation will not change the rate of polarization by nuclear spin diffusion, which is only determined by the density of ^{29}Si nuclei and the nuclear T_2, but increases the number polarization sites around the particle surface participating in the DNP process, and so increases the polarization generated.

5.3.3 Microwave power and temperature dependence

The response of the polarization to applied microwave power (measured at the input to the cryostat) is shown in Fig. 5.3.3 (a). Both the modulated (f_{mod}= 60 kHz, BW_{mod} = 70 MHz) and unmodulated ^{29}Si nuclear polarizations increase with applied microwave power, but the effects of modulation are strongest at moderate applied power $\sim$+10 dBm. In the low power regime, both responses follows a power law dependence $\propto H_1^a$, where H_1 is the strength of the microwave field. Fits to the experimental data give $a = 0.27$ for modulation and $a = 0.4$ without modulation. These responses are significantly weaker than the $a = 2$ response predicted by a rate equation

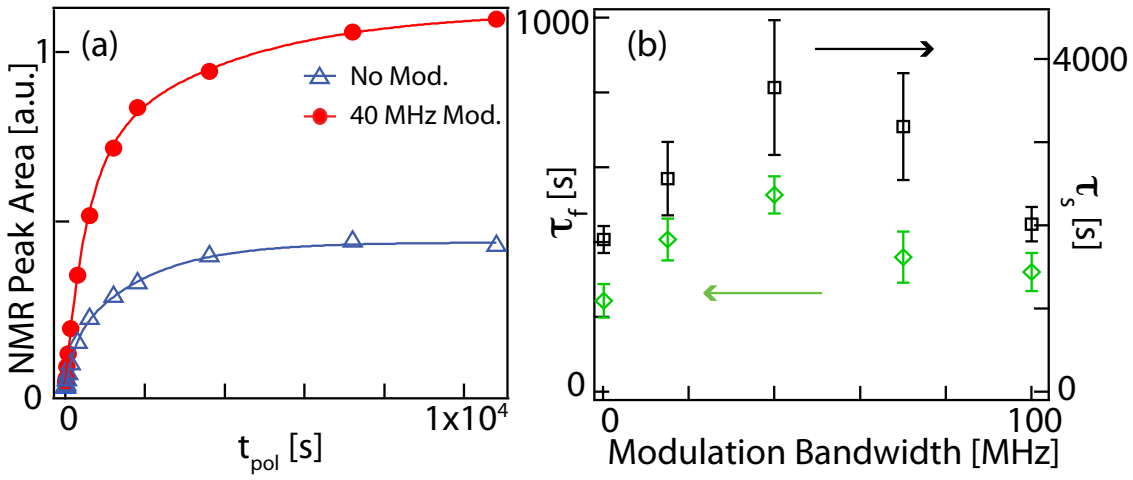

Figure 5.3.2: (a)^{29}Si NMR peak area as a function of DNP polarization time with (f_{mod}= 60 kHz, BW_{mod} = 40 MHz) and without frequency modulation of the μW source. (b) Polarization time constants τ_f and τ_s as a function of modulation bandwidth show an increase the polarization rate with increasing bandwidth. The time constants are extracted from biexponential fits of the nuclear polarization as a function of polarization time described by the equation in the text. In all cases the μW source was centered at 80.966 GHz.

analysis for direct DNP [100]. This is because, despite t_{pol} being short compared to the overall nuclear polarization time for the sample, it is still much longer than the time taken to efficiently saturate each electron spin packet τ_{sat}. Much of the signal thus comes from nuclei polarized by nuclear spin diffusion, rather than direct polarization. It is important to note that despite the highest ^{29}Si nuclear polarizations being achieved with the fully amplified source, modulation of the output of the 20 dBm source alone can generate close to the same polarization as unmodulated irradiation with a much higher power source.

The temperature dependence of the ^{29}Si nuclear polarization with (f_{mod}= 60 kHz, BW_{mod} = 70 MHz) and without modulation, together with the enhancement is shown in Fig. 5.3.3 (b). Power law fits to the data (solid lines) show an enhancement $\propto T^{-\kappa}$, with $\kappa = 0.9$ in the case of modulation and $\kappa = 1.3$ without. Increasing the temperature from 3 K to 20 K significantly decreases the polarization of the electron spin system (from ~60% to 10%) and therefore the amount of energy that can be transferred to the nuclear spin bath. Additionally, the spin lattice

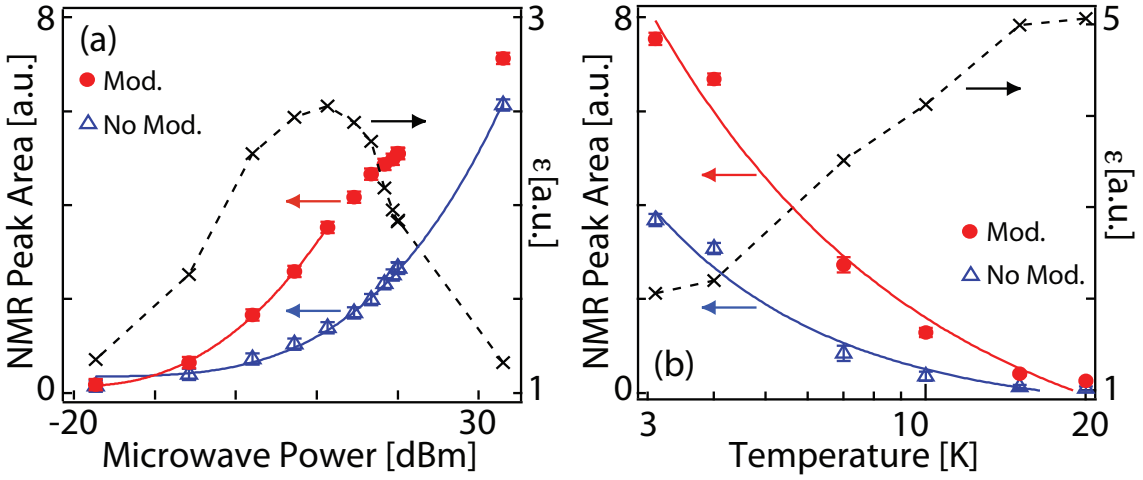

Figure 5.3.3: (a) Microwave power and (b) temperature response of the ^{29}Si NMR peak area under DNP conditions with (f_{mod}= 60 kHz, BW_{mod} = 70 MHz) and without frequency modulation. The enhancement due to frequency modulation is shown on the right hand axis. Fits to the data (solid lines) are described in the text.

relaxation time of the P_b defect has a strong temperature dependence $T_{1e} \propto T^{-2}$ in the range of 2-20 K [165] making it more difficult to saturate the electron spin system at higher temperatures.

5.3.4 Dependence on modulation frequency and bandwidth

To further investigate the dynamics of the DNP process with frequency modulation, we study the enhancement as a function of the modulation sweep frequency and bandwidth after a polarization time t_{pol} = 300 s at + 20 dBm applied microwave power. This time is long enough to give a high signal to noise, but is before the spin-diffusion regime dominates the data. Figure 5.3.4(a) shows the evolution of the ^{29}Si polarization enhancement ε with f_{mod} after μW irradiation at 80.966 GHz at a fixed bandwidth BW_{mod} = 35 MHz. Four distinct regions can be identified. At very low modulation rates(I) (f_{mod} < 1 Hz), the polarization is approximately equal to the unmodulated value ($\varepsilon \sim 1$). As the modulation frequency is increased above $\sim$1 Hz (II), the enhancement also increases, before saturating again at a value of $\sim$ 100 Hz (III). At large modulation rates ($f_{mod} > \sim$100 kHz) (IV), the enhancement decreases due to a capacitive response of the microwave source, resulting in a reduction in the actual modulation bandwidth that can be

generated. The enhancement in Fig. 5.3.4(a) is independent of the duty cycle and direction of applied modulation, and so we assume no coherent processes are being driven in the electron spin system.

For each of the regions in Fig. 5.3.4(a) we measure ε as a function of BW_{mod} (f_{mod} = 0.1 Hz, 50 Hz, and 50 kHz), shown in Fig. 5.3.4(b). At f_{mod} = 0.1 Hz, no enhancement effect is evident across the range of modulation bandwidths studied. At f_{mod} = 50 Hz, the polarization enhancement steadily increases from the case of no modulation (300 kHz intrinsic bandwidth) until it saturates at approximately the NMR frequency of the sample. When the modulation is very fast (f_{mod}=50 kHz) ε continues to increase with increasing BW_{mod}.

The transitions between regions (I-III) in Fig. 5.3.4(a) are characterized by two distinct modulation rates, $f_{\text{I}-\text{II}}$, and $f_{\text{II}-\text{III}}$. We measure ε as a function of f_{mod} for a range of values of BW_{mod} (Fig. 5.3.4(c)), and extract these characteristic modulation frequencies from biexponential fits $\varepsilon = \left(Ae^{-f_{mod}/f_{(\text{I}-\text{II})}} + Be^{-f_{mod}/f_{(\text{II}-\text{III})}}\right)$ to the data. The intrinsic packet width is set by T_{2e}^{-1} where T_{2e} = 0.86 μs is the homogeneous intrinsic spin-spin coupling which we extract by extrapolating the peak widths of the ESR and unmodulated DNP data from Fig. 5.3.1 to zero field. We normalize these characteristic frequencies to a time spent irradiating a packet of width T_{2e}^{-1} as $t_{\text{I}-\text{II}(\text{II}-\text{III})} = (f_{\text{I}-\text{II}(\text{II}-\text{III})}.BW)^{-1}$ (inset Fig. 5.3.4(c)) finding $t_{\text{I}-\text{II}(\text{II}-\text{III})} = 5e^{-3}(1e^{-3})$ approximately constant across the range of bandwidths studied. The movement of these transition regions is also strongly dependent on temperature (Fig. 5.3.4(d)), and values of $t_{\text{I}-\text{II}}$ and $t_{\text{II}-\text{III}}$ as a function of temperature also plotted (inset Fig. 5.3.4(d)) together with fits of the form $y_o + AT^{-2}$ (solid lines). The T^{-2} behavior is consistent with previous low temperature measurements of T_{1e} of P_b defects showing $T_{1e} \propto T^{-2}$ [165].

5.3.5 Theoretical model

Realistically, the packets e_1 and e_2 in Fig. 5.3.1 are not isolated from other packets within the electron spin system, and dipolar order will propagate through the spin system in a process known as

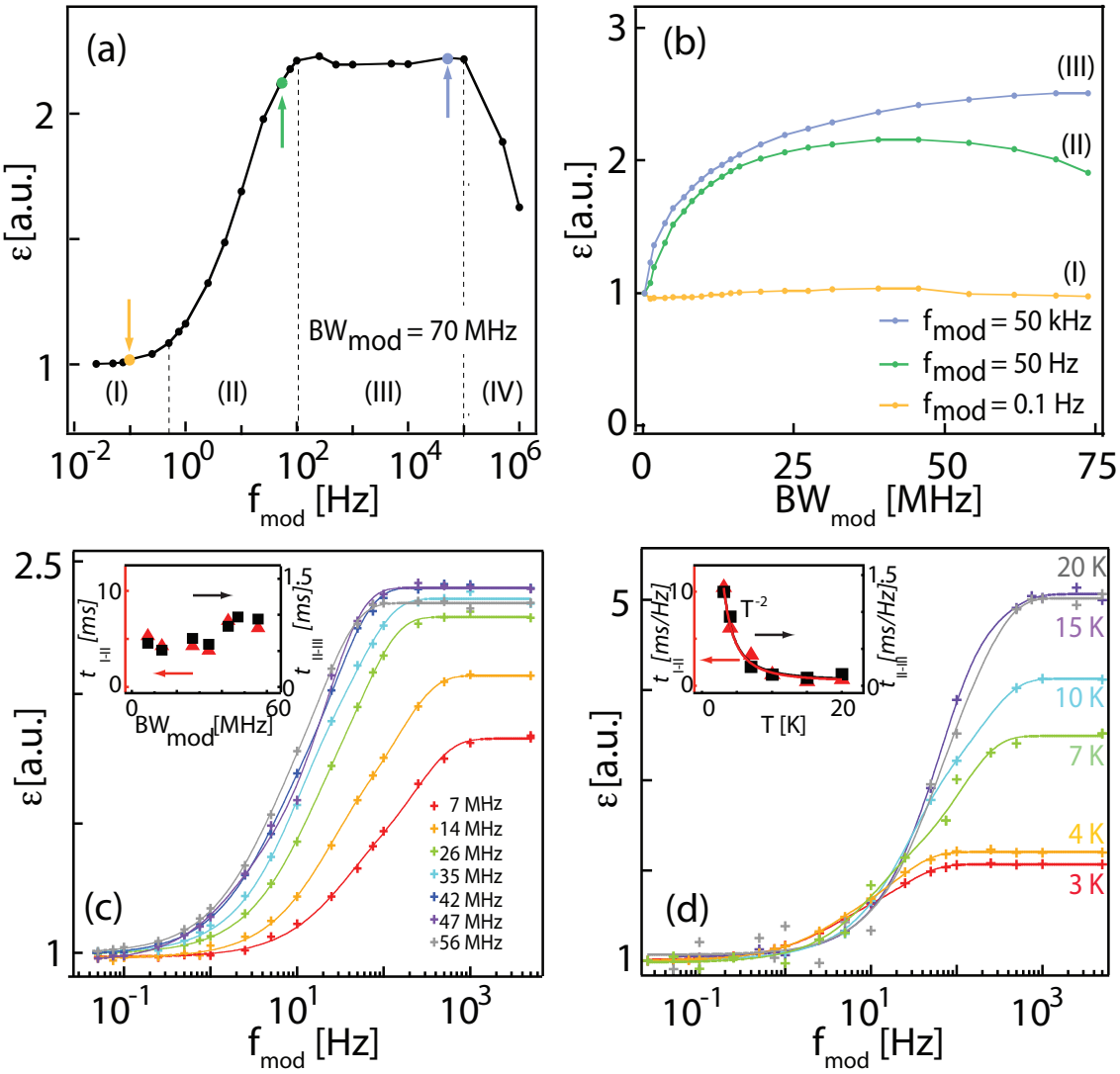

Figure 5.3.4: DNP enhancement ε as a function of (a, c, d) modulation frequency, (b) modulation bandwidth after 300 s of microwave irradiation centered at 80.966 GHz. Movement of the characteristic modulation frequencies with increasing modulation bandwidth (c) and temperature (d). In (a) and (b) lines are provided to guide the eye. The solid lines in (c) and (d) are biexponential fits described in the text. The insets in (c) and (d) show the characteristic modulation frequencies extracted from the fits.

spectral diffusion. The dipolar order created by saturating a packet e_1 at frequency ω_{e1} will therefore be transferred to other frequency-separated packets in the spin system. These packets can then undergo their own flip-flops and polarize local nuclear spins. The timescale for this diffusion of dipolar order follows a Lorentzian diffusion kernel in systems with similar concentrations of paramagnetic defects [111], where the magnetization $M(t, \delta, \delta_0)$ at time t at a frequency δ away from the irradiation frequency δ_0 is,

$$M(t, \delta, \delta_0) = \frac{mt/\pi}{(mt)^2 + (\delta - \delta_0)^2} \tag{5.1}$$

where $m = (\Delta\omega)_{1/2}/(2t_L)$ is the diffusion parameter for the spin system and $(\Delta\omega)_{1/2}$ is the ESR line width and $t_L^{-1} = {T_{1e}}^{-1} + {T_{1e}}^{-2}$ is the spectral diffusion time.

After the microwave saturation of packet e_1 ceases as the modulation frequency moves through the ESR line, the dipolar order created during the saturation process will thermalize back to the lattice on time scale T_{1e}. Modulation competes with this natural spectral diffusion, by artificially enhancing the saturation of other packets within the ESR line. The natural spectral diffusion process is temperature independent at low temperatures [111], however due to the strong temperature dependence of T_{1e}, artificial modulation will have a temperature dependence as observed in Fig. 5.3.3 and Fig.5.3.4. As the temperature is increased, T_{1e} approaches T_{2e} and the spin packet e_1 will relax back to the lattice before undergoing any dipolar interaction. Therefore less natural spectral diffusion takes place, and the effects of artificial modulation are enhanced (Fig. 5.3.3(b)). Similarly, increasing the applied microwave power increases the saturation of the irradiated electron spin packet. At high microwave powers, this increased saturation leads to an enhancement in natural spectral diffusion, and so the effects of artificial modulation are reduced (Fig. 5.3.3(a)).

5.4 Conclusion

For the silicon microparticle sample under study, the greatest ^{29}Si polarization is achieved with the highest applied microwave power and lowest operating temperature. Nevertheless, the modulation technique applied to a lower power source generates polarizations almost as high as the unmodulated high power case. This technique may prove useful to compensate for the lack of a high power source, or for when experimental limitations prevent the lowering of the temperature. We note that the technique is not specific to defects in silicon, and it may be useful for enhancing the nuclear polarization of any system that has an inhomogeneously broadened ESR line where $T_{2e}^{-1} << \omega_n << (T_{2e}^{*})^{-1}$.

Acknowledgments

We thank C. Ramanathan for many helpful discussions. We acknowledge support from the the BISH Program (CBET-0933015) and the Harvard NSF Nanoscale Science and Engineering Center.

6

Synthesis of High-Quality Silicon Nanoparticles for Hyperpolarized ^{29}Si Magnetic Resonance Imaging

We describe the synthesis, materials characterization and dynamic nuclear polarization (DNP) of silicon nanoparticles (SiNPs) for use as hyperpolarized magnetic resonance imaging (MRI) agents. The particles are synthesized through a metathesis reaction between sodium silicide and silicon tetrachloride then surface functionalized with a variety of passivating ligands. These particles show significantly longer

size-adjusted ^{29}Si spin lattice relaxation (T_1) times (> 600 s) than other silicon particles measured previously, and retain these long-T_1 times after hyperpolarization by low temperature DNP.[1]

6.1 Introduction

Silicon nanoparticles (SiNPs) with sizes ranging from 1 nm to 100 nm are of great interest across many areas of research including thermoelectrics, photovoltaics, nanoelectronics and nanomedicine. The smaller sizes (< 5 nm) emit light due to quantum confinement effects [166, 167] while larger sizes (> 10 nm) have desirable electronic transport properties are highly pursued for the production of photovoltaics [168, 169]. Silicon and its oxide derivatives have emerged as materials of choice for applications in nanomedicine due to their biocompatibility and biodegradability *in-vivo* [39, 170], and are under investigation as drug delivery vehicles [38, 161, 171, 172] and imaging agents [38, 39, 138, 173, 174]. *In-vivo* imaging of silicon nanoparticles has been achieved via a variety of techniques including optical imaging [38, 39, 173, 174] positron emission tomography (PET) [9] and magnetic resonance imaging (MRI) [171, 173, 175]. MRI is an attractive technique for non-invasive imaging because it allows high-contrast imaging of opaque structures with detailed anatomical resolution without the use of ionizing radiation. *In-vivo* MRI of silicon particles has generally been performed through the incorporation of paramagnetic materials [171, 175] that disrupt the relaxation and coherence times of proximal ^{1}H nuclei resulting in negative contrast on a ^{1}H anatomical image. Recently, a new technique has been demonstrated for positive-contrast imaging of silicon particles using MRI [138] where the ^{29}Si nuclei within silicon particles (4.7 % natural abundance) are hyperpolarized and imaged directly *in-vivo* using ^{29}Si MRI. This technique allows for background-free imaging, similar to PET, but without the use

[1] This chapter is submitted for publication as *Synthesis of High-Quality Silicon Nanoparticles for Hyperpolarized ^{29}Si Magnetic Resonance Imaging* with authors T.M. Atkins, M. C. Cassidy, M. Lee, S. Ganguly, C. M. Marcus and S.M. Kauzlarich. Reproduced with permission from NanoLetters, submitted for publication. Unpublished work copyright (2012) American Chemical Society.

of ionizing radiation. The initial *in-vivo* demonstrations of ^{29}Si hyperpolarized MRI described in Chapter 8 utilized commercially sourced micron-scale particles that could be monitored in the *in-vivo* environment for over 40 minutes. In intravenous studies, these particles were confined to the vascular structure of the animal, as their size rendered them unable to cross the cell wall.

A variety of methods have been investigated for preparing silicon nanoparticles. Use of thermal techniques such as laser pyrolysis and thermal decomposition has been widespread [5, 176–178], but control over size and materials properties using these techniques is poor. There has been some success in producing 5 - 20 nm diameter SiNPs by reverse micelle under high temperatures and pressures, with limited yield [179]. Synthetic colloidal chemistry allows the simultaneous control of both the size and surface of the nanoparticle, offering prospects of creating large quantities of high purity monodisperse silicon nanoparticle samples. To date, prior research investigated the reaction of metal silicides with silicon tetrachloride in dimethoxyethane with silicon nanoparticles 1 - 2 nm in diameter reported [180]. The reaction of the Zintl salt with ammonium halide has also been reported with average sizes of 4 nm [181]. Therefore, the scope exists for refinement of these techniques to produce larger silicon nanoparticles with diameters greater than 10 nm that may be used for hyperpolarized ^{29}Si *in-vivo* imaging within the cellular environment.

At standard experimental temperatures and magnetic fields the polarization of a bath of nuclear spins is extremely low, on the order of one part in 10^{-5} - 10^{-7} depending on the nuclear species. Hyperpolarization increases the nuclear spin polarization by several orders of magnitude, allowing the investigation of weak nuclear species by nuclear magnetic resonance (NMR) in low concentrations [84]. The effect has been exploited across many areas of chemistry, biology, physics and medicine. Hyperpolarization has been used in materials science as a nanoscale characterization tool [182, 183], while in biochemistry it has been used to revealed the structure of complex biomolecules such as proteins and peptides [184–186]. In clinical applications, hyperpolarized noble gases have allowed detailed imaging of the lung [53] and metabolites such as ^{13}C labeled pyruvate have been used for monitoring therapy in oncology [55, 61].

The spin lattice relaxation time (T_1) sets the approximate time scale for which the signal from the hyperpolarized nuclei can be observed for imaging. Most enriched metabolites and noble gases have T_1 times on the order of 5 - 30 s in the *in-vivo* environment, as the nuclei are strongly coupled to local ^{1}H spins. In solid-state spin-1/2 materials, such as silicon, the primary source of nuclear spin-lattice relaxation is via an interaction with unbonded electrons or holes which occur in the form of free carriers, or paramagnetic centers existing at lattice defect sites or at the surface. If the material is pure, the nuclear spin polarization is largely protected from sources of relaxation, resulting in bulk times of many hours. [79, 84, 138]. Previous NMR investigations of silicon micro and nanoparticles showed that reducing the bulk to the nanoscale results in T_1 times that are strongly dependent on the particle size, purity and density of isolated defects [138]. The ^{13}C nucleus in diamond is another solid-state spin-1/2 system under investigation as a hyperpolarized imaging agent, however measured T_1 times are extremely short, less than 2 s for particles 5 - 30 nm in diameter [187].

In this Chapter we describe the colloidal synthesis of high-quality silicon nanoparticles with size 10 nm. By controlling stoichiometry and systematically varying the solvent and capping ligands, the materials properties such as size, purity and surface termination could be tuned. This results in particles that have significantly longer size-adjusted ^{29}Si nuclear spin relaxation (T_1) times than other commercially sourced silicon particles [138], as well as diamond nanoparticles of similar sizes [187]. We show that all of these particles can be hyperpolarized by DNP and hold their polarization. These silicon nanoparticles may be useful for *in-vivo* imaging studies using silicon nanoparticles that are small enough to enter the cellular environment.

6.2 Samples and experimental methods

6.2.1 Chemicals

Silicon tetrachloride ($SiCl_4$, 99.998 %) was purchased from Aldrich and was distilled. Silicon tetraiodide (SiI_4, 99 %) and silicon tetrabromide ($SiBr_4$, 99%) were purchased from Alfa Aesar and were used without further treatment. Sodium hydride powder (NaH, 95 %) and silicon powder (Si, 99 %) were purchased from Sigma-Aldrich and were used without further treatment. Ammonium bromide (NH_4Br > 99.99 %) was purchased from Sigma-Aldrich and dried before use. The aromatic halide 4-bromoaniline (C_6H_6BrN, 97 %) and the alkyl halide octyl bromide ($C_8H_{16}Br$, 99 %) were purchased from Aldrich and were used without further treatment. Tetraethylorthosilicate (TEOS, 99.999%) and poly(ethylene glycol) methyl ether (PEG) were purchased from Aldrich. Aminopropyltrimethoxysilane (APTMS, 97%) and dioctylether (DOE, 99%), dimethoxyethane (DME, 99%) and squalane ($C_{30}H_{62}$) were purchased from Aldrich. All manipulations were carried out under dry N_2, in either a glove box or a Schlenk line, using standard anaerobic and anhydrous techniques. CAUTION: Sodium hydride powder is reactive to oxygen, moisture and must be handled under an inert atmosphere with care.

6.2.2 Preparation of Na_4Si_4 precursor

Sodium silicide, was prepared according to a modified procedure published in Ref [166]. A high-energy Spex 8000 M ball mill with a tungsten carbide milling vial and two tungsten carbide balls (diameter of 1 cm) was used to ball-mill mixtures of NaH and Si. The starting materials were transferred to a milling vial inside a glove box filled with N_2. The milling vial was wrapped in saran wrap in order to reduce oxygen diffusion during ball-milling. The milling was performed for 30 min to obtain a homogenous powder followed by which the milling vial was transferred back to the glove box. The milled mixture of NaH and Si was placed into a 1 mL alumina crucible with a 1.5 mL alumina boat as a cover. The crucibles were placed into a quartz tube with rubber stopcocks

on both ends. The quartz tube was removed from the glove box and placed in a horizontal tube furnace and connected to Ar flowing at 30 mL/min with a mineral oil bubbler outlet. The quartz tube was heated at 420°C for 48 h. After cooling to room temperature, the black product was transferred in an air-free manner to the glove box for further manipulation. CAUTION: Na_4Si_4 is highly reactive to moisture and must be handled under an inert atmosphere with care.

6.2.3 Synthesis of Silicon NPs via Sodium Silicide with Silicon tetrachloride

Aniline and alkyl terminated silicon nanoparticles were prepared by reacting the halogenated silicon nanoparticles with either 2.0 mL of 0.5M 4-Dimethyl amino phenylmagnesium bromide (C_6H_6NMgBr) in THF or 2.2 mL of 0.5M octylmagnesium bromide ($C_8H_{16}MgBr$) in THF respectively. The Grignard reaction was performed using 4:1, 3:1, and 2:1 ratios of Na_4Si_4 to $SiCl_4$. The cooled halogenated silicon nanoparticle solution was evaporated and 100 mL of anhydrous THF was placed in the flask and allowed to stir. The Grignard reagent was added dropwise. The mixture was allowed to reflux overnight. The reaction was allowed to cool and the solution was separated by centrifugation (8000 rpm for 20 min). The liquid layer was decanted and the solid was placed into a separatory funnel with a water hexane layer and the suspended layer of solid between the water/hexane layer was isolated. The solid was washed three times with a total of 60 mL of methanol and centrifuged. This produced silicon nanoparticles with a yield of approximately 30%.

6.2.4 Synthesis of Silicon NPs via Sodium Silicide with silicon tetrachloride, annealing and amino propyl trimethoxysilane coating

The coating was a modified procedure previously published in Ref. [188]. The washed solid obtained from the synthesis of sodium silicide with SiCl4 was placed into 5 mL of methanol and allowed to stir overnight. The solvent was evaporated by rotary evaporation and was annealed at 650°C for 20 minutes under an 80:20 H_2/N_2 gas flow mixture. The solid was placed back in fresh

DME and 5 mL of H_2O was added and allowed to stir overnight followed by the addition of 0.3 mL (1.8 mmol) of amino propyltrimethoxysilane and the resulting solution was stirred overnight. The solvent was evaporated under reduced pressure. The solid was washed with HPLC H_2O to remove any un-reacted APTMS.

6.2.5 Characterization

Powder X-ray diffraction (XRD) were performed using an air sensitive holder on a Bruker D8 diffractometer operating at 40 kV and 40 mA with CuK radiation (λ = 0.154184 nm). Morphology and chemical functionality were analyzed by a CM-12 transmission electron microscope (TEM) with an accelerating voltage of 120 kV and a Shimadzu IR Prestige-21 Fourier transform infrared spectrophotometer (FTIR). High resolution TEM (HRTEM) was performed on a JEOL 2500SE Schottky emitter microscope operating at 200kV and equipped with a Gatan multiscan camera. TEM samples were prepared by dissolving the silicon nanoparticles into isopropanol and dipping the grids into the solution. For HRTEM, a drop of the solution was put on the copper grid and dried overnight under a heat lamp. Raman spectroscopy was performed on a Renishaw RM1000 laser Raman microscope equipped with Argon 514nm laser for excitation guided by a microprobe. Continuous wave x-band electron spin resonance measurements were performed on the samples at room temperature (Bruker ElexSys E500). The a.c. field (amplitude 0.001 mT, f_{mod} = 100 kHz) was swept from 343.5 mT to 358.5 mT over a period of 60 s. An estimate of the electron spin concentration on the particle surface was made by taking ESR spectra with a piece of phosphorus-doped silicon wafer also inserted in the spectrometer cavity. The addition of the wafer piece resulted in the appearance of additional ESR signal due to the n-type doping. Comparing the peak areas and using the known doping level of the wafer piece (0.008 - 0.01 Ω.cm) yielded an order-of-magnitude estimate of the mean volume density of defect spins.

6.2.6 Room temperature ^{29}Si T_1 measurements.

The room temperature T_1 of the samples were measured at B = 2.89 T with a saturation recovery Carr-Purcell-Meiboom-Gill (CPMG) sequence. A train of 32 hard $\pi/2$ pulses saturated residual magnetization, and the sample was allowed to polarize for a time τ. The magnetization was rotated to the transverse plane with a single $\pi/2$ pulse and (N=200) π pulses performed. The echos following each of the π pulses were Fourier transformed and the height of the peak was used as a measure of the nuclear polarization. The data was fitted with an exponential function $P = P_0 + Ae^{-\tau/T_1}$ and the characteristic polarization time constant (T_1) extracted.

6.2.7 ^{29}Si dynamic nuclear polarization.

Low temperature microwave induced dynamic nuclear polarization (DNP) was performed at T = 3.6 K using a home-built DNP polarizer operating at B = 2.89 T, f_{ESR} = 81 GHz. Details of the polarizer construction are described in Appendix A. A saddle coil that could be tuned across a wide range of temperatures was used for NMR detection. The ^{29}Si nuclear polarization was measured in-situ under DNP conditions using a saturation recovery sequence. A train of 32 hard $\pi/2$ pulses saturated residual magnetization, and the sample was allowed to polarize for a time τ. The magnetization was rotated to the transverse plane with a single $\pi/2$ pulse and the free induction decay measured. The area under the Fourier transformed peak was used as a measure of the ^{29}Si nuclear polarization. For depolarization measurements, the samples were polarized at the frequency giving the highest nuclear polarization for 6 h. The microwaves were then turned off and the remaining ^{29}Si polarization measured with series of 20 degree pulses separated by 100 s. A mathematical correction was applied in post processing to take into account the excess magnetization used up by earlier pulses in the sequence.

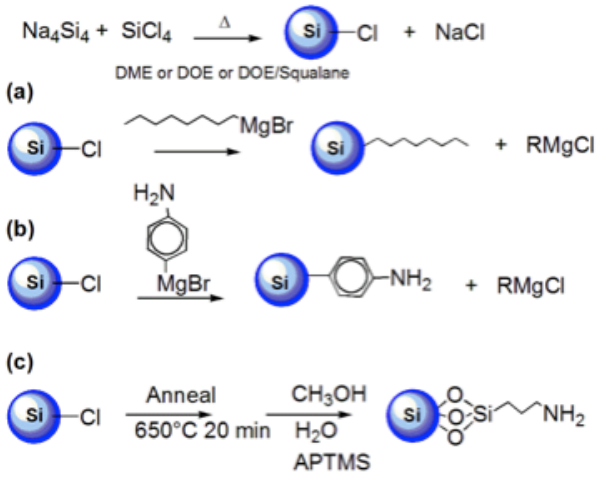

Figure 6.3.1: Synthetic scheme used to produce SiNPs with sizes ∼10 nm. (a) Zintl salt, Na4Si4 with SiCl4, reacted with octylmagnesium bromide, (b) Zintl salt, Na4Si4 with SiCl4, reacted with 4-dimethylaminophenylmagnesium bromide and (c) Zintl salt, Na4Si4, with SiCl4 and annealed and passivated with aminopropyltrimethoxy silane.

6.3 Results

6.3.1 Materials characterization

We used a metathesis reaction of sodium silicide (Na_4Si_4) with a silicon tetrachloride ($SiCl_4$) as a basis for forming chlorinated SiNPs (Fig. 6.3.1). This consistently produced SiNPs with narrow size distributions. Silicon tetrabromide and silicon tetraiodide were also investigated as precursors and produced similar results.

The chlorinated SiNPs were surface passivated with an alkane or an aromatic amine by reacting them with Grignard reagents octylmagnesium bromide ($C_8H_{16}MgBr$) (Fig. 6.3.1(a)) and 4-dimethyl amino phenylmagnesium bromide (C_6H_6NMgBr) (Fig. 6.3.1(b)) in dimethoxyethane (DME) or dioctyl ether (DOE)/Squalane. To enhance the crystallinity of the SiNPs, we annealed the chlorinated SiNPs in forming gas at 650° for 20 mins and passivated these SiNPs with amino propyltrimethoxy silane (APTMS) (Fig. 6.3.1(c)). Representative transmission electron microscope (TEM) images of SiNPs produced by separate reactions are shown in Fig. 6.3.2 and have

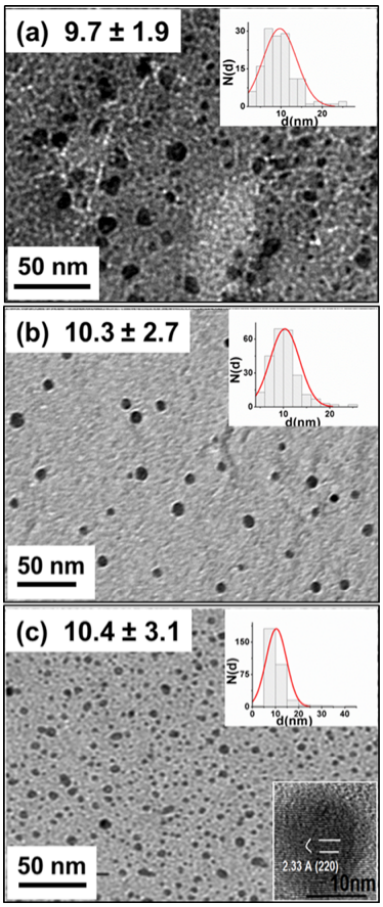

Figure 6.3.2: Representative TEM images of SiNPs for the three synthetic schemes described in Fig. 6.3.1(a-c). The size distributions are shown in the inset. Additional inset in (c) shows HRTEM of crystalline SiNPs following annealing.

size distributions of (a) 9.7 ± 1.9 for the octyl terminated SiNPs, (b) 10.3 ± 2.7 nm for the aniline terminated SiNPs and (c) 10.4 ± 3.1 nm for the annealed amine terminated trimethoxysilane. All reaction schemes produced dispersed SiNP samples that suspended in solution and were free from aggregation, indicating good termination of the particle surface. The annealed SiNPs showed a visible diamond crystalline lattice structure under high resolution TEM (inset, Fig. 6.3.2(c)) and showed no additional aggregation after annealing due to sintering.

We used powder x-ray diffraction (XRD) and Raman spectroscopy to determine the degree of crystallinity of the as-grown and annealed particles (Fig. 6.3.3). The metathesis reaction scheme consistently produced amorphous SiNPs, as determined by their negligible XRD signal (Fig. 6.3.3(a))

	Bulk crystalline Si	Bulk amorphous Si	Nanoscale Si
Raman Stretch (cm^{-1})	525	480	505

Table 6.3.1: Raman stretches of bulk, amorphous and nanoscale silicon

and a Raman stretch of 497 cm-1 (Fig. 6.3.3b), which is indicative of the broadened and shifted transverse-optical Raman mode associated with amorphous silicon (Table 6.3.1). After annealing, strong XRD peaks were observed at positions agreeing with those corresponding to a bulk crystalline silicon standard. The broadened and skewed Raman mode at 501 cm^{-1} was also consistent with models for crystalline silicon nanoparticles [166]. Analysis of the XRD peaks by the Scherrer equation and a Gaussian size distribution on the most intense peak of the diffraction pattern (111) indicated a crystallite size of 14 ± 3 nm, in good agreement with sizing by TEM, indicating that there was close to 100% conversion from the amorphous to crystalline phase.

The surface passivation for each of the samples was determined by infrared spectroscopy (Fig. 6.3.4). The octyl terminated SiNPs (Fig. 6.3.4a) show stretches of the methylene groups at 2964 and 2891 cm-1, together with a long chain methyl group observed at a wavelength of 796 cm-1. The SiNPs passivated using 4-dimethyl aminophenylmagnesium bromide show evidence of the amine group, indicated by a 3592 and 3517 cm^{-1} stretch, together with the N-H bend and the N-H wag at 1639 cm^{-1} and 802 cm^{-1} respectively (Fig. 6.3.4(b)). For SiNPs that were terminated with APTMS, the N-H bend and wag were observed at 1449 and 800 cm^{-1} respectively. All samples showed evidence of oxidation, indicated by the Si-O-Si stretch at 1000-1100 cm-1 due to incomplete surface passivation.

6.3.2 ^{29}Si NMR and DNP measurements

Figure 6.3.5 shows the measured ^{29}Si nuclear spin lattice relaxation times (T_1) of a range of synthesized SiNP with different diameters. The T_1 and sizes of silicon particles measured in previous

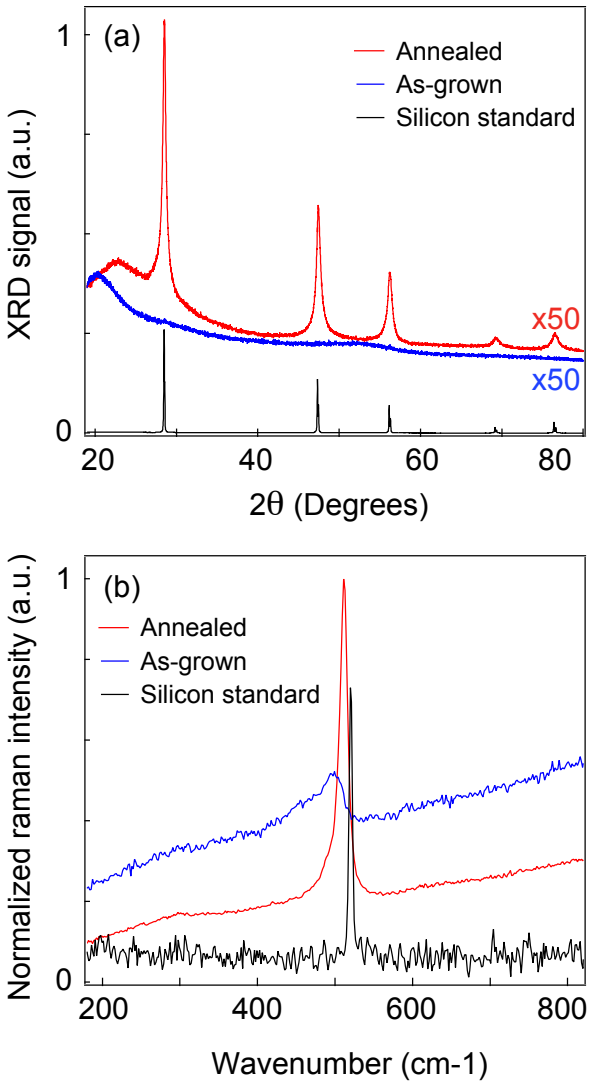

Figure 6.3.3: Crystallinity of as-grown and annealed silicon nanoparticles. (a) X-ray diffraction and (b) Raman spectroscopy of silicon nanoparticles before and after annealing shows a transition from amorphous to crystalline states.

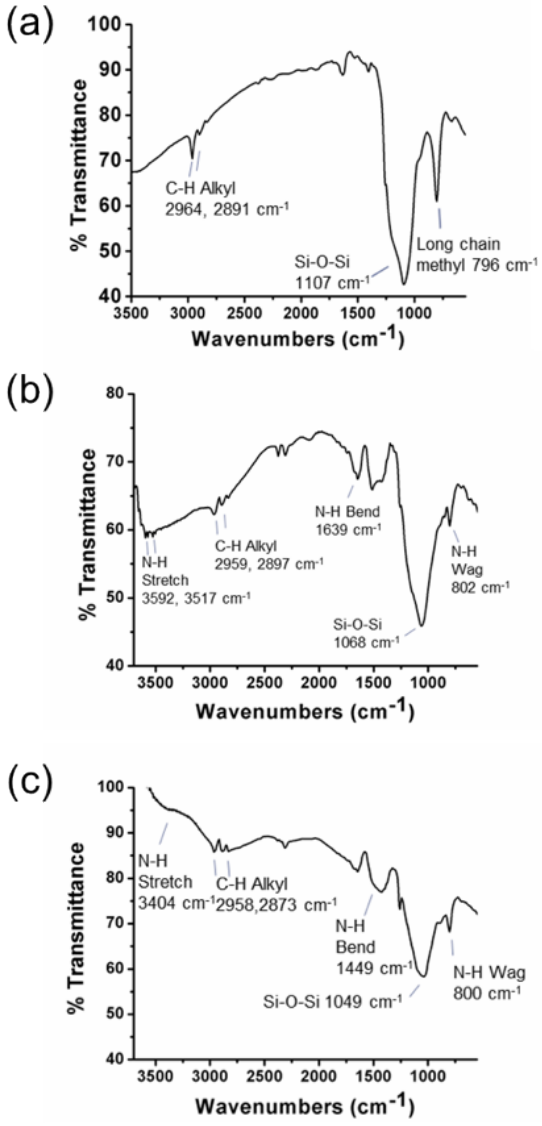

Figure 6.3.4: Infrared spectra of alkyl, aromatic and silane terminated SiNPs. (a) Octyl terminated SiNPs, (b) Aniline terminated SiNPs (c) Amine terminated trimethoxysilane SiNPs.

investigations are shown as a reference [138], together with a nuclear spin diffusion-based model for T_1 relaxation. All synthesized particles showed extremely long size-adjusted T_1 times, $\sim$ 600 s for the annealed samples, similar to T_1 times measured for particles 60 nm in diameter also synthesized by wet synthesis techniques. For high purity silicon particles the primary mechanism for relaxation is spin diffusion of the nuclear polarization, P, from the center of the particle to the particle surface, according to $\frac{dP}{dt} = D\Delta P$ where D is the spin diffusion constant, and so T_1 scales quadratically with particle diameter. Unbonded electrons at the particle surface (primarily at the silicon-silicon dioxide interface), and proximal spins contained within the passivating moiety can then drive local nuclear relaxation. The rate of this relaxation is set by the density of these spins and their own relaxation time [94], and scales with distance r^{-6}, where r is the distance between the ^{29}Si nucleus and relaxing spin. Impurities within the particle, such as free carriers, unbonded electrons or metal contaminants cause additional relaxation and shorten the ^{29}Si nuclear T_1 time. Similar T_1 times were seen for the alkane and aromatic terminated particles, indicating that the choice of passivating moiety had little effect on the internal spin dynamics of the particle. We note that the T_1 times of the crystalline samples are shorter than the amorphous samples, potentially due to the introduction of isolated point defects in the silicon lattice brought about by the annealing process.

Natural oxidation of the surface of crystalline silicon creates a source of unbonded electrons that can be used for DNP. Electron spin resonance (ESR) was performed to determine the nature of these defects and their density (N_e). For each reaction scheme, the weight-adjusted ESR spectra (B=0.35 mT, T = 300 K) is shown together with the ^{29}Si nuclear polarization as a function of microwave frequency (B = 2.89 T and T = 3.6 K) (Fig. 6.3.6). In each case the ESR and DNP data is plotted across the same range of g-factors to aid in comparison. The g-factors extracted for each sample, determined by the zero crossing in the ESR and DNP data differ slightly (Table 6.3.2), ranging from 2.0059 to 2.0087, however there is good agreement seen between the room temperature ESR and low temperature DNP data in each case. The samples show defect densities ranging

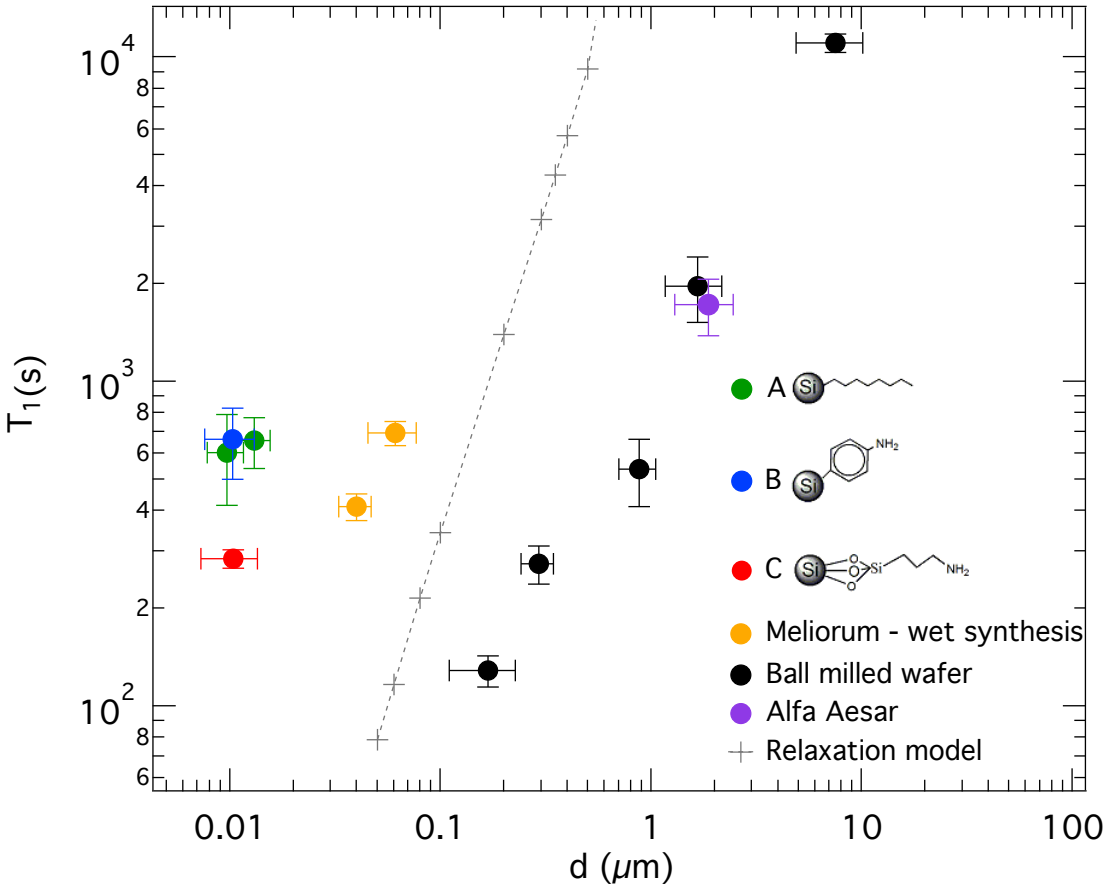

Figure 6.3.5: Nuclear spin relaxation (T_1) times at 2.9 T and 300 K as a function of particle diameter d for Si nanoparticles synthesized by schemes described in Fig. 6.3.1. Measurement of other silicon particles previously reported are shown as a reference [138]. Simulations of nuclear relaxation based on a spin diffusion model are also shown. Vertical error bars are from exponential fits to relaxation data; horizontal error bars are from size distributions.

g-factor	A	B	C
ESR (9 GHz 300K)	2.0078	2.0087	2.0059
DNP (81 GHz 3.6 K)	2.0078	2.0089	2.0062
N_e (cm^{-2})	$4.3e^{12}$	$1.3e^{13}$	$3.7e^{13}$

Table 6.3.2: Electron g-factors as determined by ESR and DNP in silicon nanoparticles

from $4e^{12}$-$4e^{13}$ cm^{-2}. The g-factor for P_b defects occurring due to an oxygen vacancy at the interface between crystalline silicon and silicon oxide is strongly anisotropic [132] and depends on the orientation of the underlying crystalline lattice. For spherical nanoparticles, where one lattice orientation does not dominate over another, the orientation averaged g factor for these defects is g = 2.006 which is in good agreement with the g-factor observed for our crystalline samples. Both amorphous samples show similar g-factors in the range 2.0078-2.0087. These are higher than the g = 2.005-2.0059 previously reported for bulk amorphous silicon, [189, 190] potentially due to asymmetric strain.

All samples show positive nuclear polarization at microwave frequencies below the ESR frequency and negative polarization at frequencies above it, indicating that the polarization is generated by a dipolar interaction rather than a contact hyperfine interaction between the un-bonded electrons and nearby ^{29}Si nuclei (Fig. 6.3.6b). The width of the DNP response is significantly narrower for the amorphous samples when compared to the crystalline samples, perhaps indicating that the polarization mechanism is due to a single electron single nucleus dipole-dipole interaction for the amorphous samples, rather than a multi-electron single nucleus dipole-dipole interaction which occurs in the crystalline samples. The ^{29}Si NMR spectra for the three samples after 3 h of DNP polarization are shown in Fig. 6.3.6c. The amorphous samples show a broad resonance with a linewidth (full width at half maximum) of ~3.6 kHz. The crystalline sample shows a slightly narrower resonance (linewidth ~2.2 kHz) shifted by -600 Hz from the amorphous peak. This is significantly narrower than the 500 Hz linewidth observed for crystalline silicon [128] and 1.8

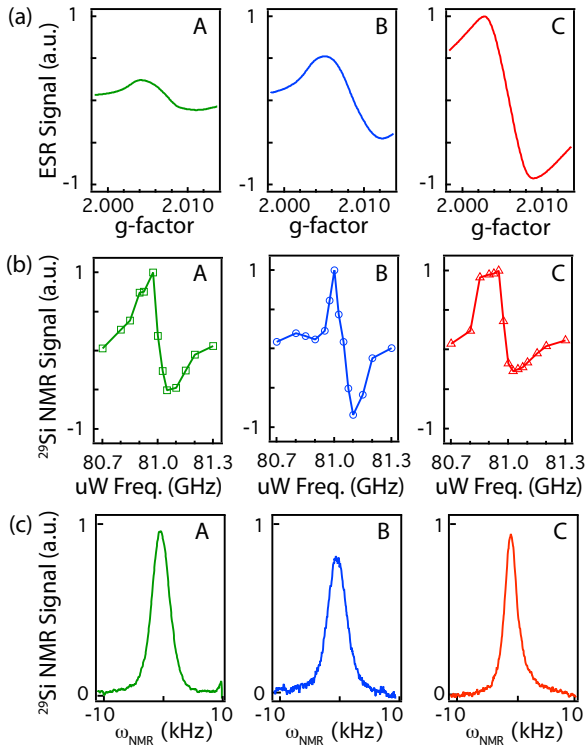

Figure 6.3.6: (a) Electron spin resonance signal and (b) ^{29}Si nuclear polarization as a function of microwave frequency under DNP conditions.

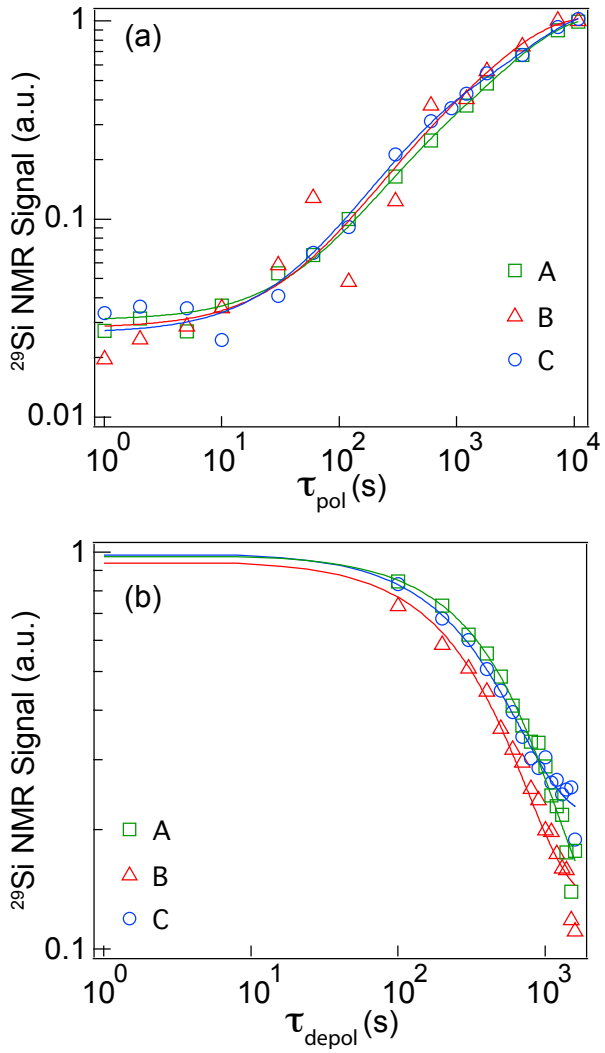

Figure 6.3.7: Time dependence of ^{29}Si polarization in SiNP at 3.6 K. (a) ^{29}Si NMR signal as a function of polarization time τ_{pol}. The data is well fit by a biexponential function described in the text with two distinct time constants T_1, f and T_1, s. (b) Depolarization of the ^{29}Si nuclear polarization at 3.6 K after 6 hours of DNP. The data is well fit by a single exponential with time constant T_1, dep, as described in the text.

Sample	$T_{1,f}$ (s)	$T_{1,s}$ (s)	$T_{1,dep}$ (s)
A	370±70	4300±250	590±30
B	460±120	5760±1250	390±30
C	390±680	3170±1340	400±20

Table 6.3.3: Polarization and depolarization time constants for silicon nanoparticles measured at 4 K.

kHz linewidth observed for bulk amorphous silicon [190], most probably due to strain.

The time evolution of the ^{29}Si nuclear polarization under DNP conditions for each of the samples is shown in Fig. 6.3.7 (a). For each measurement, the microwave frequency was set to the peak value in Fig. 6.3.6 (b) before a saturation recovery sequence performed and the ^{29}Si NMR signal measured with a $\pi/2$ pulse. All polarization curves are well fit by a biexponential function $P = P_0 + Ae^{-\tau/T_{1,f}} + Be^{-\tau/T_{1,s}}$ with a short time constant T_1, f 400 s, and a longer time constant T_1, s ranging from 3200 - 5700s (Table 6.3.3). Fig. 6.3.7 (b) shows the decay in ^{29}Si nuclear hyperpolarization measured at 3.6 K for each of the SiNP samples. The samples were polarized for 6 h with microwave irradiation at the peak value in Fig. 6.3.6 (b), then the microwaves were then turned off and the hyperpolarization allowed to decay. The data is well fit by a single exponential $P = P_0 + Ae^{-\tau_{depol}/T_{1,dep}}$ with all samples showing a depolarization time constant $T_{1,dep}$ greater than 300 s (Table 6.3.3). This is surprising, as previous DNP investigations of silicon microparticles composed of amorphous and crystalline silicon showed relaxation of the amorphous component within seconds after microwave irradiation was ceased [128].

6.4 Conclusion

We have produced long-T_1 SiNPs with narrow size distributions of diameter $\sim$ 10 nm using a metathesis reaction of sodium silicide with a silicon tetrachloride. Combining these SiNPs with Grignard reagents resulted particles that were partially passivated with alkyl and aromatic compounds. The partial surface passivation allows sufficient oxidation to provide hyperpolarization

sites for DNP without compromising the non-aggregating characteristics of the sample. Additionally, the as-grown amorphous SiNP samples could be annealed into crystalline SiNPs that retained their nanoscale size and did not lead to bulkier aggregates due to sintering. Both the amorphous and crystalline SiNPs showed T_1 times more than two orders of magnitude larger than diamond nanoparticles of similar sizes [187], and a five fold improvement on size-adjusted T_1 times when compared to silicon particles previously studied [138]. All SiNPs synthesized in this study could be hyperpolarized by low temperature dynamic nuclear polarization, and retained their polarization for greater than 300 s.

7

Radical-free Dynamic Nuclear Polarization Using Electronic Defects in Silicon

Direct dynamic nuclear polarization of ^1H nuclei in frozen water and water-ethanol mixtures is demonstrated using silicon nanoparticles as the polarizing agent. Electron spins at dangling-bond sites near the silicon surface are identified as the source of the nuclear hyperpolarization. This novel polarization method open new avenues for the fabrication of surface engineered nanostructures to create high nuclear-spin polarized solutions without introducing contaminating radicals, and for the study of molecules ad-

sorbed onto surfaces. [1]

7.1 Introduction

Dynamic nuclear polarization (DNP) has recently emerged as a powerful technique for improving the sensitivity of nuclear magnetic resonance (NMR) experiments, leading to new insights in materials characterization [91, 106, 128, 183], complex biomaterials [59, 184, 185], and diagnostic medicine using magnetic resonance imaging (MRI) [54, 55, 61, 64]. By applying microwave (μW) irradiation at or near the electron Larmor frequency, a sizable nuclear spin polarization can be generated via the transfer of electron spin polarization to nearby nuclear spins. The effect can be enhanced by operating at low temperatures or high magnetic fields, where the equilibrium electron polarization can approach unity. The electrons used in the polarization process may originate from free radicals or paramagnetic metal ions introduced into the system, or be intrinsic to the material being polarized. Both the rate and saturation magnitude of nuclear polarization depend strongly on the concentration of unpaired electrons. This is because spin transport via nuclear spin diffusion is slow [94, 99] and competing relaxation processes means that a high radical concentration is required to achieve large polarizations on experimentally relevant time scales.

Most biological applications of DNP involve systems that have no intrinsic unpaired electrons for polarization, and so a significant effort has been undertaken to develop a range of free radicals [60, 191, 192] that can be dissolved in a solvent (such as water, ethanol, or glycerol) along with the biomolecular substrate to be polarized before freezing for DNP. However, the presence of these radicals in the polarized substrate after polarization reduces the spin lattice relaxation time (T_1) of the polarized substrate [193, 194], interferes with the chemical environment of molecules under study [195] and, for biological experiments, poses significant toxicity issues. To reduce contamination of the sample by residual radicals, filtering [196] and radical scavenging [193] under-

[1] This chapter is submitted for publication as *Radical-free Dynamic Nuclear Polarization Using Electronic Defects in Silicon with authors M. C. Cassidy, C. Ramanathan, D.G. Cory and C. M. Marcus.*

taken post-dissolution have been attempted with limited success. The radicals may be bound into a porous organic matrix [197, 198], though filtration is still necessary. Alternatively, the source of polarization may be physically separated from the material to be polarized. It has been shown that the large nuclear spin polarizations present in optically pumped noble gases and semiconductors can be transferred to a variety of materials using a Hartmann-Hahn cross-polarization sequence [199–202] or, in the case of gases, via a direct nuclear dipole-dipole interaction [203]. Surface defects in porous carbon chars have also been shown to polarize ^{1}H nuclei in solution at room temperature via a contact hyperfine interaction [204].

In this Chapter, we demonstrate that naturally occurring paramagnetic defects at the surface of silicon nanoparticles (SiNP) can directly polarize ^{1}H nuclei in a bulk frozen matrix near the surface of the particle as well as the ^{29}Si nuclei in the particles. Two distinct nuclear spin baths are observed, one consisting of nuclei polarized directly by surface electrons, and a second consisting of nuclei polarized indirectly by nuclear spin diffusion. By comparing natural abundance and isotopically enriched samples, we find that ^{1}H polarization is strongly affected by the isotopic concentration of ^{29}Si nuclei inside the particles. This technique allows uncontaminated hyperpolarized solutions to be generated benefitting a range of applications from polarized targets to molecular imaging.

7.2 Samples and experimental methods

Samples consisted of natural abundance (^{29}Si = 4.8%) polycrystalline powder (Alfa Aesar, $d = 3\ \mu$m), and isotopically enriched (^{29}Si = 91.4%) [205] silicon particles of diameter $d = 200$ nm made by ball milling bulk silicon and then size-separated by centrifugal sedimentation [138]. Particle sizes were confirmed by scanning electron microscopy (SEM). Suspensions of these particles in water (1:1 Si:H_2O by weight), and ethanol and water (10:9:1 Si:EtOH:H_2O by weight) were prepared by sonication and then degassed with a freeze-pump-thaw cycle before being loaded into the cryostat for measurement.

DNP experiments were performed at 4.2 K using a continuous flow cryostat in an applied field, B, of 2.35 T ($\omega_n^{^{29}\mathrm{Si}}$ = 20 MHz, $\omega_n^{^{1}\mathrm{H}}$ = 100 MHz). The sample was housed in a glass capillary tube in direct contact with the flowing helium vapor. A Bruker NMR spectrometer with a home-built probe and solenoidal coil [206] were used for NMR detection. Microwave irradiation was provided through a 90 mW Gunn diode source (Millitech), and the μWs were coupled from room temperature to the sample via a mm waveguide and horn antenna. The nuclear polarization was measured with a saturation recovery sequence (^{29}Si) $(\pi/2)^{16} - t - (\pi/2)_X$ or saturation recovery solid echo sequence (^{1}H) $(\pi/2)^{16} - t - (\pi/2)_X - t_d - (\pi/2)_Y$ due to the rapid decay of the ^{1}H signal, corresponding to a $\sim$ 100 kHz ^{1}H dipolar linewidth.

7.3 Results

7.3.1 Frequency dependence of the ^{1}H and ^{29}Si dynamic nuclear polarization

Figure 7.3.1(a) shows the μW frequency dependence of the ^{1}H NMR signal for solid H_2O samples, with and without suspended SiNP (natural isotopic abundance), for a μW irradiation time of 120 s. For the sample with SiNP, the ^{1}H nuclear polarization depended strongly on the applied μW frequency, while no change in ^{1}H polarization was seen for the sample without SiNP. A similar dependence on μW frequency of the ^{29}Si NMR signal for the same sample of SiNP suspended in frozen water (Fig. 7.3.1(b)) after 600 s of μW irradiation. No ^{1}H signal was observed from a sample of dry SiNP. Representative ^{1}H and ^{29}Si spectra at a μW frequency of 65.875 GHz are shown in the insets [207]. We note that no change in the room temperature ^{1}H spectrum was seen in a similarly prepared sample after repeated measurements over a period of a week. This suggests that chemical reactions at the silicon/water interface leading to Si-H bond formation is insignificant, and that the ^{1}H NMR signal results from ^{1}H nuclei outside of the particle rather than absorbed into the oxide or particle itself.

Both ^{1}H and ^{29}Si polarizations show inversions at the same μW frequency, $\omega_\circ = 65.95$ GHz, in-

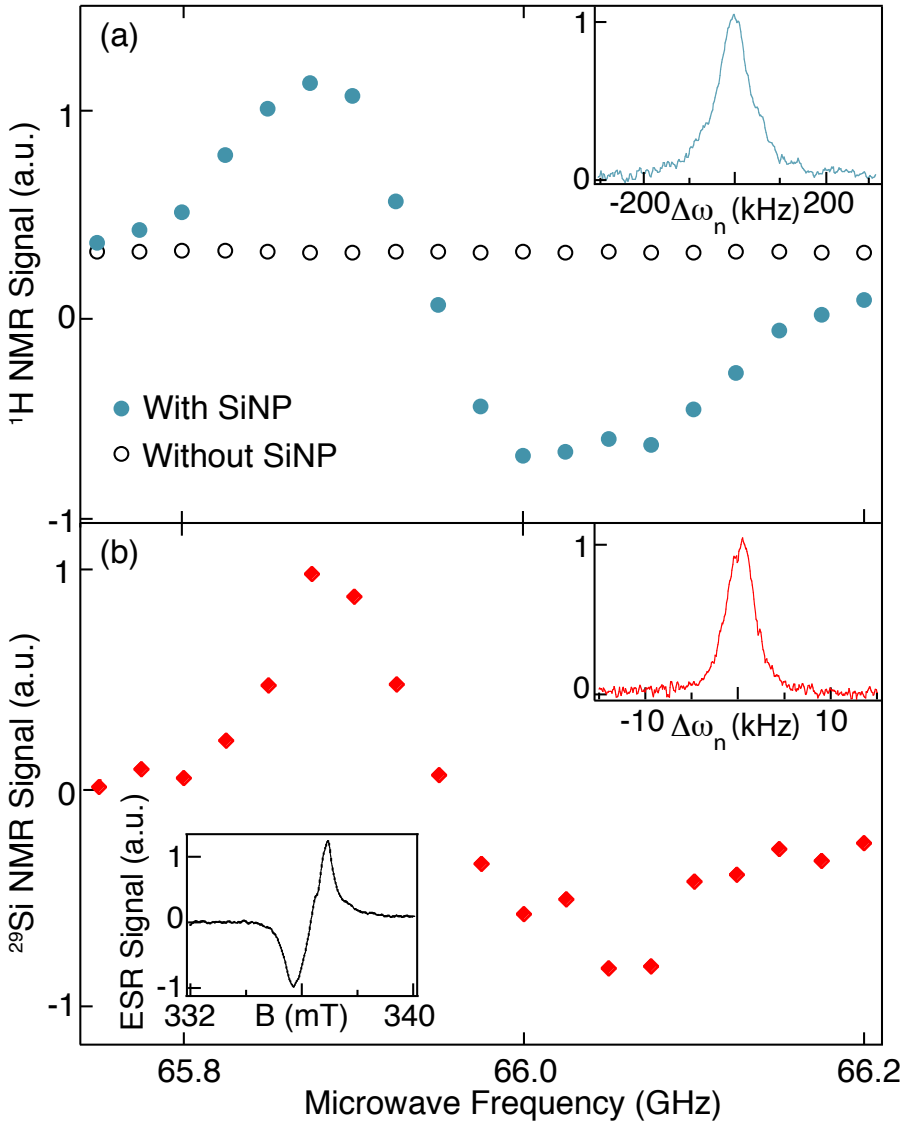

Figure 7.3.1: Microwave frequency dependence of the (a) ^{1}H NMR signal (closed circles) and (b) ^{29}Si NMR signal from a sample of natural isotopic abundance SiNP suspended in frozen water, measured at 4.2 K. No change in the ^{1}H NMR signal was observed for the same sample without the SiNP (open circles), and no ^{1}H signal was observed from a dry sample of SiNP. Upper insets in (a) and (b): ^{1}H and ^{29}Si spectra for μW irradiation frequency of 65.875 GHz. Lower inset in (b): Room temperature ESR signal of natural abundance SiNP.

dicating that polarization of both nuclear species originates from electrons with the same g-factor. Room temperature X-band electron spin resonance (ESR) (lower inset of Fig. 7.3.1(b)) of the particles shows a single broad peak at $B = 335.9$ mT and frequency 9.444 GHz, corresponding to g = 2.006. This g-factor is consistent with the orientation-averaged signal from unpaired electrons at P_b defects, which are known to occur at the silicon-silicon dioxide interface [208]. To confirm the role of these defects in the polarization process we prepared a similar sample where the surface oxide was removed by a hydrofluoric acid etch in an inert atmosphere and suspended in glycerol. This sample showed no ESR signal and no ^{1}H or ^{29}Si DNP enhancement under similar conditions. Additionally, the sign of polarization enhancement is the same for both nuclear species for frequencies either side of ω_o, despite the gyromagnetic ratios of the ^{1}H and ^{29}Si nuclei being opposite in sign. From this we can determine that the ^{1}H nuclei are being polarized through a direct interaction with the electron dipolar spin bath, rather than via a dipolar interaction with polarized ^{29}Si nuclei close to the surface. The direct interaction scales $\propto \gamma_n^2$ [100], independent of the sign of γ_n, the nuclear gyromagnetic ratio. If instead the ^{1}H polarization was mediated by a dipolar interaction with the polarized ^{29}Si nuclei, opposite nuclear polarizations would be generated in the two nuclear species for the same polarizing frequency.

A schematic model of the system is shown in Fig. 7.3.2. The anisotropic g factor of the P_b defect ($g = 2.002 - 2.010$) [208], together with the high density of unpaired electrons at the sample surface ($\sim 10^{13}\text{cm}^{-2}$) [209] yields a broad spectrum of electron-electron dipolar interactions with energies at or near the Larmor frequency of each nuclear species. This results in a broad μW frequency response of both ^{1}H and ^{29}Si nuclei (Fig. 7.3.1), consistent with previous DNP studies of silicon microparticles [128].

7.3.2 Time evolution of the ^{1}H polarization under dynamic nuclear polarization

The time evolution of the ^{1}H polarization of various frozen suspensions of natural abundance and ^{29}Si-enriched SiNP in frozen water and water-ethanol mixtures at μW frequency of 65.875 GHz is

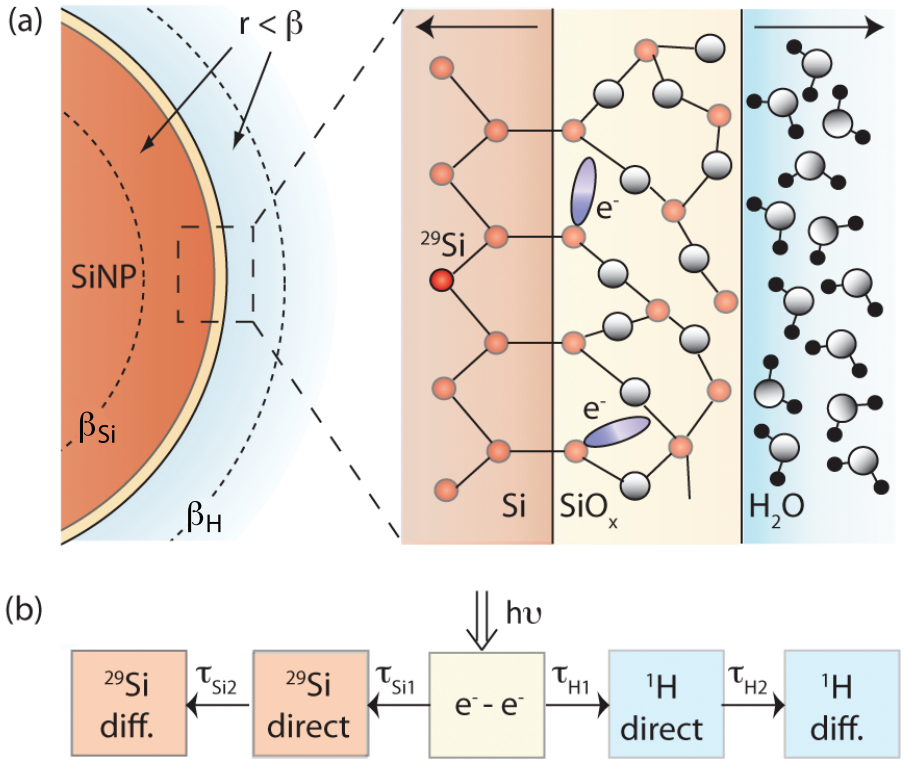

Figure 7.3.2: (a) Schematic model showing the location of DNP-active electron spins at and near the silicon-silicon oxide interface. Arrows indicate the directions of nuclear polarization flow away from the surface of the particle. (b) Thermodynamic model (see text) for the polarization process of both the ^{1}H and ^{29}Si nuclear spin baths. ^{29}Si and ^{1}H nuclei near the defect electrons are polarized directly through a dipolar interaction on time scales τ_{Si1} and τ_{H1}. Nuclei far away from the surface are then polarized by nuclear spin diffusion on time scales τ_{Si2} and τ_{H2} that are dependent on the spatial separation of the nuclear spins.

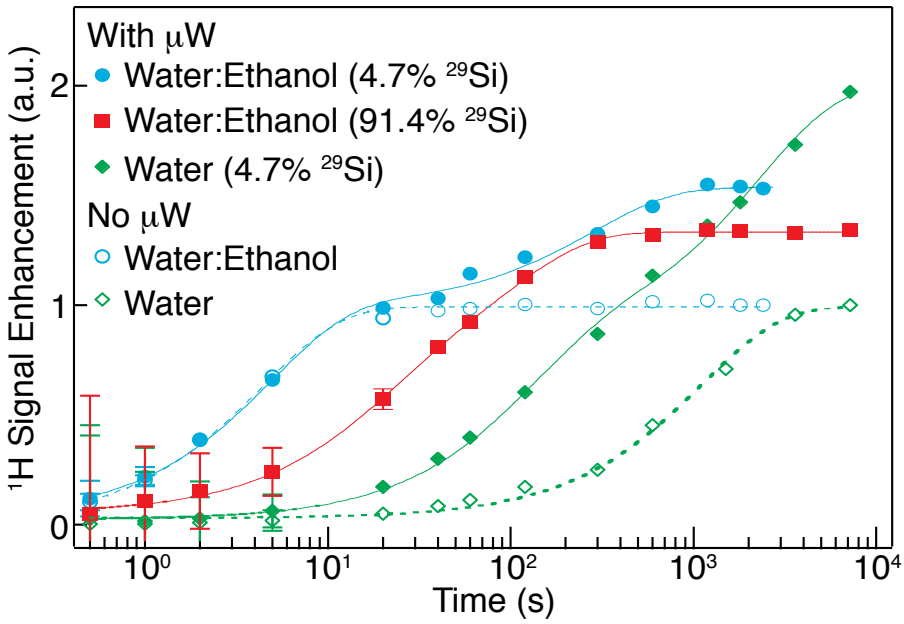

Figure 7.3.3: Time evolution of the ^{1}H nuclear polarization with (solid shapes) and without (open shapes) applied μW irradiation for frozen solutions of SiNP : H_2O (4.7% ^{29}Si) and SiNP : EtOH : H_2O (4.7% ^{29}Si, 91.4% ^{29}Si). The enhancements are scaled relative to the 4.2K equilibrium polarization. Fits are exponential (dashed lines) or biexponential (solid lines), see text. Error bars are shown when greater than the data symbol.

shown in Fig. 7.3.3. All data are normalized to the ^{1}H equilibrium polarization (P_B) at 4.2 K without μW irradiation. The enhancement curves with μW irradiation display biexponential behavior, well fit by the form $P = P_\infty \left(1 - \left(Ae^{-t_{pol}/\tau_1} + Be^{-t_{pol}/\tau_2}\right)\right)$ (solid lines). This is in contrast to the time evolution of the ^{1}H NMR signals without μW irradiation, which are better described by a single exponential, $P = P_B \left(1 - e^{-t_{pol}/T_1}\right)$ (dashed lines). Best fit values for these characteristic times are given in Table 7.3.1.

Note in Fig. 7.3.3 that the long-time induced polarization in the water-ethanol sample is suppressed relative to the water sample. We attribute this to fast nuclear relaxation caused by the rotating methyl group in ethanol, which creates an oscillating magnetic field with a characteristic time constant of a few seconds even at cryogenic temperatures (methyl rotamer effect [210]). Increasing the ^{29}Si isotopic concentration from 4.7% to 91.4% and reducing the particle size from 3 μm to 200 nm reduces the polarization rates and the total ^{1}H polarization enhancement by a fac-

Sample		T_1(s)	τ_{H1}(s)	τ_{H2}(s)
Si:H_2O	(4.7% ^{29}Si)	1113 ± 96	120 ± 14	2304 ± 307
Si:EtOH:H_2O	(4.7% ^{29}Si)	4.3 ± 0.4	4.6 ± 0.8	217 ± 58
Si:EtOH:H_2O	(91.4% ^{29}Si)		16 ± 3	97 ± 17

Table 7.3.1: ^{1}H polarization times fitting to experimental data in Fig. 3. T_1 is the characteristic time taken for the ^{1}H nuclei to return to the equilibrium polarization without μW irradiation. τ_{H1} and τ_{H2} are fast and slow polarization times which form two additive components of the polarization process corresponding to polarization dominated by direct DNP and spin diffusion respectively.

tor of two, from 1.5 to 1.25 times the Boltzmann polarization at 4.2 K. This is particularly notable given the higher number of polarization sites arising from surface area to volume ratio that is 15 times larger in these samples. Despite this significant increase in the availability of directly polarization sites, the higher concentration of ^{29}Si nuclear spins in the NP are able to absorb a greater total angular momentum transfer from the surface electrons compared to the natural abundance samples. This results in a slower direct polarization rate of the ^{1}H nuclear spins close to the surface. However, the relaxation due to the methyl rotamer effect and other electronic defects within the frozen matrix remains the same as for the natural abundance samples, and so competes more strongly with polarization by spin diffusion and hence causes the ^{1}H polarization to saturate earlier and at a lower absolute value.

It is possible to estimate the size of the region of direct polarization for each nuclear species. Upon μW irradiation of the electron spin bath, the polarization of nuclei within a radius $r < \beta$ is through a direct dipolar interaction with a pair of electrons at a rate $\tau_1^{-1} = \Gamma/r^6$, where $\Gamma = KCG(\omega_0 - \omega^*)$, $K = \pi\gamma_e B_1^2\tau/2$ is the saturation strength of the microwave field,

$$C = \frac{3}{10}\frac{\hbar^2\gamma_e^2}{B^2}\frac{B^2\gamma_n^2 T_{2e}}{1 + B^2\gamma_n^2 T_{2e}^2}, \tag{7.1}$$

is a constant describing the nature of the electron-nuclear dipolar interaction, and $G(\omega - \omega^*)$ is the electron lineshape function [100]. Here B_1 is the strength of the μW magnetic field, τ is the corre-

lation time of the electron spin magnetization orientated along the direction of the static magnetic field ($1/\tau = 1/T_{1e} + 1/T_{2e}$), T_{1e} is the electron spin lattice relaxation time and T_{2e} the transverse electron spin relaxation time. The distance $\beta = (C/D)^{1/4}$ (D is the spin-diffusion constant), characterizes the cross-over radius between direct and diffusion-mediated hyperpolarization [100] .

For nuclei located outside this radius ($r > \beta$), polarization occurs predominantly via nuclear spin diffusion with a rate $\tau_2^{-1} = \frac{\partial P}{\partial t} = D\nabla^2 P$ [99]. $D = Wa^2 \sim a^2/(50\, T_{2n})$ is the spin-diffusion constant, with a the average separation between nearest-neighbor nuclei, W the probability of a flip-flop transition between nuclei due to dipole-dipole interaction, and T_{2n} the transverse nuclear spin relaxation time [100]. For the present system, we estimate $\beta_{\mathrm{H}} \simeq 3$ nm and $\beta_{\mathrm{Si}} \simeq 4$ nm, given $T_{1e} \simeq 30\mu$s and $T_{2e} \simeq 1$ ns [128], $a_{\mathrm{H(Si)}} \approx 1.3\,(4.1)$ Å, and $T_{2n\mathrm{H(Si)}} = 0.01\,(5.6)$ ms. Transmission electron micrograph studies of the SiNP show an oxide thickness of a few nm, a distance small enough for this direct polarization process to take place. We note that β is not a hard cutoff of the distance for direct polarization to take place, rather it gives a transition point between polarization dominated by direct DNP and spin diffusion.

Although the total enhancement (ranging from $\sim 1.5 - 3$) over all ^{1}H spins in the sample is relatively low compared to enhancements in concentrated radical solutions [211], the enhancement near the surface of the particles is significant. Numerical modeling of the polarization as a function of distance from the particle surface shows a characteristic length of order 10 nm. This is consistent with studies of polarization as a function of radical concentration [194]. Estimating the enhanced polarization of ^{1}H nuclei within 10 nm of the surface of the SiNP (corresponding to $\sim 1.2\%$ of all ^{1}H nuclei in the sample) based on the model above, we find a factor of ~ 50 above equilibrium polarization at 4.2 K for the natural abundance particles in the ethanol solution, corresponding to an enhancement of $\sim$ 3000 times the room temperature equilibrium polarization. This enhancement exceeds the reported enhancements of functional groups on silica surfaces using artificial free radicals and much higher power microwave sources, estimated at ~ 30 times the equilibrium polarization at 77 K for molecules within 1 nm of the surface [212].

7.4 Conclusion

This effect may be optimized for enhanced solution polarization or studies of surface functionalization by reducing the ^{29}Si concentration, increasing the surface area of the SiNP, using porous silicon, or engineering thinner surface oxides with higher defect densities. Additionally we note that this effect may be revealed in other solid state systems with a lower nuclear spin concentration or lower gyromagnetic ratio. In particular, ^{13}C DNP has been demonstrated in a variety of diamond materials [91] (1% ^{13}C natural abundance) and nanodiamond and has surface active electronic defects [213] that may be suitable as polarizing agents by mechanisms similar to those described in this paper.

Acknowledgements

We acknowledge support from the National Science Foundation under NSF-0702295, the BISH Program (CBET-0933015), the Harvard NSF Nanoscale Science and Engineering Center, and the Canada Excellence Research Chairs Program. Fabrication used the Harvard Center for Nanoscale Systems (CNS), an NSF National Nanotechnology Infrastructure Network (NNIN) site (ECS 0335765). Work at the LBNL (^{29}Si synthesis) was supported by the Director, Office of Science, Office of Basic Energy Sciences, Materials Sciences and Engineering Division of the US Department of Energy (DE-AC02-05CH11231).

8

In-vivo Magnetic Resonance Imaging of Hyperpolarized Silicon Particles

Silicon-based micro and nanoparticles have gained popularity in a wide range of biomedical applications due to their biocompatibility and biodegradability in-vivo *[39, 170], as well as a flexible surface chemistry, which allows drug loading, functionalization and targeting [38, 39, 161, 171–173]. To date,* in-vivo *imaging and tracking of silicon particles has been realized via confinement-enhanced optical activation [39] or by the incorporation of imaging agents such as fluorescent markers [38], paramagnetic compounds for conventional magnetic resonance imaging (MRI) [174, 175], or radionuclides for*

positron emission tomography (PET) [214]. Here we report direct in-vivo *imaging of hyperpolarized* ^{29}*Si nuclei silicon microparticles by MRI. Natural physical properties of silicon provide surface electronic states for dynamic nuclear polarization (DNP), extremely long depolarization times, insensitivity to the* in-vivo *environment or particle tumbling, and surfaces favorable for functionalization. Applications to gastrointestinal, intravascular, and tumor perfusion imaging at sub-picomolar concentrations are presented. These results demonstrate a new background-free imaging modality applicable to a range of inexpensive, readily available, and biocompatible Si particles.* [1]

8.1 Introduction

Magnetic resonance imaging (MRI) is an attractive technique for both *in-vivo* studies and clinical diagnosis as it is non-invasive, yields high anatomical resolution, and requires no ionizing radiation. However, the small magnetic moment of atomic nuclei means that large numbers of nuclei are required for imaging under conventional conditions. One approach to increasing the MRI signal is to increase polarization far beyond its equilibrium value—a technique known as hyperpolarization. For instance, hyperpolarized noble gases have shown great promise in structural imaging of the lungs [52, 53, 215], while hyperpolarized ^{13}C and ^{15}N metabolites have been used for studies of metabolism and pH in oncology [54–57]. A key requirement for hyperpolarization is the transfer of angular momentum from a highly polarized source to the target nuclei. For example, the source of angular momentum in the noble gas experiments is an optically excited vapor [58]. For liquid state metabolites, the source is the spin of free radicals (unpaired electrons) combined with the metabolite of interest for low temperature dynamic nuclear polarization (DNP) [59–61], or parahydrogen in combination with an organo-metallic catalyst [57, 61].

MRI using silicon is particularly attractive for several reasons. First, the nuclear magnetic mo-

[1] This chapter is submitted for publication as *In-vivo Magnetic Resonance Imaging of Hyperpolarized Silicon Particles* with authors M. C. Cassidy, H. R. Chan, B.D. Ross, P.K. Bhattacharya and C.M. Marcus

ment of ^{29}Si is close to that of ^{13}C and ^{15}N, putting it within tuning range of commercial multinuclear MRI systems. Second, direct imaging of ^{29}Si is essentially background free, as the body contains only trace quantities of Si naturally. Third, because native Si consists of a dilute (4.6%) concentration of spin-1/2 ^{29}Si nuclei in a nuclear-spin-free lattice, the weak dipolar interaction between ^{29}Si nuclei, and their insensitivity to crystalline electric fields (unique to spin 1/2 nuclei) results in remarkably long relaxation times (T_1), up to several hours in high purity samples [79, 138], coherence times (T_2) of several seconds [141], and an insensitivity to lattice orientation or rotation. Fourth, while there are few unpaired electrons within bulk of high purity crystalline Si, surface defects comprising unpaired electrons are prevalent at the naturally occurring silicon/silica (silicon dioxide) interface (Fig. 8.3.1(a)). Surface defects are ideal for DNP [128], and, because they are remote from most ^{29}Si nuclei, do not lead to rapid relaxation of nuclear hyperpolarization.

8.2 Materials and experimental methods

8.2.1 Preparation of silicon particles

Silicon powder (2 μm APS, 99.9985% elemental purity, Alpha Aesar) was used both as supplied and following surface functionalized with polyethyleneglycol (PEG) for biocompatibility. Particles were suspended in acidified ethanol (pH 3.5, Sigma 100%) and placed in an ultrasonic bath for 5 min. 3-aminopropyltriethoxysilane (APTES, Sigma 99%) was added at a concentration of 100 μL/g of silicon and the sample shaken on a plate shaker for 24 h. Excess silanes were removed by centrifugation and rinsing, and the particles resuspended in ethanol buffer. NHS-dPEG4-(m-PEG12)3-ester (Quanta Biodesign) was added at a concentration of 100 mg/g of silicon and the sample was shaken at 45° C for 12 h. The particles were then rinsed in acidified ethanol buffer and concentrated by centrifugation.

Samples (~100 mg) were packed into thin wall Teflon tubes that withstood the rapid thermal

cycling involved with the polarization process, before being loaded into the polarizer.

8.2.2 Particle size analysis

The size distributions of the particles were determined by scanning electron microscopy. Dilute suspensions of silicon particles in methanol were sonicated for 10 mins before being pipetted onto a graphite substrate which was mounted on a standard specimen holder with conducting carbon tape. Particle diameters were extracted from analysis of the SEM images with particle-measuring software (Gatan Digital Micrograph). Approximately 500 particles were analyzed, sourced from $\sim$ 10 images. From this the volume weighted size distribution $n(d).d^3$ was plotted, showing an average volume weighted particle diameter of $\sim$ 2 μm (Fig. 8.2.1).

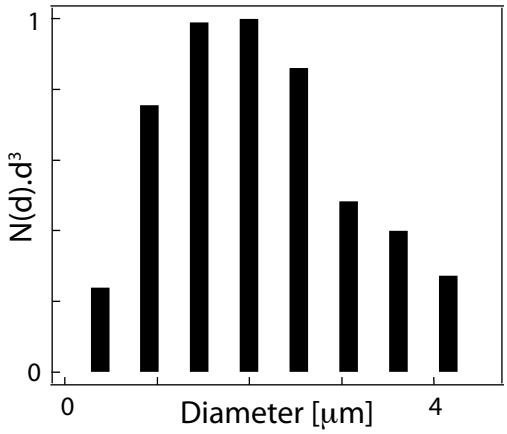

Figure 8.2.1: Volume weighted particle size distribution obtained by SEM image analysis showing an average particle size of 2μm.

8.2.3 Surface area analysis

The particle surface area was determined by nitrogen adsorption-desorption volumetric isotherm (BET) analysis using a Micromeritics ASAP 2020 System.

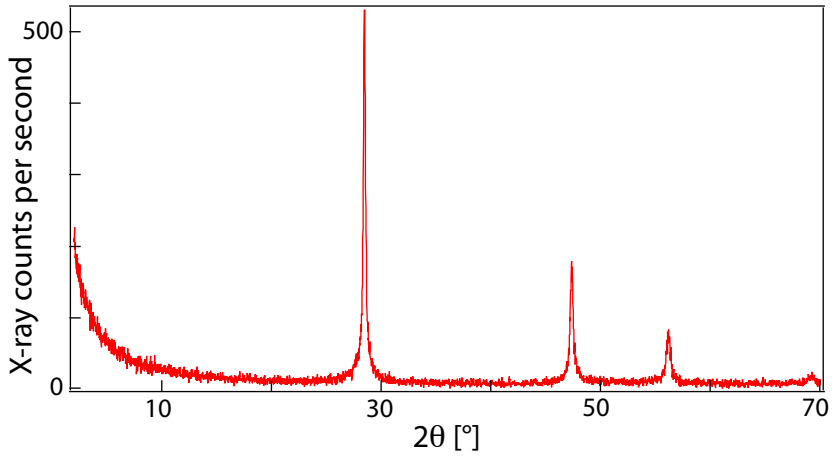

Figure 8.2.2: X-ray diffraction powder spectrum of the silicon particles. The peaks at 28°, 47°, 56° and 69° agree with the peak locations of a known silicon standard (10μm APS, NIST). By comparing the broadening of these peaks compared to the standard we estimate that the particles are approximately 80% crystalline with an average crystallite size of 350 nm.

8.2.4 Crystallite size measurements

Powder x-ray diffraction measurements (Scintag XDS2000) were performed to analyze the particle crystallinity and average crystallite size. The peaks at 28°, 47°, 56° and 69° (Fig. 8.2.2) agree with the peak locations of a known silicon standard (10 μm APS, NIST). By comparing the broadening of these peaks compared to the standard we estimate that the particles have an average crystallite size of approximately 350 nm.

8.2.5 Defect density measurements

Continuous wave electron spin resonance (ESR) measurements were performed on bulk samples of the particles at 3.4 K (Bruker ElexSys E500) (Fig. 8.3.2 (b)). An estimate of the electron spin concentration on the particle surface was made by taking ESR spectra with a piece of phosphorus-doped silicon wafer also inserted in the spectrometer cavity. The addition of the wafer piece resulted in the appearance of additional ESR signal due to the n-type doping. Comparing the peak areas and using the known doping level of the wafer piece (0.008 – 0.01 Ω. cm) yielded an order-

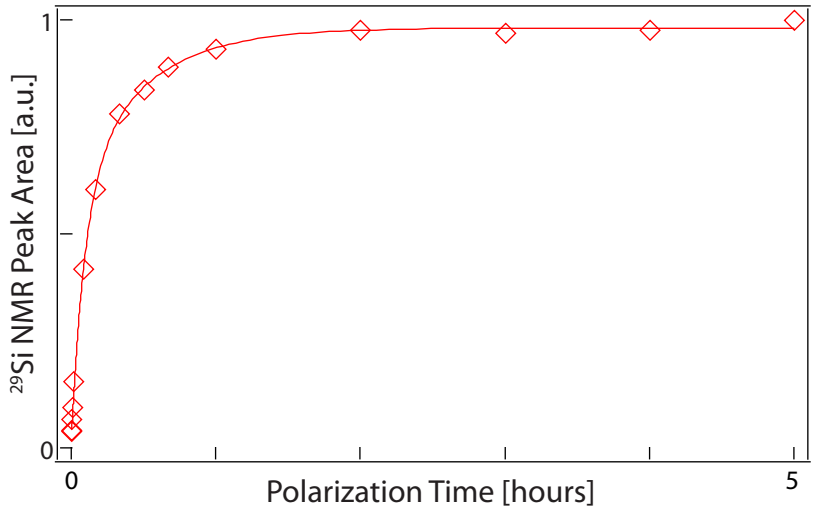

Figure 8.2.3: Room temperature ^{29}Si nuclear T_1 measurement of the silicon particles at 2.9 T measured with a saturation recovery CPMG sequence.

of-magnitude estimate of the mean volume density of defect spins 10^{18} cm^{-3}. Assuming a surface-to-volume ratio of 2 μm diameter spheres, the mean volume density corresponds to a surface defect concentration of 10^{13} cm^{-2}.

8.2.6 Room temperature T_1 measurements

The room temperature T_1 of the sample was measured with a saturation recovery Carr-Purcell-Meiboom-Gill (CPMG) sequence [96, 97] (Fig. 8.2.3). A train of 32 hard $\pi/2$ pulses saturated residual magnetization, and the sample was allowed to polarize for a time τ. The magnetization was rotated to the transverse plane with a single $\pi/2$ pulse and (N=200) π pulses performed. The echo following each of the π pulses were Fourier transformed and the height of the peak was used as a measure of the nuclear polarization. The data is fitted with a biexponential function $P = P_0 + \left((1-a)e^{-\tau/T_{1,f}} + ae^{-\tau/T_{1,s}}\right)$ and two time components are extracted. $T_{1,f} = 6 \pm 1$ min. corresponds to nuclei within the shell of the particle, and $T_{1,s} = 29 \pm 6$ min corresponds to nuclei within the core of the particles.

8.2.7 ^{29}Si dynamic nuclear polarization

We used a home-built DNP polarizer operating at a magnetic field of 2.9 T and temperature of 3.4 K located adjacent to a 4.7 T animal MRI system. At low temperatures and high magnetic fields, unpaired electrons at the particle surface are highly spin polarized. By applying microwave irradiation slightly below the electron spin resonance frequency, spin flip-flops are driven between nearby dipolar-coupled electrons, leading to a net transfer of spin polarization from the electrons to ^{29}Si nuclei near the surface. Over time, ^{29}Si nuclei in the particle core become hyperpolarized via nuclear spin diffusion from the surface. Nuclei in the core region are protected from relaxation, the dominant pathway being slow nuclear spin diffusion back to the surface. The time scale for this process is independent of ambient magnetic field [209] and temperature [94], depending only on polarization time, particle size and the purity of the particle [138]. This allows the hyperpolarized particles to be transported through an environment of varying magnetic fields from the polarizer to the MRI system over several minutes without a significant loss of polarization.

DNP was performed at 3.4 K in a custom built polarizer operating at 2.9 T for polarization times in the range 4 - 24 h. Frequency modulated microwave irradiation was applied between 80.83 - 80.91 GHz (10 kHz ramp modulation) with a 2 W microwave source (Quinstar) located at room temperature and coupled to the sample via a mm waveguide. Details of the polarizer construction and frequency modulation technique are described in Appendix A.

8.2.8 Sample transfer and dissolution

Solid samples were removed from the polarizer and transported to the face of the magnet for dissolution. Phosphate buffered saline (0.5 - 1 mL) or ethanol was added and the sample suspended by manual agitation. The total transport and dissolution time was approximately 2 min.

8.2.9 NMR experiments

The characteristic depolarization time constant $T_{1,dep}$ was measured in the animal scanner using a variable flip angle sequence that preserved the intrinsic T_1 decay of the sample. For N experiments, the flip angle for the n^{th} pulse was calculated by $\theta_n = tan^{-1}(\frac{1}{N-n})$.

All ^{29}Si spectra were exported to Igor Pro (v 6.22, Wavemetrics) for analysis. A 5 ms exponential filter was applied to the complex time domain data before Fourier transform.

8.2.10 MRI experiments

All phantom and animal MRI experiments were performed at 4.7 T in a horizontal bore animal scanner (Bruker Biospin) outfitted with a high-resolution gradient set. Control of the experiment was performed using the preclinical software Paravision (v 3.0.2 Bruker Biospin). A dual coil setup was used for co-registered ^{1}H :^{29}Si imaging. A ^{1}H volume coil was used for sample placement and anatomical imaging. ^{29}Si imaging and spectroscopy was performed with a custom built surface coil (38 mm ID) that was placed on the abdominal region of the animal. The coil size was slightly increased (45 mm ID) for the TRAMP animal due to the size of the tumor. A small ($\sim$ 1 mL) phantom of tri-methyl silanol (TMS, 99% Sigma) was located in the volume coil 1 cm above the face of the surface coil as a ^{29}Si spectroscopic reference. For phantom imaging, the phantom was placed in a holder centered in the volume coil with a vertical displacement of 1 cm above the face of the surface coil. In Fig. 8.3.6(a), the phantom size was $\sim$ 2 x 14 pixels within the 64 x 64 imaging matrix (individual segments were $\sim$ 2 x 2 pixels). For Fig. 8.3.6(b) the phantom size was $\sim$ 6 x 22 pixels within the 64 x 64 imaging matrix.

Anatomical imaging was performed with a standard ^{1}H multiple-slice multiple-echo (MSME) spin echo sequence. The imaging parameters were as follows: coronal orientation, 8 slices, slice thickness = 3 mm, 256 x 256 pixel resolution, field of view (FOV) = 6 cm. A custom spin echo pulse sequence was written for ^{29}Si imaging to take advantage of the particular decoherence properties of solid silicon. Due to the weak dipolar coupling of the ^{29}Si nuclei in the crystalline lattice,

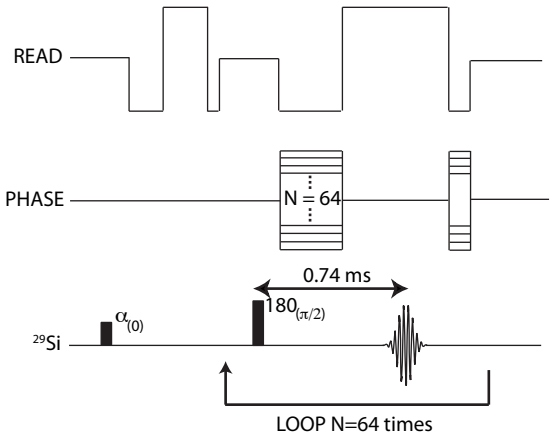

Figure 8.2.4: Pulse sequence used for ^{29}Si imaging. A single α pulse tipped the magnetization into the transverse plane. Each line of k space was acquired from a spin echo after (N = 64) steps in the phase encode gradient.

the rapid application of hard π pulses in a CPMG sequence can extend the coherence time by several orders of magnitude [98]. This results in an effective line-width narrowing, which we utilize for imaging the entire 2D image from a single excitation α to the transverse plane.

The ^{29}Si imaging pulse sequence diagram is shown in Fig. 8.2.4. The imaging parameters were as follows: coronal orientation, single slice, slice thickness = 60 mm, $\alpha = 20^\circ - 90^\circ$, repetition time (TR) = 1.5 ms, echo time (TE) = 0.74 ms, field of view (FOV) = 40 x 40 mm, 64 x 64 pixel resolution, with a total imaging time of 300 ms. The FOV was increased to 45 x 45 mm for the TRAMP animal images due to the large size of the tumor.

^{29}Si images were exported to Igor Pro (v 6.22, Wavemetrics) for post-processing. Each row of raw k-space data was filtered with a Hanning window to reduce Gibbs ringing and zero-filled to 128 x 128 pixels before a 2D inverse Fourier transform was applied. The magnitude of the resulting image was then taken. Consistent magnitude scaling was used across all phantom and animal experiments. Co-registered images were systematically thresholded so that pixels less than 3 standard deviations above the noise were set transparent and the remaining pixels colored on a gamma function color scale. ^{1}H images were processed within the Paravision environment.

In Fig. 8.3.6(b) the results of 8 successive averages were added together to form the image displayed within the paper. These are all from single polarization events, and used in the case that the $\alpha = 90^\circ$ intended was not accurate across the entire sample and some residual polarization remained. All other images are the result of 1 average.

For the *in-vivo* images, a 10 dimensional principle component analysis was applied to the magnitude image matrix to reduce the effects of instrumentation noise.

^{29}Si phantom images in Fig. 8.3.6 were cropped from 40 mm to 15 mm in the horizontal direction after post processing for formatting. This did not remove any visible signal from the image.

8.2.11 Mouse handling

All animal work was performed in accordance with the institutional animal protocol guidelines in place at the Huntington Medical Research Institute, and was reviewed and approved by the Institute's Animal Research Committee. Male BALB/c mice ($\sim$ 20 g) (Harlan Laboratory, Livermore CA) were used for the normal experiments. Male TRansgenic Adenocarcinoma of Mouse Prostate (TRAMP) mice (Jackson Laboratory, Bar Harbor, ME) were used for prostate tumor experiments. The animals were anesthetized by face mask (1% isoflurane in 0.8 L/min oxygen) and a catheter was positioned intragastrically (GI), intraperitoneally (IP) or intraveneously (IV) or within the tumor. The animal was placed into a custom heated holder compatible with the MRI coils and kept anesthetized with a nose cone during the experiment.

The hyperpolarized silicon particles were suspended in phosphate buffered saline (Baxter Healthcare) before being injected through the catheter with a 25 Gauge syringe. The suspension amount was 0.3 mL for GI and IP, and 1mL for IV. Additionally, unfunctionalized particles used for the GI experiments were first suspended in 0.2mL of ethanol for enhanced surface stabilization. The injection was followed by 0.2 mL of saline to clear the catheter. After the experiment, the animals were sacrificed while still anesthetized and internal organs (spleen, liver, kidneys) were harvested for further study.

8.2.12 *In-vivo* toxicity

Animals (N=2 for each concentration) were injected with concentrations up to the imaged concentrations via tail vein injection, intragastrical feeding needle, or intraperitoneal injection and monitored for a period of two weeks. The concentrations per kg of body weight were 500 $mg.kg^{-1}$, 1500 $mg.kg^{-1}$, 3000 $mg.kg^{-1}$ (IV), 500 $mg.kg^{-1}$, 1000 $mg.kg^{-1}$, 2000 $mg.kg^{-1}$ (IP), 500 $mg.kg^{-1}$, 2500 $mg.kg^{-1}$, 7500 $mg.kg^{-1}$ (GI).

8.2.13 Histology

Samples were fixed in 10% buffered formalin for 24 hours. After fixation the samples were routinely processed and embedded into paraffin blocks. 4 micron sections were then cut and mounted to positively charged slides. 4 step sections at 50 micron intervals were cut. A routine hematoxylin and eosin staining procedure was then performed to visualize the slides. Slides were examined with an Olympus BX51M microscope.

8.3 Results

In this study, we used commercially available high purity silicon particles with a mean diameter of 2 μm (Alfa Aesar, 99.9985% Si, Fig. 8.2.1). Each particle consists of a number of crystalline cores ($\sim$ 350 nm diameter as determined by XRD analysis, Fig. 8.2.2) surrounded by amorphous silicon and a silicon oxide shell. Particles were either used in their as-supplied condition or were surface functionalized with polyethylene glycol (PEG). The complex surface structure of the particles (Fig. 8.3.1(a-b)) results in a high surface-to-volume ratio (0.9 m^2/g, determined by nitrogen adsorption-desorption isotherms), giving a large density ($\sim$ 10^{13} cm^{-2}) of defect-bound electrons (Fig. 8.2.3).

8.3.1 In-vivo decay of nuclear hyperpolarization

A comparison of ^{29}Si spectra for dry particles and *in-vivo* measurements in the MRI system after a depolarization time τ_{dep} = 30 min following hyperpolarization is shown in Fig. 8.3.1(c). Both spectra show a line width (full width at half maximum) of $\sim$ 400 Hz, consistent with the dipolar line width for crystalline silicon. A slight additional broadening is seen in the dry sample, presumably corresponding to ^{29}Si nuclei close to the particle surface. We attribute the absence of this additional broadening in the *in-vivo* case to nearby ^{1}H nuclear spins in the *in-vivo* environment that cause surface ^{29}Si nuclei to relax on times scales of roughly T_1 of the bordering ^{1}H nuclei. Figure 8.3.1(d) shows the decay of ^{29}Si polarization for dry and *in-vivo* particles using a variable flip angle sequence following a polarization time τ_{pol} = 18 h. Despite the difference in absolute ^{29}Si signal between the two measurements, the characteristic depolarization time $T_{1,dep}$ is approximately the same for the dry ($T_{1,dep} = 38 \pm 2$ min) and *in-vivo* cases ($T_{1,dep} = 39 \pm 3$ min). This is longer than the ensemble-averaged relaxation time, $T_1 = 29 \pm 5$ min, of the sample measured by a saturation recovery method at 2.9 T and 300 K.

Isolated defects within the particle core can act as local relaxation sites, though they may be ineffective for DNP. Depolarization measurements following DNP are dominated by contributions from nuclei far from local relaxation points, giving a larger value of T_1 for depolarization from the hyperpolarized state than for polarization under Boltzmann conditions. We note that measured depolarization times could be lengthened by increasing the polarization efficiency or polarization time (Fig. 8.3.4), or improving the internal crystal structure of the particles (Fig. 8.3.5). By comparing the signal strength to that of a co-located ^{29}Si phantom we estimate a ^{29}Si nuclear polarization of roughly 1% in the imager. We attribute the difference in absolute signal to sample loss in the dilution and injection procedures, a reduced concentration of silicon particles within the active region of the coil, as well as a contribution from enhanced surface relaxation.

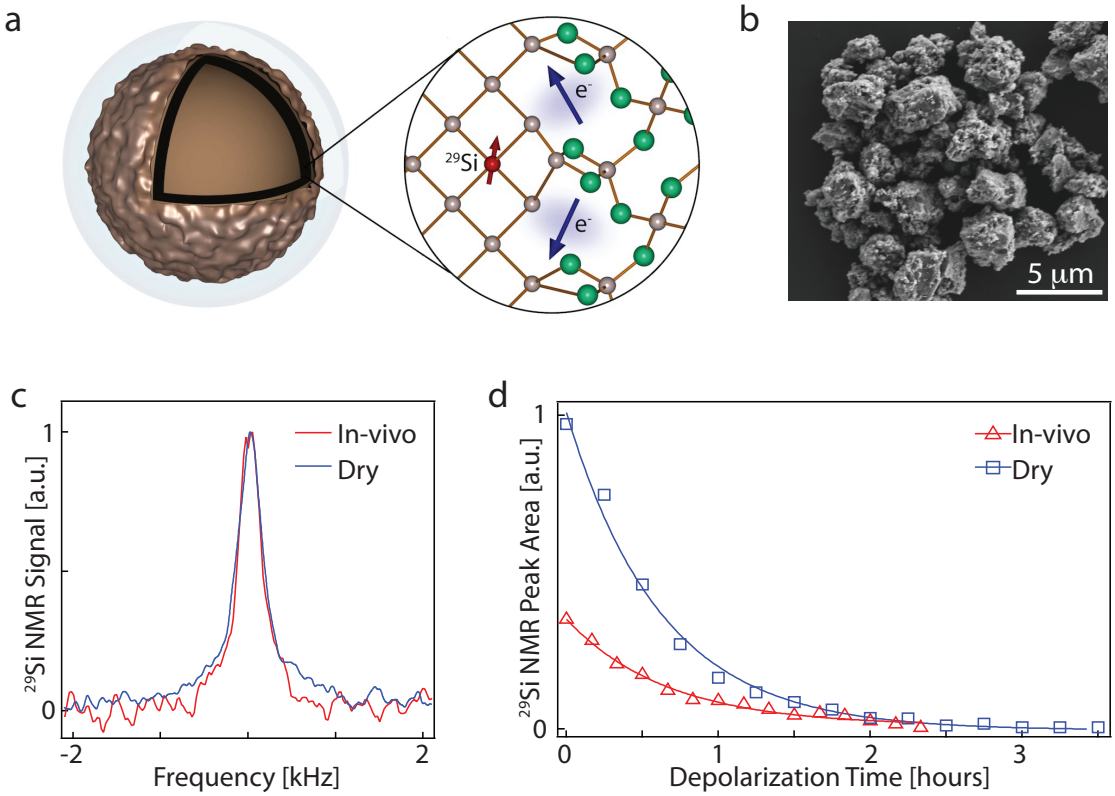

Figure 8.3.1: Characterization of silicon particles. (a) Schematic diagram showing the compound core-shell structure of the silicon particles surface functionalized with biocompatible polymers. Unbonded electrons naturally occurring at the silicon-silicon dioxide interface polarize nearby ^{29}Si nuclear spins through DNP. (b) SEM image of the silicon particles used in this experiment. (c) ^{29}Si NMR spectrum of hyperpolarized particles recorded *in-vivo* (red) and dry (blue) at 30 min delay. (d) Decay of ^{29}Si nuclear polarization in hyperpolarized silicon particles recorded *in-vivo* (red) and dry (blue). Both show a characteristic decay $T_{1,dep} \sim$ 40 min for polarization time τ_{pol} = 18 h using a variable flip angle acquisition. The difference in absolute signal is mainly due to reduced concentration within the active region of the coil.

8.3.2 Low temperature DNP measurements

The ^{29}Si nuclear polarization was measured under dynamic nuclear polarization conditions at 2.9 T in the polarizer using a saturation recovery sequence. A saddle coil that could be tuned across a wide range of temperatures was used for NMR detection. A train of 32 hard $\pi/2$ pulses saturated residual magnetization, and the sample was allowed to polarize for a time τ_{pol} before the magnetization was measured with a single $\pi/2$ pulse. The area under the Fourier transformed peak was used as a measure of the nuclear polarization.

The microwave frequency dependence of ^{29}Si dynamic nuclear polarization measured at 3.4 K is shown in Fig. 8.2.3(a). The ESR signal measured at 9 GHz and 3.4 K is shown in Fig. 8.2.3(b) and is plotted over the same range of g-factors as the data in Fig. 8.2.3(a). The ^{29}Si nuclear polarization scales proportional to the derivative of the ESR line $\propto \left(\frac{dG}{dB}\right)$ with the cross over frequency between negative and positive nuclear polarization occurring at the average value of the electron g-factor of the system (g=2.0065). This is consistent with a DNP mechanism driven by dipolar interactions between a dense bath of electron spins [100].

The time evolution of the ^{29}Si nuclear polarization for particles with and without surface functionalization with PEG is shown inFig. 8.3.3. No significant difference is observed in the ^{29}Si polarization rate for short time periods, where the polarization rate may be affected by nearby ^{1}H nuclei within the PEG chain. This is not unexpected, as the APTES linker contains few spinful nuclei and provides a buffer between the particle surface and the ^{1}H rich PEG. At times greater than 30 minutes the ^{29}Si polarization is dominated by nuclei polarized by nuclear spin diffusion.

Figure 8.3.4 (a) shows the decay of nuclear polarization measured in the 4.7 T animal imager measured with a variable flip angle sequence for polarization times τ_{pol} = 4 h, 6 h, 12 h and 18 h. The data is well fit by a single exponential and the depolarization time constant $T_{1,dep}$ is extracted for each case showing that the depolarization time constant increases for increasing polarization

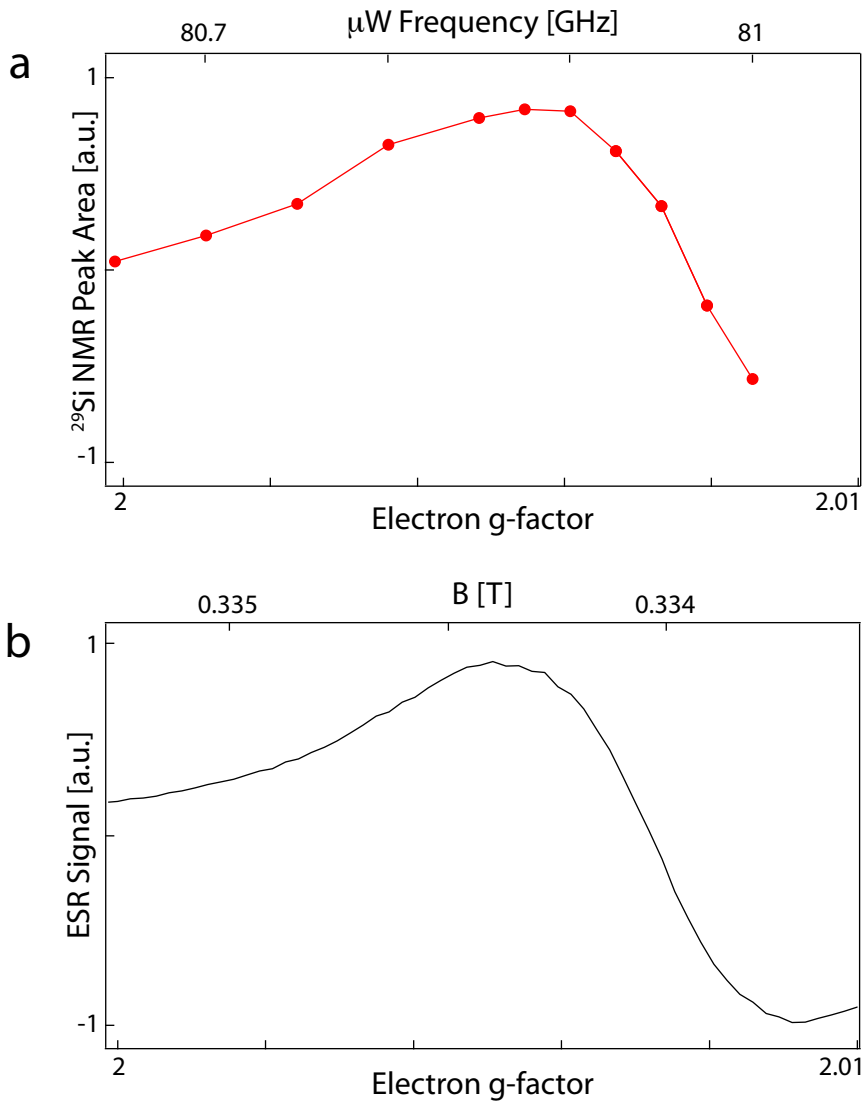

Figure 8.3.2: (a) Microwave frequency dependence of the ^{29}Si nuclear polarization acquired at constant magnetic field at 3.8 K. (b) Electron spin resonance signal as a function of magnetic field acquired at constant microwave frequency at 3.8 K. Both sets of data are plotted over the same range of g-factors. Good agreement is seen between the ESR and DNP despite the difference in magnetic field and microwave frequency for the measurements.

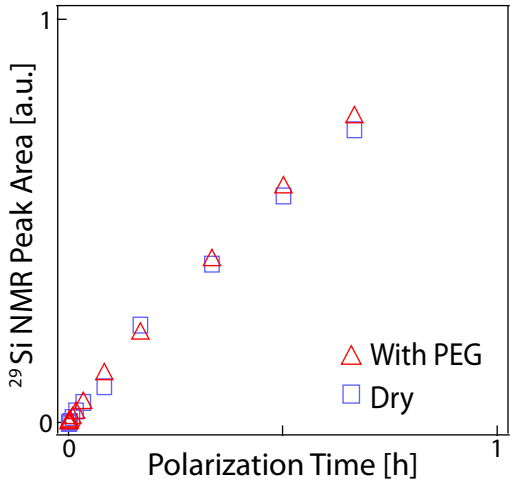

Figure 8.3.3: Time evolution of the ^{29}Si nuclear polarization under DNP conditions for particles with and without surface functionalization with PEG. The signal is normalized by sample weight. No significant difference is observed in the ^{29}Si polarization rate for short time periods, where the polarization rate may be affected by nearby ^{1}H nuclei. At times greater than 30 minutes the ^{29}Si polarization is dominated by nuclei polarized by nuclear spin diffusion.

time. This is consistent with a model of spin diffusion limited polarization.

8.3.3 Simulation of depolarization as a function of particle size

We numerically modelled nuclear spin relaxation from a pre-hyperpolarized state for particles with diameters ranging from 50 nm to 2 μm (Fig. 8.3.5). The model assumed that the particles were spherical with natural abundance (4.7%) ^{29}Si concentration and paramagnetic defects located on the surface. The initial polarization $P(r, t = 0)$ was set to 1 % uniformly throughout the particle, and the polarization decay simulated as it returned to the Boltzmann polarization at a depolarizing field B_{dep} = 4.7 T and T = 300 K. We considered a volume weighted 1D radial model consisting of 100 distinct spin packets with the decay of polarization in each packet at radial position r described by contributions from nuclear spin diffusion and direct relaxation,

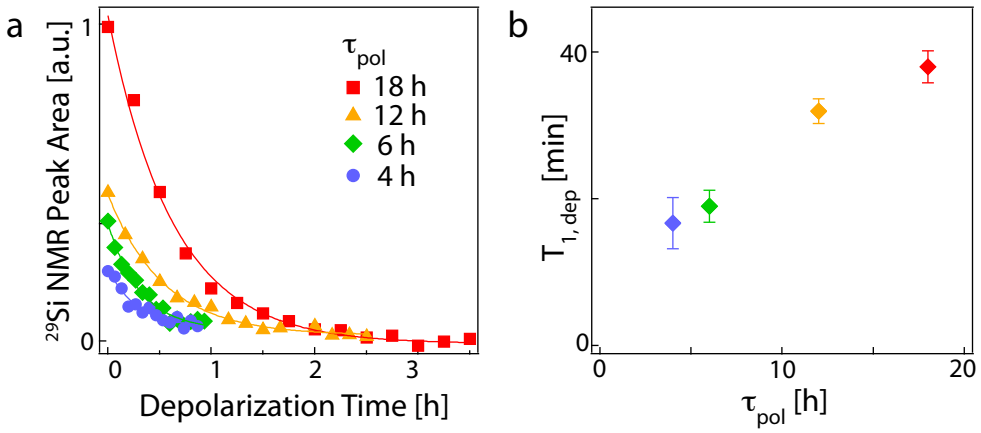

Figure 8.3.4: (a) Decay of ^{29}Si nuclear hyperpolarization in dry particle phantoms recorded in the imager for polarization times of 4, 6, 12, and 18 hours. (b) Characteristic ^{29}Si depolarization time constants ($T_{1,dep}$) for different polarization times extracted from the decay curves in (a).

$$\frac{dP(r,t)}{dt} = \left(\frac{dP(r,t)}{dt}\right)_{diff.} + \left(\frac{dP(r,t)}{dt}\right)_{direct}. \tag{8.1}$$

The rate of change in nuclear polarization for a spatially inhomogeneous distribution of nuclear polarization is given by,

$$\left(\frac{dP(r,t)}{dt}\right)_{diff.} = \sum_{\alpha,\beta=1}^{3} D^{\alpha\beta}\left(\frac{\partial^2}{\partial x^\alpha \partial x^\beta}\right)P(r,t), \tag{8.2}$$

where $D^{\alpha\beta}$ is the $\alpha\beta$ component of the spin-diffusion tensor. We assume $D^{\alpha\beta} = 0$ for $\alpha \neq \beta$ and $D^{1,1} = D^{2,2} = D^{3,3} = D$.

As the depolarizing field is greater than the ^{29}Si nuclear dipolar field (0.08 mT), the nuclear dipolar spin diffusion rate is independent of magnetic field [84], and for a face centered cubic diamond lattice, the diffusion constant is well described by $D = Wa^2 \sim a^2/(50\,T_2)$, where $a = 0.414$ nm is the average separation between nearest-neighbor nuclei, W is the probability of a flip-flop transition between nuclei due to dipole-dipole interaction, and $T_2 = 10$ ms is the

nuclear decoherence time [100]. Due to strong gradients in the nuclear Larmor frequency very close to each paramagnetic impurity, nuclear spin diffusion is suppressed ($D = 0$), creating a barrier to diffusion of radius $b = a(\hbar\gamma_e^2 B_{dep}/\gamma_n 2k_B T)^{1/4}$ [100]. Here γ_n and γ_e are the nuclear and electronic gyromagnetic ratios, $\hbar$ is the Planck constant and k_B the Boltzmann constant.

The contribution from direct relaxation of the nuclear spins by the surface electrons is given by

$$\left(\frac{dP(r,t)}{dt}\right)_{direct} = \frac{P_0 - P(r,t)}{T_{1n,direct}(r)}, \tag{8.3}$$

where

$$T_{1n,direct}(r)^{-1} = \frac{K}{|R-r|^6} \tag{8.4}$$

Here $|R - r|$ is the distance of the nuclear spin packet from the particle surface, and K the strength of the interaction between nuclear and electron spins.

We have previously determined that a model of nuclear relaxation at the particle surface that includes three-spin processes involving pairs of interacting electrons best describes the nuclear spin dynamics in particles similar to these [209]. This model gives

$$K = \frac{3}{10}\frac{\hbar^2\gamma_e^2}{B_{dep}^2}\frac{B_{dep}^2\gamma_n^2 T_{2e}}{1 + B_{dep}^2\gamma_n^2 T_{2e}^2}\int_{-\infty}^{\infty}\frac{g(\omega)g(\omega-\omega_n)}{g(0)}\,d\omega \tag{8.5}$$

where T_{2e} = 0.025 μs is the electron spin-spin coupling and $g(\omega)$ is the normalized electron absorption lineshape function [92, 151].

This model accounts for flip-flop transitions between nearby electron pairs, occurring on a time scale $T_{2e} \ll T_{1e}$, which provide the fluctuating magnetic field that can flip nuclear spins. For a Lorentzian electron spin resonance lineshape, the integral in (5), which describes the probability of finding two electrons within the ESR line differing in frequency by ω_n, can be replaced with the function $2/(4 + \omega_n^2 T_{2e}^2)$.

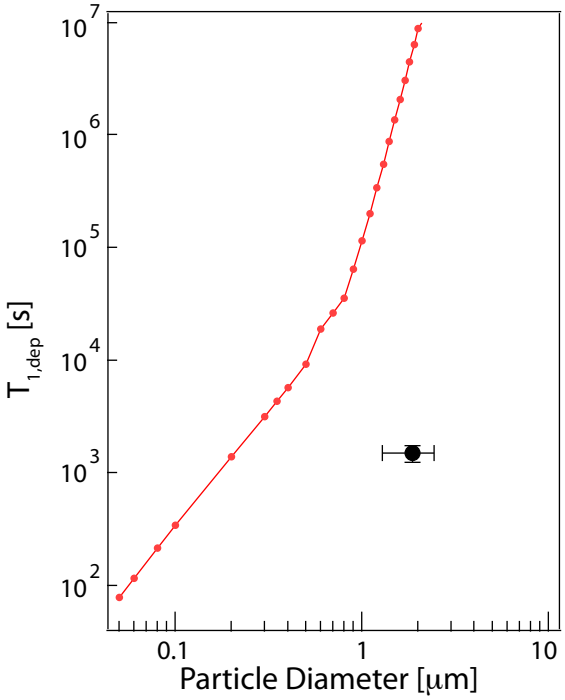

Figure 8.3.5: Theoretical plot of the nuclear depolarization time constant, $T_{1,dep}$, as a function of particle size at 4.7 T and 300 K. The simulations assume a purely crystalline spherical particle with electronic defects located on the particle surface that cause relaxation. The measured room temperature T_1 of the sample is also shown.

The average particle size and measured room temperature T_1 of the sample used in this study is also plotted in Fig. 8.3.5. The measured value of T_1 is significantly lower than what would be expected for a particle with diameter of 2 μm, however the simulated value of $T_{1,dep}$ agrees well with the 350 nm average crystallite size found by XRD analysis. It should be possible to reduce the actual particle size down to the crystallite size without significantly changing the nuclear spin dynamics reported in this study. Alternatively, the ability to manufacture and polarize large crystalline particles could lead to depolarization times of many hours, or even days.

8.3.4 Imaging window and concentration phantoms

To establish a practical time window for obtaining hyperpolarized MRI images, we imaged a millimeter-scale phantom constructed from pixels of dry silicon particles separated by teflon spacers (Fig. 8.3.6

(a)). Images were recorded 0, 30, 60, and 90 min after placing the phantom in the MRI imager, using separate polarizations for each time interval. The phantom image is clearly visible at τ_{dep} = 0, 30 and 60 min for a single average with a signal to noise ratio (SNR) greater than 12. After 90 min, only the top 3 pixels are visible (SNR > 3), probably due to a variation in polarization across the sample resulting from an uneven microwave field distribution in the polarizer.

Figure 8.3.6(b) shows the concentration sensitivity for the hyperpolarized particles. The images are of 250 μL cylindrical phantoms containing between 66 and 5 mg/mL of silicon particles dispersed in ethanol. A sensitivity limit is set by the silicon particle concentration in the outer two columns of the least concentrated sample. Assuming a uniform distribution of particles within the phantom and taking into account the cylindrical projection onto the plane, this equates to a visible single pixel concentration of $\sim$10 μg of hyperpolarized silicon particles per pixel. For a particle diameter of 2 μm, we estimate an absolute sensitivity of $\sim$ 5 x 10^5 individual particles/pixel, or a molar sensitivity of $\sim$ 4.2 x 10^{-13} mol/L at a depth of 1 cm from the face of the imaging coil. This is comparable in sensitivity with other reported paramagnetic MRI nanoparticle agents [216] and ^{19}F labelled cells [217].

8.3.5 *In-vivo* studies

We have carried out a number of *in-vivo* imaging studies to demonstrate a range of potential applications for hyperpolarized silicon particles.

8.3.5.1 Gastrointestinal imaging

Figure 8.3.7 shows coregistered ^{1}H:^{29}Si images of hyperpolarized silicon particles injected via a catheter into the gastrointestinal (GI) tract of a mouse. Immediately following the injection (< 1 min), the image shows the particles accumulating in the stomach and the duodenum. After 30 min, the particles appear to have moved further into the small intestine of the animal, revealing a more detailed structure of the small intestine. Delivery into the intraperitoneal (IP) cavity reveals

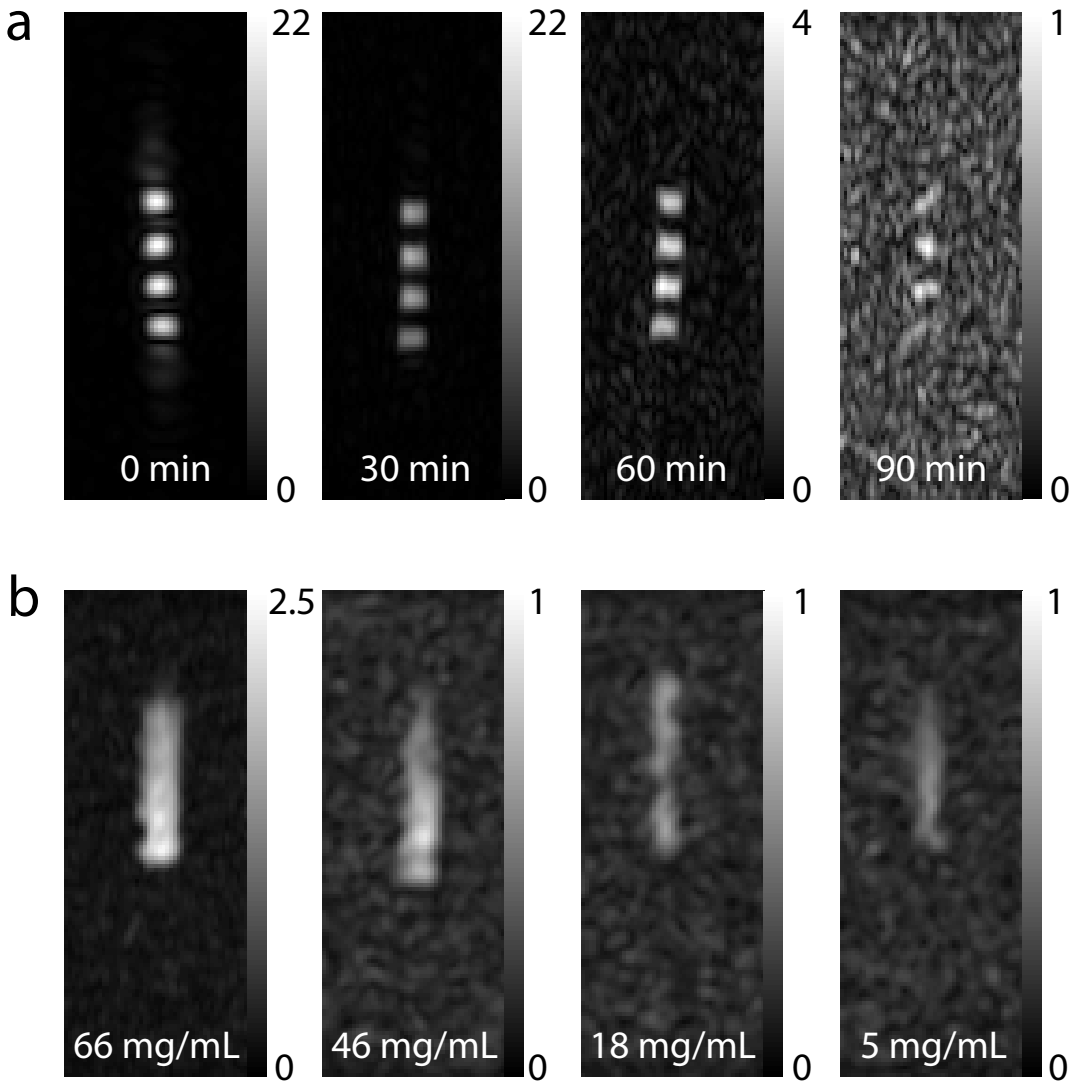

Figure 8.3.6: Phantom Imaging. (a) ^{29}Si MRI of a pixelated phantom containing silicon particles ($\sim$ 15 mg in each pixel) with a delay of 0, 30, 60 and 90 min from when the phantom was loaded into the magnet until imaging. (b) Imaging of a cylindrical concentration phantom showing imaging of solution phantoms with particle concentrations of 66 mg/mL, 46 mg/mL, 18 mg/mL and 5 mg/mL. Images have been cropped from 40 mm to 15 mm in the horizontal dimension after processing.

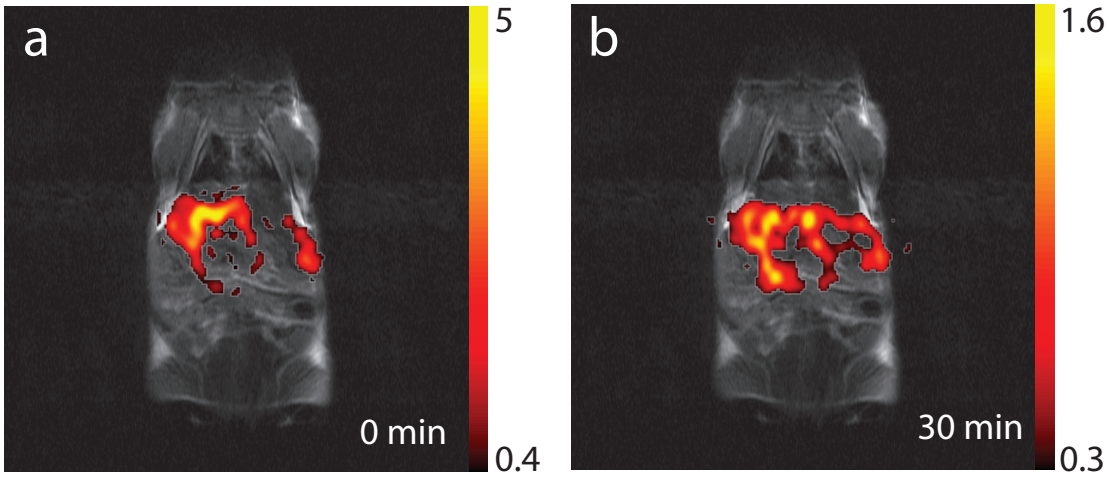

Figure 8.3.7: ^{29}Si MRI of hyperpolarized silicon particles administered intragastrially. Immediately after injection the particles are concentrated in the stomach and duodenum of the animal. After 30 min the particles have moved further into the small intestine, revealing detailed structure of the upper gastrointestinal tract.

detailed external structure of the GI tract imaged over 40 min (Fig. 8.3.8).

Diagnostic imaging of the small intestine is notoriously difficult as it is inaccessible to traditional endoscopic techniques. Current non-invasive GI imaging techniques using computerized tomography (CT) or ^{1}H MRI, with a combination of positive and negative contrast agents delivered intravenously and intragastrically for delineating internal structure [218]. For MRI, the complex air-tissue interfaces of the GI region cause susceptibility gradients that dominate over the change in signal induced by the paramagnetic agent. Silicon has been studied as a nutritional supplement [219, 220] and is a common food additive (up to concentrations of 2%) in its oxide form [224]. Hybrid gold-silicon nanoparticles are currently under investigation as targeted colorectal optical imaging agents and show no evidence of toxicity [225]. Hyperpolarized silicon particles appear well suited for structural and targeted imaging of GI disease by MRI.

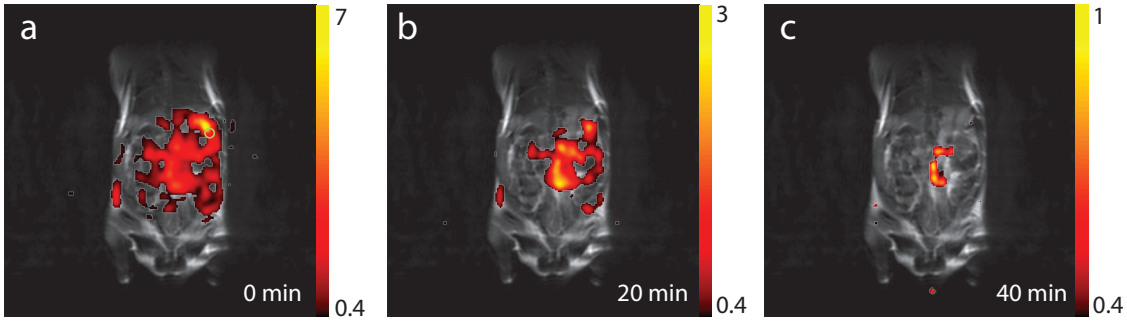

Figure 8.3.8: ^{29}Si MRI of hyperpolarized silicon particles injected intraperitoneally. The green circle shows the approximate location of the catheter in the animal. The particles coat the outside of the stomach and gastrointestinal tract, moving to the center of the animal over longer time periods.

8.3.5.2 Intravenous imaging

For particles administered intravenously (IV) via a tail vein catheter (Fig. 8.3.9), the vena cava is visible immediately after injection and continues to be visible one and two minutes later. The PEG chain used to functionalize the particles was chosen as it is known to enhance the circulation of similarly sized particles [170]. The high concentration of particles carried in the vena cava, and the proximity of the vena cava to the imaging coil results in this signal dominating over signals from other areas in the animal. After two minutes, some particle accumulation is observed in the organs of the mononuclear phagocyte system (MPS), consistent with accumulation patterns of similar sized materials imaged optically [39].

8.3.5.3 Perfusion imaging in a prostate tumor model

As a preliminary demonstration of perfusion imaging with hyperpolarized silicon MRI, we administered hyperpolarized silicon particles into the prostate tumor of a TRansgenic Adenocarcinoma of Mouse Prostate (TRAMP) mouse (Fig. 8.3.10). The particles used in this study are too large to enter the cellular structure of the tumor, however they accurately map the blood vessel microstructure inside the tumor, as well as the direction of blood flow within the tumor. Initially the

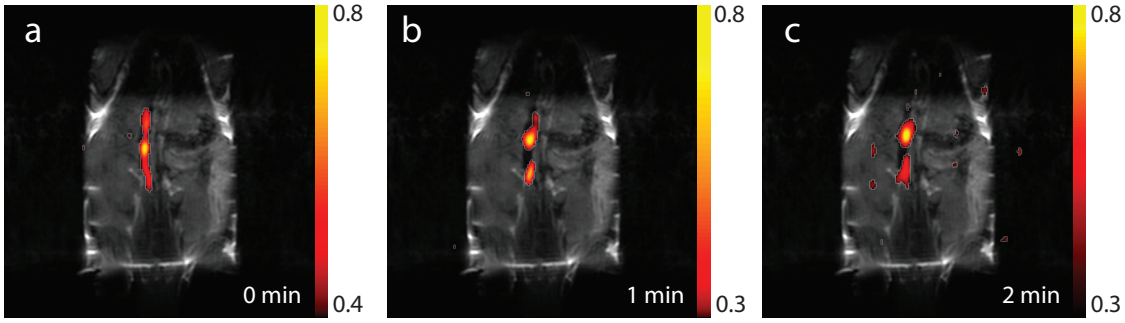

Figure 8.3.9: ^{29}Si MRI of hyperpolarized silicon particles injected intravascularaly via a tail vein catheter. The vena cava is visible immediately after injection. Images taken one minute and two minutes after the injection show particle accumulation in the portal veins and liver and spleen.

^{29}Si MRI shows accumulation at the lower right quadrant of the tumor while later images show a higher concentration in the upper right quadrant. There was little ^{29}Si signal observed on the left side of the tumor at any imaging time, suggesting an area of necrosis. This observation was confirmed visually post-mortem.

8.3.6 *In-vivo* toxicity

A key advantage of hyperpolarized ^{29}Si MRI is biocompatibility. Silica is frequently used as a biocompatible coating for other nanoscale probes [226, 227], and several studies have reported negligible toxicity of silicon particles [39, 225]. In these investigations, the clearance mechanism has been attributed to degradation of silicon and silica into soluble silicic acid followed by excretion within a few days. Our preliminary study of in-vivo toxicity of these particles up to the imaging concentrations show no decrease in animal viability over a two week period for particles administered via GI, IP or IV routes. Comparison of MPS organ tissue sections between those harvested three hours after IV administration and two weeks (Fig. 8.3.11) show that these silicon particles appear to be efficiently cleared within the two week period.

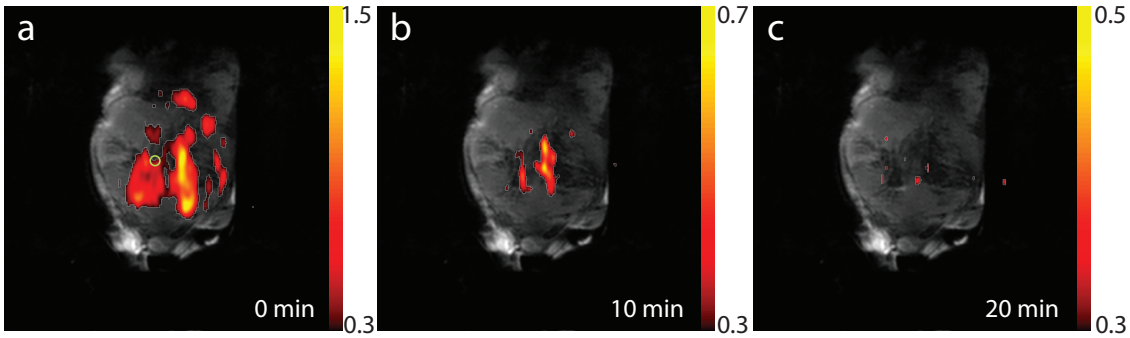

Figure 8.3.10: Perfusion imaging using ^{29}Si MRI of hyperpolarized silicon particles.^{29}Si MRI of hyperpolarized silicon particles injected into the tumor of a prostate cancer (TRAMP) animal. The green circle shows the approximate location of the catheter in the tumor. Silicon particles are more concentrated on the lower right side of the tumor. At 10 and 20 min, the silicon particles are more concentrated in the upper right side of the tumor indicating the area of blood flow from the tumor. The signal decays significantly faster than for the GI or IP injection, indicating that the particles are entering the blood stream of the animal.

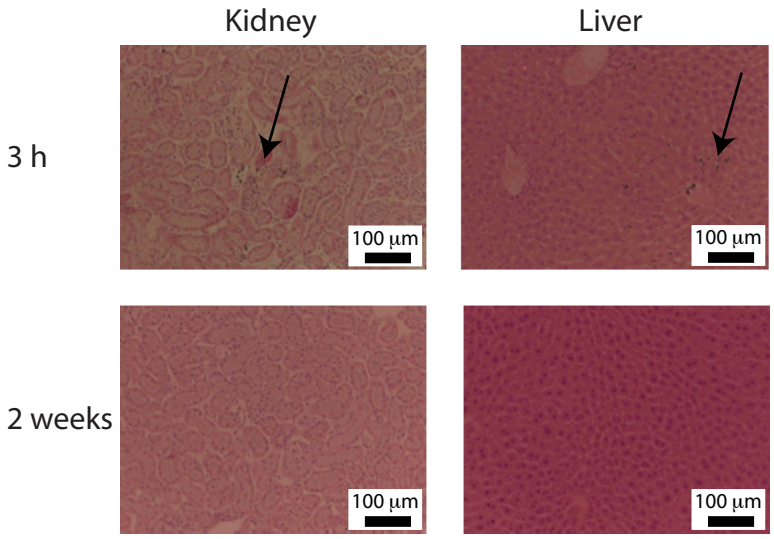

Figure 8.3.11: Representative sections of kidney and liver tissue collected from mice three hours and two weeks after intravenous injection of silicon particles. Organs were stained with haematoxylin and eosin. Silicon particles were observable in both the liver and kidney samples collected three hours after delivery (arrows), but not in any of the samples collected two weeks after delivery. The scale bar is 100 μm for all images.

8.4 Conclusion

Several orders of magnitude improvement in the concentration threshold and imaging time-frame presented here are possible. Eliminating isolated defects in the internal crystal structure and chemically enhancing the surface defect density, would result in more efficient polarization and significantly longer depolarization times. The hyperpolarization mechanism via surface defects is applicable to silicon particles of any size, with the imaging window ultimately set by the polarization time and the distance the nuclear spin hyperpolarization has to diffuse to relax. Previous studies [138] indicate that the hyperpolarization times observed here ($\sim$ 40 min) do not decrease significantly as particle size is reduced by an order of magnitude below those used in this study.

Because the time scale for depolarization does not depend on surface functionalization, targeting strategies developed for silica coated nanovectors can be applied to particles optimized for hyperpolarized ^{29}Si MRI. Surface doping may allow for extremely large nuclear polarizations to be generated [80, 108] through combined optical-microwave techniques. Additionally, as the T_1 times are at least two order of magnitude longer than those of hyperpolarized ^{13}C[61] and ^{129}Xe[67], it may be possible to use the nuclear hyperpolarization within the particles to store polarization (as a battery), then transferring polarization to read-out nuclei with higher gyromagnetic ratio via established cross-polarization techniques.

In summary, we have demonstrated *in-vivo* imaging of hyperpolarized silicon particles by MRI, and investigated a range of potential applications. By choosing particles with a crystalline Si core protected a surface oxide, the polarization generated in the particles is unaffected by the *in-vivo* environment or particle tumbling. Magnetic resonance offers not only the possibility of structural imaging, but also also functional imaging of flow, particle binding, or the local environment through surface functionalization. The lack of *in-vivo* ^{29}Si background signal has the potential for quantification of the ^{29}Si magnetic resonance label, opening up the possibility to track the particle biodistribution systematically, analogous to the use of nuclear tracers.

Acknowledgements

This research is supported by the NIH (1R21 CA118509, 1R01NS048589), the NCI (5R01CA122513), the Tobacco Related Disease Research Program (16KT-0044), NSF BISH (CBET-0933015), and the NSF through the Harvard NSEC. M.C.C. acknowledges financial support from the R.G. Menzies Foundation. We thank L. W. Jones for the generous gift of the TRAMP mouse, N. Zacharias for assistance with histology, M. Lee, L. Robertson and B. D. Armstrong for assistance with the initial stages of the experiment and L. W. Jones, C. Ramanathan and R. W. Mair for many helpful discussions.

9

Additional Results

This chapter contains a number of small investigations into the nuclear spin dynamics of silicon micro and nanoparticles that may be of interest to the reader.

9.1 Optical effects on room temperature T_1 in silicon micro and nanoparticles

9.1.1 Introduction

Undoped semiconductors such as silicon typically have small concentrations of thermally activated carriers at room temperature, on order 10^{10} cm^{-3} at 300 K [87]. However, illumination with light of energy above the semiconducting bandgap generates carrier pairs close to the silicon surface. These electrons and holes possess a non-zero spin and can therefore interact with the ^{29}Si nuclear spins within the lattice by a contact hyperfine interaction. This contact hyperfine interaction can drive both nuclear polarization and relaxation, and understanding its effect on different sized particles is important for preserving nuclear hyperpolarization in samples that transit through a white-light environment.

9.1.2 Samples and experimental methods

Four samples of silicon particles were investigated. Sample A was composed of ~ 5 μm diameter particles produced by ball-milling undoped float-zone grown Si wafers (Silicon Quest International) and size-separated by centrifugal sedimentation [138]. Sample B consisted of commercially sourced polycrystalline silicon particles of diameter ~ 2 μm. Samples C and D consisted of crystalline particles of diameter ~ 10 nm (C) and ~ 20 nm (D) produced by wet synthesis as described in Chapter 6.

Room temperature NMR experiments were performed at 300 K in a 2.9 T superconducting NMR magnet with a home-built probe and spectrometer. T_1 at 2.9 T was determined by performing saturation-recovery experiments, wherein nuclear polarization is nulled by a series of 16 $\pi/2$ pulses, then allowed for time τ_{pol} to recover the polarization. The recovered polarization was

measured by a Carr-Purcell-Meiboom-Gill (CPMG) sequence [98]

$$(\pi/2)_X - [\tau/2 - (\pi)_Y - \tau/2 - \text{echo}]^n$$

with $\tau = 1$ ms and $n = 400$. T_1 was then extracted by fitting the evolution of polarization versus τ_{pol} as exponentially approaching thermal equilibrium. The light source (EKE 21V150W) was a 150 W halogen light bulb, and the light was coupled to the sample through an optical fiber light-guide.

9.1.3 Results

Figure 9.1.1(a) shows the saturation-recovery of nuclear polarization in sample A under light and dark conditions. No change in T_1 is observed between the two situations. Similar results were observed for sample B. In sample C (Fig. 9.1.1(b)) T_1 is seen to decrease notably under illumination. In the dark, $T_1 = 675 \pm 124$ s and under illumination, $T_1 = 395 \pm 118$ s In both cases some portion of the magnetization recovers very quickly and then the polarization exponentially approaches thermal equilibrium. Similar results were observed for sample D.

The relative change in room temperature T_1 due to light ($T_{1,light}/T_{1,dark}$) is shown as a function of particle diameter in Fig. 9.1.2. Because the sample tube was packed tightly with silicon particles in all cases, the samples' differing responses to illumination cannot be attributed to a large variation in optical penetration into the sample volume. Assuming a model close packed spheres, the distance between particles in both cases is below the wavelength of the light, and so the light penetrates the sample volume by scattering [228]. Based on the difference in particle sizes of the samples, we would expect stronger penetration of the light into the sample volumes of the larger particles, rather than the small particles. Therefore the appearance of a nontrivial effect of illumination only for small nanoparticles indicates that the relative surface to volume ratios of the particles plays a role. Light is strongly attenuated at larger distances from the silicon surface, [229] and so

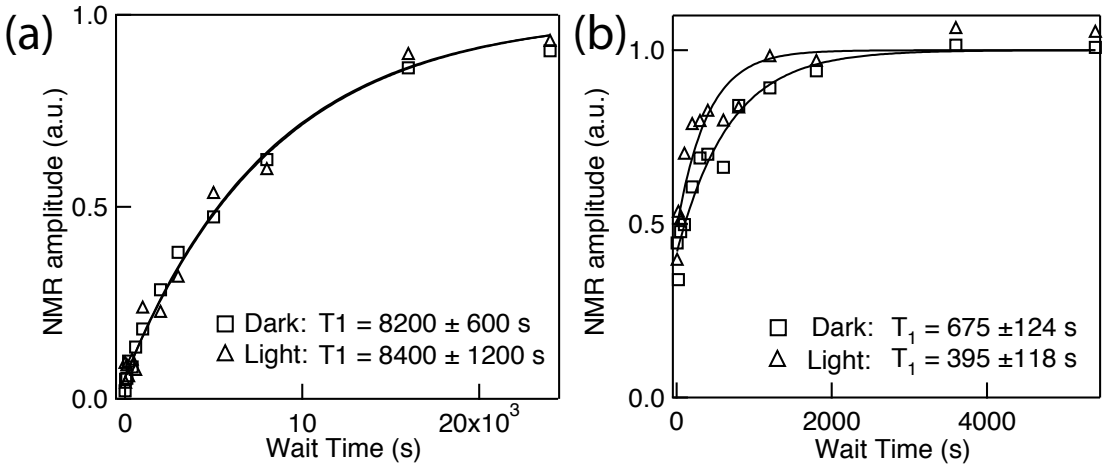

Figure 9.1.1: Nuclear spin lattice relaxation, with and without optical illumination, in (a) large and (b) small silicon nanoparticles, measured by recovery of spin polarization after saturation at $B = 2.9$ T.

it is likely that carriers are only generated within the first $\sim$100 nm from the particle surface. For the large particles, this region only constitutes a few percent of the volume of each particle, corresponding to only a few percent of the ^{29}Si contributing to the ^{29}Si NMR signal. For the smaller particles this constitutes the entire volume of each particle and so all nuclei are affected.

9.1.4 Conclusion

The effect of optical illumination on spin-lattice relaxation in silicon nanoparticles have also been measured. A significant shortening of T_1 (by $\sim$ 40%) due to illumination is observed in small, 10-20 nm nanoparticles but not in large particles with diameters of 2 μm and 5 μm. This difference between small and large nanoparticles indicates that the relative surface to volume ratios has nontrivial effects on the spin dynamics in silicon at nanometer scale.

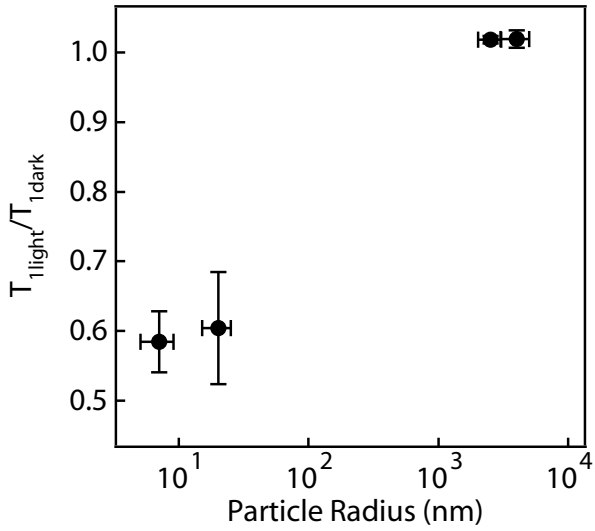

Figure 9.1.2: Change in room temperature T_1 due to light ($T_{1,light}/T_{1,dark}$) as a function of particle diameter.

9.2 Optical effects on low temperature dynamic nuclear polarization in silicon microparticles

9.2.1 Introduction

Dynamic nuclear polarization requires the transfer of angular momentum from a highly polarized spin bath to the target nuclear spins to enhance their polarization far above the equilibrium level. In many cases, this polarized spin bath takes the form of paramagnetic defects that occur naturally within the system [128], or are introduced via gamma ray irradiation [208], or the incorporation of a chemical radical species [59]. These paramagnetic defects are very efficient at driving dynamic nuclear polarization under microwave irradiation, however once the microwave irradiation is turned off, they provide the main mechanism for loss of nuclear polarization through spin lattice relaxation. In semiconducting materials, above band gap optical irradiation can be used to generate carriers in excess of the thermally generated carriers. These carriers only exist while the optical irradiation is on, relaxing back to their lattice sites once it is switched off. This provides a unique opportunity to efficiently generate high nuclear polarizations that are protected from relaxation after the polarization process is complete.

The optical pumping effect has been investigated extensively in III-V materials such as GaAs and InP, where by using polarized light, spin polarized carriers can be generated that then polarize the nuclear spins via a contact hyperfine interaction. A number of NMR studies in silicon crystals by Bagraev et al. have reported on T_1 and its dependence on magnetic field for silicon under optical pumping conditions, where different material treatments such as doping, [146, 147] compensation, [148] and mechanical deformations [149] have been applied to the crystal. Optical pumping is achieved by the absorption of circularly polarized photons which produces a large number of photoexcited carriers with a distribution of spin polarization far from equilibrium. Through an exchange interaction this also results in nonequilibrium polarizations

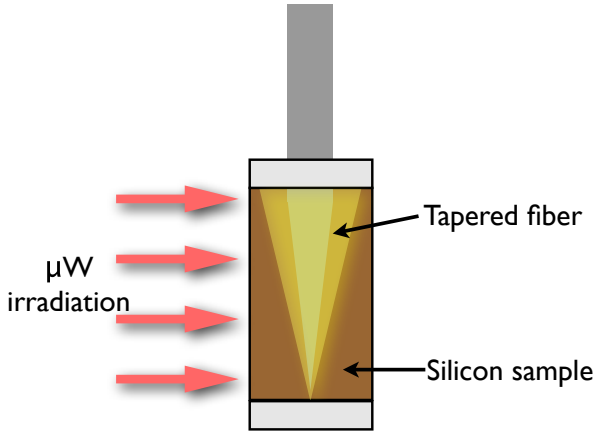

Figure 9.2.1: Schematic of the setup used for combined optical and microwave induced dynamic nuclear polarization.

of electrons localized at donors. The relaxation of those electron spins take place through flip-flop transitions of the coupled electron-nuclear system, consequently hyperpolarizing the nuclear spin [83, 84, 106, 128, 145]. Unpolarized light can also be employed, and in either case nuclear relaxation measurements can provide information on the details of the involved spin processes [221–223].

9.2.2 Samples and experimental methods

For this study our sample was $\sim$ 10 mg of natural abundance (^{29}Si = 4.8%) polycrystalline silicon powder (Alfa Aesar, d = 3 μm). Dynamic nuclear polarization was performed in a continuous flow cryostat at 3.6 K, in a 2.89 T superconducting NMR magnet (ω_n = 24.404 MHz). The sample was packed in a thin walled teflon tube which was held in direct contact with the flowing helium vapor. A custom insert for the cryostat and a home built spectrometer with a saddle coil were used for NMR detection. A +20 dBm (100 mW) Gunn diode tunable from 80 – 82 GHz was used as the microwave source. The microwave frequency for irradiation was set by adjusting the DC bias of the Gunn diode. The DC bias was modulated using the cascaded output of two function generators (HP33250A). The light source (EKE 21V150W) was a 150 W halogen light bulb. The cryostat was

equipped with an optical vacuum feedthrough and the light was coupled to the sample through an optical fiber light-guide. The light-guide was tapered at the end and situated concentric with the sample volume (Fig. 9.2.1) to ensure maximum irradiation of the sample. Microwaves were coupled to the sample using a mm waveguide with a slot antenna that provided uniform irradiation along one side of the sample.

The g-factor for optically generated carriers (g=2.002) is significantly different to the g-factor for fixed paramagnetic defects (g=2.006) within the silicon sample and so the two electron species have significantly resonant frequencies. Additionally, for the optically generated we would expect polarization via a contact hyperfine interaction [83, 108], with maximum polarization occurring at the resonant frequency for these carriers ($\omega = \omega_{e1}$), opposed for the fixed paramagnetic defects where polarization occurs at a frequency below the resonant frequency ($\omega = \omega_{e2} - \Delta\omega$)

We used three different microwave irradiation schemes to try to selectively drive polarization for each of the two mechanisms (Fig. 9.2.2). Scheme A used irradiation modulated around the frequency know to drive maximum polarization by the paramagnetic defects $\omega_{e2} - \Delta\omega = 80.96$ GHz. Scheme B used irradiation at the resonant frequency of the optically generated carriers $\omega_{e1} = 80.4$ GHz. Scheme C used a double modulation where the microwave irradiation was set to jump between the two resonant frequencies at a duty cycle of 0.5.

9.2.3 Results

The time evolution of ^{29}Si nuclear polarization in the light (blue) and dark (red) for the three different microwave irradiation schemes is shown in Fig. 9.2.3. The data is well fit by a biexponential function $P = P_\infty \left(1 - A_1 e^{-\tau_{pol}/T_{pol,1}} - A_2 e^{-\tau_{pol}/T_{pol,2}}\right)$ with two distinct time constants. $T_{pol,1}$ and $T_{pol,2}$ shown in Table 9.2.1.

In all cases the addition of white light decreased the ultimate nuclear polarization generated by DNP after an irradiation time τ_{pol}. The rates of polarization also decreased, suggesting that the

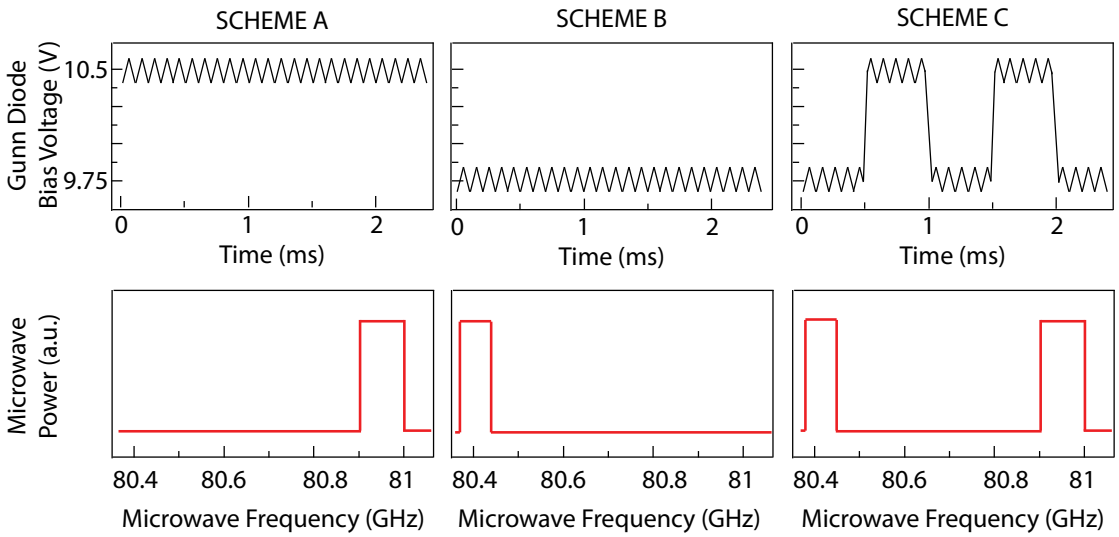

Figure 9.2.2: Microwave modulation schemes for optically enhanced DNP experiments.

carriers were depolarizing nuclei that had been polarized in the dark by nuclear spin diffusion.

Efficient nuclear polarization via a contact hyperfine interaction with mobile carries requires that the polarization of the carriers is high. At the temperature (T=3.6 K) and magnetic field (B = 2.89 T) investigated, the electron polarization is $\sim$ 50%. As $\sim$ half the generated carriers are unpolarized, and interactions between them and ^{29}Si nuclei will result in an additional relaxation $T_{1,x} \propto N_o T^{1/2} A^2$ according to,

$$\frac{dP(r,t)}{dt} = \frac{P_o - P}{T_x} + D\nabla^2 P + W\sum \frac{P - \eta P_o}{|r - r_m|^6} \tag{9.1}$$

where W is the rate of DNP generated by the paramagnetic defects.

9.2.4 Conclusion

A combined optical irradiation and microwave induced dynamic nuclear polarization was investigated as a mechanism for increasing the nuclear polarization in microscale silicon particles. No enhancement in ^{29}Si nuclear polarization due to the optical carriers was observed at the temperature and magnetic field investigated. Instead, the optical carriers generated provide an additional relax-

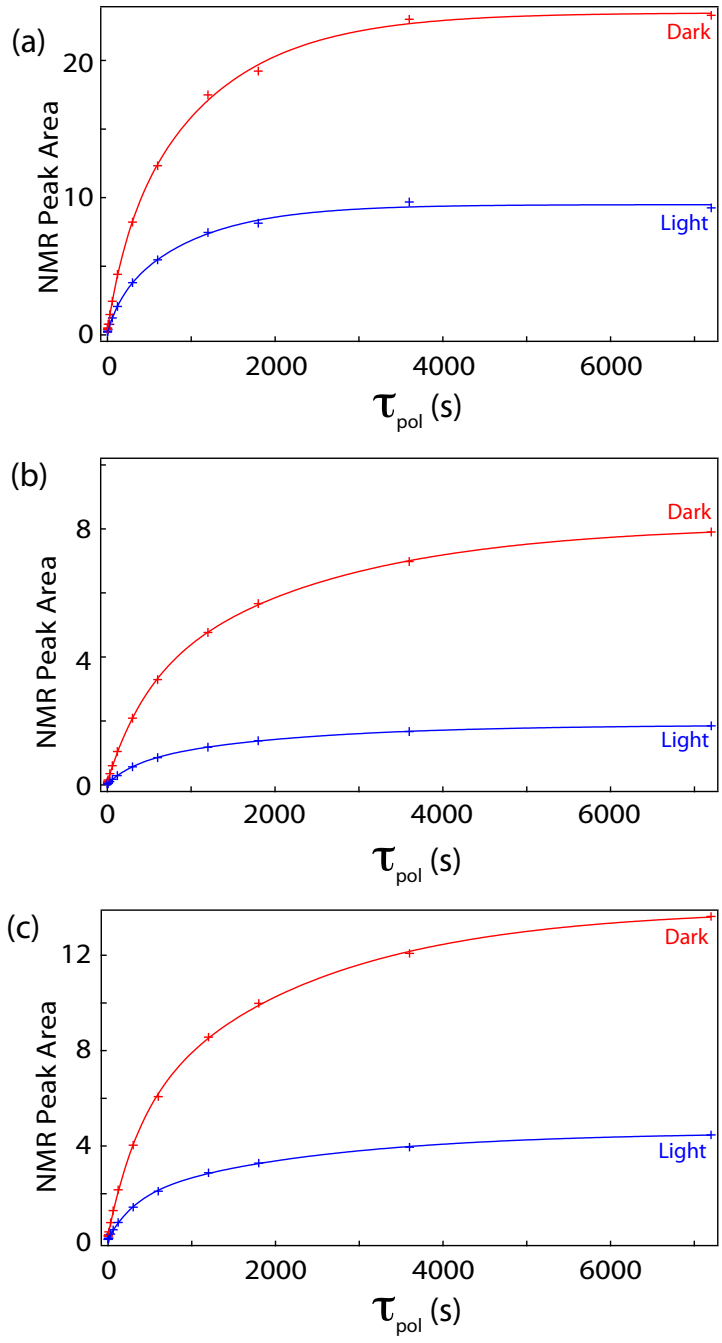

Figure 9.2.3: Effect of white light illumination on microwave induced DNP in silicon microparticles for microwave irradiation (a) at the resonant frequency of the defects, (b) at the resonant frequency of the carriers (c) modulated between the two resonant frequencies.

Scheme		$T_{pol,1}(s)$	$T_{pol,2}(s)$
A	Light	150 ± 80	950 ± 130
	Dark	220 ± 80	1150 ± 125
B	Light	320 ± 20	1970 ± 100
	Dark	420 ± 30	2300 ± 140
C	Light	310 ± 30	2330 ± 220
	Dark	350 ± 40	2220 ± 200

Table 9.2.1: Polarization times fitting to experimental data in Figure 9.2.3. $T_{pol,1}$ and $T_{pol,2}$ are fast and slow polarization times which form two additive components of the polarization process.

ation mechanism for nuclear polarization generated by irradiation of fixed paramagnetic defects, resulting in a lower ultimate polarization generated compared to microwave irradiation alone. Repeating the experiment at a higher magnetic field and lower temperatures, similar to the case investigated by McCamey et al. [108] where the electron polarization was $> 90\%$ may result in the anticipated enhancement in nuclear polarization via a contact hyperfine interaction. Additionally, the use of smaller particles where the optical irradiation can fully penetrate each particle volume (such as those described in Section 9.1), or those without a surface oxide, would lead to a higher number of carriers generated and increase the rate of hyperfine interactions between spin polarized carriers and ^{29}Si nuclei within the lattice.

9.3 Temperature dependence of the decay of nuclear hyperpolarization in silicon microparticles

9.3.1 Introduction

Low temperature dynamic nuclear polarization utilizes the high spin polarization of a bath of paramagnetic defect electrons for polarizing nuclear spins far above their thermal polarization. The nuclear polarization dynamics are determined by the location and concentration of these electrons with respect to the target nuclei, as the rate of direct polarization scales strongly with the distance r between them (r^{-6}). Once the nuclei are hyperpolarized, the primary mechanism for the depolarization of the nuclear spins is via an interaction with the paramagnetic defects that polarized them, however isolated or non-resonant defects may also cause additional depolarization.

For clinical applications, samples that are hyperpolarized at low temperatures via dynamic nuclear polarization typically undergo large changes in magnetic field and temperature in their transit from the polarizer to when they are administered in an imaging magnet. The coupling between the electron spins and the lattice is strongly dependent on both magnetic field and temperature, and so it is expected that there will be both a temperature and magnetic field dependence to the decay in nuclear hyperpolarization.

Crystalline silicon microparticles consist of two distinct nuclear spin baths; spins that are in direct contact with paramagnetic defects at the surface via a dipolar interaction, and spins that are contained deep within the core of the particle and protected from these defects. Nuclear spin diffusion is an energy conserving process, and so for depolarization dominated by nuclear spin diffusion, relaxation should be independent of both magnetic field and temperature [94]. We have previously studied the decay in nuclear hyperpolarization from Boltzmann polarization as a function of depolarizing magnetic field and observed two distinct nuclear spin baths, one which was dependent on magnetic field, and another that decayed independent of magnetic field.

In this study we examine the temperature dependence of the decay in nuclear hyperpolarization in silicon microparticles, and compare it to the decay in nuclear polarization observed when the particles are transited through a varying magnetic field to the imaging magnet. Understanding this temperature dependence may determine if there is an optimal temperature for storing hyperpolarized samples before they are administered.

9.3.2 Samples and experimental methods

For this study our sample was $\sim$ 20 mg of high purity (99.99985% Si) natural abundance (^{29}Si = 4.8%) silicon powder (Alfa Aesar, d = 2 μm), as used in the imaging studies in Chapter 8. Dynamic nuclear polarization was performed in a continuous flow cryostat equipped with a variable temperature control, in a 2.89 T superconducting NMR magnet (ω_n = 24.404 MHz). The sample was packed in a thin walled teflon tube which was held in direct contact with the flowing helium vapor. A custom insert for the cryostat and a home built spectrometer with a saddle coil were used for NMR detection. A +20 dBm (100 mW) Gunn diode tunable from 80 $-$ 82 GHz was used as the microwave source. The microwave frequency response of the ^{29}Si nuclear polarization was calibrated to determine the optimal conditions for polarization (Fig 9.3.1). For polarization, the microwave source was centered at the peak value in Fig 9.3.1, and the DC bias of the Gunn diode was modulated with a symmetric ramp function at a frequency f_{mod} = 10 kHz and amplitude corresponding to a bandwidth of BW_{mod} = 70 MHz. At the beginning of each experiment, the residual nuclear polarization was nulled with a series of $\pi/2$ pulses, and the sample allowed to polarize for a period of time t_{pol} = 12 h at T = 3.6 K. At the end of the polarization period, the microwave irradiation was switched off using an inline high-isolation TTL switch, the temperature raised to the depolarizing temperature T_{dep} = 4, 20, 77 or 300 K and the decay in nuclear polarization measured with a series of 20° pulses separated by 900 s. A mathematical correction (where the i^{th} free induction decay was scaled by $(1/cos((1/4.5) * \pi/2)^i * sin((1/4.5) * \pi/2))/(sin((1/4.5) * \pi/2)))$ was applied to the data to correct for the decreasing fraction of residual magnetization consumed

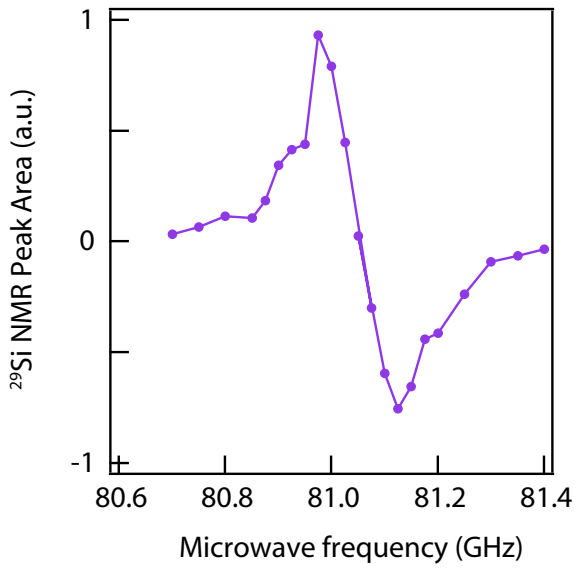

Figure 9.3.1: ^{29}Si nuclear polarization as a function of microwave irradiation frequency at B = 2.89T and T = 3.6 K. echos

in later pulses.

9.3.3 Results

The decays in nuclear polarization for depolarization temperatures of 4 K, 20 K, 77 K and 300 K are shown in Fig. 9.3.2 (a). The data is well fit by a single exponential in each case and a characteristic decay time $T_{1,dep}$ is extracted for each temperature. The values of $T_{1,dep}$ for the different values of depolarizing temperature are shown in Fig. 9.3.2 (b). A factor of two reduction in the depolarization time is observed over this temperature range, with the largest changes observed for the temperature range 4 - 20 K. The characteristic depolarization time measured for the same sample under similar polarization conditions, but measured at 300 K within the bore of a 4.7 T MRI scanner is also shown (Chapter 8). This sample is subject to a wide range in magnetic fields as it is moved from within the 2.89 T polarizer into the bore of the 4.7 T MRI scanner (with a minimum of $\sim$ 50 mT) that may contribute to the nuclear depolarization, however no significant different in the two depolarization times are observed for the same polarization conditions.

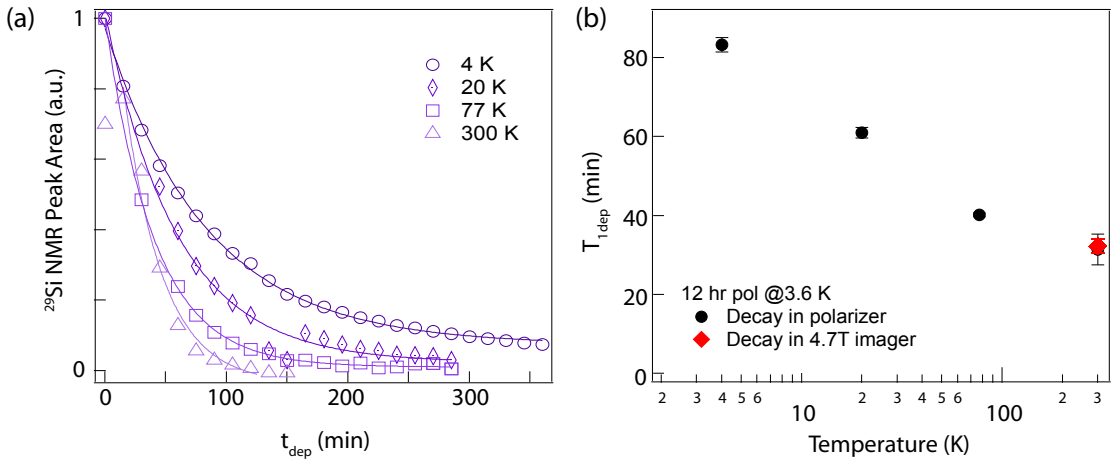

Figure 9.3.2: Decay of nuclear hyperpolarization as a function of temperature. (a) Decay of ^{29}Si nuclear hyperpolarization in the polarizer at depolarizing temperatures of 4 K, 20 K, 77 K and 300 K after DNP for 12 hours at 3.6 K. (b) Characteristic ^{29}Si depolarization time constants ($T_{1,dep}$) for different depolarizing temperatures extracted from the decay curves in (a).

We have previously identified multi-electron dipole-dipole interactions occurring between as the primary relaxation mechanism for Boltzmann hyperpolarized ^{29}Si nuclei at different magnetic fields at room temperature [209]. These electrons are located primarily on the surface of the particles and relax nuclei at a rate that is dependent on the distance R between the defects and the nuclei according to,

$$T_1^{-1} = \frac{K}{r^6} \tag{9.2}$$

where

$$K = \frac{3}{10}\frac{\gamma_e^2\hbar^2}{B_0^2}\frac{\omega_n^2 T_{2e}^{ss}}{1+\omega_n^2(T_{2e}^{ss2})^2}\int_{-\infty}^{\infty}\frac{g(\omega)g(\omega-\omega_n)}{g(0)}d\omega \tag{9.3}$$

This has no explicit temperature dependence and so the strong temperature dependence observed is surprising. However, the relaxation caused by a single electron thermalizing with the

lattice is dependent the rate of this thermalization, T_{1e} by,

$$T_1^{-1} = \frac{C}{r^6} \tag{9.4}$$

where

$$C = \frac{3}{10}\gamma_e^2\gamma_n^2\hbar^2\frac{2T_{1e}}{1+\omega_n^2T_{1e}^2}. \tag{9.5}$$

The defect electrons at the surface of the particle have a strong temperature dependence $T_{1e} \propto T^{-2}$ between 4 - 20 K [165] that would contribute to the additional relaxation observed via a single electron dipolar process.

The lack of change between depolarization in the polarizer and in the imaging magnet is not surprising. By the time that the particles are moved to the low field environment, the electrons at the particle surface have thermalized to the environment ($T_{1e} \ll 1s$) and relaxation of nuclei within a certain radius of the particle surface has already occurred. Moving the hyperpolarized particles through a varying magnetic field environment (above the dipolar field of the nuclei) therefore has no additional effect on nuclear depolarization, as the nuclei that remain hyperpolarized are located far from these paramagnetic defects and can only relax via nuclear spin diffusion.

9.3.4 Conclusion

We have measured the decay in nuclear hyperpolarization for high purity silicon microparticles at temperatures ranging from 4 - 300 K. A factor of two decrease in depolarization time is observed over this temperature range, with the largest change occurring in the temperature range between 4 - 20 K. There is little change in depolarization time constant observed for the sample depolarizing at 300 K within the polarizer compared to the sample that has been subject to large changes in ambient magnetic field as it is moved from the polarizer to an imaging magnet. Samples that have been hyperpolarized for longer times will have a higher proportion of nuclear polarization

contained within the crystalline core, and their depolarization should show a weaker temperature dependence.

9.4 Effect of the ^{1}H environment on ^{29}Si DNP in natural abundance and enriched particles

9.4.1 Introduction

The silicon oxide surface that naturally encapsulates silicon micro and nanoparticles is strongly hydrophobic, and so these particles need to be surface functionalized with a biocompatible polymer to ensure stability in biological media. This surface functionalization is performed as a wet chemistry process before the ^{29}Si hyperpolarization is generated by low temperature DNP. The functional moieties are attached to the particle surface, within a few nm of the electrons that provide the polarization source for ^{29}SiDNP. Understanding the effect of a nearby ^{1}H rich spin bath from the functional moieties and residual solution on the ^{29}Si DNP process is important for applications of these materials for medical imaging.

9.4.2 Samples and experimental methods

The samples and measurement techniques for this section are the same as in Chapter 7.

The samples consisted of high purity natural abundance (^{29}Si = 4.8%) silicon particles (Alfa Aesar, d = 3 μm), and isotopically enriched (^{29}Si = 91.4%) [205] silicon particles (d_o = 200 nm) made by ball milling bulk silicon and then size-separated by centrifugal sedimentation [138]. Both samples were undoped and polycrystalline. Particle sizes were confirmed by Scanning Electron Microscopy (SEM). Suspensions of these particles in ethanol and water (10:9:1 Si:EtOH:H_2O by weight) were prepared by sonication in an ultrasonic bath and then degassed with a freeze-pump-thaw cycle before being loaded into the cryostat for measurement. The ethanol and water mixture breaks the hydrophobic effect normally observed for silicon particles suspended in water alone, bringing ^{1}H spins close to the particle surface.

DNP experiments were performed at 4.2 K in a continuous flow cryostat in a B = 2.35 T (20

MHz ^{29}Si frequency, 100 MHz ^{1}H frequency) superconducting NMR magnet. The sample was housed in a glass capillary tube which was held in direct contact with the flowing helium vapor. A Bruker NMR spectrometer with a home-built probe and solenoidal coil [206] was used for NMR detection. Microwave (μW) irradiation was provided through a 90 mW Gunn Diode source (Millitech), and the μWs were coupled from room temperature to the sample via a mm waveguide and horn antenna. The nuclear polarization was measured with a saturation recovery sequence $(\pi/2)^{16} - t - (\pi/2)_X$.

9.4.3 Results

Figure 9.4.1 shows the time dependence of the ^{29}Si NMR signal for samples of natural abundance (4.7% ^{29}Si) and enriched (92% ^{29}Si) SiNP both dry and suspended in a frozen matrix of ethanol and water at a μW frequency of 65.875 GHz. To exclude the effects of differences in sample volume, all data sets are normalized to the NMR peak value at 7200 s. The data is well described by a biexponential function $P = P_\infty \left(1 - A_1 e^{-t/\tau_{Si_1}} - A_2 e^{-t/\tau_{Si_2}}\right)$ with two distinct time constants. τ_{Si_1} and τ_{Si_2}, summarized in Table 9.4.1. We attribute τ_{Si_1} to the polarization of nuclei near the surface of the particle, and τ_{Si_2} to polarizing nuclei in the core of the particles by nuclear spin diffusion. When the particles are suspended in the solution, the initial polarization time τ_{Si_1} is reduced by a factor of 2-3, whilst τ_{Si_2} remains approximately the same for both types of particles. Even though spin diffusion is expected to be much faster for the ^{29}Si enriched nanoparticles, we do not see a discernible difference in τ_{Si_2} between the two sets of particles, probably due to the difference in size.

Polarization in these silicon samples is generated by fixed paramagnetic defects located at the silicon-silicon dioxide interface close to the particle surface. The ^{1}H nuclei within the water:ethanol mixture are located close enough to these defect spins to be directly polarized through the same dipolar interaction that polarizes the ^{29}Si nuclei within the particle. For a given microwave energy

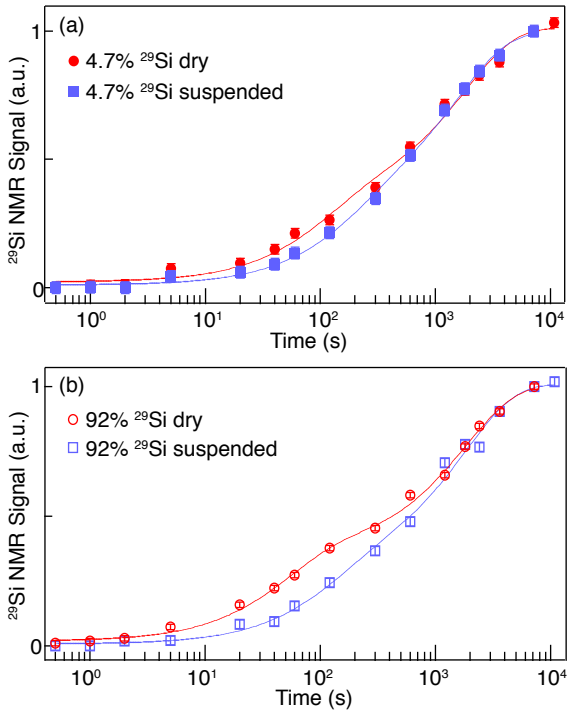

Figure 9.4.1: ²⁹Si nuclear polarization for (a) natural abundance (4.7 % ²⁹Si) and (b) isotopically enriched (91.4 % ²⁹Si) particles dry and in a frozen ethanol:water matrix.

Sample		$\tau_{Si1}(s)$	$\tau_{Si2}(s)$
4.7% ²⁹Si	dry	85 ± 26	1714 ± 254
(3 μm)	suspended	172 ± 41	1570 ± 181
92% ²⁹Si	dry	49 ± 6	1816 ± 169
(200 nm)	suspended	123 ± 41	1798 ± 263

Table 9.4.1: Polarization times fitting to experimental data in Figure 9.4.1. τ_{Si1} and τ_{Si2} are fast and slow polarization times which form two additive components of the polarization process.

irradiating the electron spin bath, some of the energy from the electron dipolar bath will transfer to the ^{1}H Zeeman bath, and some to the ^{29}Si Zeeman bath, reducing the initial polarization rate of the ^{29}Si spins.

In contrast, the initial polarization rates of similar particles with and without surface functionalization with APTMS and PEG showed little dependence on the presence of the extra organic moieties. The amount of polarization generated via direct DNP a distance r from the electrons scales as r^{-6} for each nuclear species. The APTMS/PEG complex has very few spinful nuclei very close to the particle surface (Appendix C) and, due to its electrochemical structure, excludes water from within it. Therefore the relative size of the ^{1}H spin bath in these surface functionalized particles is significantly smaller compared to the particles investigated in this study that have been suspended directly in water and ethanol.

9.4.4 Conclusion

We have measured the effect of a proximal ^{1}H rich solution on the DNP of silicon particles with natural abundance (4.7%) and isotopically enriched (91.4%) concentrations of ^{29}Si nuclei. The addition of the ^{1}H rich solution reduces the efficiency of ^{29}Si DNP, as part of the energy is now transferred to the ^{1}H spin bath. A stronger effect on the initial polarization dynamics is observed in the enriched sample than in the natural abundance sample, however later stage polarization in both samples is largely unaffected by the ^{1}H rich spin bath.

To get something new done you have to be stubborn and focused, to the point that others might find unreasonable.

Jeff Bezos

10

Conclusions and future outlook

The aim of this thesis was to take the idea of a biocompatible long-T_1 targeted medical imaging agent from concept to application, and provide a framework for understanding the physical processes that underly both polarization and depolarization within these particles.

A variety of samples were measured that were made by a range of techniques including ball milling silicon wafer, wet synthesis, and explosion synthesis. Most samples suffered from internal crystal defects that acted as isolated relaxation sites during the polarization process, significantly slowing the rate of polarization and impacting on the ultimate polarization achievable, as well as the depolarization times. The samples that had the best spin-lattice relaxation properties were

those made by wet synthesis, however obtaining large quantities of these high quality samples was difficult. Therefore improved synthesis techniques to make large quantities of high-quality silicon particles with larger sizes (up to several μm) would be desirable.

Several aspects could be improved in the polarization process. Reducing the temperature of operation to below 1 K would significantly increase the electron spin polarization, and hence the ultimate ^{29}Si nuclear polarization achievable. This may be offset by a subsequent increase in the electron T_{1e} that would slow down the rate of polarization, however this could be compensated for by increasing the electron concentration. Chemical modification of the silicon surface, for instance with controlled oxidation, could allow the defect density to be tailored so that the hyperpolarization process is optimized. A strategy to quickly terminate these defects after polarization, for instance by using forming gas, could further enhance the relaxation times achievable. Optically enhanced DNP is also more likely to be observed at these lower temperatures, and could be used to generate polarization in samples without a surface oxide that could have very long relaxation times once the illumination is turned off. These particles could be used as a polarization 'battery' where nuclear hyperpolarization could be transferred via a Hartmann-Hahn cross polarization process to other nuclear spins at the surface of the particle for enhanced readout[1]. Other improvements, such as using a microwave cavity for enhancing the strength of the microwave irradiation should also be investigated.

The imaging procedure could also be significantly improved. A purpose built ^{1}H: ^{29}Si volume coil would allow for coregistered 3D imaging. The imaging sequence could also be improved, for instance by the use of shorter echo times and signal averaging by taking advantage of the 'long-tail' of echoes generated under the CPMG conditions. Additionally, the MRI system used for these studies was not shielded from electromagnetic noise, and so a significant amount of background noise should be able to be eliminated.

[1]Note that this process is unlikely to work in particles with a high concentration of electrons at the particle surface, as the strongly dipolar coupled electron bath has a wide spectral distribution that will short-circuit the cross polarization process.

The most promising in-vivo application of silicon particles appears to gastrointestinal imaging, due to the existing usage of silicon within the food industry. The particles could be used for positive contrast imaging of the internal structure of the GI tract, and be surface functionalized to target specific sites of disease. Additionally, their in-vivo dynamics could be used to read out biophysical parameters such as pH, with for instance, a pH active surface polymer that causes them to agglomerate or disperse and change their (T_2^*). Investigations should span other clinical applications however, such as tracking drug-delivery, as the ultimate level of sensitivity of this technology is still unknown. At least two orders of magnitude in signal are achievable by increasing the nuclear polarization, and potentially another order of magnitude achievable with improved imaging techniques such as averaging, and reducing ambient noise. This would take the detectable concentration required to $< 10^2$ particles per voxel, which may open up applications in stem cell tracking and monitoring drug delivery, as well as many other applications not yet considered.

Over the time span of this thesis, dynamic nuclear polarization has moved from to a technique confined to low temperature physics and physical chemistry laboratories in universities, to a technology accessible to many researchers through the purchase of a commercial Hypersense polarizer from Oxford Instruments, and soon to be clinical researchers through the SpinLab polarizer manufactured by GE. These commercial polarizers have optimized the quality control and dissolution process, ensuring that the maximum amount of hyperpolarized sample is administered. It is important to note that the methods described in this thesis for ^{29}Si DNP in silicon particles are also achievable with these commercial polarizers.

References

[1] R. P. Feynman, J. Robbins, and F. J. Dyson, The pleasure of finding things out: The best short works of Richard P. Feynman (PerseusBooks, Cambridge, MA, 1999).

[2] C. B. Murray, C. R. Kagan, M. G. Bawendi Self-organization of CdSe nanocrystallites into three-dimensional quantum dot superlattices. Science, **270**, 1335-1338 (1995).

[3] H. W. Kroto, J. R. Heath, S. C. O'Brien, R. F. Curl, R. E. Smalley, C60: Buckminsterfullerene. Nature **318**, 162-163 (1995).

[4] W. Stober, A. Fink, E. Bohn Controlled growth of monodisperse silica spheres in the micron size range. J. Colloid. Interface Sci., **26**, 62-69 (1968).

[5] J. R. Heath, A Liquid-Solution-Phase Synthesis of Crystalline Silicon. Science **258**, 1131-1133 (1992).

[6] A. P. Alivisatos, Semiconductor clusters, nanocrystals, and quantum dots. Science **271**, 933 (1996).

[7] H. Dai, E.W. Wong, Y.Z. Lu, S. Fan, and C.M. Lieber, Synthesis and characterization of carbide nanorods. Nature **375**, 769-72 (1995).

[8] C. M. Lieber, A. M. Morales, P. E. Sheehan, E. W. Wong, P. Yang, One-dimensional nanostructures: Rational synthesis, novel properties and applications. Proceedings of the Robert A. Welch Foundation 40th Conference on Chemical Research: Chemistry on the Nanometer Scale, R. A. Welch Foundation, Houston 165-187 (1997).

[9] J. Hu, T.W. Odom, and C.M. Lieber, Chemistry and Physics in One Dimension: Synthesis and Properties of Nanowires and Nanotubes, Acc. Chem. Res. **32**, 435-445 (1999).

[10] T. Guo, P. Nikolaev, A. Thess, D. Colbert, R. Smalley, Catalytic growth of single-walled nanotubes by laser vaporization. Chem. Phys. Lett. **243**, 49-54 (1995).

[11] T. W. Ebbesen, P. M. Ajayan, Large-scale synthesis of carbon nanotubes. Nature **358**, 220-222 (1992).

[12] J. B. Jackson and N.J. Halas Surface-enhanced Raman scattering on tunable plasmonic nanoparticle substrates. Proc. Natl. Acad. Sci. USA **101**, 17930-17935 (2004).

[13] S. J. Oldenburg, R. D. Averitt, S.L. Westcott, and N. J. Halas, Nanoengineering of optical resonances. Chem. Phys. Lett. **288**, 243-247 (1998).

[14] M. A. Reed *et al.,* Observation of discrete electronic states in a zero-dimensional semiconductor nanostructure. Phys. Rev. Lett. **60**, 535-537 (1988).

[15] R. Langer, and J. Folkman, Polymers for the sustained release of proteins and other macromolecules. Nature **263**, 797-800 (1976).

[16] K. Kazunori *et al.,* Block copolymer micelles as vehicles for drug delivery. J. Control Release **24**, 119-132 (1993).

[17] D. C. Drummond, O. Meyer, K. Hong, D. B. Kirpotin and D.Papahadjopoulos, Optimizing Liposomes for Delivery of Chemotherapeutic Agents to Solid Tumors. Pharmacol. Rev. **51**, 691-744 (1999)

[18] H. Kataoka *et al.,* Spontaneous formation of polyion complex micelles with narrow distribution from antisense oligonucleotide and cationic block copolymer in physiological saline. Macromolecules **29**, 8556-8557 (1996).

[19] J.-W. Nah, L. Yu, S.-O. Han, C.-H. Ahn, S.W. Kim, Artery wall binding peptide-poly(ethylene glycol)-grafted-poly(l-lysine)-based gene delivery to artery wall cells. J. Control Release **78**, 273-284 (2002).

[20] M. Yokoyama *et al.,* Incorporation of water-insoluble anticancer drug into polymeric micelles and control of their particle size. J. Control Release **55**, 219-229 (1998).

[21] Y. Bae, *et al.,* Preparation and biological characterization of polymeric micelle drug carriers with intracellular pH-triggered drug release property: tumor permeability, controlled subcellular drug distribution, and enhanced in vivo antitumor efficacy. Bioconjug Chem. **16**, 122-130 (2005).

[22] F. J. Martin, Clinical pharmacology and antitumor efficacy of DOXIL (pegylated liposomal doxorubicin) in Medical Applications of Liposomes, (Elsevier Science BV, New York), 635-688 (1998).

[23] A. N. Lukyanov, and V. P. Torchilin, Micelles from lipid derivatives of water-soluble polymers as delivery systems for poorly soluble drugs. Adv. Drug Deliv. Rev. **56**, 1273-1289 (2004).

[24] J. C. Olivier, Drug transport to brain with targeted nanoparticles. NeuroRx. **2**, 108-119 (2005).

[25] D. J. Bharali *et al.,* Organically modified silica nanoparticles: a nonviral vector for in vivo gene delivery and expression in the brain. Proc. Natl. Acad. Sci. USA **102**, 11539-11544 (2005).

[26] C. J. Hu, S. Aryal and L. Zhang, Nanoparticle-assisted combination therapies for effective cancer treatment. Therapeutic Delivery **1**, 323-334 (2010).

[27] P. Decuzzi, *et al.,* Size and shape effects in the biodistribution of intravascularly injected particles. J. Control Release **141**, 320-327 (2010).

[28] Y. Geng, *et al.,* Shape effects of filaments versus spherical particles in flow and drug delivery Nature Nanotech. **2**, 249 - 255 (2007).

[29] G. Adriani, *et al.,* The preferential targeting of the diseased microvasculature by disk-like particles. Biomaterials **33**, 5504-5513 (2012).

[30] G. F. Paciotti *et al.,* Colloidal gold: A novel nanoparticle vector for tumor directed drug delivery. Drug Delivery **11**, 169-183 (2004).

[31] Y. Matsumura and H. Maeda A new concept for macromolecular therapeutics in cancer chemotherapy: mechanism of tumoritropic accumulation of proteins and the antitumor agent SMANCS. Cancer Res **46**, 6387-6392 (1986).

[32] R. K. Jain, Delivery of molecular medicine to solid tumors. Science **271**, 1079-1080 (1996).

[33] S. Kumaresh *et al.,* Biodegradable polymeric nanoparticles as drug delivery devices. J. Control Release **70**, 1-20 (2001).

[34] B. C. Tang et al, Biodegradable polymer nanoparticles that rapidly penetrate the human mucus barrier. Proc. Natl. Acad. Sci. USA **106**, 19268-19273 (2009).

[35] X. Sun et al Nano-graphene oxide for cellular imaging and drug delivery. Nano Research **1**, 203-212 (2008).

[36] Z. Liu *et al.,* Drug delivery with carbon nanotubes for in vivo cancer treatment. Cancer Res. **68**, 6652 (2008).

[37] J. Choi, *et al.,* Core-shell silica nanoparticles as fluorescent labels for nanomedicine. J. Biomedical Opt. **12**, 1-11 (2007).

[38] E. Tasciotti, *et al.,* Mesoporous silicon particles as a multistage delivery system for imaging and therapeutic applications. Nature Nanotech. **3**, 151 (2008).

[39] J. H. Park, *et al.,* Biodegradable luminescent porous silicon nanoparticles for in vivo applications. Nature Materials **8**, 331 (2009).

[40] N. Singh, *et al.,* Bioresponsive mesoporous silica nanoparticles for triggered drug release. J. Am. Chem. Soc. **133**, 19582-19585 (2011).

[41] Siemens 2010 Preclinical images of the year. www.siemens.com/preclinical M. Lin, *et al.,* Imaging the pancreatic B-cell. UT Southwestern Medical Center, Dallas, TX. USA. This image is reproduced with permission, copyright Siemens Healthcare (2010), all rights reserved.

[42] Li-Cor Biosciences - Applications for the Pearl Impulse Imager *http : //www.licor.com/bio/applications/pearl$_a$pplications/small$_a$nimal$_i$maging.jsp. This image is reproduced with permission, copyright Li-Cor Biosciences (2011), all rights reserved.*

[43] R. Smith-Bindman, et al., Radiation Dose Associated With Common Computed Tomography Examinations and the Associated Lifetime Attributable Risk of Cancer. Arch Intern Med. **169**2078-2086 (2009).

[44] F. Bloch, Nuclear Induction. Phys. Rev. **70**, 460-474 (1946).

[45] N. Bloembergen, E.M. Purcell, and R.V. Pound, Relaxation Effects in Nuclear Magnetic Resonance Absorption. Phys. Rev. **73**, 679 (1948).

[46] C. B. Seymour and C. Mothersill, Radiation-induced bystander effects - implications for cancer. Nature Reviews Cancer **4**, 158-164 (2004).

[47] M. de Jong *et al.,* Somatostatin receptor-targeted radionuclide therapy of tumors: preclinical and clinical findings. Semin Nucl Med. **32**, 133-140 (2002).

[48] R. Fazel *et al.,* Exposure to Low-Dose Ionizing Radiation from Medical Imaging Procedures. N Engl J Med **361**, 849-857 (2009).

[49] P.C. Lauterbur, Image formation by induced local interactions: Examples employing nuclear magnetic resonance. Nature **242**, 190-191 (1973).

[50] T. R. Brown, B. M. Kincaid, and K. Ugurbil, NMR chemical shift imaging in three dimensions. Proc. Natl. Acad. Sci. USA **79**, 3523-3526 (1982).

[51] The FDA Safety Information and Adverse Event Reporting Program Safety Information. *www.fda.gov/Safety/MedWatch/SafetyInformation/ucm*190426*.htm* accessed August 13, 2012

[52] M. S. Albert *et al.,* Biological magnetic resonance imaging using laser-polarized 129Xe. Nature **370**, 199-201 (1994).

[53] S. Fain *et al.,* Functional lung imaging using hyperpolarized gas MRI. J. Mag. Res. **25**, 910-923 (2007).

[54] S. E. Day *et al.,* Detecting tumor response to treatment using hyperpolarized 13C magnetic resonance imaging and spectroscopy. Nature Med. **13**, 1382-1387 (2007).

[55] F. A. Gallagher *et al.,* Magnetic resonance imaging of pH in vivo using hyperpolarized 13C-labelled bicarbonate. Nature **453**, 940-943 (2008).

[56] K. R. Keshari *et al.,* Hyperpolarized 13C dehydroascorbate as an endogenous redox sensor for in vivo metabolic imaging. Proc. Natl. Acad. Sci. USA **108**, 18606-18611 (2011).

[57] N. M. Zacharias *et al.,* Real-time molecular imaging of tricarboxylic acid cycle metabolism in vivo by hyperpolarized 1-(13)C diethyl succinate. J. Am. Chem. Soc. **134**, 934-943 (2011).

[58] T. G. Walker and W. Happer, Spin-exchange optical pumping of noble-gas nuclei. Rev. Mod. Phys. **69**, 629-642 (1997).

[59] D. A. Hall, D. Maus, G. J. Gerfen, and R. G. Griffin, Polarization-enhanced NMR spectroscopy of biomolecules in frozen solution. Science, **276**, 930-932 (1997).

[60] J. H. Ardenkjaer-Larsen *et al.,* Increase in signal-to-noise ratio of >10,000 times in liquid-state NMR. Proc. Natl. Acad. Sci. USA **100**, 10158-10163 (2003).

[61] K. Golman *et al.,* Molecular imaging with endogenous substances. Proc. Natl. Acad. Sci. USA **100**, 10435-10439 (2003).

[62] M. Lingwood *et al.,* Hyperpolarized water as an MRI contrast agent: feasibility of in vivo imaging in a rat model. Radiology. In press, (2012).

[63] D.M. Wilson *et al.,* Multi-compound polarization by DNP allows simultaneous assessment of multiple enzymatic activities in vivo. J. Mag. Res. **205**, 141-147 (2010).

[64] D.M. Wilston *et al.,* Generation of hyperpolarized substrates by secondary labeling with [1,1-13C] acetic anhydride. Proc. Natl. Acad. Sci. USA **106**, 5503-5507 (2009).

[65] E. Y. Chekmenev *et al.,* PASADENA hyperpolarization of succinic acid for MRI and NMR spectroscopy. J. Am. Chem. Soc. **1304212**-4213 (2008).

[66] L. Schroder, T. J. Lowery, C. Hilty, D. E. Wemmer and A. Pines, Molecular imaging using a targeted magnetic resonance hyperpolarized biosensor. Science **314**, 446-449 (2006).

[67] J. Wolber *et al.,* Spin-lattice relaxation of laser-polarized xenon in human blood. Proc. Natl. Acad. Sci. USA **96**, 3664-3669 (1999).

[68] H. E. Moller *et al.,* Measurements of Hyperpolarized gas properties in the lung. Part III: 3He T1. Magn. Res. Med. **45**, 421-430 (2001).

[69] K.F. Stupic, N.D. Elkins, G. E. Pavlovskaya, J. E. Repine, and T. Meersmann, Effects of pulmonary inhalation on hyperpolarized krypton-83 magnetic resonance T1 relaxation. Phys. Med. Biol. **56**3731-3748 (2011).

[70] P. Bhattacharya *et al.,* Hyperpolarized 15N magnetic resonance. Proc. Intl. Soc. Mag. Reson. Med. **17**, 2451 (2009).

[71] C. Alric *et al.,* Gadolinium chelate coated gold nanoparticles as contrast agents for both x-ray computed tomography and magnetic resonance imaging. J. Am. Chem. Soc. **130**5908-5915 (2008).

[72] R. Popovtzer, *et al.*, Targeted Gold Nanoparticles Enable Molecular CT Imaging of Cancer. Nano Lett. **8**, 4593-4596 (2008).

[73] D. Kim, Y. Jeong and J. A. Sangyong, Drug-loaded aptamer-gold nanoparticle bioconjugate for combined CT imaging and therapy of prostate cancer. ACS Nano **4**, 3689-3696 (2010).

[74] D. Kim *et al.*, Antibiofouling polymer-coated gold nanoparticles as a contrast agent for in vivo x-ray computed tomography imaging. J. Am. Chem. Soc., **129**, 7661-7665 (2007).

[75] A. C. Silva *et al.*, Application of hyperthermia induced by superparamagnetic iron oxide nanoparticles in glioma treatment. Int J Nanomedicine. **6**, 591-603 (2011).

[76] Q. A. Pankhurst, J. Connolly, S. K. Jones and J. Dobson Applications of magnetic nanoparticles in biomedicine. J. Phys. D: Appl. Phys. **36**,167 (2003).

[77] Y. M. Kwon *et al.*, Dose-dependent cytotoxicity of clinically relevant cobalt nanoparticles and ions on macrophages in vitro. Biomed. Mater. **4**, 025018 (2009).

[78] M. Srinivas *et al.*, 19F MRI for quantitative in vivo cell tracking. Trends Biotech. **28**363-370 (2010).

[79] R. G. Shulman, B. J. Wyluda, Nuclear Magnetic Resonance of Si29 in n- and p-Type Silicon. Phys. Rev. **103**, 1127-1129 (1956).

[80] N. T. Bagraev, L. S. Vlasenko, and R. A. Zhitnikov, Optical orientation of Si29 nuclei in compensated silicon. Sov. Phys. JETP Lett. **23**, 586 (1976).

[81] G. Feher, Nuclear polarization via hot conduction electrons. Phys. Rev. Lett. **3**, 135 (1959).

[82] D. Jerome, C. Ryter, and J. M. Winter, Physics,**2**, 81 (1965).

[83] G. Lampel, Nuclear dynamic polarization by optical electronic saturation and optical pumping in semiconductors. Phys. Rev. Lett. **20**, 491 (1968).

[84] A. Abragam, J. Combrisson, and I. Solomon, Compt. Rend. Acad. Sci. 247, 2337 (1958).

[85] V. Dyakonov and G. Denninger, Overhauser-shift measurements on Si:P near the metal-insulator transition. Phys. Rev. B **46**, 5008 (1992)

[86] A. Henstra, P. Dirksen, J. Schmidt, and W. Wenckebach, Nuclear spin orientation via electron spin locking (NOVEL). J. Magn. Reson. **77**, 389 (1988).

[87] A. B. Sproul and M. A. Green, Improved value for the silicon intrinsic carrier concentration from 275 to 375 K. Journal of Applied Physics **70**,846-854 (1991).

[88] W. R. Thurber, R. L. Mattis, Y. M. Liu, and J. J. Filliben, The Relationship Between Resistivity and Dopant Density for Phosphorus and Boron-Doped Silicon. NBS Special Publication 400-64, National Bureau of Standards, Washington, DC (1981).

[89] E. C. Reynhardt, G. L. High and J. A. van Wyk, Temperature dependence of spin-spin and spin-lattice relaxation times of paramagnetic nitrogen defects in diamond. J. Chem. Phys. **109**, 8471 (1998).

[90] M.J.R. Hoch, E.C. Reynhardt, Nuclear spin-lattice relaxation of dilute spins in semiconducting diamond. Phys. Rev. B **37**, 9222 (1988).

[91] E.C. Reynhardt, C.J. Terblanche, 13C relaxation in natural diamond. Chem. Phys. Lett. **269**, 464 (1997).

[92] C. J. Terblanche, E. C. Reynhardt, S. A. Rakitianskia, and J. A. Van Wyk, 13C spin-lattice relaxation in natural diamond: Zeeman relaxation in fields of 500 to 5000 G at 300 K due to fixed paramagnetic nitrogen defects.. Sol. State Nucl. Magn. Reson. **19**, 107 (2001).

[93] P. J. Caplan, E. H. Poindexter, B. E. Deal, and R. R. Razouk, ESR centers, interface states, and oxide fixed charge in thermally oxidized silicon wafers . J. Appl. Phys. **50**, 5847 (1979)

[94] A. Abragam, *Principles of Nuclear Magnetism*(Oxford University Press, 1983)

[95] E.L. Hahn, Spin Echoes. Phys. Rev. 80, 580-594 (1950).

[96] H.Y. Carr, E.M. Purcell, Effects of diffusion on free precession in nuclear magnetic resonance experiments. Phys. Rev. **94**, 630 (1954).

[97] S. Meiboom, D. Gill, Modified spin-echo method for measuring nuclear relaxation times. Rev. Sci. Instrum. **29**, 6881 (1958).

[98] D. Li *et al.*, Intrinsic origin of spin echoes in dipolar solids generated by strong π pulses. Phys. Rev. B **77**, 214306 (2008).

[99] N. Bloembergen, On the interaction of nuclear spins in a crystalline lattice. Physica **15**, 386 (1949).

[100] G. R. Khutsishvili, Spin diffusion. Sov. Phys. Usp. **8**, 743 (1966).

[101] N. Bloembergen, Nuclear magnetic relaxation in semiconductors. Physica **20**, 1130 (1954).

[102] A. Abragam and M. Goldman *Nuclear Magnetism: Order and Disorder*(Oxford University Press, 1982)

[103] D. S. Wollan, Dynamic nuclear polarization with an inhomogeneously broadened ESR line: Theory. Phys. Rev. B, **13**, 3671 (1976).

[104] A. W. Overhauser, Polarization of nuclei in metals. Phys. Rev. **92**, 411-415 (1953).

[105] T. R. Carver and C. P. Slichter, Experimental verification of the overhauser nuclear polarization effect. Phys. Rev. **102**, 975-980 (1956).

[106] H. Hayashi, T. Itahashi, K. M. Itoh, L. S. Vlasenko, and M. P. Vlasenko, Dynamic nuclear polarization of 29Si nuclei in isotopically controlled phosphorus doped silicon. Phys. Rev. B **80**, 045201 (2009).

[107] A. E. Dementyev, D. G. Cory, and C. Ramanathan, High-field Overhauser dynamic nuclear polarization in silicon below the metal-insulator transition J. Chem. Phys. **134**, 154511 (2011).

[108] D. R. McCamey, J. van Tol, G. W. Morley, and C. Boehme, Fast nuclear spin hyperpolarization of phosphorus in silicon. Phys. Rev. Lett. **102**, 027601 (2009).

[109] T. J. Schmugge and C. D. Jeffries, High dynamic polarization of protons. Phys. Rev. **138**, A1785 (1965).

[110] G. M. Van den Heuvel, T. J. B. Swanenburg and N. J. Poulis, Proton spin-lattice relaxation in LaMN with Nd. Physica **56**, 356 (1971).

[111] W.B. Mims, K.Nassau and J.D. McGee Spectral diffusion in electron resonance lines. Phys. Rev. **12**, 2059-2069 (1961).

[112] I. Solomon, *Magnetic and Electric Resonance and Relaxation*ed. J Schmidt (Amsterdam:North-Holland, 1963).

[113] B.N. Provotorov, Magnetic resonance saturation in crystals. Sov. Phys. JETP **14**, 1126-1131 (1962).

[114] V.A. Atsarkin, Dynamic nuclear-polarization in dielectric solids. Uspekhi. Fizicheskikh. Nauk. **126**, 3-39 (1978).

[115] M. Borghini, Spin-temperature model of nuclear dynamic polarization using free radicals. Phys. Rev. Lett. **20**, 419 (1968)

[116] X. Gao, Y. Cui, R. M. Levenson, L. W. Chung, S. Nie, *In-Vivo*cancer targeting and imaging with semiconductor quantum dots. Nat. Biotechnol., *22*, 969-976 (2004).

[117] W. Liu *et al.*, Compact biocompatible quantum dots functionalized for cellular Imaging. J Am Chem Soc. 130, 1274-1284 (2008).

[118] L. R. Hirsch, *et al.*, Nanoshell-mediated near-infrared thermal therapy of tumors under magnetic resonance guidance. Proc. Nat. Acad. Sci.**100**, 13549-13554 (2003).

[119] R. Weissleder, *et al.*, Ultrasmall superparamagnetic iron oxide: Characterization of a new class of contrast agents for MR imaging. Radiology **175**, 489-493 (1990).

[120] T. Atanasijevic, M. Shusteff, P. Fam, and A. Jasanoff, Calcium-sensitive MRI contrast agents based on superparamagnetic iron oxide nanoparticles and calmodulin. Proc. Natl. Acad. Sci. USA **103**, 14707-14712 (2006).

[121] M. E. Akerman, W. C. W. Chan, P. Laakkonen, S. N. Bhatia, E. Ruoslahti, Nanocrystal targeting *In-vivo*. Proc. Natl. Acad. Sci. USA **99**, 12617-12621 (2002).

[122] R. Weissleder, K. Kelly, E. Y. Sun, T. Shtatland, and L. Josephson, Cell-specific targeting of nanoparticles by multivalent attachment of small molecules. Nat. Biotechnol. **23**, 1418-1423 (2005).

[123] D. Högemann, V. Ntziachristos, L. Josephson, R. Weissleder, High throughput magnetic resonance imaging for evaluating targeted nanoparticle probes. Bioconjugate Chem. **13**, 116-121 (2002).

[124] D. Simberg, *et al.*, Biomimetic amplification of nanoparticle homing to tumors. Proc. Natl. Acad. Sci. USA **104**, 932-936 (2004).

[125] J. C. Leawoods, *et al.*, Hyperpolarized He-3 gas production and MR imaging of the lung. Concepts Magn. Reson.**13**, 277-293 (2001).

[126] S. Patz *et al.*, Human pulmonary imaging and spectroscopy with hyperpolarized Xe-129 at 0.2 T. Acad. Radiol.**15**, 713-727 (2008).

[127] T. D. Ladd, D. Maryenko, Y. Yamamoto, E. Abe, K . M. Itoh, Coherence time of decoupled nuclear spins in silicon. Phys. Rev. B **71**, 014401 (2005).

[128] A. E. Dementyev,D. G. Cory, and C. Ramanathan, Dynamic nuclear polarization in silicon microparticles. Phys. Rev. Lett. **100**, 127601 (2008).

[129] C. Brown, Particle size distribution by centrifugal sedimentation. J. Phys. Chem. **48**, 246-258 (1944).

[130] H. Xu, F. Yan, E. Monson, and R. Kopelman, Room-temperature preparation and characterization of poly (ethylene glycol)-coated silica nanoparticles for biomedical applications. J. Biomed. Mater. Res. **66A**, 870-879 (2003).

[131] W. Jiang, B. Kim, J. T. Rutka, and W. C. W. Chan, Nanoparticle-mediated cellular response is size-dependent. Nature Nanotech. **3**, 145-150 (2008).

[132] Y. Nishi, Study of silicon-silicon dioxide structure by electron spin resonance I. Jpn. J Appl. Phys. **10**, 52-62 (1971).

[133] T. D. Shen, *et al.*, The Structure and Property Characteristics of Amorphous/Nanocrystalline Silicon Produced by Ball Milling. J. Mat. Research **10**, 139-148 (2005).

[134] L. Zhao, *et al.*, Gradient Echo Imaging Considerations for Hyperpolarized 129Xe MR. J. Magn. Reson. Ser. B **113**, 179-183 (1996).

[135] G. Ledoux, J. Gong, F. Huisken, O. Guillois, and C. Reynaud, Photoluminescence of size-separated silicon nanocrystals: Confirmation of quantum confinement. Appl. Phys. Lett. **80**, 4834 (2002).

[136] B. Delley and E. F. Steigmeier, Size dependence of band gaps in silicon nanostructures. Appl. Phys. Lett. **67**, 2370 (1995).

[137] T. Y. Kim, *et al.*, Quantum confinement effect of silicon nanocrystals in situ grown in silicon nitride films. Appl. Phys. Lett. **85**, 5355 (2004).

[138] J. Aptekar *et al.*, Silicon nanoparticles as hyperpolarized magnetic resonance imaging agents. ACS Nano. **3**, 4003-4008 (2009).

[139] D. Pines, J. Bardeen, and C. P. Slichter, Nuclear polarization and impurity-state spin relaxation processes in silicon. Phys. Rev. **106**, 489 (1957).

[140] A. Yang, *et al.*, Simultaneous subsecond hyperpolarization of the nuclear and electron spins of phosphorus in silicon by optical pumping of exciton transitions. Phys. Rev. Lett. **102**, 257401 (2009).

[141] T. D. Ladd, D. Maryenko, Y. Yamamoto, E. Abe, and K. M. Itoh, Coherence time of decoupled nuclear spins in silicon Phys. Rev. B **71**, 014401 (2005).

[142] B. E. Kane, A silicon-based nuclear spin quantum computer. Nature **393**, 133 (1998).

[143] T. D. Ladd, J. R. Goldman, F. Yamaguchi, Y. Yamamoto, E. Abe, and K. M. Itoh, An all silicon quantum computer. Phys. Rev. Lett. **89**, 017901 (2002).

[144] K. Itoh, An All-Silicon Linear Chain NMR Quantum Computer. Sol. Stat. Comm. **133**, 747 (2005).

[145] A. S. Verhulst, I. G. Rau, Y. Yamamoto, and K. M. Itoh, Optical pumping of 29Si nuclear spins in bulk silicon at high magnetic field and liquid helium temperature. Phys. Rev. B **71**, 235206 (2005).

[146] N. T. Bagraev, E. P. Bochkarev, L. S. Vlasenko, V. P. Grishin, and Yu. A. Karpov, Nuclear relaxation due to optical pumping of silicon doped with arsenic and bismuth. Sov. Phys. Solid State **21**, 305 (1979).

[147] N. T. Bagraev, L. S. Vlasenko, and R. A. Zhitnikov, Nuclear spin-lattice relaxation in doped silicon under optical pumping conditions. Sov. Phys. Solid State **24**, 1972 (1982).

[148] N. T. Bagraev, L. S. Vlasenko, and R. A. Zhitnikov, Nuclear relaxation in silicon in weak magnetic fields. Sov. Phys. JETP **49**, 278 (1979).

[149] N. T. Bagraev and L. S. Vlasenko, Optical polarization of lattice nuclei in strongly deformed silicon. Sov. Phys. Solid State **24**, 1974 (1982).

[150] S. Y. Paik, S. Y. Lee, W. J. Baker, D. R. McCamey, and C. Boehme, T1- and T2-spin relaxation time limitations of phosphorous donor electrons near crystalline silicon to silicon dioxide interface defects. Phys. Rev. B **81**, 075214 (2010).

[151] M. J. Duijvestijn, R. A. Wind, J. Smidt, A quantitative investigation of the dynamic nuclear polarization effect by fixed paramagnetic centra of abundant and rare spins in solids at room temperature. Physica B+C. **138**, 147 (1986).

[152] C. Ramanathan, Dynamic nuclear polarization and spin diffusion in nonconducting solids. Appl. Magn. Reson. **34**, 409 (2008).

[153] E. Shabanova, K. Schaumburg, and J. P. F. Sellschop, 13C NMR investigations of spin-lattice relaxation in 99% 13C-enriched diamonds. J. Magn. Reson. **130**, 8 (1998).

[154] A. M. Panich, A. I. Shames, H. M. Vieth, E. Osawa, M. Takahashi, and A. Ya. Vul', Nuclear magnetic resonance study of ultrananocrystalline diamonds. Eur. Phys. J. B **52**, 397 (2006).

[155] S. F. J. Cox, V. Bouffard, and M. Goldman, The coupling of two nuclear Zeeman reservoirs by the electronic spin-spin reservoir. J. Phys. C: Solid State Phys. **6**, 100 (1973).

[156] M. Goldman, S. F. J. Cox, and V. Bouffard, Coupling between nuclear Zeeman and electronic spin-spin interactions in dielectric solids. J. Phys. C: Solid State Phys. **7**, 2940 (1974).

[157] W. E. Blumberg, Nuclear spin-lattice Relaxation caused by paramagnetic impurities. Phys. Rev. **119**, 79 (1960).

[158] I. J. Lowe and D. Tse, Nuclear spin-lattice relaxation via paramagnetic centers. Phys. Rev. **166**, 279 (1968).

[159] G. M. van den Heuvel, C. T. C. Heyning, T. J. B. Swanenburg, and N. J. Poulis, Experimental evidence of the influence of electron dipole dipole interaction on nuclear spin lattice relaxation. Phys. Lett. **27A**, 38 (1968).

[160] W. T. Wenckeback, G. M. va der Heuvel, H. Hoogstraate, T. J. B. Swanenburg, and N. J. Poulis, Experimental proof of the strong coupling between the electron spin-spin reservoir and a nuclear spin system in dilute paramagnetic crystals. Phys. Rev. Lett. **22**, 581 (1969).

[161] S. Tanaka and H.Y. Fan, Impurity conduction in p-type silicon at microwave frequencies. Phys. Rev. **132**, 1516 (1963).

[162] Y. Kisselev, The modulation effect on the dynamic polarization of nuclear spins. Nucl. Instrum. Methods Phys. Res. (1995).

[163] Continuous wave ESR measurements were taken at 4 K at a frequency of 9.3838 GHz (Bruker 300 E) with an a.c. field amplitude 0.05 mT and modulation frequency of 100 kHz swept from 286 mT to 386 mT over a period of 120 s.

[164] The surface defect density was estimated by comparing the relative size of the ESR spectrum to that from a bulk Si:P sample co-located in the cavity.

[165] J. Braet and A. Stesmans, Physica B **126**, 463-464 (1984).

[166] W. L. Wilson, P. F. Szajowski, L. E. Brus, Quantum confinement in size-selected, surface-oxidized silicon nanocrystals. Science **262**, 1242 (1993).

[167] A. G. Cullis, L.T. Canham, P. D. J. Calcott, The structural and luminescence properties of porous silicon. J. Appl. Phys. **82**, 909 (1997).

[168] B. Z. Tian, *et al.*, Coaxial silicon nanowires as solar cells and nanoelectronic power sources. Nature **449**, 885-888 (2007).

[169] S. Pillai, K. R. Catchpole, T. Trupke, and M. A. Green, Surface plasmon enhanced silicon solar cells. J. Appl. Phys. **101**, 093105 (2007).

[170] B. Godin, *et al.* Tailoring the degradation kinetics of mesoporous silicon structures through PEGylation. J Biomed Mat Res A. **94**, 1236-43 (2010).

[171] N. Singh, *et al.* Bioresponsive mesoporous silica nanoparticles for triggered drug release. J. Am. Chem. Soc. **133**, 19582-19585 (2011).

[172] A. P. Mann, *et al.* E-selectin-targeted porous silicon particle for nanoparticle delivery to the bone marrow. Adv. Mater. **23**, 278-282 (2011).

[173] E. Tasciotti *et al.* Near-infrared imaging method for the in vivo assessment of the biodistribution of nanoporous silicon particles. Mol. Imaging **10**, 56-68 (2011).

[174] L. Gu, *et al.* Magnetic luminescent porous silicon microparticles for localized delivery of molecular drug payloads. Small **6**, 2546-2552 (2010).

[175] J. S. Ananta, *et al.* Geometrical confinement of gadolinium-based contrast agents in nanoporous particles enhances T1 contrast. Nature Nanotech. **5**, 815-821 (2010).

[176] C.M. Hessel, E.J. Henderson, J.G.C. Veinot, Hydrogen silsesquioxane: A molecular precursor for nanocrystalline Si-SiO2 composites and freestanding hydride surface terminated silicon nanoparticles. Chem. Mat., **18**, 6139-6146 (2006).

[177] R. D. Tilley, *et al.*, Micro-emulsion synthesis of monodisperse surface stabilized silicon nanocrystals Chem. Comm. 1833-1835 (2005).

[178] J. D. Holmes, *et al.*, Highly luminescent silicon nanocrystals with discrete optical transitions. J. Am. Chem. Soc. **123**, 37-43 (2001).

[179] H. Kim, *et al.*, J. Angewandte Chemie-International Edition **49**, 2146 (2010).

[180] R. A. Bley, and S. M. Kauzlarich, Low-temperature solution phase route for the synthesis of silicon nanoclusters. J. Am. Chem. Soc. **118**, 12461 (1996).

[181] D. Neiner, H. W. Chiu, S. M. Kauzlarich, Low-temperature solution route to macroscopic amounts of hydrogen terminated silicon nanoparticles. J. Am. Chem. Soc. **128**, 11016 (2006).

[182] R. A. Wind, M. J. Duijvestijn, C. van der Lugt, A. Manenschijn, J. Vriend, Applications of dynamic nuclear polarization in 13C NMR in solids. Prog. NMR. Spec., **17**, 33-67 (1985).

[183] M. Lelli *et al.*, Fast characterization of functionalized silica materials by silicon-29 surface-enhanced NMR spectroscopy using dynamic nuclear polarization. J. Am. Chem. Soc., **133**, 2104-2107 (2011).

[184] P. van der Wel *et al.*, Dynamic nuclear polarization of amyloidogenic peptide nanocrystals: GNNQQNY, a core segment of the yeast prion protein Sup35p J. Am. Chem. Soc. **128** , 10840-10846 (2006).

[185] B.D. Armstrong *et al.*, Site-specific hydration dynamics in the nonpolar core of a molten globule by dynamic nuclear polarization of water. J. Am. Chem. Soc. **133** , 5987-5995 (2011).

[186] V.S. Bajaj *et al.*, Proc. Nat. Acad. Sci. **106**, 9244 - 9249 (2009).

[187] L. B. Casabianca, *et al.*, Factors affecting DNP NMR in polycrystalline diamond samples. J. Phys. Chem. C **115**, 19041 (2011).

[188] J. Zou, *et al.*, Solution synthesis of ultrastable luminescent siloxane-coated silicon nanoparticles. Nano Letters **4**, 1181 (2004).

[189] P. A. Thomas *et al.*, Electron spin resonance of ultrahigh vacuum evaporated amorphous silicon: In situ and ex situ studies. Phys. Rev. B **18**, 3059 (1978).

[190] H. Lock, R.A. Wind and G.E. Maciel, 29Si Dynamic nuclear polarization of dehydrogenated amorphous silicon. Solid State Comm. **64**, 1 41-44 (1987).

[191] K. Hu, V. Bajaj, M. Rosay, and R.G. Griffin, Dynamic nuclear polarization with biradicals. J. Chem. Phys. **126**, 044512 (2007).

[192] C. Song *et al.*, High-frequency dynamic nuclear polarization using biradicals: A multifrequency EPR lineshape analysis. J. Am. Chem. Soc. **128**, 11385-11390 (2006).

[193] P. Mieville *et al.*, Scavenging free radicals to preserve enhancement and extend relaxation times in NMR using dynamic nuclear polarization. Angew. Chem. **122**, 6318-6321 (2010).

[194] F. Kurdzesau *et al.*, Dynamic nuclear polarization of small labelled molecules in frozen water-alcohol solutions. J. Phys. D: Appl. Phys. **41**, 155506 (2008).

[195] E.R. McCarney, B.D. Armstrong, M.D. Lingwood, and S. Han, Dynamic nuclear polarization enhanced nuclear magnetic resonance and electron spin resonance studies of hydration and local water dynamics in micelle and vesicle assemblies. Proc. Nat. Acad. Sci. **104**, 1754-1759 (2007).

[196] A. M. Leach, P. Miller, E. Telfeyan, and D.B. Whitt, (General Electric), USA US2009263325A1, (2009).

[197] H. C. Dorn, T. E. Glass, R. Gitti, and K. H. Tsai, Transfer of 1 H and 13 C dynamic nuclear polarization from immobilized nitroxide radicals to flowing liquids. Appl. Magn. Res. **2**, 9-27 (1991).

[198] E. McCarney, and S. Han, Spin-labeled gel for the production of radical-free dynamic nuclear polarization enhanced molecules for NMR spectroscopy and imaging. J. Magn. Res. **190**, 307-315 (2008).

[199] D. Raftery *et al.*,Spin-polarized xenon-129 NMR study of a polymer surface. J. Phys. Chem. **97**, 1649-1655 (1993).

[200] L. Goehring, and C.J. Michal, Nuclear spin polarization transfer across an organic-semiconductor interface. Chem. Phys. **119**, 10325-10328 (2003).

[201] A. Goto, T. Shimizu, K. Hashi, and S. Ohki, Appl. Phys. A Surface-sensitive NMR in optically pumped semiconductors. Appl. Phys. A **93**, 533-536 (2008).

[202] R. Tycko, Optical pumping in indium phosphide: P-31 NMR measurements and potential for signal enhancement in biological solid state NMR. Solid State Nucl. Magn. Reson. **11**, 1 (1998).

[203] C. Bowers *et al.*, Cross polarization from laser-polarized solid xenon to (Co2)-C-13 by low-field thermal mixing. Chem. Phys. Lett. **205**, 168-170 (1993).

[204] E. Erb, J. L. Motchane, and J. Uebersfeld Effect of nuclear polarization in liquids and gas adsorbed on charcoal. Compt. Rend.**243** 2121-2123 (1958)

[205] J.W. Ager *et al.*, High-Purity, Isotopically enriched bulk silicon semiconductor devices, materials, and processing. J. Electrochem. Soc. **152**, 448-451 (2005).

[206] H. Cho *et al.*, Low temperature probe for dynamic nuclear polarization and multiple-pulse solid-state NMR. J. Magn. Res. **187**, 242-250 (2007).

[207] The narrow ($\sim$ 500 Hz) peak in the otherwise broad ($\sim$ 2 kHz) ^{29}Si spectrum emerges only for times > 600 s. This peak corresponds to ^{29}Si nuclei located in crystalline sections of the SiNP that are polarized by nuclear spin diffusion from ^{29}Si nuclei (that make up the broad line) located near the polarizing electrons.

[208] P.J. Caplan, J. N. Helbert, B.E. Wagner, and E.H. Poindexter, Paramagnetic defects in silicon/silicon dioxide systems. Surf. Sci. **54**, 33-42 (1976).

[209] The surface defect density was estimated by comparing the relative size of the ESR spectrum to that from a bulk Si:P sample co-located in the cavity.

[210] S. Clough *et al.*, The independence of methyl group rotation and proton spin symmetry in crystals . J. Phys. C: Solid State Phys. **15**, 2495-2508 (1982).

[211] J. Ardenkjaer-Larsen, S. Macholl, and H. Johannesson, Dynamic nuclear polarization with trityls at 1.2 K. Appl. Magn. Res. **34**, 509-522 (2008).

[212] A. Lesage *et al.*, Surface enhanced NMR spectroscopy by dynamic nuclear polarization. J. Am. Chem. Soc. **132**, 15459-15461 (2010).

[213] A.I. Shames *et al.*, Defects and impurities in nanodiamonds: EPR, NMR and TEM study. J. Phys. Chem. Solids **63**, 1993-2001 (2002).

[214] C. Tu, *et al.* PET imaging and biodistribution of silicon quantum dots in mice. ACS Med. Chem. Lett. **2**, 285-288 (2011).

[215] R. W. Mair, *et al.* 3He lung imaging in an open access, very-low-field human magnetic resonance imaging system. Mag. Res. Med. **53**, 745-749 (2005).

[216] L. S. Bouchard, *et al.* Picomolar sensitivity MRI and photoacoustic imaging of cobalt nanoparticles Proc. Natl. Acad. Sci. USA **106**, 4085-4089 (2009).

[217] E. T. Ahrens, R. Flores, H. Xu, and P. A. Morel, In vivo imaging platform for tracking immunotherapeutic cells. Nat. Biotech. **23**, 983 - 987 (2005).

[218] H. W. Umschaden, *et al.* Small-Bowel Disease: Comparison of MR Enteroclysis Images with Conventional Enteroclysis and Surgical Findings. Radiology, **215**, 717-725 (2000).

[219] R. Jugdaohsingh, *et al.* Dietary silicon intake is positively associated with bone mineral density in men and premenopausal women of the Framingham Offspring cohort. J. Bone Miner. Res., **19**, 297-307 (2004).

[220] L. T. Canham, Nanoscale semiconducting silicon as a nutritional food additive. Nanotechnology, **18**, 185704 (2007).

[221] N. T. Bagraev, L. S. Vlasenko, and R. A. Zhitnikov, Optical orientation of 29Si nuclei in n-type silicon and its dependence on the pumping light intensity. Sov. Phys. JETP **44**, 500 (1976).

[222] N. T. Bagraev, L. S. Vlasenko, and R. A. Zhitnikov, Dynamic polarization and magnetic resonance of nuclear moments in optically pumped silicon. Sov. Phys. Solid State **19**, 1467 (1977).

[223] N. T. Bagraev and L. S. Vlasenko, Spectral distribution of polarization of nuclei in impurity absorption of light in silicon. Sov. Phys. JETP Lett. **28**, 488 (1978).

[224] U.S. Food and Drug Administration, Food additives permitted for direct addition to food for human consumption - anticaking agents 21CFR172.480 (2011).

[225] A. S. Thakor, *et al.* The fate and toxicity of raman-active silica-gold nanoparticles in mice. Sci. Transl. Med. **3**, 79ra33 (2011).

[226] Gerion, D., *et al.* Synthesis and Properties of Biocompatible Water-Soluble Silica-Coated CdSe/ZnS Semiconductor Quantum Dots. J. Phys. Chem. B, **105**, 8861-8871 (2001).

[227] Selvan, S. T., Patra, P. K., Ang, C. Y., and Ying, J. Y. Synthesis of silica-coated semiconductor and magnetic quantum dots and their use in the imaging of live cells. Angew. Chem., Int. Ed., **46**, 2448-2452 (2007).

[228] I. M. Krieger and F. M. O'Neill, Diffraction of light by arrays of colloidal spheres. J. Am. Chem. Soc. **90**, 3114-3120 (1968).

[229] D. E. Aspnes, Optical functions of intrinsic Si: Table of refractive index, extinction coefficient and absorption coefficient vs energy (0 to 400 eV) *Properties of Silicon, EMIS Datareviews Series No. 4*London, Institution of Electrical Engineers, (1988).

[230] E. Fukushima and S. B. W. Roeder, *Experimental Pulse NMR*(Westview Press, 1981)

[231] S Chung et al. Biological sensing with magnetic nanoparticles using Brownian relaxation J. Appl. Phys. **97**, 10R101 (2005).

[232] J Langea et al., Magnetorelaxometry - a new binding specific detection method based on magnetic nanoparticles. J. Magn. Magn. Mater. **252**, 381-383 (2002).

[233] J. P. Yesinowski, High-resolution NMR spectroscopy of solids and surface-adsorbed species in colloidal suspension: phosphorus-31 NMR spectra of hydroxyapatite and diphosphonates. J. Am. Chem. Soc. **103**, 6266 (1981).

[234] V. Lebret *et al.*, Surface functionalization of two-photon dye-doped mesoporous silica nanoparticles with folic acid. J.Sol-Gel Science and Technology **48**, 32-39 (2008).

[235] K. Kelly *et al.*, Detection of Early Prostate Cancer Using a Hepsin-Targeted Imaging Agent. Cancer Res. **68**, 2286-2291(2008).

[236] M. Ferrari, Cancer nanotechnology: Opportunities and challenges. Nat. Rev. Cancer **5**, 161-171 (2005).

[237] J Nam *et al.*, Nanoparticle-Based Bio-Bar Codes for the Ultrasensitive Detection of Proteins. Science **301**, 1884-1886 (2003).

[238] T Jøssang *et al.*, Photon correlation spectroscopy of human IgG. Protein Chem. **7**, 165-171 (1988).

[239] E. Anglin *et al.,* Porous silicon in drug delivery devices and materials. Adv. Drug Deliv. Rev. **60**, 1266-1277 (2008).

[240] A. Aqil *et al.,* Magnetic nanoparticles coated by temperature responsive copolymers for hyperthermia. J. Mat. Chem. **18**, 3352-3360 (2008).

A

Design and construction of the DNP-NMR system

A.1 Introduction

Two NMR/DNP setups were built by the author as part of the thesis. One setup was located in the Marcus Lab at Harvard University, and the other in the Enhanced MR Lab at Huntington Medical Research Institutes in Pasadena, CA and later moved to the Small Animal Imaging Facility at MD Anderson Cancer Center in Houston, TX. The Harvard NMR magnet was a 1982 Oxford narrow bore (54 mm ID) magnet obtained from the NMR facility in the Chemistry department at Harvard University. The HMRI/MDA magnet was a 2002 Oxford wide bore (89 mm ID) obtained from the Yamamoto Lab at Stanford University. Both magnets were powered up to 2.89 T, to be compatible with the microwave equipment available. A picture of the DNP system at Harvard with key components labelled is shown in Fig. A.1.1. The rest of this appendix is devoted to a description of each of the components of the combined NMR/DNP system.

A.2 Room temperature NMR probe

This was a summer project for high school student Sam Rodriques supervised by the author.

A custom NMR probe was built for room temperature NMR measurements at 2.89 T. The magnetic field studies performed in Chapter 4 required rapid transiting (< 1 s) of the probe between high and low field environments. To minimize the effect of eddy currents which would slow down this transit, we constructed the probe body from fiberglass tubing (FR4/G10, Mcmaster Carr) Fig. A.2.1(a). The diameter was kept tight with the magnet bore so that the coil would be centered

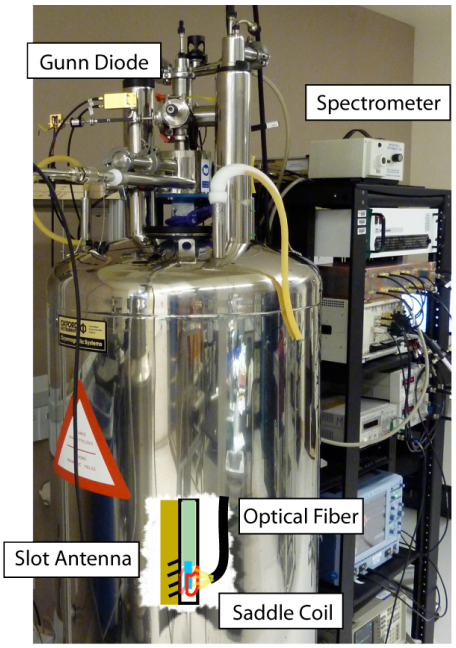

Figure A.1.1: A picture of the Harvard DNP polarizer showing key components.

in the magnet. Fiberglass components were held together with a two part epoxy (Stycast 1266, Ellsworth Adhesive). The end plate of the probe body was made from thin aluminum sheeting so that the resonant circuit would be shielded from electrical noise. Non-magnetic copper semi-rigid coaxial cable (UT-85 C, Microstock Inc) was used between the top plate and the PCB. A small port was drilled in the top plate that allowed an optical fiber to pass through the probe body to illuminate the sample for the measurements in Chapter 9.

A custom printed circuit board (PCB) was manufactured (Sunstone Circuits) to hold the elements of the resonant circuit (Fig. A.2.1(b-c)). The PCB design allowed for multiple probe heads to be built and easily interchanged for measurements of different nuclear species. The PCB was a microstrip design constructed from FR4 fiberglass board metallized with silver-plated copper tracks, and designed to be 50 Ω matched in the MHz frequency range. The backplane was removed near the active region of the coil to prevent losses. Non-magnetic high voltage variable capacitors (NMA55HV-E - Voltronics Corp) were used for tuning and matching the probe. Fiberglass rods were fitted to the end of the capacitors allowed the probe to be tuned while inside the magnet. A 7-turn solenoidal pickup coil made from pure copper wire (AWG) that was wound to fit tightly around the sample tube to maximize the filling factor.

A.3 Cryogenic DNP/NMR probe

Initial DNP measurements were done at 4.2K in a series of home-built bucket style cryostats constructed from fiberglass tubing with aluminized mylar as super-insulation. A variety of epoxies (LOR305, Stycast 2850FTBlue, Ellsworth) were tried to join the fiberglass parts. However, all

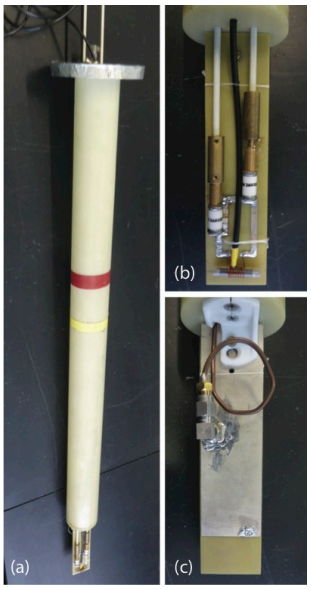

Figure A.2.1: (a) The room temperature NMR probe. (b - c) Front and back of the printed circuit board showing the tuning and matching capacitors and solenoid coil.

versions of the cryostats eventually developed cold leaks due to slightly different contraction rates between the cylindrical tubes and flat plates that were not able to be repaired, and the cryostats rendered useless.

A stainless steel flow cryostat (SpectrostatNMR, Oxford Instruments) with an operating temperature of 1.5 K-400 K was commissioned (Fig. A.3.1). Two more of these style cryostats were subsequently obtained from the Yamamoto Lab at Stanford for use in the wide-bore magnet. A low temperature insert was designed and built by the author for each of the cryostats. The frame for the insert was made from non-magnetic stainless steel and constructed by Oxford Instruments. The insert was designed with two key requirements. First, it had to fit in the very narrow bore of the cryostat (28mm ID) with adequate helium flow, and second, the sample had to be removable from base temperature to room temperature in less than 1 s.

The sample was attached at the end of a 0.125" fiberglass rod and loaded through the sample port at the top of the cryostat. This loading could only happen when the system was at room temperature or over-pressured with helium gas at base temperature. A rubber o-ring seal kept the system vacuum tight.

The insert was wired with 10 DC lines on a copper loom, and 2 semi rigid Cu coaxial cables for high frequency measurements. Cryogenic variable capacitors (NMCB10-5CKE, Voltronics Corp.) were used for tuning and matching the probe. These capacitors were located close to the pickup coil (Fig. A.3.2), and fiberglass tuning rods extended from the capacitor shafts to the top of the insert so that the tuning and matching could be adjusted at room temperature. A three-turn saddle coil made from high purity copper wire was used as the NMR pickup coil. A major source of measurement instability was probe detuning caused by structural vibrations from pumping resulting in slight capacitance shifts. To minimize these vibrations, the capacitors were fixed onto a

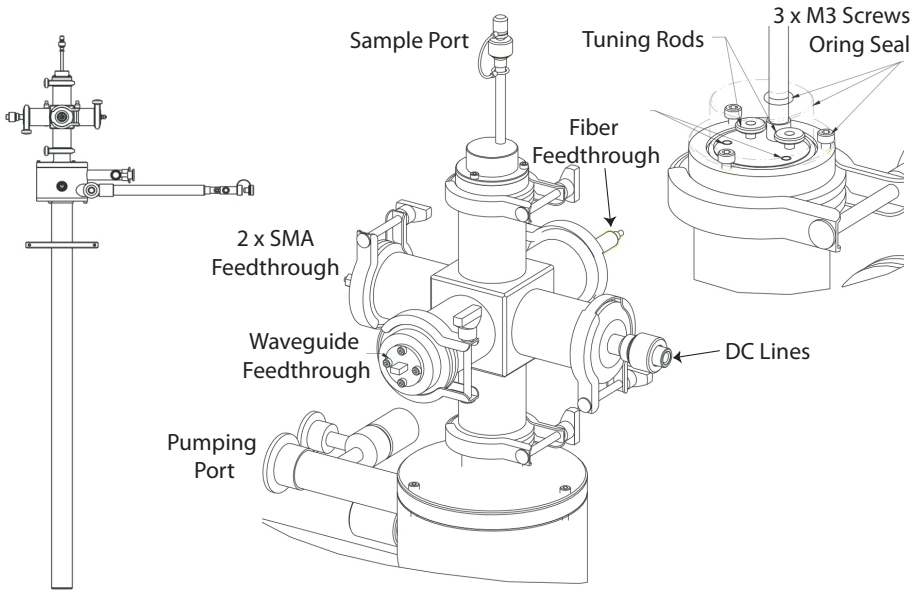

Figure A.3.1: Schematic drawings of the Harvard cryostat and top of the insert showing key features.

fiberglass plate, and the coil form milled into the outer section of a fiberglass rod. An additional baffle at the end tip of the probe further reduced vibrations, especially for higher frequency nuclei. A picture of the end piece of the insert is shown in Fig. A.3.2. A half-wavelength transmission-line probe was tested as an alternative for reducing small vibration induced capacitance shifts ((Fig. A.3.3)). In this design, small fixed capacitors are used to approximately tube the probe. The larger variable capacitors are located at room temperature and are separated from the resonant circuit by a transmission line of length $L = \lambda/2$. Although theoretically the same circuit, we found that the remote tuning design was less efficient and brought about additional rf noise into the setup.

A number of different pumping configurations were used depending on the mode of operation required. For continuous flow operation at greater than 3.5 K, a small diaphragm pump was attached to the return of the transfer line. Slightly lower temperatures (3 K) could be achieved in continuous flow operation by using a dry scroll pump (Edwards 35 or VarianTS600) in the same configuration. Even lower temperatures could be achieved by connecting the scroll pump either by itself (T = 2 K), or together with a roots blower (T = 1.5 K) directly to the main bath of the cryostat. The limiting factor in achieving lower temperatures was the flow that could be achieved through the body of the cryostat. A cernox temperature sensor capable for sensing 1.4 K - 100 K (CX-1010-AA-1.4D, Lakeshore) was attached to the outside of the saddle coil and a 4-wire measurement performed to read the temperature of the sample during microwave irradiation.

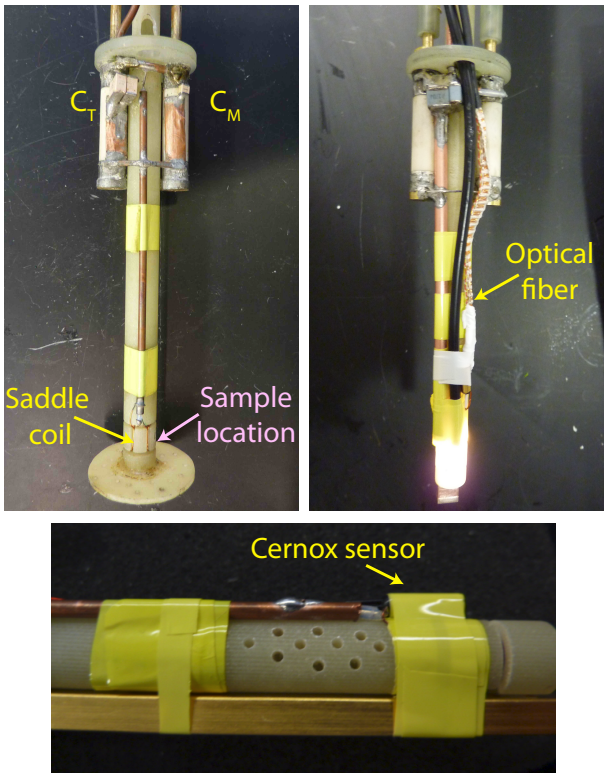

Figure A.3.2: The DNP probe showing the location of the capacitors for the resonant circuit with and without optical illumination. Holes were drilled in the support structure to ensure good helium flow directly past the sample.

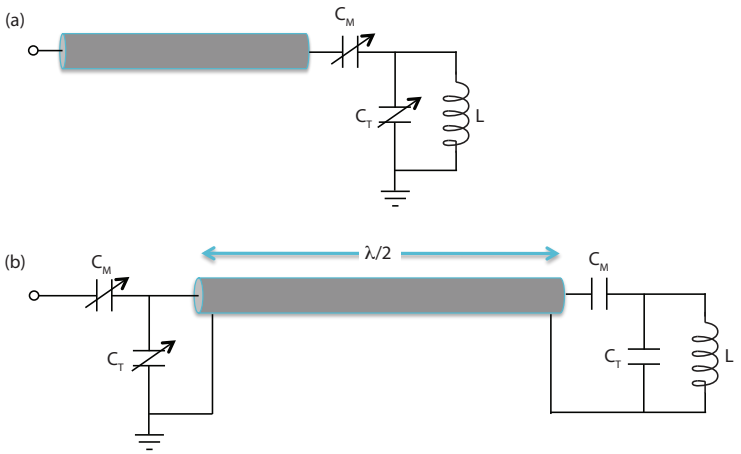

Figure A.3.3: Tuning of the resonant circuit was achieved by use of (a) local variable capacitors or (b) using a remote transmission line design..

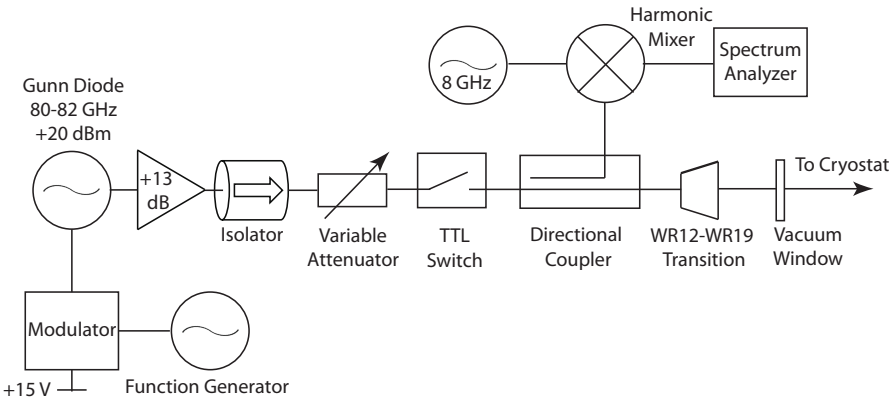

Figure A.3.4: Schematic of the microwave electronics setup showing key elements.

A.3.1 Microwave Electronics

A variety of methods can be used to generate high frequency microwave signals. For low powers (generally < 100 mW), a low frequency synthesizer can be combined with a multiplier to achieve the minimum 80-100 GHz required for high field DNP experiments. As well as affordability, the low frequency signal can be easily phase locked and so pulsed DNP with phase control as well as amplitude and frequency control is possible. For higher powers the frequency required can be generated directly using a diode oscillator (such as a Gunn or IMPATT diode), or for even higher frequencies and powers a gyrotron. We chose to use a Gunn diode oscillator as a compromise between price, output power and available laboratory space.

A schematic of the microwave electronic setup used is shown in Fig . The 100 mW Gunn diode (QTM 8121SA, Quinstar) was tunable from $80 - 82$ GHz by adjusting the internal dimensions of the cavity . For some measurements the output of the Gunn amplified to 2 W using a solid state amplifier (Quinstar) for high power measurements. The DC bias of the Gunn diode was modulated using a protection circuit (QCR10MM00, Quinstar) with a ramp function provided by a function generator (Agilent 33250). The ramp function was chosen as it provided a uniform modulation across the entire bandwidth. In comparison, a sinusoidal function overemphasizes the upper and lower frequency components of the modulated waveform. Fig. A.3.5 shows traces of the down converted signals for (a) ramp and (b) sinusoidal modulation.

A ferrite isolator (12-5000, Aerowave) was used to protect the source by preventing high power reflections. The output power of the Gunn diode was controlled with an inline variable attenuator (Millitech) and TTL driven waveguide isolation switch (HXI). The output frequency of the Gunn Diode was sampled with a directional coupler (-14 dB, 12-3000/14 Aerowave) and down converted using a harmonic mixer (HHM12C04-031, HXI) to a signal that could be directly detected on a spectrum analyzer (HP8594E). A cylindrical WR12-WR19 waveguide transition (19-1012 Aerowave) transformed the waveguide from WR12 to WR19.

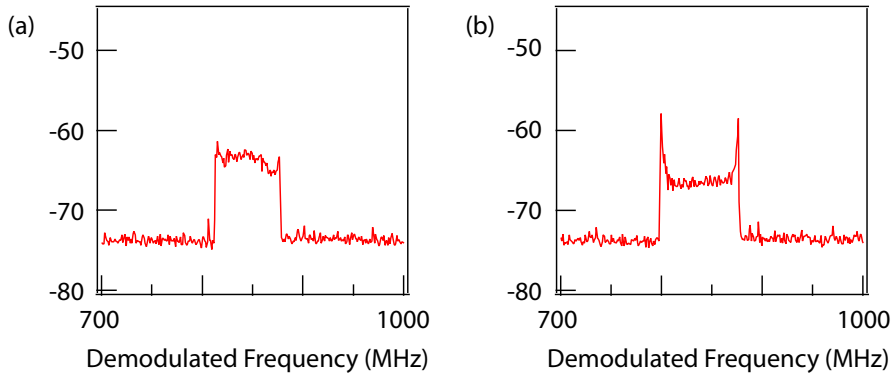

Figure A.3.5: Traces of the down converted signals for (a) ramp and (b) sinusoidal modulation of the microwave source at a rate of 2 kHz.

A.3.1.1 Waveguides and Antennas

The microwaves were transmitted from room temperature down a rectangular WR19 copper waveguide that was gold plated (non-magnetic) to prevent oxidation. Overmoding the microwaves by using the larger WR19 waveguide (instead of the WR12) reduced attenuation along the relatively large distance between the top of the cryostat and center of the magnet. The waveguide was attached to the insert via a circular flange and was thermalized at multiple stages of the insert with Cu wire. A waveguide bulkhead feedthrough (Aerowave) and mica vacuum window allowed the system to be vacuum tight.

The sample was irradiated with microwaves using a slot antenna consisting of four horizontal slots in the waveguide (Fig. A.3.6 (a)).The slot antenna design was chosen over a microwave horn as the narrow ID of the cryostat did not allow for waveguide flanges or for a 90° waveguide bend at the base. It was also compatible with the saddle coil, as the slots could line up with an opening in the side of the coil allowing for direct irradiation. A plunger at the bottom of the waveguide could be adjusted to maximize the intensity of microwave irradiation coming out of each slot.

Strong resonance occurs and electromagnetic waves are radiated when the slot length is approximately half the wavelength. The slot height is small (200 μm) when compared to the wavelength. The slots are separated vertically by a single wavelength, and the plunger is positioned with the end piece two wavelengths from the bottom slot. Adjusting the position of the plunger matches the end piece of the waveguide, and so controls the amount of power radiated out of each slot.

A.3.2 Optical Irradiation

The insert had capabilities for an optical fiber feed-through, constructed based on a design developed by Saikat Ghosh in the Ralph group at Cornell University. A small hole was drilled in a teflon piece that fitted into a Swagelok pipe fitting attached to a KF flange (Fig. A.3.7). As the swagelok fitting was tightened, it compressed the teflon piece around the optical fiber making a vacuum tight seal. The optical fiber was a 1.5mm polymer light guide (NT02-55, Edmond Optics) that

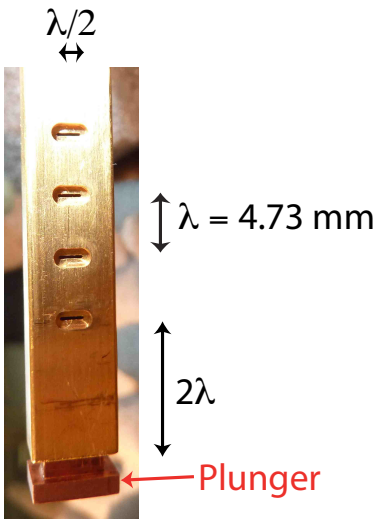

Figure A.3.6: (a) Picture of the slot antenna showing the four slots and adjustable plunger. The slots are separated by a single wavelength, and the plunger is positioned with the end piece two wavelengths from the bottom slot. Each horizontal slot is approximately half a wavelength long and the height is small (200 μm) when compared to the wavelength.

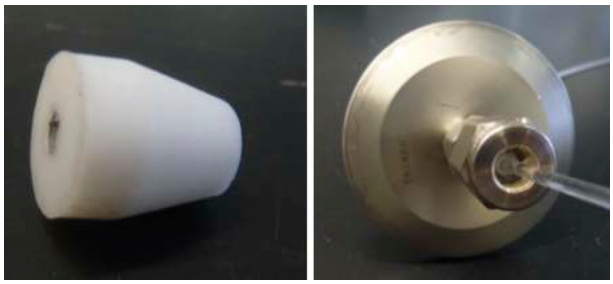

Figure A.3.7: Optical Fiber Feedthrough

allowed a large amount of power to be transmitted to the sample.

A.4 The NMR Spectrometer

We developed a compact NMR spectrometer using National Instruments (NI) (www.ni.com) PXI modular components capable of both generating phase-tunable radio-frequency (RF) signals with arbitrary quadrature amplitude modulation (QAM), and acquiring demodulated stimulus response data as needed. The system allows many pulse sequences and parameters to be specified simply and with sub-microsecond synchronization. The PXI architecture could be combined with a GPIB instrument control module allowing for control of all the other instruments in the setup.

The hardware including PXI modules, are shown in (Fig. A.4.1).

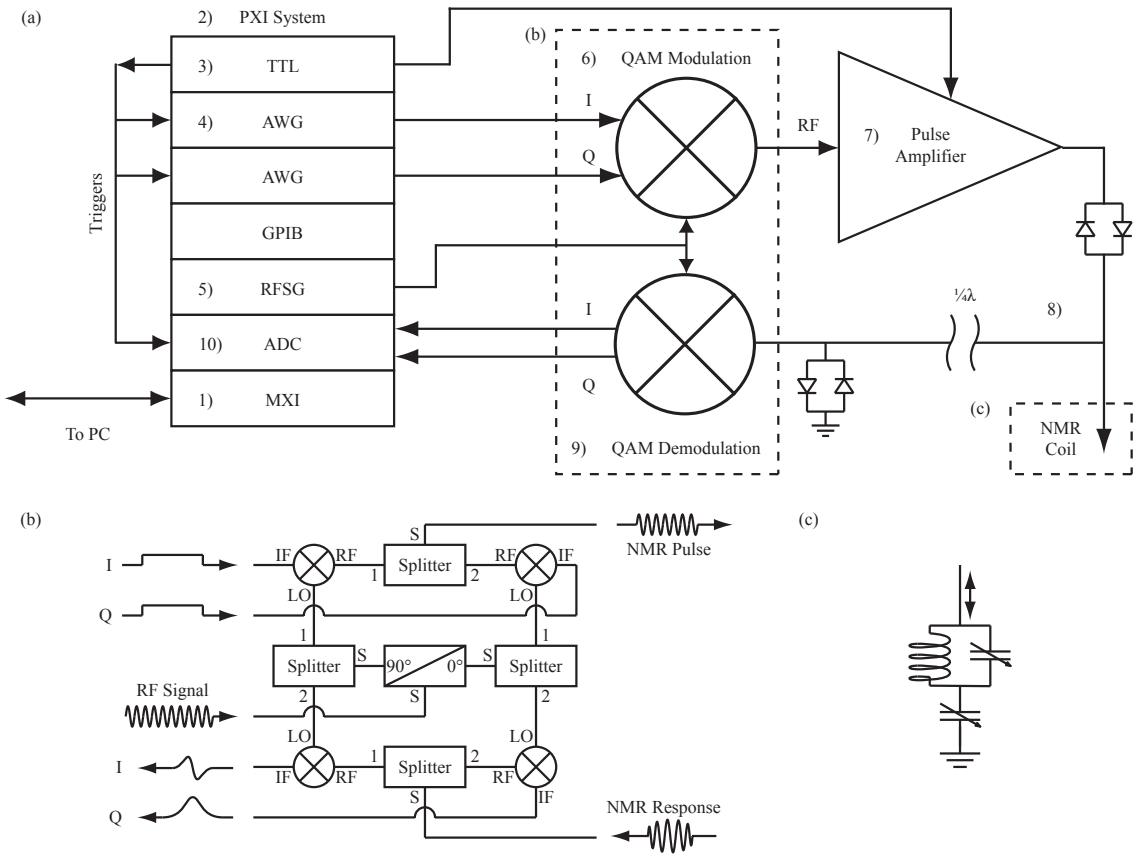

Figure A.4.1: (a) Block diagram of hardware setup. (b) Quadrature amplitude modulation/demodulation circuit that allows for phase-sensitive pulse generation and data acquisition. (c) NMR coil with tuning and matching circuit. See text for details.

1. Optical Fiber Bridge The controlling computer, a Dell OptiPlex 755 running Windows XP is connected to the PXI system via a NI PXI-PCI8336 MXI-4 optical fiber bridge. This consists of a PXI module and a standard PCI interface card for the computer connected by a 10 m fiber optic cable (up to 200 m available) providing significant noise isolation from the PC. The link can transmit at 132 Mbytes/s pulsed or 78 Mbytes/s continuous transmission.

2. PXI System The PXI modules are housed in a NI PXI-1042 8-slot chassis (up to 18 slots available). The chassis design allows modules to be exchanged rapidly, enhancing the flexibility of the system.

3. Timing and Triggering A NI PXI-6534 Digital I/O (DIO) module provides timing and triggering for the system. This module can generate up to 32 independent lines of binary digital output at up to 20 MHz. The module is loaded with an 8 to 32-bit waveform from the computer, where each bit of the waveform corresponds to a digital TTL logic output lines. These lines are fed at 2 MHz through a NI SCB-68 breakout box to each of the components requiring a TTL trigger or gate signal (Fig. A.4.1 a).

4. Pulse Generation Two NI PXI-5412 Arbitrary Waveform Generators (AWGs) modules receive TTL triggers from the PXI-6534 DIO module and use these to initiate the generation of 14-bit resolution arbitrary waveforms at up to 100 MS/s. Enabling interpolation, whereby the module intersperses data points between the samples in the waveform data, allows up to 400 MS/s output. We typically use the AWGs at 16 MS/s with 8x interpolation. Our PXI-5412 AWG has 8 MB of onboard memory (up to 256 MB allowed). The AWGS also have a sequencing mode whereby multiple waveforms can be generated serially, allowing for pulse patterning with parameters that change each cycle.

5. RF Source The NMR carrier frequency is generated by a NI PXI-5650 RF signal generator (RFSG) module. This module can generate RF signals from 500 kHz to 1.3 Ghz with 1 ppb frequency resolution at output powers up to 10 dBm.

6. Quadrature Mixing Outputs from two of the AWGs and the RFSG are fed into a quadrature amplitude modulation (QAM) circuit (Fig. A.4.1 b) [3]. The rf signal is first split and phase shifted (Minicircuits ZMSCCQ-2-50) into the inphase (I) and quadrature (Q) components of the carrier signal. Each component is then split again (Minicircuits ZFSC-2-1W-S+) before being fed to the modulation and demodulation circuits as local oscillator (LO) signals. The LOs are then mixed (Minicircuits ZFM-3-ST) with the I and Q intermediate frequency (IF) signals provided by the AWGs. The modulated I and Q signals are then recombined (Minicircuits ZFSC-2-1W-S+) into a phase-coherent pulse. This allows us to define phases and shapes for individual pulses as we choose, letting us output waveforms that can perform more complicated tasks than a single-phase output could achieve [1, 4].

7. Pulse Amplification The combined RF signal is pre-amplified to 0 dBm by a MITEQ AU-1583 low-noise amplifier then fed into a TOMCO BT00250 Alpha-S 250W RF pulse amplifier. The DIO module provides gating of the pulse amplifier. The signal is fed through a

directional coupler with 30dB reverse isolation (Werlatone C1569-10) in order to prevent power from being reflected back into the output of the pulse amplifier.

8. Transmit/Receive Isolation Series and parallel coupled crossed diodes (1N914 Philips Semiconductor, Inc), in conjunction with a $\lambda/4$ transmission line are used to isolate the NMR coil from the amplifiers similar to the method described in [5, 6]. A gated high isolation switch (Minicircuits ZASWA-2-50DR) provides further protection for the receive circuitry from the transmitted pulse.

9. Demodulation The received signal is pre-amplified by two amplifiers with 44 dB of gain (MITEQ AU-1313) and 35 dB of gain (MITEQ AU-1466) respectively. The signal is then demodulated via an equivalent mixing circuit to that described in section 6. (Fig. A.4.1 b). This produces a phase-sensitive data acquisition signal which also gives a $\sqrt{2}$ enhancement in signal-to-noise ratio (SNR)[230].

10. Data Acquisition The demodulated signal is digitally sampled by a NI PXI-5122 High-Speed Analog-to-Digital Converter (ADC). This ADC is capable of sampling at 100 MS/s with 14-bit resolution and we configured it to be triggered by an external TTL trigger. It stores data into onboard memory that can be later fetched by the PC.

A.5 Software Interface

The software interface was written by Alex Ogier and Menyoung Lee, with modifications and improvements made by the author.

The software framework for our system is based on Igor Pro, a scientific graphing and data analysis package (Wavemetrics, Inc. www.wavemetrics.com). Igor Pro contains a built-in scripting language which provides advanced mathematical functions and operations and supports the creation of custom user interfaces. NI-supplied drivers written in C together with Igor Pro's External Operation (XOP) routines provide the software interface to the PXI system. Screenshots of the software interface are shown in Fig. A.5.1. The user is given parameterized control over many aspects of the system, including design of individual waveforms and pulse sequence pattern generation with evolving parameters. A set of parameters can be specified (Fig. A.5.1 a i.) for experiment wide reference. Sequence-editing uses a matrix in an Events Panel (Fig. A.5.1 a ii.), where rows of the matrix correspond to "channels", each of which represent a device and an accompanying TTL line for triggering. This allows for hardware modules to be interchanged easily. Vertical columns correspond to "events", which are intervals of time that contain a waveform output, acquisition, or other command to be output on one or more of the TTL lines.

For each timing event, individual channels have their own event type (Fig. A.5.1 a iii.). The event type selected by the user defines the relevant parameters to create waves at runtime, select a pre-made or user-created wave for generation, or initiate an acquisition. Additional types can be defined as required to allow runtime generation of a previously undefined waveform type. Timing and positioning of each output are controlled through delay, duration and repetition parameters. Other parameters are defined by the event's type as needed. These include amplitude, frequency,

phase, bandwidth, and, in QAM-enabled pulses, a 'QCoefficient' to correct for power imbalances in the mixing circuit.

Parameter values can be entered as simple numeric values, variable references, or references to user-specified parameters. Built-in Igor mathematical expressions including function calls can be used with all of these methods. A series of global parameters can be defined in the User Parameters panel (Fig. A.5.1 b) and set by the user to allow macro scale control of the sequence. Sequences can be defined to allow easy access to more abstract values, such as the total sequence time or the amplitude of any number of transmitted waveforms, all from one global parameter.

References to user-specified parameters cascade, such that parameters can have an arbitrary number of dependencies before reaching an independent, user-entered parameter. Dependencies can be combined with mathematical expressions by including the custom function var("name"), which references parameters from inside expressions (Fig. A.5.1 b, parameter 't180'). This function can also take two special inputs, "loop" and "run". These provide access to the runtime loop and run indices so that one can make parameters dependent on their context within a sequence. Parameters are reanalyzed each time an event occurs, such as in a repeated sequence run or within a looped series of events. To define different parameter values for each iteration, semicolons are treated as delimiters by sequence run, and commas as delimiters by loop iteration. For example, in a sequence that is repeated twice, in an event that is looped 5 times, the entry

```
0, 1, 2, 3, 4; 0,(pi/2), (pi), (3*pi/2), (2*pi)
```

will increment by 1 the first 5 times through the looped event, and then increment by $\pi/2$ each loop during the second sequence run-through. Additionally, user-created waveforms can be specified, such that their values correspond to parameter values for each sequence run or looped event. For example, a waveform can be made by the standard Igor waveform assignment statements

```
Make/N=50 exponential; exponential = e^(-x/10)
```

This statement is relatively simple, and could be easily entered as an expression directly into the parameter box directly as an expression

```
e^(-var("loop")/10)
```

A.5.1 Experiment Development Cycle and Operation

In its simplest mode of operation, waveform-generation events, acquisition events, and triggers are each added to an initially blank sequence matrix, and parameters such as amplitudes and durations are specified as numeric values. Loop repetitions and sweeps are manually entered in the appropriate places within the sequence panel. Such numerically defined sequences are sufficient for simple experiments, but as experiments become more complex, it makes sense to extract some parameters to the sequence-wide User Parameters (Fig. A.5.1 b), and sequence can be saved as a template. Important parameters can be set up so as to allow a particular type of pulse sequence to be reused easily. Thus, the software can be quickly reconfigured for a different sample under study This process allows for the rapid reuse of common tasks while maintaining control of all lower-level functionality.

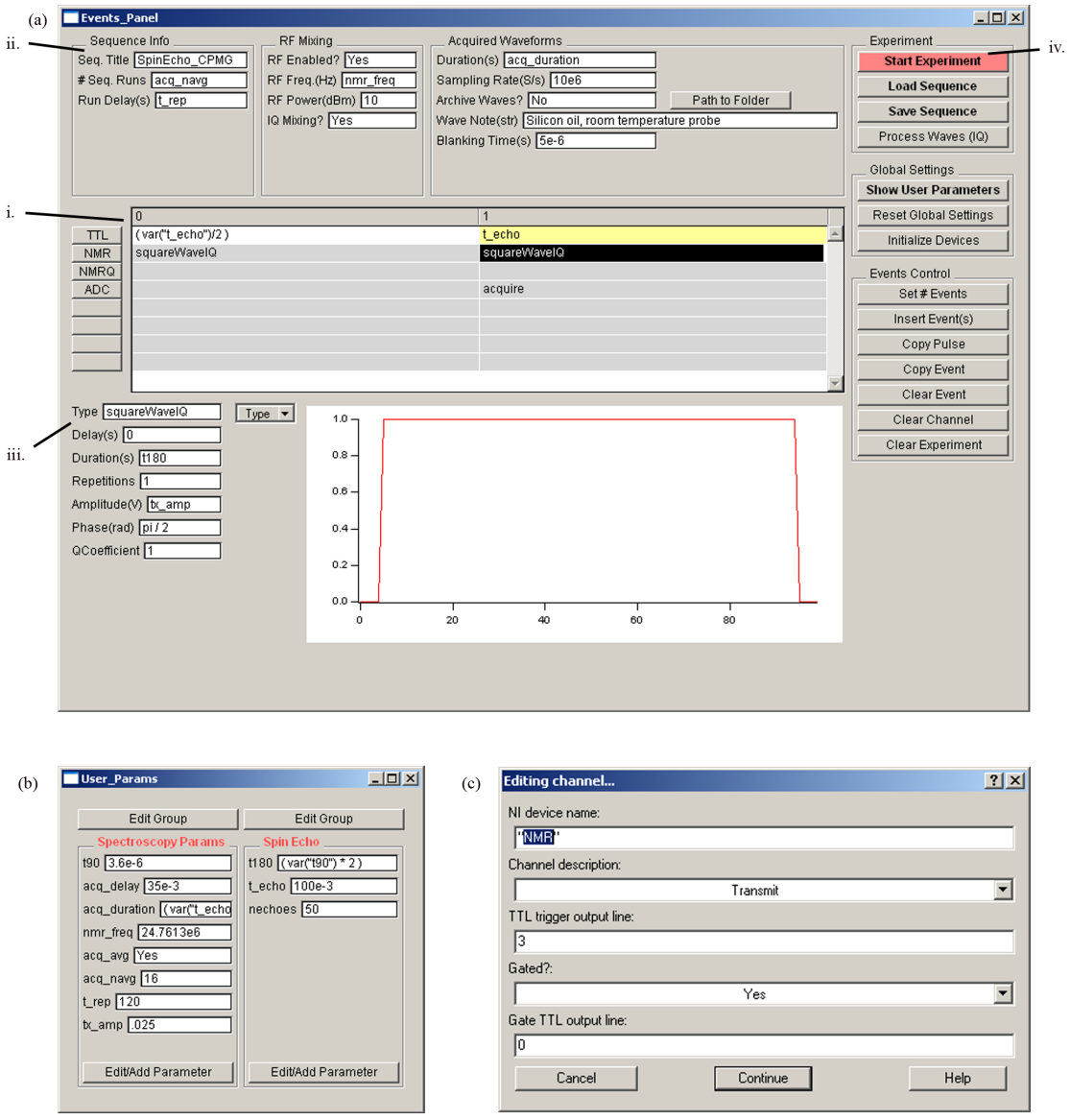

Figure A.5.1: The Igor user interface set up for a Spin Echo CPMG sequence. The sequence and panel functionality are detailed in the text. (a) Events Panel i. Sequence layout. Columns are events, rows are channels. ii. Experiment wide parameter entry boxes. iii. Pulse-specific parameters and waveform preview. iv. Experiment control buttons. (b) User Params - Customizable sequence parameters that can be called recursively from parameter entry boxes. (c) Device parameters for a channel from Events Panel.

A.5.2 Sequence Compilation and Execution

Sequence compilation and generation is a multi-step process. On the first iteration, the compiler runs through the entire sequence, resolving looped events or multi-event looped sections into a linear chain of events and defining a start time for each new event. The compiler then steps through these events and for each channel that has an output defined, creates any necessary runtime waves. Once waves are created, the compiler loops through again, loading waveforms onto the AWG cards via the NI drivers and adding triggers to the TTL waveform. After this step, the sequence is no longer controlled by the computer, and instead is timed and executed entirely onboard the PXI chassis. The computer initiates the generation, then waits for it to complete. It then retrieves any acquired data from the PXI system, and uses backwards references to the initial sequence layout to determine exactly which parameters went into each acquired waveform so that it can be named, averaged, and/or processed easily, and any accompanying parameter data that the user requests is stored along with it. This process is aware of duplicate waves, and checks each time to see if any identically parameterized waves have been created, and if so, it will use those waves rather than remake them. This allows for shorter compile times and also means that repeated waves only take up one section of memory when loaded onto an AWG.

B

Operation of the silicon polarizer - a guide for the non-physicist

This appendix acts as an operating manual for the polarizer installed first at HMRI, and later at UT-MDACC.

B.1 Cryostat preparation

i. The outer vacuum chamber (OVC) of the cryostat will need to be pumped out approximately every week. Connect the pumping line to the top of the turbo pump and to the cryostat OVC valve.

ii. Turn on the roughing pump and the turbo pump and pump the line for $\sim$ 30 min.

iii. Open the valve to the OVC and pump for > 4 hours.

iv. Close the valve before turning off the pumps. Wait until the pumps have stopped spinning before disconnecting the pumping line.

B.2 Transfer tube preparation

i. Check that the transfer tube isn't blocked. Connect a gas line to the tip of the transfer tube (Fig. B.2.1 a.). Flow dry gas (nitrogen/argon) through the transfer tube with the needle valve open and feel for flow at the end piece (Fig. B.2.1 b.).

ii. If there is no flow detected, heat gun the end piece where the needle valve is located and push nitrogen through for 10 minutes. If still blocked, it is probably a particulate rather

than ice blocking the tube. This can be removed by pushing a thin piece of wire (such as a guitar string) through the tip of the transfer tube.

Figure B.2.1: Transfer tube preparation. Check for any blockages by flowing dry nitrogen gas through the transfer tube with the needle valve open.

B.3 Sample preparation

i. Samples are packed in thin wall Teflon tubes (Wilmad LabGlass 6005). The Teflon plugs provided with these tubes make good end caps. The active area of the waveguide is 2cm, so don't make the sample much longer than this. Leave a ~3mm section empty so that the sample tube can be pushed onto the end of the sample stick.

ii. Load the sample and sample stick in via the top port and tighten the o-ring.

B.4 Cooling down to 4K

It was found that 250 L dewars could be ordered in two different heights from Praxair. The smaller dewars were better suited for use with the transfer tube and resulted in less wastage.

i. Make sure there is at least 14" of helium in the dewar (this will last for >24 hours).

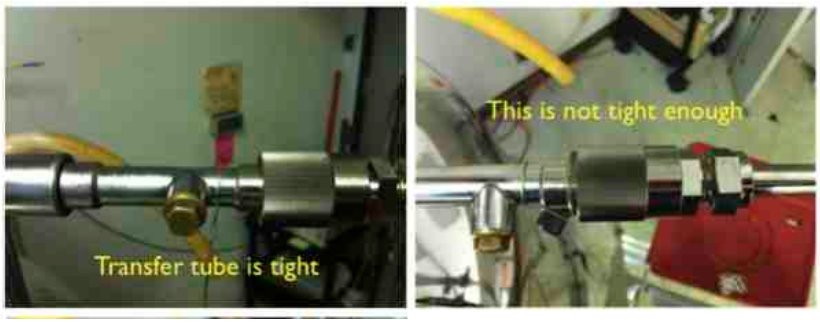

Figure B.4.1: Make sure the nut on the transfer tube is adequately tightened. A loose nut can affect the base temperature by 1 - 2 K.

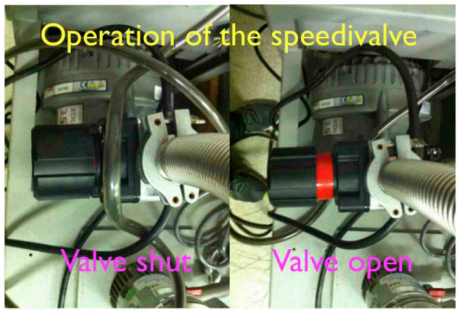

Figure B.4.2: Operation of the pump speedi-valve.

ii. Make a seal on the transfer tube with the top piece of the brass quick-connect coupler[1].

iii. Shut the overpressure valve of the dewar.

iv. Insert the long end of the transfer tube into the dewar, tightening the Christmas tree into place so that no gas escapes.

v. Take the cap off the transfer tube and insert it into the neck of the cryostat. Tighten the nut.

vi. Turn on the pump and open the speedivalve.

vii. Start the helium flow by turning the needle valve to the 9 o'clock position.

B.5 Operation of microwave components

i. Hook up the directional coupler piece to the waveguide port, and to the front of the amplifier. There is a small cut off hex wrench that works with the waveguide screws. Do not over

[1] this is sometimes called a Christmas tree

Figure B.5.1: Configuration of key microwave components.

tighten these screws as it will cause uneven pressure on the waveguide flange and result in reflections.

ii. Turn the Gunn diode (+15V) and the cooling fans (+12V) on via the Agilent power supply. Do not adjust these values or the microwave source may blow up. Turn the amplifier on by plugging in the transformer. Turn on the modulator (Agilent 33250 signal generator - ramp output, frequency = 10 kHz, amplitude = 3.3 V).

iii. Look for the signal on the spectrum analyzer. The signal should be between 830MHz-900MHz, with a peak value of 60-63dB. There is a temperature monitor on the amplifier. Make sure it stays below 35 degrees C. If it overheats it may burn out.

B.6 Polarizing

B.6.1 Checking polarization

The polarizer has a saddle coil for NMR detection at low temperatures. The resonant frequency for ^{29}Si at the polarizer field (B = 2.89 T) is 24.404 MHz. Connect the BNC to the X channel of the preamp. Usually the polarization is checked 30 minutes after the first cool down either with no saturations (zg program) or with a saturation recovery sequence with 10min delay. The SNR in XWIN via the SINO function is usually 300 for no saturations, or 60 with saturations. The program is set up in the nmrsu account in XWIN-NMR.

Figure B.5.2: There are three power supplies to turn on. (a) The Agilent DC power supply controlling the Gunn diode and cooling fans, (b) the Acopian high power supply controlling the amplifiers (28 A, 8 V) and (c) the HP function generator for controlling the modulation of the Gunn diode.

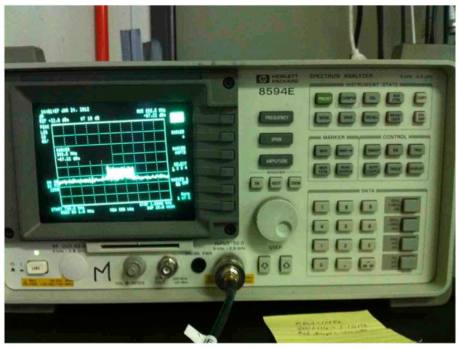

Figure B.5.3: If everything is working, you should be able to see the demodulated microwaves on the HP spectrum analyzer (0.8-0.9 GHz).

B.6.2 Polarization

The operating temperature is $\sim$ 3 - 4 K. This corresponds to 190-220 ohms on the resistance meter. The polarizer should stay cold with the needle valve at the 9 o'clock position. If there is too much flow (the speedivalve frosts up), slowly close the needle valve ($\sim$10 degrees every 30 mins) If the resistance drops (temperature increases) open the needle valve more. Alternatively, increase the pressure in the helium storage dewar (6 - 9 psi is good) using the electrical pressure builder. If this doesn't fix the problem then the helium supply is low and the experiment should be wrapped up ASAP.

B.7 Removing sample for measurement

i. Stop pumping by shutting the speedivalve (don't turn off the pump until the speedivalve is shut).

ii. Open the needle valve (anti-clockwise) to increase the flow.

iii. Wait until the cryostat over-pressures (you will hear a hissing sound from one of the valves) and then unscrew the sample stick and pull out.

iv. When climbing down the ladder make sure that the sample remains orientated towards the bore of the magnet, with the sample stick going first.

B.8 Warming up

i. Put the cap back on the sample stick port as soon as possible and close the needle valve.

ii. Turn off the amplifier, microwave source power supply and the modulator.

iii. Unhook the microwave setup from the cryostat.

iv. Remove the transfer tube from the cryostat neck. Depressurize the dewar and remove the transfer tube.

B.9 Troubleshooting and Maintenance

i. Cryostat doesn't start to cool down.- The transfer tube is probably blocked with ice. Pull it out and warm it up with a hair dryer/heat gun on low setting. Flow dry nitrogen through to dry out the needle valve.

ii. No signal after polarization check - Check power output and frequency on the spectrum analyzer. Check wobb of NMR detection coil. You will have to warm up to adjust this. The waveguide may have ice in it. Warm up and clean it out with ethanol. Remove the plunger and the mica window. You will have to recalibrate the plunger afterwards. This is complicated so avoid doing this.

C

Detection of particle binding by rotation motion

The ability to detect the presence and location of specific molecular compounds *in-vivo* is an outstanding problem in the biological sciences. In this Appendix we examine a scheme for detecting the successful of binding of biological compounds to the surface of functionalized silicon nanoparticles. Binding is detected through a change in the line width of the ^{29}Si NMR signal that occurs due to a slowing of the rotational motion of the nanoparticle that occurs with an increase in particle radius. We model the rotational correlation times of silicon nanoparticles of a range of sizes in a variety of fluids, and discuss the possibility of this scheme successfully detecting binding to the cell wall of cancer cells and small proteins in solution.

Detection of biological binding using the Brownian motion of magnetic nanoparticles has previously been performed using a direct measurement of the ac magnetic susceptibility [231]. The binding of avidin-coated Fe_2O_3 nanoparticles to biotinylated S-protein suspended in phosphate buffered saline (PBS) was detected by inductively monitoring the change in frequency and phase of an AC field applied with a nearby coil [231]. More sensitive measurements of nanoparticles binding to a surface have been performed using a high-temperature dc superconducting interference device (SQUID). In the presence of an aligning field the nanoparticles develop a net magnetization, which relaxes as the field is turned off. Unbound nanoparticles relax rapidly by Brownian motion, whilst bound nanoparticles undergo a slow Neel magnetic relaxation which is detectible by the SQUID [232]. Although successful as a proof of concept, *in-vivo* detection using animal models has proved difficult due to the high concentration of nanoparticles needed for accurate measurement. This technique also provides no spacial determination of the nanoparticles location *in-vivo*, and so therefore is not beneficial for detection of tumors.

C.1 Physical principles

C.1.1 Brownian motion of particles in solution

Small particles and molecules in solution undergo constant diffusion as a result of thermal fluctuations. This diffusion is dependent on the size of the particle or molecule, as well as the temperature and type fluid it is diffusing in. The hydrodynamic radius, or Stokes radius, is a measure of the radius of a solid sphere that behaves equivalently to the particle or molecule and is calculated from the particle's diffusion constant D in a fluid of viscosity η as;

$$R_H = \frac{k_B T}{6\pi\eta D} \tag{C.1}$$

where $k_B$is the Boltzmann constant and T is the temperature in Kelvin.

For a non-spherical molecule such as a protein, the hydrodynamic radius of the molecule is much less than the actual dimensions of the molecule. However, for a nanoparticle consisting of a solid core and surface functionalized with small molecules will have approximately the same hydrodynamic radius its actual radius.

C.1.2 Motional Narrowing in Nuclear Magnetic Resonance

The relaxation of spin-1/2 nuclei such as ^{29}Si in a rigid lattice is dominated by dipole-dipole interactions between the nuclei and other nearby magnetic fields. In liquids and gases, however, rapid motions amongst spins cause a significant narrowing of the Fourier-transformed linewidth, as the local field seen by a given spin will fluctuate rapidly in time. If the fluctuations occur at a rate much faster than the nuclear Larmor frequency, then the nuclei will see only the averaged field over this period, which is much smaller than the instantaneous value of the local field. Assuming the particles undergo Brownian motion, the rate of fluctuations in the field can be described by the Stokes-Einstein equation with a rotational correlation time τ_c,

$$\tau_c = \frac{4\pi\eta r^3}{3k_B T} \tag{C.2}$$

where η is the viscosity of the medium,r is the radius of the particle, $k_B$is the Boltzmann constant and T the temperature in Kelvin[1]. This is a well understood phenomenon and has been widely used in protein characterization, as the longer coherence times brought about by tumbling offer enhanced signal resolution.

A colloid of well dispersed nanoparticles will also undergo the same motional narrowing phenomenon, whereby the degree of narrowing is determined by the size and shape of the nanoparticle, as well as the temperature and viscosity of the solution. The degree of narrowing will not be as great as for individual molecules, as in each nanoparticle there will be many spins nearby to one and other that will rotate together as the particle tumbles in solution. The use of colloidal suspensions in specific cases has been used as an alternative to NMR of solids, in cases where magic

[1]This equation assumes that the particles are spherical.

Material	Viscosity (Pa.s)
Methanol	5.44×10^{-4}
Water	1×10^{-3}
Glycerol	1.5
Blood Plasma	8×10^{-3}
Cell Culturing Material	1.2×10^{-3}
HeLa Cell Cytoplasm	1.4×10^{-3}

Table C.2.1: Body temperature viscosities of modeled fluids.

angle spinning is not available. A thirty fold reduction in the width of the ^{31}P line has been seen when comparing 25 nm calcium hydroxyapatite particles in a colloidal suspension compared to the solid form [233].

C.2 Modeling

Numerical modeling was undertaken to determine changes in the rotational correlation times of nanoparticles under a number of different binding scenarios, including binding of nanoparticles to a cell wall and binding to specific proteins inside the cell in a range of different fluids (Table C.2.1).

Figure C.2.1 shows calculated rotational correlation times versus hydrodynamic radius for nanoparticles in fluids described in Table C.2.1. All simulations are carried out at body temperature (37° C). The shaded area is the range of rotational correlation times close to the Larmor frequency available for ^{29}Si in clinical MRI scanners. A detectable change in the NMR line width should be observable for situations where the hydrodynamic radius changes between the shaded and unshaded regions. From this we can see that the upper size limit where motional narrowing will be seen is approximately 200 nm.

C.2.1 Binding of Functionalized Nanoparticles to Cells

Nanoparticles can be surface functionalized with a variety of ligands that show preferential binding to cancer cells *in-vivo*[235]. As the nanoparticle is injected through the vascular system, its size is limited to $\sim 250\ nm$, and so therefore is significantly smaller than the cell that it attaches to ($\sim 5 - 8\ \mu$m).

C.2.1.1 Folic acid

Nanoparticles surface functionalized with folic acid have been shown to have preferential binding to prostate cancer cells [235], due to the increase in activity of folic acid detectors on the surfaces of these cells. The attachment of folic acid to aminated nanoparticles is undertaken by the reaction

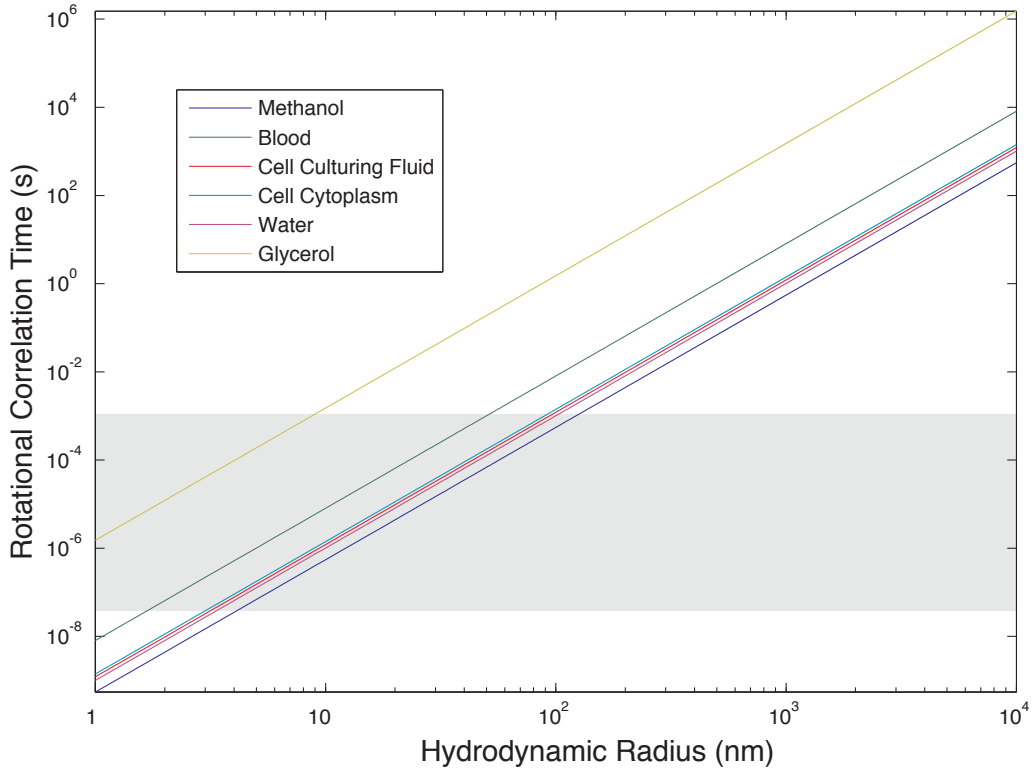

Figure C.2.1: Rotational correlation time versus nanoparticle hydrodynamic radius for nanoparticles suspended in fluids of different viscosities. All simulations are carried out at body temperature (37°C). The shaded area is the range of rotational correlation times close to the Larmor frequency available for in clinical MRI scanners.

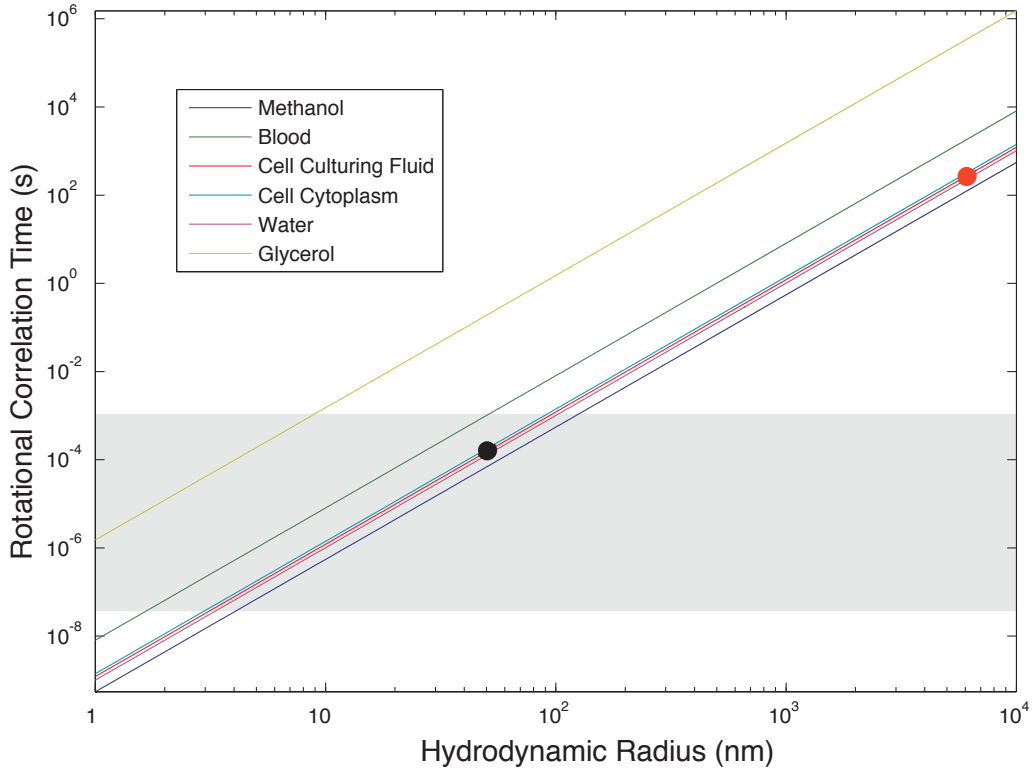

Figure C.2.2: Binding of a 20 nm silicon nanoparticle functionalized with folic acid (total size $\sim$ 54 nm) to the cell wall of a cancer cell of size $\sim$ 8μm in blood plasma, the rotational correlation time will change from 10^{-4} s (black) to 100 s (red)

with an activated ester derivative of folic acid [234], and results in an increase of 34 nm in the hydrodynamic radius of the particle. Thus, this sets a lower limit on the initial hydrodynamic radius of the particle before binding occurs. If we consider a 20 nm silicon nanoparticle functionalized with folic acid (total size $\sim$ 54 nm) binding to a cell of size $\sim$ 8μm in blood plasma, the rotational correlation time will change from $10^{-4}s$ to 100 s, and a significant change in the NMR line width should be observable (Fig. C.2.2).

C.2.2 Detection of Proteins

Nanoparticles can be functionalized with DNA that is unique to a protein target of interest [236]. Ultra-sensitive detection of protein targets using magnetic separation of functionalized magnetic nanoparticles has been achieved in a laboratory environment [237], however this technique is complex, and does not allow for detection *in-vivo*. The attachment of monoclonal antibodies such as immunoglobulin increases the hydrodynamic radius of the nanoparticle by approximately 5 nm [238], and the binding of another protein to the monoclonal antibody increases the hydrodynamic radius by an additional 1-5 nm. If we consider a 10 nm silicon nanoparticle functionalized

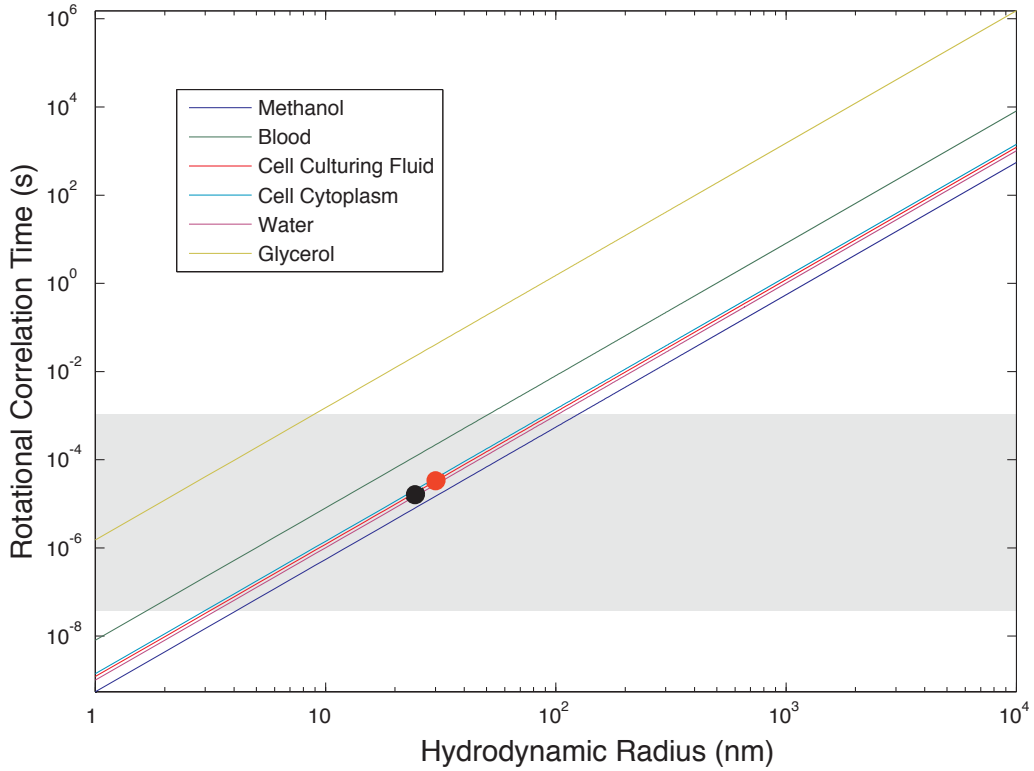

Figure C.2.3: Binding of 10 nm silicon nanoparticle functionalized with immunoglobulin (total size $\sim$ 15 nm) to proteins in the cell cytoplasm, the rotational correlation time will change from $1x10^{-5}s$ (black) to $2x10^{-5}s$(red)

with antibodies, giving a change in rotational correlation time of $1e^{-5}$ s.

C.3 Conclusion

We have briefly examined the detection of binding of functionalized silicon nanoparticles to targets such as cells and proteins *in-vivo* using magnetic resonance. For small nanoparticles of less than 200 nm in size, there should be a significant observable change in the NMR line width when the nanoparticle binds to the wall of a cell with dimensions of between 5-10 μm.

The same principles described here may be used to detect the location and timing of the delivery of a payload from nanomaterials such as porous silicon that are currently being investigated a drug delivery devices [239]. A change in the magnetic susceptibility of the material that is contained in the pores of porous silicon nanoparticles, such as therapeutic agent to cytoplasm fluid, may also lead to a detectable change in the NMR line width. Additionally, nanoparticles functionalized with temperature-responsive N-isopropylacrylamide-based functional copolymers [240] could act as a local temperature sensor and lead to further understanding of the cellular processes changing in situations of hypothermia *in-vivo*. This copolymer group has a critical transition tem-

perature of approximately 32 C, whereby the structure changes from a coil shape to globule. The hydrodynamic radius of 25nm nanoparticles has been demonstrated to change by a factor of 50% (from 60nm at 25 °C to 30nm at 39 °C) around this critical temperature point.

D

Preparation and Characterization of Silicon Particles

D.1 Ball milling silicon particles from silicon wafer

A variety of silicon wafers of different doping density were investigated for use as long-T_1 imaging agents. The particles with the best size-adjusted T_1 times were made from nominally undoped float-zone grown Si wafers (Silicon Quest International $\langle 111 \rangle$ oriented) with residual p-dopants and nominal resistivity 30-100 kΩ-cm, depending on batch.

Ball-milled particle were processed as follows. Whole wafers were shattered using a mortar and pestle. Batches of 8.5 g wafer shards were dry ground for 10 minutes at 400 rpm in a planetary ball mill (Retsch PM100) using ten 1 cm diameter zirconia balls. The resulting powder was mixed with 20 ml of ethanol and milled under similar conditions for another 3.8 h. For a final milling, also at 400 rpm, fifty 3 mm diameter zirconia balls were used. The slurry was milled for times ranging from 1 h to 26 h, to give a size distribution between 10 nm and 10 μm depending on the milling time.

D.2 Size separation of silicon particles by centrifugal sedimentation

The ball-milled silicon nanoparticles in ethanol were separated by size using a centrifugal sedimentation process. Centrifuge parameters were calculated using the Stokes equation[129] according to,

$$\vec{v}_a = \frac{2}{9}\frac{(\rho_p - \rho_f)}{\mu} d^2 \vec{a} \tag{D.1}$$

where $\vec{v}_a$ is the velocity of the particles settling along an acceleration vector $\vec{a}$, which can be due to gravity or centrifugation. The density of the particles is ρ_p, the density of the fluid is ρ_f, μ is the viscosity of the fluid and d is the diameter of the particles.

In a laboratory centrifuge, the velocity and acceleration vectors are substantially along a radial line R and centripetal force is responsible for the primary component of acceleration of particles suspended in the fluid.

Eq. D.3 can be rewritten as a first order differential equation

$$\frac{dR}{dt} = C_o \omega^2 R \tag{D.2}$$

where

$$C_o = \frac{2}{9}\frac{(\rho_p - \rho_f)}{\mu} d^2 \tag{D.3}$$

Solving this we can extract a cutoff diameter

$$d_{co} = \sqrt{ln(\frac{R_f}{R_o})\frac{9\mu}{2(\rho_p - \rho_f)\omega^2 t}} \tag{D.4}$$

where R_o represents an initial position of a particle in the fluid, R_f represents a final position of a particle in the fluid, and t represents the duration of centrifugation at angular velocity ω.

Centrifuge conditions can therefore be set such that particles that remain in the supernatant are all smaller than d_{co}. Those that collect at the bottom of the tube, commonly referred to as the pellet, are a range of sizes. However, repeated sonication and centrifugation with the same parameter set will eventually result in a clear supernatant. At this point, all particles in the pellet are larger than d_{co}.

From repeated sonication and centrifugal separation with an upper and lower cutoff, a number of discrete particle size groups could be obtained from a ball milled sample with a wide range of initial sizes (Fig. D.2.1). The actual diameter of the particles measured by SEM image analysis was generally twice as big as those calculated by Eq. D.4.

Generally swinging rotors were used in the centrifuge as they resulted in the pellet being collected in the bottom of the centrifuge tube.

D.3 Surface functionalization of silicon particles

Functionalization of the silicon surface is essential for biocompatibility and also targeting. Figure D.3.1 shows a schematic of the two step functionalization process used for the in-vivo experiments. A silane linker ((3-Aminopropyl)triethoxysilane) was first attached that directly bonds to the silicon oxide surface. The end of this linker chain was chosen to have an amine functional group that is used for later bioconjugation steps, however the chain could be chosen to have a variety of other chemical groups that can be used to modify the surface electrochemistry or if different second functionalization step was required. The amine group is reactive with the ester

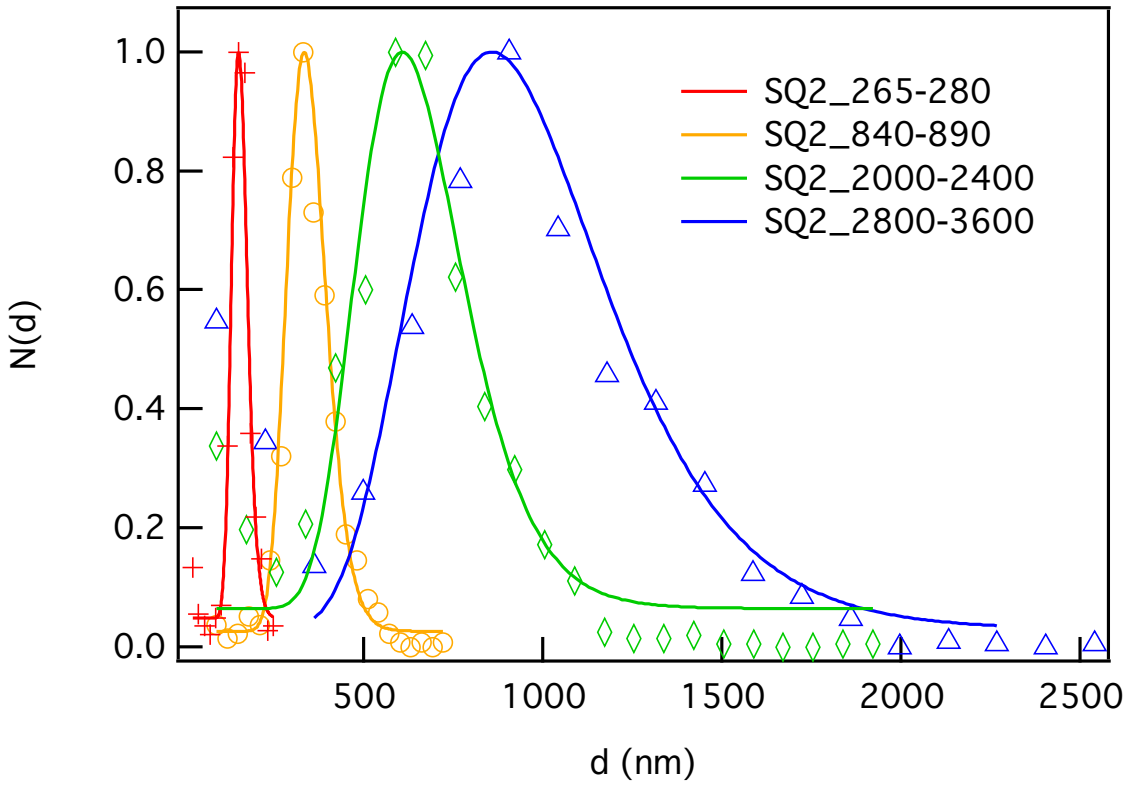

Figure D.2.1: Silicon particles could be size separated by centrifugal sedimentation into distinct batches. Size distributions of ball milled silicon nano and microparticles were determined by SEM image analysis.

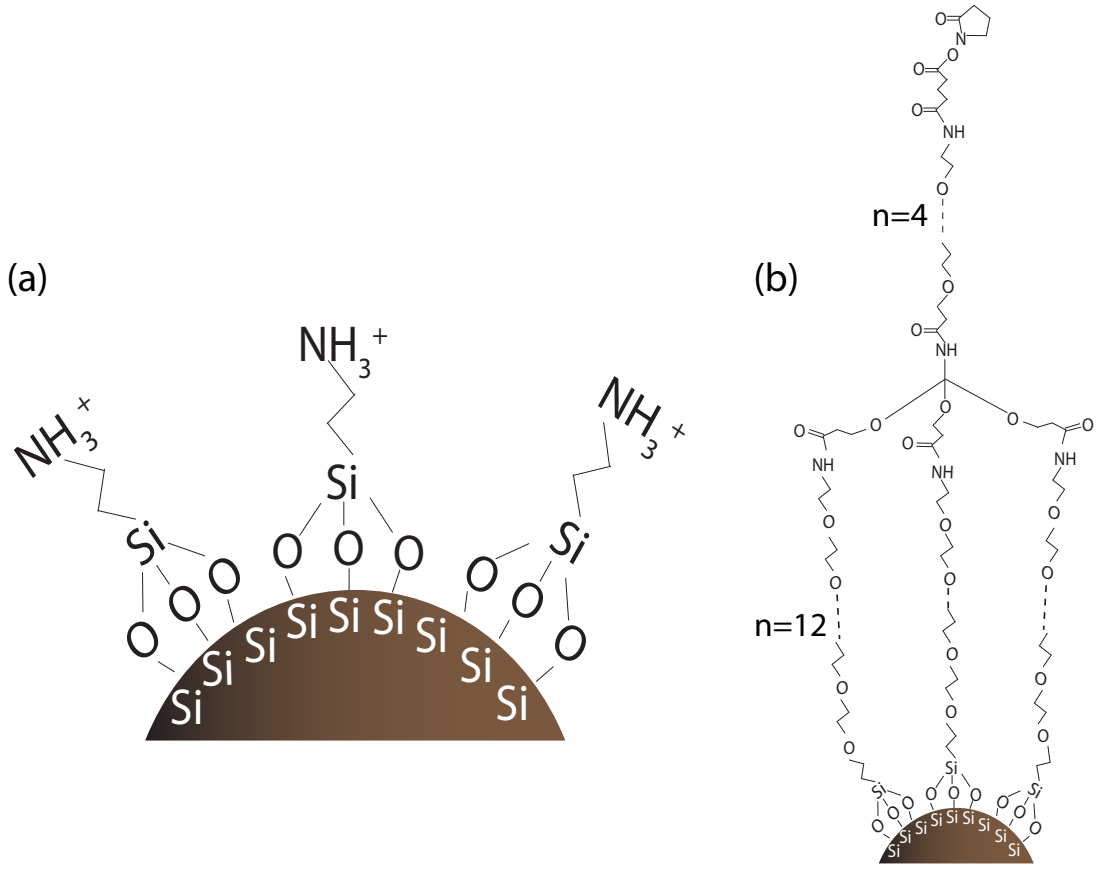

Figure D.3.1: Schematic of nanoparticle functionalization. (a) The silicon oxide surface is first functionalized with APTES. The amine group at the end of the APTES molecule is highly reactive. (b) (NHS-dPEG4-(m-PEG12)3-ester is used as the second functionalization group.

groups in the (NHS-dPEG4-(m-PEG12)3-ester molecule, and a second functionalization step is achieved. The PEG chain neutralizes the surface charge of the particles and prevents them from agglomerating in biological media.

D.3.1 Amination using (3-Aminopropyl)triethoxysilane

Amination was performed using (3-Aminopropyl)triethoxysilane (APTES, Sigma, 99%). Approximately 100 mg of silicon nanoparticles were added to 45 mL of acidified 70% ethanol (0.04% v/v, adjusted to pH 3.5 with HCl) and the solution was placed in an ultrasonic bath for five minutes. APTES (0.15 M) was then added and the solution was shaken for 24 hours on a plate shaker. Excess silanes were removed from the nanoparticle solution by washing and resuspending three times in ethanol buffer, with the final resuspension performed with 10 mL of ethanol buffer.

D.3.2 Fluorescamine assay

Successful amination was assessed using fluorescence spectroscopy. The concentrations of all of the particles were equalized by adjusting their absorption at 420 nm using a spectrophotometer (SpectraMax Plus, Molecular Devices). The fluorescamine reagent was prepared by dissolving 3.5 mg of fluorescamine (Sigma) in 1 mL of dimethyl sulfoxide (DMSO). Within a 96-well standard opaque tray, 10 μL of the fluorescamine solution were added simultaneously to each well containing 40 μL of nanoparticles and mixed thoroughly for one minute. Fluorescence was measured using an excitation at 390 nm and emission at 465 nm (SpectraMax Gemini XPS, Molecular Devices).

D.3.3 Pegylation

1 g of PEG (NHS-dPEG4-(m-PEG12)3-ester (Quanta Biodesign)) was mixed in 500 μL of ethanol buffer and heated briefly at 50 °C to dissolve. Approximately 1 g of aminated particles were added to this solution and it was placed in a heated ultrasonic bath for 24 h. To remove the unreacted PEG, samples were centrifuged and resuspended twice in acidified ethanol and finally in a phosphate-buffered saline solution (PBS, 0.015 M NaCl buffer).

E

Animal Surgery Procedures

E.1 Intragastric catheter

A normal saline-primed two-foot length of PE-50 tubing was inserted into the stomach through a left upper quadrant abdominal incision after overnight fasting (at least 8 hours). The catheter tip was given a very slight bevel ($\sim$10 °from vertical) so that the catheter could pierce the stomach wall under finger pressure but not lacerate the stomach from the inside. Stomach puncture occurred midway along the greater curvature through a purse string suture, formed by 6-0 silk ligature. Peritoneum and skin were then closed around the catheter with 4-0 silk.

E.2 Intraperitoneal catheter

A saline-primed two-foot length of PE-50 tubing was inserted into an 18 gauge needle so that the needle could act as the cutting tip for the catheter. The catheter/needle combination was then inserted through a tented patch of suprapubic abdominal skin. The needle was withdrawn over the catheter, and the catheter was secured to the skin with 4-0 silk suture.

E.3 Intravenous catheter

Multiple attempts were made through various routes to gain intravenous access. The silicon suspension flowed best under continuous sections of large bore tubing and appeared to exhibit shear thickening when exposed to the pressure from the syringe. The small scale of mouse anatomy, however, did not lend itself well to the placement of large bore catheters nor the infusion of large volumes (> 1 cc). The typical mouse tail vein catheter (Braintree Scientific MTV-1), for instance, had a joint between two different tubing sizes (25 to 32 gauge inner diameter) and often blocked at

the joint between the two tubing sizes. The largest catheter that could be reliably fit into the mouse tail vein was PE-20 ($\sim$ 22 gauge I.D.). The PE-20 catheter occasionally collapsed the opening to the vein and insinuated itself between the vein and its vascular sheath. Additionally, the catheter was quite stiff due to its thick wall and sometimes lacerated the vein if a bevel was introduced to facilitate cannulation. There was room for optimization of the catheter system.

E.4 Tumor catheter

The in situ prostate tumor of TRAMP mice was catheterized in a way similar to the intraperitoneal method. Typical tumors were large enough (ca. 2 cm) to palpate and immobilize without abdominal incision. PE-50 tubing was inserted with the aid of an 18 gauge needle, and the needle was removed over the catheter. 4-0 silk suture secured the catheter to the skin.

This thesis was typeset using LaTeX, originally developed by Leslie Lamport and based on Donald Knuth's TeX. The body text is set in 11 point Arno Pro, designed by Robert Slimbach in the style of book types from the Aldine Press in Venice, and issued by Adobe in 2007. The template for this thesis was modified from one provided by Jordan Suchow released under the permissive MIT (X11) license.